Kyaw, Si Thu (2013) Finite element modelling of stresses and failure within plasma spray thermal barrier coating systems. PhD thesis, University of Nottingham.

**Access from the University of Nottingham repository:**
http://eprints.nottingham.ac.uk/27952/1/605801.pdf

**Copyright and reuse:**

The Nottingham ePrints service makes this work by researchers of the University of Nottingham available open access under the following conditions.

- Copyright and all moral rights to the version of the paper presented here belong to the individual author(s) and/or other copyright owners.
- To the extent reasonable and practicable the material made available in Nottingham ePrints has been checked for eligibility before being made available.
- Copies of full items can be used for personal research or study, educational, or not-for-profit purposes without prior permission or charge provided that the authors, title and full bibliographic details are credited, a hyperlink and/or URL is given for the original metadata page and the content is not changed in any way.
- Quotations or similar reproductions must be sufficiently acknowledged.

Please see our full end user licence at:
http://eprints.nottingham.ac.uk/end_user_agreement.pdf

**A note on versions:**

The version presented here may differ from the published version or from the version of record. If you wish to cite this item you are advised to consult the publisher's version. Please see the repository url above for details on accessing the published version and note that access may require a subscription.

For more information, please contact eprints@nottingham.ac.uk

The University of
Nottingham

# Finite Element Modelling of Stresses and Failure within Plasma Spray Thermal Barrier Coating Systems

**SI THU KYAW**
BEng (Hons)
The University of Nottingham

**This thesis is submitted to The University of Nottingham for the degree of Doctor of Philosophy**

April 2013

# Abstract

Air plasma sprayed thermal barrier coating (APS TBC) systems are usually applied to engine components to reduce the temperature of the substrate and increase the efficiency of engines. However, failure of these coatings leads to oxidation and corrosion of the substrate. Therefore, a thorough understanding of the coating failure is necessary to predict the lifetime of coated components.

This project has carried out stress analysis and prediction of subsequent failure of APS TBC systems associated with sintering of the TBC, oxidation of the bond coat (BC), substrate geometry, undulations at the coating interfaces and coating fracture toughness. Stress analysis is crucial for predicting TBC failure as stresses in the vicinity of the coating interfaces cause cracks and subsequent coating delamination.

The Finite element (FE) method was used for stress analysis of TBC systems at high temperature stage and at cooling stage after operation. Initially, FE model of an axisymmetric unit cell representing the slice of a coated cylinder was used. Different radii for cylinders were used to investigate the significance of substrate curvature on coating stresses. The effect of asperities at the coating interface on residual stresses was observed using 3D models. The models were built based on the actual geometries of asperities, which were extracted from 3D SEM images of the coating interfaces. An Arrhenius approach was utilised to implement changes in mechanical and physical properties of TBC due to sintering. BC oxidation and related changes in its composition were also implemented. The accuracy of assumptions for FE models was validated by comparing the evaluated stresses against experimental results by project partners. Finally, the effects of stresses and fracture toughness of the coatings and coating interfaces on failure of the TBC system were studied, using cohesive surface modelling and extended finite element modelling (XFEM) methods.

# Acknowledgements

I would like to give my kindest gratitude to my supervisors, Dr Arthur Jones, Prof. Tom Hyde and Prof. Graham McCartney for their assistance in technical issues and for giving me encouragement throughout the process of my PhD.

I would like to acknowledge the support of The University of Nottingham, The Energy Programme, which is a Research Councils UK cross council initiative led by EPSRC and contributed to by ESRC, NERC, BBSRC and STFC, and specifically the **Supergen** initiative (Grants GR/S86334/01 and EP/F029748). I am also grateful to David Rickerby, Paul Morrell and Gyaneshwara Brewster (Rolls Royce), Jon Wells (RWE npower) for their contributions in providing experimental data and technical advices.

I like to thank Prof. Hugh Evans from The University of Birmingham for advice about oxidation process of the MCrAlY BC. I extend my sincere thanks to project partners, Dr Dong Liu and Prof. Peter Flewitt (The University of Bristol), for their contributions in stress measurements data. I like to thank Prof. Graham McCartney and Dr. Saman Saeidi for supplying coating specimens for stress measurements. My sincere gratitude also goes to Dr Mudith Karunaratne and Dr Mark Jepson from University of Loughborough for their contribution in data for finite diffusion model and three-dimensional images of coating interfaces.

Special thank is given to my colleagues, particularly Dr Rupesh Patel, Dr David Tanner and Dr Anas Yaghi, for their support.

Finally, I would like to thank my parents (U Shein Min and Daw Chu Khin Ma), my family and my friends from Myanmar for giving me moral support.

# CONTENTS

# Nomenclature

| | |
|---|---|
| APS | Air plasma spayed |
| BC | Bond coat |
| BDTT | Brittle to ductile transition teamperature |
| C3D8 | 8-node linear brick elements |
| CAX4R | 4-node axisymmetric elements with reduced integration scheme |
| CETOL | Creep strain error tolerance |
| CIM | Cohesive surface interaction method |
| COPEN | Direct crack opening |
| CPE4R | 4-node plane strain elements with reduced integration scheme |
| CPEG4R | 4-node generalised plane strain elements with reduced integration scheme |
| CSLIP | Shear crack opening |
| CSYS | Coordinate system |
| CTE | Coefficient of thermal expansion |
| CZM | Cohesive zone modelling |
| DEPVAR | Solution dependent variable within ABAQUS subroutines |
| d.o.f | Degree of freedom |
| EB-PVD | Electron beam vapour deposition |
| FD | Finite difference model |
| FEA | Finite element analysis |
| FNPS | Fogale nanotech profilometry software |
| GPS | Generalised plane strain |
| HVOF | high velocity oxygen fuel coating |
| LMP | Larson-Miller parameters |

| | |
|---|---|
| OEM | Original equipment manufacturer |
| OOF | Object oriented finite element analysis |
| PBR | Pilling-bedworth ratio |
| PLPS | Photo-stimulated luminescence piezo-spectroscopy |
| PPM | Portable pixel map |
| PS | Piezospectroscopic |
| ROM | Rule of mixture |
| RS | Raman spectroscopy |
| SD | Standard deviation |
| SEM | Scanning electron microscope |
| SPCT | Small punch creep test |
| SPPS | Solution-precursor plasma sprayed process |
| TBC | Thermal barrier coating |
| TGO | Thermally grown oxide |
| UEL | User defined element |
| UMAT | User material subroutine within ABAQUS |
| UTEMP | User defined temperature subroutine within ABAQUS |
| XFEM | Extended finite element method |

# Chapter 1

# Introduction

## 1.1 Background

The current research is funded by SuperGen, Sustainable Power Generation & Supply, (details in the Acknowledgements section) Phase II and an extension from the Phase I project, which ended in 2009. The overall aim of the Supergen project is to develop novel tools and methodologies in order that the life of existing conventional steam and combined cycle power plants can be extended. The components at the engine inlet are usually coated with thermal barrier coatings (TBC) to protect them from extreme working conditions. When the coating delaminates, the underlying layer will be exposed to dangerously high temperatures and corrosive gases, which will lead to failure of the power plant and cause service disruption. Hence the lifetime of a power plant is linked to the durability of the TBC and factors affecting TBC durability are investigated in this thesis.

Since the original equipment manufacturer (OEM) cost of a gas turbine unit is very high (£200-£700 per kW output, depending on the size of the engine [1]), it is desirable to predict the failure and lifetime of a TBC coated engine component without carrying out extensive experiments on prototypes. Hence, having the ability to predict the failure by use of modelling techniques is highly desirable. For this purpose, finite element analysis (FEA) has been used extensively by many researchers. FEA was also used in this project to estimate stresses within the TBC and to predict the crack growths within the TBC driven by those stresses that lead to final failure of the TBC. This project aims to achieve a better understanding of the range of parameters that are needed to maximise the lifetime of a coated components while maintaining the maximum output from the engine.

## 1.2 Engine requirements and role of ceramic coating

In its simplest form, a simple cycle gas turbine system can be represented as shown in Fig 1 (i). The thermal cycle efficiency against the specific output of the engine is illustrated in Fig 1 (ii). A specific output shows the amount of energy per kg of air flow. The higher this number is, the smaller the engine size that is required for the same amount of energy; hence the overall OEM of an engine and its weight are reduced. Meanwhile thermal efficiency affects the fuel costs.

From Fig 1 (ii), it can be seen that the higher the turbine inlet temperature ($T_F$ in Fig 1 (ii)), the higher the specific output will be if other factors are fixed. This provides an incentive to discover ways to increase the inlet temperature without compromising the engine lifetime. The main breakthroughs have occurred since the 1960s. During those decades, engine components were cast from polycrystalline alloys, which could withstand the temperature of up to 700°C, instead of the 600°C limit imposed by previously used wrought alloys [2]. However, because of progressive demand for higher output capability from the turbine engines, more investigations were carried out to increase the turbine inlet temperature further. It was found that by using cooling systems and by applying coatings, the temperature capability of the engine components [3] could be improved further. The history of improvements of temperature capability of turbines based on different factors is demonstrated in Fig. 1.2. It can be observed that the increase in maximum inlet temperature by use of a coating is more subtle than the limit imposed by the use of cooling systems. Nevertheless, usage coatings is a much more economical solution since usage of a cooling system usually requires a constant air flow, throughout the operation of engines.

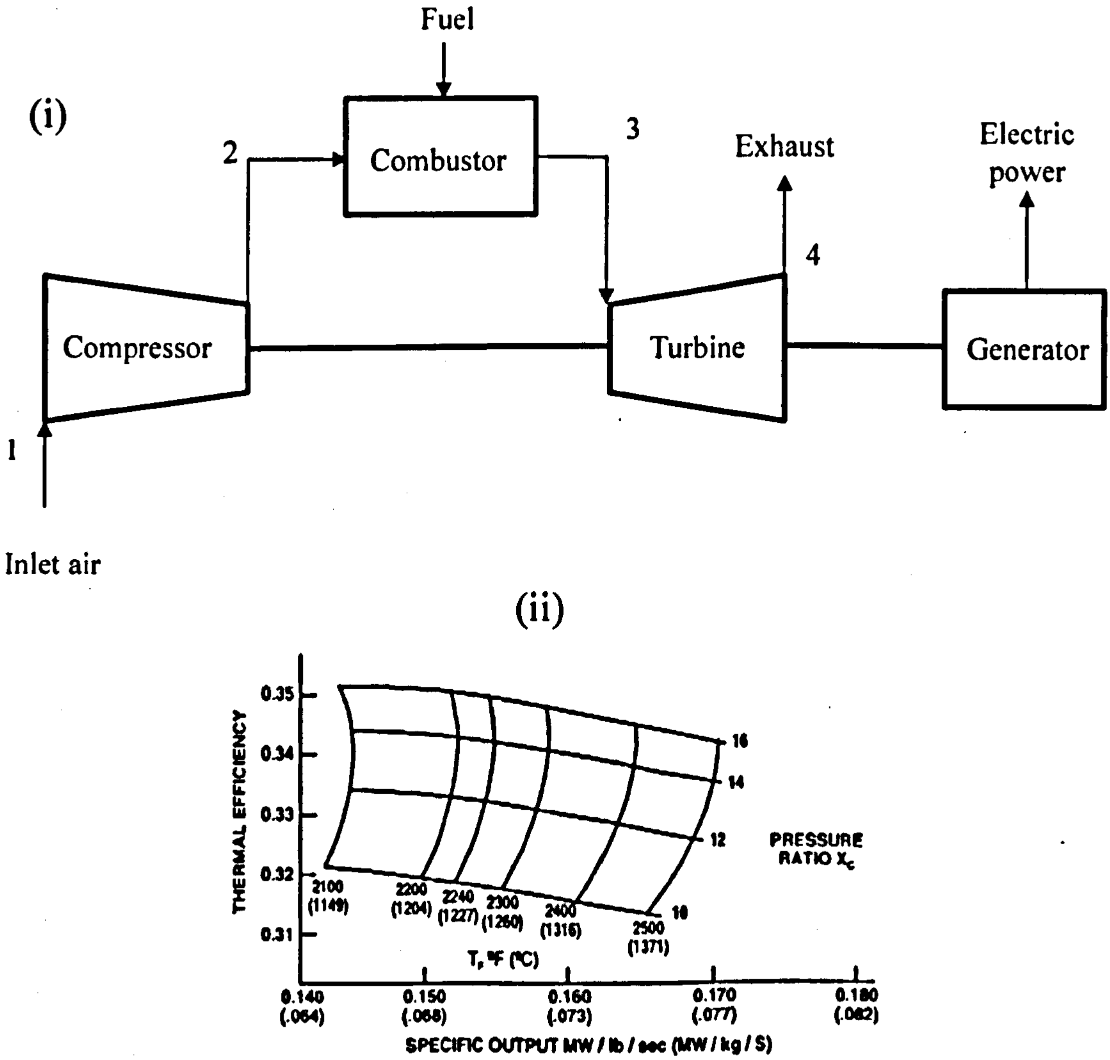

**Fig. 1.1 (i) A single cycle gas turbine engine (ii) Efficiency plot [4]**

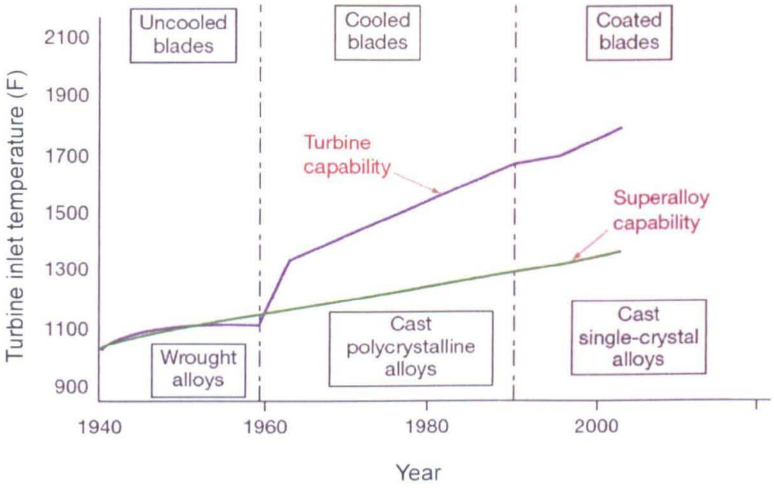

**Fig. 1.2 Turbine inlet temperature capability evolution through decades [5]**

## 1.3 Development of modern TBC system

Research on coatings to protect engine components from high temperature dates back to the late 1940s when different ceramic coatings and their effects on the lifetime of coated turbine blades were tested [3, 6]. The low thermal conductivity of the ceramic TBC was a key factor contributing overall temperature reduction. However, there are other factors to be considered too; high CTE mismatch between the TBC and substrate alloy causes high mismatch stress at the end of the thermal cycle resulting in a reduction of overall coating lifetimes. Moreover, TBCs are porous in nature whatever process was used to provide adhesion it to the substrate. In fact, the trapped air within the pores actually brings the thermal conductivity down. However, porous TBCs provide passages for oxygen towards the substrate alloy. This allows alloy substrate to be oxidised when the engine operates at extreme temperatures. Usually, if an alloy is optimised for mechanical properties (such as creep and fatigue resistance), its resistance to oxidation becomes lower. By taking account of the factors mentioned above in addition to resistance to the temperature, a modern TBC system was introduced in the middle of the 1970s by NASA [7, 8] and it was initially used mainly in commercial combustors [9].

For a modern TBC system, zirconia is used to form a ceramic TBC since it is a good thermal insulator while yttrium oxide ($Y_2O_3$) is usually added to stabilise the zirconia. To accommodate the high CTE mismatch between a TBC and the substrate, a new layer of metal coating was introduced. This metal coating is sandwiched between the TBC and the substrate. The coating is often known as the bond coat (BC) as it improves the bonding of the TBC to the substrate alloy. MCrAlY (where M stands for metals usually Ni or Co) is commonly used as a metal coating within power generation engines. By adjusting the properties of the different elements within the BC, the required CTE as well as other desirable mechanical properties can be obtained.

Among the metal contents of the BC, Al is the least noble element and its concentration is usually optimised so that the selective oxidation of Al occurs. According to Wagner's theory [10], the critical concentration (N) of the least noble element, Al for the case of MCrAlY BC, before oxides of other elements are forming simultaneously, can be defined as shown below.

$$N = \frac{V}{z_{Al} M_o} \left( \frac{\pi k_p}{D_{Al}} \right)^{0.5} \tag{1}$$

where V is the molar volume of the metal coating, $z_{Al}$ is the valance of Al, $M_O$ is the atomic weight of oxygen, $k_p$ is the parabolic rate constant of formation of alumina, and $D_{Al}$ is the aluminium diffusion coefficient in the alloy.

The selective oxidation of the BC leads to formation of thermally grown oxide (TGO), $Al_2O_3$. This oxide layer is beneficial since it is a dense, stabilised and slow-growing oxide, which slows down further migration of oxygen. As long as the Al concentration is higher than the critical concentration shown in Eq (1), $Al_2O_3$ continues to form and it prevents the formation of fast growing oxides of other metallic components of the BC. To summarise, the various layers of a modern TBC system (ceramic TBC, metallic BC and TGO) can be illustrated as shown in Fig. 1.3.

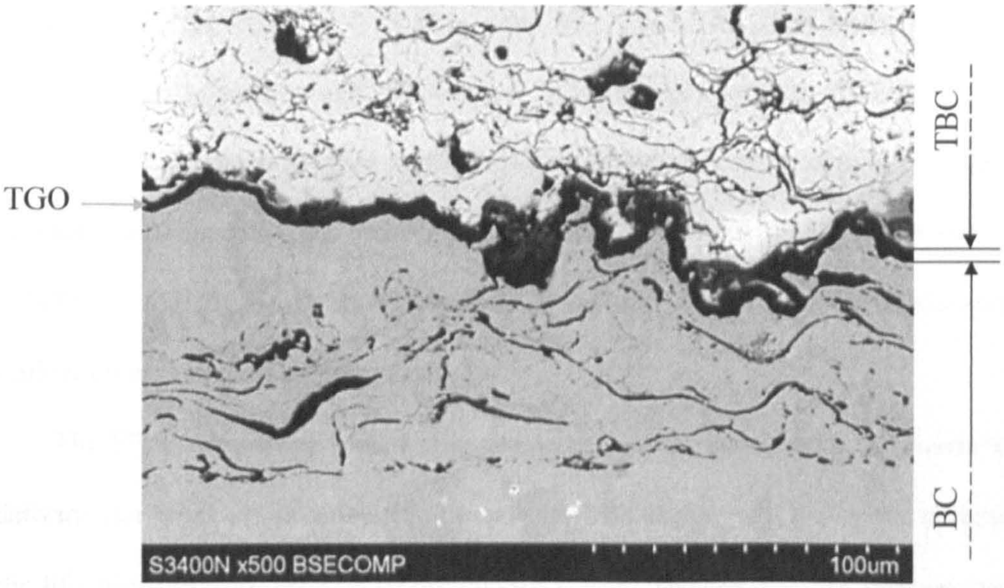

**Fig. 1.3: Modern TBC system [11]**

## 1.4 Spraying processes

Although diffusion processes can be used for some types of coatings such as platinum-aluminide (Pt-Al) BC, the processes described here will only focus on overlay coatings. Spraying processes used for both TBCs and BCs can be categorised into either thermal spray techniques or the electron beam vapour deposition (EB-PVD) technique. Moreover, the former technique can be further sub-divided into processes for specific applications of which air plasma spayed (APS) is the most common one. The resultant coating microstructures and mechanisms for failure from these two main coating techniques are vastly different.

### 1.4.1 Dependence of microstructure and failure of TBC on coating processes

EB-PVD results in a columnar structure and those columns are separable at high temperature, which increases the strain tolerance of coating. Moreover, the TGO interfaces at the microscopic level are much smoother than the thermal sprayed coating interface. This reduces out-of-plane tensile stresses, which are undesirable since they cause the opening of cracks within the TBC. The TGO layer, however, experiences high in-plane compressive stress at the end of cooling. As a result, the TGO of EB-PVD system buckles as the thermal cycling continues especially if there are cavities/initial pores at the TGO interface. When buckling occurs, separation of the TGO at the BC/TGO interface and subsequent large scale (macroscopic) delamination at the interface are expected.

The EB-PVD coating used within the aerospace industry has higher tolerance to deformation strain produced during operation of the engine and hence has a higher cyclic life. Nevertheless, the cost of production is very high for low risk engines used within the power generation industry and it is more economical to use thermal sprayed coatings such as APS. APS coatings are manufactured by spraying molten powder onto the substrate with multiple passes. Therefore, the coating has a lamellar structure. Additionally, the interface of the APS TBC is much rougher than the interface of the EB-PVD system. The roughness, sometimes, is introduced to BC surfaces to provide a better a mechanical lock to the TBC. However, the undulated interface also creates significant out-of-plane tensile stresses, at or near the TGO interface, when there is thermal mismatch during heating-up or cooling. These tensile out-of-plane stresses are orthogonal to the gap between the layers of the TBC and this causes opening of initial discontinuities of the TBC. These crack openings, combined with vertical cracking, resulting from in-plane tensile stresses, lead to partial spallation of the TBC [12].

For both types of TBC, oxidation of the BC plays a major role in their failure mechanisms. In addition to changes of mechanical properties, so-called 'chemical failure' occurs when a significant amount of aluminium has depleted, within the BC, to a value below the concentration shown in Eq (1) [13]. This results in the formation of fast growing oxides of Co, Cr or Ni. Significant out-of-plane tensile stresses, at the TGO interface, originate from these oxide growths. In turn, these stresses introduce delamination cracks at the coating interfaces.

For both types of TBC, failure can be caused by TBC sintering due to closure of pores at high temperature. Sintering leads to an isotropic increase in the elastic modulus of thermal sprayed TBC while the modulus increment is non-isotropic for EB-PVD coatings. As a result, strain tolerance is reduced and higher stress concentration and crack opening within the TBC are expected to occur. The final type of failure, common to both types of TBC, is caused by the degradation of the interfacial toughness due to fatigue loading. This leads to large scale or macro delamination in the vicinity of the TGO interface.

## 1.5 Simplifications applied to coating microstructures for modelling purposes

Various simplifications are made to complex microstructures of the coatings for FE modelling of the TBC systems as follows. At the scale of a few μm, gaps between successive splats of plasma sprayed YSZ (yttria stabilised zirconia) TBC can be observed as shown in Fig. 1.4 (i). At the scale below 1μm, each splat of the TBC film is found to be composed of columnar features with voids between them especially if the TBC is deposited at low temperatures as shown in Fig. 1.4 (ii). Because of these discrete features, material properties of a thin YSZ film differ from that of isotropic and fully dense amorphous YSZ. Additionally, anisotropy of the film is also expected as mentioned in [14]. These discrete features and related anisotropy of the TBC are not incorporated in FE model of the TBC system for this project for simplicity. Alternatively, as with other researchers [13, 15, 16], the TBC is assumed to be an isotropic continuous material. Empirical measurements for evolutions of material properties of YSZ film, due to reduction in gaps and voids while sintering at high temperatures, are used as material properties for YSZ coating of FE model. Similarly, it is assumed that the TGO or $AL_2O_3$ layer is an isotropic material. The assumption is supported by the experimental results from [17], which demonstrate the isotropy of $Al_2O_3$.

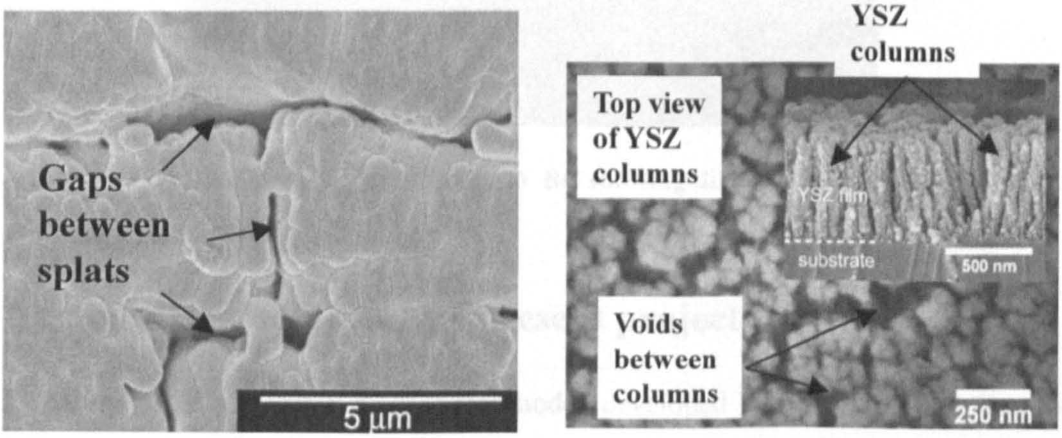

**Fig. 1.4: Microstructure of APS YSZ TBC (i) at micron scale [18] and (ii) at submicron scale [19]**

As demonstrated by micrographs (Fig. 1.5), MCrAlY BC is made up of three different phases, namely $\gamma$ (Ni), $\gamma'$($Ni_3Al$) and $\beta$ (NiAl). Aggregate material properties of an equivalent homogeneous material for the BC can be evaluated using the Eshelby's theorem for inhomogeneous inclusions [20]. By applying Eshelby's theorem, Hermosilla [21] has developed constitutive models for equivalent elastic and creep properties of the multiphase BC, during Stage I of the project. A finite difference model [22], which predicts changes in volumetric phase proportions within the BC, due to BC oxidation or diffusion at the BC/substrate interface at elevated temperatures, were also coupled to the model. This constitutive model is adopted here to model the BC as a continuous mass within the FE model. However, different shapes of inclusions were not taken into account while evaluating aggregate properties, due to high complexity of Eshelby's shape tensors [20]; shape of inclusion is assumed as sphere.

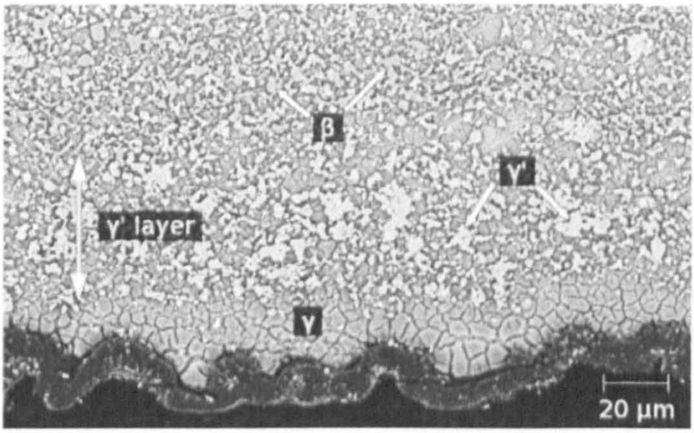

**Fig. 1.5: Micrographs of MCrAlY BC showing different phases [22]**

## 1.6 Starting point for the present project

As described above, a numerical model, developed in Stage I of SuperGen by Hermosilla [21], was mainly focused on mechanical properties of the coating system. The model can then be used to carry out stress-strain analyses of the TBC systems to predict crack growth and subsequent failure of the system. Nevertheless, Stage I project only considered the steady state stresses and completely omitted the cooling down stresses created by thermal mismatch.

## 1.7 Aims of the project

The aims of the current project are to investigate further mechanical properties and various interface shapes of APS TBC systems, which affect the failure of the system after cooling at the end of a thermal cycle. Additionally, comparisons of the residual stresses, predicted by FEA to the newly available measurements from experimental non-destructive stress within the consortium, were made. Fracture mechanics based crack propagation analysis, using an extended finite element method (XFEM), was also introduced, to understand fully how the interactions between residual stresses within the system and crack propagation lead to the ultimate failure of the TBC system.

# Chapter 2

# Literature review

## 2.1 Introduction

Advanced FE models have been introduced over the years to model residual stresses development due to different aspects of TBC systems under operation. The review mainly focuses on factors to be considered for modelling of the stresses built up within TBC systems and hence for predicting eventual spallation. In general, it is necessary to understand three areas to carry out stress analysis of TBC systems. They are oxidation of the BC and related growth strain, material properties of coatings, and geometries of the coating interface and of the substrate. Additionally, consideration is given to the comparison between stresses predicted by FE analysis and from the experimental measurements, and to the modelling crack propagation and failure/spallation within TBC based on evolution of stresses. Finally, lifetime assessment methods, which can be applied to the current work for possible continuation of the project, are also elaborated. In the light of this review, the scope and structure of the thesis are then explained.

## 2.2 Oxidation of the BC and TGO growth

Ceramic TBCs are oxygen permeable. As the BC is exposed to high temperature in a non-vacuum environment, an oxide layer will form between the BC and the TBC. As aluminium (Al) is the most reactive constituent of the MCrAlY BC, a dense alumina layer is usually formed as a result of oxidation. Since the diffusion of the oxygen within the alumina is much slower than Al, the alumina layer functions as an oxygen barrier, inhibiting formation of other fast growing oxides of Cr and Co. The oxidation of aluminium continues until Al content within the BC is depleted. At the same time, strain relating to the TGO growth within the constrained region creates stresses at the BC/TGO and TGO/TBC interfaces. Assumptions made by different researchers for TGO growth strain are described as follows.

### 2.2.1 TGO growth modelled by swelling strain

This method relates the changes in TGO thickness to the growth strain produced within the TBC model. Changes in TGO thicknesses at different stages of the thermal cycle can be investigated by analysing cross sectional SEM images of the TBC systems. Thereafter, the empirical relationship between oxidation time (t) and TGO thickness (x) can be found. The relationship is generally parabolic and it can be expressed as shown in Eq (2.1). By utilising the parabolic relationship, Martena et al. [23] modelled different TGO thickness at the pre-processing (assembly) stage to study the relationship between the duration at the operating temperature and residual stresses within the TBC. However, the method is over-simplified since it ignores the strain arising from the TGO growth during steady state.

$$x = \sqrt{k_p t} \tag{2.1}$$

where $k_p$ is a parabolic constant

A continuous parabolic TGO growth can be implemented by assuming that the strain rate in the thickness direction ( $\dot{\varepsilon}$ ) is the ratio of the change in thickness of the TGO ( $\dot{x}$ ) to the original oxide thickness (x) as shown in Eq (2.2). Implementation of this type swelling strain within the FE model for a growing TGO layer can be found in [16, 24].

$$\dot{\varepsilon} = \dot{x}/x = \frac{1}{2} \cdot k_p / x^2 \tag{2.2}$$

Swelling strain from Eq (2.2) is assumed to be isotropic. However, Karlsson and Evans [25] proposed that oxide growth is anisotropic, and in-plane growth strain of an oxide layer is one tenth of the growth strain in the direction of oxide thickness. Nevertheless, extensive experiments are required to obtain an exact factor. Anisotropic TGO swelling strain can also related to increase in volume of the material due to oxidation ($dV/V_0$) as shown in Eq (2.3) by Jinnestrand and Sjöström [26]. The volume increase due to the formation of alumina from aluminium phases of the BC for the TBC system was assumed to be 25%, which is consistent Pilling-Bedworth ratio (PBR) of aluminium. PBR is defined as the ratio of molar volume of the oxide formed to that of the metal from which the oxide is formed.

$$1 + \frac{dV}{V_0} = \left(1 + \Delta\varepsilon_1^{sw}\right)\left(1 + \Delta\varepsilon_2^{sw}\right)\left(1 + \Delta\varepsilon_3^{sw}\right) \tag{2.3}$$

where $\Delta\varepsilon_i^{sw}$ is the anisotropic increment of swelling strain in the principal directions.

By applying a simple swelling strain model for the TGO growth, it is possible to determine the critical thickness by comparing the resultant stress distribution and tensile strengths of coatings and the TGO adhesion strength. However, the analysis completely ignores the formation of spinels or non-aluminium oxides. It assumed that the resultant oxide is alumina even after a lengthy oxidation process which results in depletion of aluminium content within the BC.

### 2.2.2 Uneven TGO growth due to aluminium depletion within MCrAlY BC

A high aspect ratio of BC roughness is one of the factors which causes premature failure of a TBC system because of rapid conversion of asperities, at which aluminium is depleted, into breakaway oxides (spinels) mainly of Ni, Co and Cr [27]. Unlike alumina, these breakaway oxides are non-protective and the corresponding growth strain imposed by breakaway oxides is much higher than the strain from alumina formation due to the higher PBR of Ni and Cr. For example, the PBR of one of the breakaway oxides, $NiCr_2O_4$, is 2.05 compared to the PBR of alumina, which is 1.25. This results in higher out of plane tensile stresses in the TBC when the oxide grows during steady state. These stresses, in combination with out of plane tensile stress created by coefficient of thermal expansion (CTE) mismatch between TBC and oxides during cooling, nucleate TBC cracks and also drive propagation of initial TBC discontinuities.

By processing SEM images of the TBC systems with breakaway oxides statistically, Che et al. [28] extracted geometries for the FE model with a TGO interface with the presence of spinels. Afterwards, through-thickness tensile stresses near the TGO interfaces were compared to the model using the geometries from the system with only pure alumina TGO. A significant increase in out-of-plane tensile stress at the BC/TGO interface was discovered. Counter-intuitively, an uneven TGO interface produces lower tensile through-thickness stresses at the TGO/TBC interface. However, it is noteworthy that a continuous increase in tensile stresses, due to TGO growth, was not considered for the analysis as only stresses created from CTE mismatch during cooling, with even and uneven TGO interfaces, were modelled. Hence, the resultant tensile stresses will be underestimated.

Following a similar approach by Che et al. [28], Busso et al. [13] used SEM images to investigate continuous changes in TGO thickness because of breakaway oxidation. In contrast, Busso also implemented the strain arising from the TGO growth during steady state. The model has no TGO layer initially and the layers of the BC are transformed into the TGO according to an empirically derived oxide growth law. The thickness variations with time, t, for a pure alumina ($h_{al}$) can be expressed as Eq (2.4). This oxide was assumed to grow towards the BC and hence it is called internal oxide growth. Additional elements which are external to the existing aluminium oxide layers were transformed into spinels once the time reaches $t_{break}$; hence it is known as external oxidation. Experimentally, it was shown that the thickness of breakaway oxides at the peak ($h_{peak}$) is an order of 10 higher than that at the valley region as shown in Eq (2.5) & (2.6). Different PBRs were also applied for external and internal oxide growths whereas the value for the former oxide growth is around 60% higher than the respective value for the latter.

$$h_{al} = 5.72 \cdot 10^{-9}\, t^{0.5} \tag{2.4}$$

$$h_{peak} = 2.78 \cdot 10^{-11}\, (t - t_{break}) \tag{2.5}$$

$$h_{valley} = 2.78 \cdot 10^{-12}\, (t - t_{break}) \tag{2.6}$$

Busso et al. [13] compared maximum out of plane tensile stresses within the system before and after breakaway oxidation. Breakaway oxide growth was implemented within the system after 100h of oxidation at 1100°C. For the same initial aspect ratio of oxide interface, it was found out that maximum out-of-plane tensile stresses, at the TBC/TGO interface at 25°C after 200h at 1100°C, are around four to six times higher than the maximum tensile stress for the system cooled down after 100h of oxidation at 1100°C. The difference in stresses is more prominent for the system with rougher oxide interface. Hence, it can be concluded that breakaway oxides have a negative impact on the coating durability because of higher tensile out-of-plane stresses associated with their growth strains.

By implementation of the uneven swelling strain rate across the TGO interface, stresses associated with spinel formation can be modelled. Nevertheless, the model also has to take into account of relevant changes of the BC composition due to oxidation as it significantly influences the mechanical properties (elastic, creep and CTE) of the BC and hence residual stresses.

### 2.2.3 Diffusion-based oxidation of MCrAlY BC

TGO formation is controlled by both inward diffusion of oxygen (internal oxidation) and outward diffusion of aluminium from the BC phases towards the TGO/BC interface. BC composition is made up of easily oxidised phases, β (NiAl) and γ' ($Ni_3Al$) with oxidation resistant phases, σ (Cr) and γ (Ni). This BC composition, especially in the vicinity of the TGO, changes through the formation of oxides.

By using a self-diffusion coefficient of aluminium and oxygen within the alumina scale ($D_{Al}$ and $D_O$), Martena et al. [23] formulated a parabolic constant as shown in Eq (2.7). This constant, otherwise, is found empirically, and it can be used to calculate strain associated with oxide growth as shown in Eq (2.1). When TGO thickness calculated using this diffusion model was compared to the experimentally measured thickness, a discrepancy of 1μm of thickness was observed at the steady state. Nevertheless, the thickness growth given by the diffusion model shows similar two-stage oxidation process: a fast primary transient stage followed by a linear secondary stage.

$$k_p = \int_{p'_{O_2}}^{p^0_{O_2}} \left( D_O + \frac{z_{Al}}{|z_O|} D_{Al} \right) d\left(\ln p_{O_2}\right) \qquad (2.7)$$

where $p^0_{O_2}$ and $p'_{O_2}$ are partial pressures of oxygen at the free surface of the TGO and at the BC/TGO interface. They can be calculated by thermodynamic equilibrium conditions. $z_{Al}$ and $z_O$ are the ion valance for aluminium and oxygen, respectively. $D_{Al}$ and $D_O$ have an Arrhenius relationship with their self-diffusivities within the alumina.

Unlike the model by Martena et al. [23], Karunaratne et al. [22] presented a diffusion model for calculation of full phase evolution within the BC by taking account of diffusion coefficients within every BC phases and diffusion at the substrate/BC interface. For atomic flux of Al at the BC/TGO interface, the empirical oxide formation rate, as shown in Eq (2.8), was used as the boundary condition. The composition of phases were then calculated by Karunaratne [22] using a CALPHAD model. This model can be used to predict not only Al depletion related to oxidation but also phase evolution within the MCrAlY BC. By using the composition of phases, the aggregate material properties of the BC can then be calculated which is presented in Section 2.3.

$$\dot{\delta} = 0.332 \left\{ \exp\left[ Q\left( \frac{1}{2423.7} - \frac{1}{T} \right) \right] t \right\}^{0.332} t^{-0.668} \qquad (2.8)$$

where T is the oxidation temperature in Kelvin and t is oxidation time.

## 2.3 Coupled diffusion-mechanical model for stress analysis

As mentioned in Section 2.2.3, oxidation of the BC changes the compositions of the BC phases. These changes have to be considered for stress analysis of TBC systems since material properties of the BC are largely dependent on the BC composition. The constitutive model for local stresses rate which developed within the multiphase BC ($\dot{\sigma}_{ij}$) was proposed by Busso [29] using Hooke's law as in Eq (2.9).

$$\dot{\sigma}_{ij} = \left\{C : \left(\dot{\varepsilon}_{ij} - \dot{\varepsilon}_{ij}^{in}\right)\right\} - 3K\alpha\dot{T}\delta_{ij} \tag{2.9}$$

where $\delta_{ij}$, K, $\dot{T}$ and $\alpha$ are the Kronecker-delta, bulk modulus, rate of change in temperature and CTE respectively. C is a stiffness tensor. $\dot{\varepsilon}_{ij}$ and $\dot{\varepsilon}_{ij}^{in}$ are total and inelastic strain rate tensors respectively for the multiphase BC.

In terms of the Lamé parameters, Eq (2.9) can be expressed as shown in Eq (2.10).

$$\dot{\sigma}_{ij} = \delta_{ij}\lambda\dot{\varepsilon}_{trace} + 2\mu\left(\dot{\varepsilon}_{ij} - \dot{\varepsilon}_{ij}^{in}\right) - 3K\alpha\dot{T}\delta_{ij} \tag{2.10}$$

where $\lambda$ and $\mu$ are the Lamé parameters and their relation to isotropic elastic modulus (E) and Poisson's ratio ($\nu$) are shown as in Eq (2.11) and (2.12).

$$\lambda = \frac{E\nu}{(1+\nu)(1-2\nu)} \tag{2.11}$$

$$\mu = \frac{E}{2(1+\nu)} \tag{2.12}$$

The inelastic strain rate, $\dot{\varepsilon}_{ij}^{in}$, is the combined strain rates of creep and of the volume increase of BC phases due to oxidation $\left(\dot{\varepsilon}_{ij}^{cr}\ and\ \dot{\varepsilon}_{ij}^{ox}\right)$ as shown in Eq (2.13).

$$\dot{\varepsilon}_{ij}^{in} = \dot{\varepsilon}_{ij}^{cr} + \dot{\varepsilon}_{ij}^{ox} \tag{2.13}$$

Lamé parameters and creep strain rates for a multiphase BC from Eq (2.10) and Eq (2.13) are dependent on the BC phase composition, which evolves according to oxidation. Coupling the Busso model with the composition of the BC phases, calculated from the finite difference (FD) model of Karunaratne [22], was carried out by Hermosilla [21]. The approach is based on Eshelby's theorem of inhomogeneous inclusions (inclusions have different material properties to those of matrix; in case of homogeneous inclusions, both matrix and inclusions have identical material properties) [20]. The major assumption imposed was that the stress tensors for inhomogeneous inclusions $\left(\sigma_{ij}^{m}\right)$ is identical to the one for the homogenous inclusions $\left(\sigma_{ij}\right)$ when external strain ($\varepsilon_{kl}^{0}$) is applied. The stress tensors for inhomogenous and equivalent homogeneous inclusions are shown in Eq (2.14) and (2.15) respectively. It was also assumed that the sum of the volumetric compositions of all phases $\left(\sum_{i=1}^{n} f^{i}\right)$ is unity. It was assumed that the shape of the inclusions is spherical and their properties are isotropic [21] to simply the stiffness matrix. Using the existing theorem for multiphase composites [30-33], which are based on Eshelby's theorem, parameters from Eq (2.10) & (2.13) can be expressed in terms of material parameters of individual phases. Deriving aggregate elastic properties of the BC based on this approach is shown as an example in the following section.

$$\sigma_{ij}^{m} = C_{ijkl}^{m}\left(S_{klmn}\varepsilon_{mn}^{*} + \varepsilon_{kl}^{0}\right) \tag{2.14}$$

$$\sigma_{ij} = C_{ijkl}\left(S_{klmn}\varepsilon_{mn}^{*} + \varepsilon_{kl}^{0} - \varepsilon_{kl}^{*}\right) \tag{2.15}$$

where $\varepsilon_{mn}^{*}$ and $\varepsilon_{kl}^{*}$ are eigenstrains; the name is given to strains which are free from external stress (e.g thermal expansion, phase transformation strains) [34]. $C_{ijkl}^{m}$ and

$C_{ijkl}$ are elastic stiffness tensors for inhomogeneous and homogenous inclusions respectively. $S_{klmn}$ is an Eshelby tensor which is dependent on the shape of the inclusion.

## 2.4 Aggregate material properties of the BC based on its phase composition

Budiansky [31] derived shear and bulk modulus (K, G) of a heterogeneous material under shear loading using Eshelby's technique. They can be expressed in terms of the properties of the phases, using Eshelby's shear elastic accommodation factor ($\beta_t$) and Eshelby's volumetric accommodation factor ($\beta_n$), as shown in Eq (2.16) & (2.17). Eshelby's accommodation factors can be related to the Poisson's ratio (v) as shown in Eq (2.18) and (2.19). In turn, the Poisson's ratio (v) is related to bulk and shear moduli by Eq (2.20). By simultaneously solving Eq (2.16) to Eq (2.21) using a root finding technique such as the Newton-Raphson method, the bulk and shear moduli and Poisson's ratio of heterogeneous composites can be evaluated, based on the corresponding properties of the individual phases. To reduce the computation time for the Newton-Raphson method, the initial aggregate bulk and shear moduli were evaluated from rule of mixtures techniques; for example bulk moduli by the rule of mixture techniques is shown in Eq (2.21).

$$\sum_{i=1}^{n} \frac{f^i}{1+\beta_t\left(\frac{G^i}{G}-1\right)} = 1 \tag{2.16}$$

$$\sum_{i=1}^{n} \frac{f^i}{1+\beta_n\left(\frac{K^i}{K}-1\right)} = 1 \tag{2.17}$$

$$\beta_t = \frac{2(4-5\nu)}{15(1-\nu)} \tag{2.18}$$

$$\beta_t = \frac{1+\nu}{3(1-\nu)} \tag{2.19}$$

$$\nu = \frac{3K-2G}{6K+2G} \tag{2.20}$$

$$K_{\text{rule of mixture}} = \sum_{i=1}^{n} f^i K_i \tag{2.21}$$

Using a similar approach, aggregate CTE and creep strain under load were also calculated in terms of the properties of individual phases, as demonstrated in [21], using theorems from [32, 33]. Thereafter, various thermo-mechanical stress analyses were carried out for different heat treatment cycles and different initial composition of the BC.

## 2.5 Sintering of ceramic coating

The main purpose of the TBC is to reduce the temperature of the underlying substrate allowing increase in the engine inlet temperature for its efficiency. As a TBC encounters high temperature, its porosity is reduced. Depending on the microstructures of the TBC (EBPVD or APS), the reduction in TBC porosity occurs due to fusion of pores and gaps within the TBC. The thermal conductivity (κ) and elastic modulus (E) of the TBC are largely dependent on the porosity and both increase with decrease in porosity. Increase in E will reduce the strain tolerance of the TBC, so that it is subjected to higher tensile stresses during cooling and spallation can occur. Increase in k will increase the temperature of the substrate layers, which could be higher than the temperature limit, and premature failure could occur during the steady state operation. Because of these effects, sintering related changes in material properties have to be implemented in FE models for thermo-mechanical stresses analysis of TBC systems. The phenomena causing the sintering, which can be observed from different experimental works, and the previous efforts in implementation of sintering within the FE models of the TBC are presented as below.

### 2.5.1 Sintering mechanisms for EB-PVD and APS TBCs

Lughi et al. [35] has illustrated stages of the sintering process for EBPVD TBC as shown in Fig. 2.1. The TBC has a feather-like columnar structure at the initial stage as shown in Fig. 2.1 (i) and sintering occurs at two different length scales; microscopic and nanoscopic scales. At the microscopic level, the undulations of the limbs along the column of the TBC smooth out after a few hours (50h at 1100°C for the case of Lughi et al. [35]), as shown in Fig. 2.1 (ii). Afterwards, both surface undulation and necking were observed due to diffusion-driven surface undulations (Fig. 2.1 (iii)). Because of bridging of the EBPVD columns, the coating porosity should be decreased. However, Busso et al. [36] argued that the micro cracks are also formed within the sintered TBC and therefore, overall porosity actually increased at the microscale after sintering. On the other hand, strain tolerance reduction is induced by reduction in the porosity at the nanoscopic scale because of fusion of pores within the TBC column as described in [37].

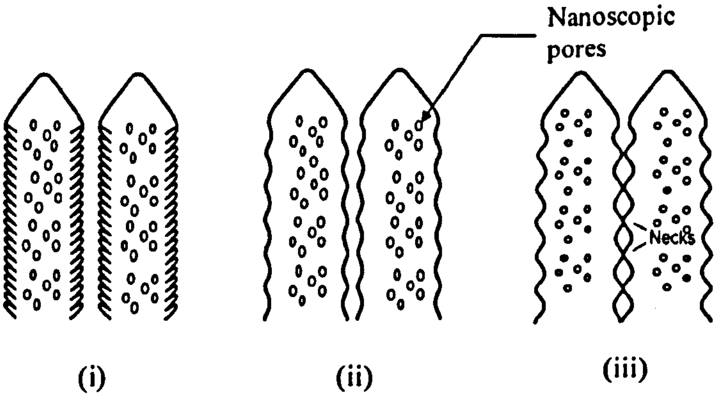

**Fig. 2.1: i) Feathery morphology ii) Smoothening of the columnar structures during the early stage of sintering iii) undulation and necking between the columns of EBPVD TBC**

As in the case of EBPVD coating, two stages of sintering can be observed for APS TBC. Nevertheless, APS TBC has different microstructures compared to EB-PVD TBC. Due to the multi-pass spraying process, APS TBC has a lamellar structure, with each layer having columnar grains and microcracks. A schematic diagram of the microstructure of APS TBC is shown in Fig. 2.2 (i). Thompson et al. [38] explained that Stage I sintering of APS TBC occurs when there is fusion of interlamellar pores (Fig. 2.2 (ii)) whereas the stage II sintering is driven by the healing of micro cracks (Fig. 2.2 (iii)). For the specimen heated at a temperature lower than 1200°C, only stage I sintering is believed to occur. This is because only grain growth between splats of TBC can be seen from SEM micrographs but closure of microcracks was not observed even after 100h of sintering. By contrast, both stage I and stage II sintering were observed within the TBC sintered at 1300°C.

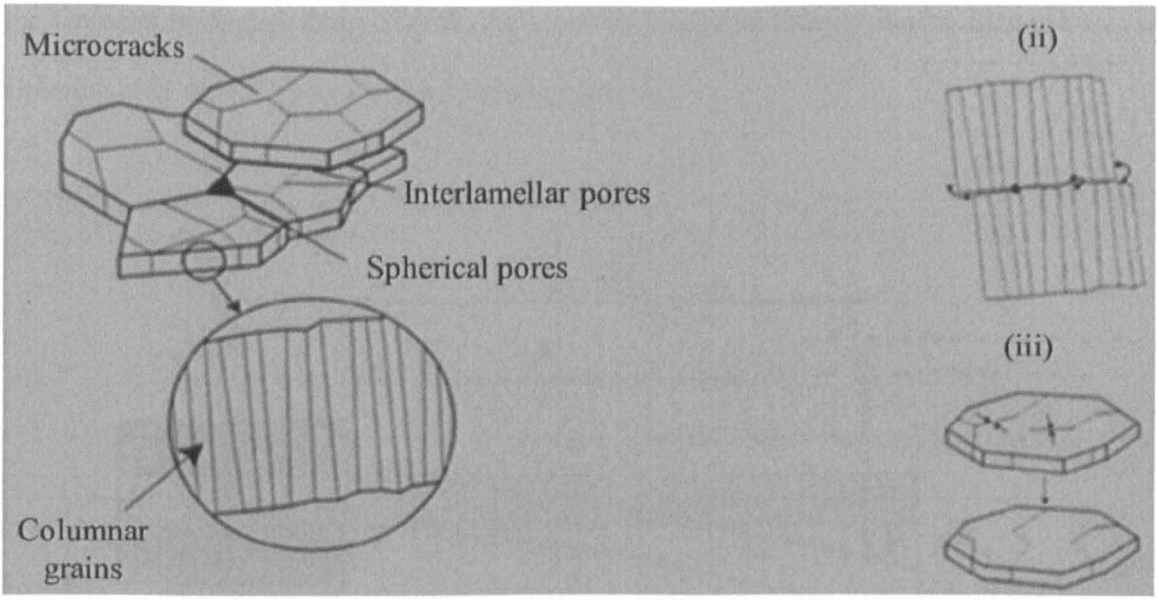

Fig. 2.2: (i) Microstructures of APS TBC ii) stage I sintering iii) stage II sintering [38]

### 2.5.2 Measurement of elastic modulus of TBC as affected by sintering

Thompson et al. [38] measured elastic modulus of the APS TBC specimen which has been sintered at different temperatures and durations using the cantilever bending technique. The set-up is shown in Fig. 2.3. P, L, y and x from Fig. 2.3 are respectively applied load, distance from the clamp to the loading point, deflection of the beam and the position at which deflection is measured using laser extensometer. From the experiments, modulus of the TBC (E) can be evaluated using Eq (2.22).

$$E = \frac{\mathrm{P}}{\mathrm{y}\,(\text{second moment of area})}\left[\frac{Lx^2}{2} - \frac{x^3}{6}\right] \tag{2.22}$$

From the measurements, it was found out that the elastic modulus for the specimen heated at or below 1200°C, increases rapidly for the first 5h of sintering as the result of Stage I sintering from Fig. 2.2. However no significant increase in modulus was observed after 5h of sintering. Conversely, for the specimen heated at the temperature higher than 1200°C, the modulus increased linearly due to Stage II sintering after the first 5 h of Stage I sintering period.

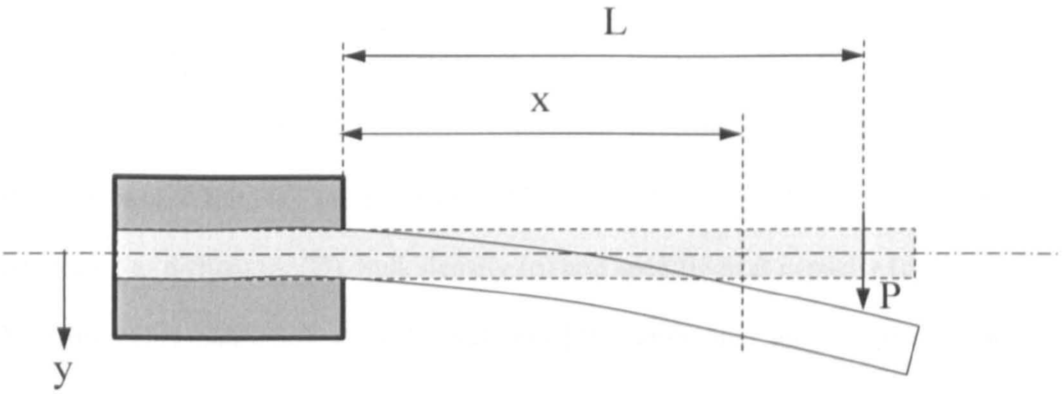

**Fig. 2.3: Experimental set-up for measurements of the elastic modulus of a specimen using cantilever bending technique [38]**

Changes in elastic modulus of the ceramic coating can also be investigated using the nanoindentation technique as described in [39]. The test was carried out on a TBC with thickness of 1.5mm, which experienced a temperature gradient ranging from 900°C at the BC/TBC interface to 1500°C at the TBC surface. In contrast to the results from the cantilever bending method [38], a linear relationship was found between coating stiffness and temperature at which sintering took place. However, the conclusion is made from data from only one set of measurements. By contrast, similar nanoindentation measurements from Zhu and Miller [40] show two-stage sintering of the TBC at a temperature higher than 800°C.

### 2.5.3 Measurement of thermal conductivity of TBC as affected by sintering

It is noteworthy that sintering of the TBC also affects its thermal conductivity. A change in thermal conductivity creates thermal gradient across the TBC especially for thick TBCs (>200μm). The thermal gradient in turn creates different densification rates across the thickness changing TBC thermal conductivities and thermal gradient. The measurement of thermal conductivity is usually carried out by a laser flash technique. This technique involves exposing one side of the coating to a laser and measuring the temperature at the opposite side. If the whole process is assumed to be adiabatic, empirical thermal diffusivity (D) can be expressed using the simplified Parker's expression [41] as shown in Eq (2.23). Finally, thermal conductivity ($\kappa$) can be related to diffusivity (D), bulk density (ρ) and specific heat capacity ($c_p$) by (2.24). Measurements published in both [42] and [40] show that an increase in thermal conductivity is only obvious for a sintering temperature higher than 1100°C. The trend of increase in conductivity is also similar to the increase in modulus due to sintering; the conductivity increases rapidly during the first 5-6 h of sintering followed by a steady state with lower rate of sintering.

$$D = 0.1388.{}^{x^2}\!/_{t_{1/2}} \tag{2.23}$$

where x is the sample thickness and $t_{1/2}$ is the time taken for the face of the sample (opposite to laser source) to reach 50% of maximum temperature.

$$\kappa = D\rho c_p \tag{2.24}$$

As an alternative method to the laser flash technique for measuring thermal conductivity, a method using object oriented FE analysis (OOF) for predicting thermal conductivity of sintered TBC was proposed in [43]. The method aims to avoid the cost of extensive experiments by carrying out virtual experiments based on micrographs of TBC at different stages of sintering. The micrographs are converted into portable pixel map (PPM) binary images before being meshed using the PPM2OOF software [44]. The process is illustrated in Fig. 2.4. Using differences in contrast of colours in micrographs, phases can be differentiated from each other. Corresponding material properties (thermal conductivity of air and dense zirconia) can then be applied to the gaps within the TBC and to zirconia TBC. Afterwards, the heat transfer process can be simulated using the obtained OOF models. It was observed that the resultant thermal conductivity is sensitive to the sample area and at 1200x75μm sample size, the results are within the 5% error range of values measured by traditional laser flash technique. Additionally, it was also found that conductivity is underestimated when there are vertical cracks within the TBC. This is because the analysis was carried in the 2D plane and cracks are, therefore, assumed to penetrate through the out-of-plane direction. Better accuracy is expected if the coating is reconstructed in 3D using OOF3D method [45] as it will take account of internal microcracks (refer to Fig. 2.2) in the construction of OOF meshes.

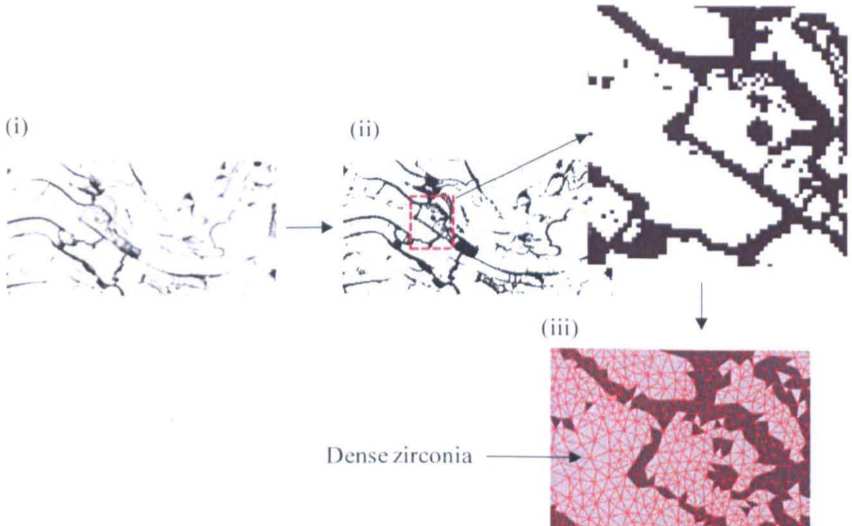

**Fig. 2.4: (i) Micrograph (ii) the portable pixel map (PPM) binary image and (iii) OOF mesh of APS TBC using PPM [43]**

### 2.5.4 Implementation of a sintering model within FE models of TBC systems

Busso and Qian [36] have evaluated the sintering-dependent elastic modulus of the TBC based on the mechanism demonstrated in Fig. 2.1. Micro and nano porosities ($p_m$ and $p_n$) were related to respective relative densities ($\rho_m$ and $\rho_n$) by Eq (2.25). By considering nano pores as randomly distributed spherical pores within a transversely isotropic TBC, out-of-plane modulus ($E_{2'}$) can be related to the density of the coating, Poisson's ratio and isotropic modulus of fully dense zirconia ($E_{2(dense)}$) as shown in Eq (2.26).

$$\rho_m = 1 - p_m, \rho_n = 1 - p_n \tag{2.25}$$

$$E_{2'} = \left(1 + \frac{1.5(1-\rho_n)(1-\nu_{2'1'})(9+5\nu_{2'1'})}{7-5\nu_{2'1'}}\right)^{-1} E_{2(dense)} \tag{2.26}$$

$v_{2'1'}$ is the Poisson's ratio of the transversely isotropic TBC. 2' represents the local coordinate direction perpendicular to the TGO/TBC interface while the direction parallel to the interface is represented by 1'. Finally, in-plane modulus of the TBC ($E_{1'}$) can be related to $E_{2'}$, overall relative density ($\rho$) and initial overall relative density ($\rho_0$) as shown in Eq (2.27). Overall relative density can be estimated using macro and nano porosities, which can be obtained from image studies of the SEM micrographs of the TBC at different stages of sintering, as shown in Eq (2.28).

$$E_{1'} = \left(\frac{\rho-\rho_0}{1-\rho_0}\right) E_{2'} \tag{2.27}$$

$$\rho = 1 - (p_m + p_n) \tag{2.28}$$

Direct implementation of empirical measurements of elastic modulus within the FE model of TBC can also be found in the literature [15]. However, the model did not consider the two-stage sintering of APS TBC as mentioned in Section 2.5.1 and 2.5.2 since the experimental data were only collected after 100h of sintering i.e. the early stage of sintering was ignored. Similarly, empirical measurements or OOF predictions of sintering dependent thermal conductivity from Section 2.5.3 can be implemented within the mechanical FE models of the TBC to update the temperature gradient across the coating. However, this implementation has not yet been observed in the literature.

## 2.6 Ductility of coatings within the TBC system

Ductility plays an important role in materials science to determine whether the failure mechanism is ductile or brittle. Properties of ceramic TBC, MCrAlY BC and alumina TGO from the literature are reviewed here. The stress-strain response of TBC can be observed from the uniaxial tests for which loads are applied in the direction of YSZ deposits of free standing TBC [46]. The response can be illustrated as shown in Fig. 2.5, and the failure type shown is brittle at both room temperature and the operating temperature of 2200°F or 1200°C. Interestingly, the deformation from Fig. 2.5 is non- linear especially at high temperature. In spite of this finding, FE models for TBC models available in the literature assume that TBC has a linear-elastic behaviour, for simplicity, while the elastic modulus measured using either nano-indentation or contilever bending technique was used.

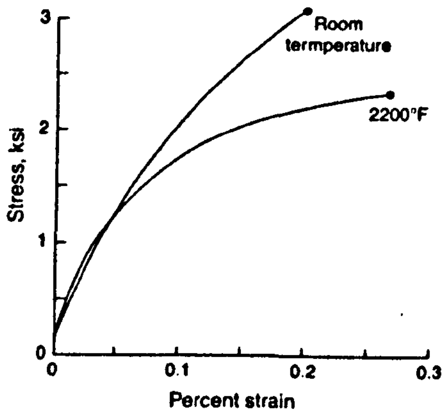

**Fig. 2.5: Stress-stress curve of standalone TBC [46]**

As for alumina, the coating is brittle at room temperature but a sudden change to ductile behaviour is expected if the glassy grain boundary phase occurs at high temperature (>1000°C) as reported by Munro [17]. This brittle to ductile transition teamperature (BDTT) can also be observed for two phase (β-γ) MCrAlY alloy as demonstrated in Fig. 2.6. At high temperature, a superplastic-like deformation with very high strain to failure can be found for MCrAlY but the the actual mechnism, which controls the deformation, is still unknown as mentioned in [47]. Nevertheless, high failure strain at high temperature prevents the failure of the BC for which the deformation is given by creep of the coating. Although the MCrAlY BC is assumed to be brittle at room temperature when cooling is applied within most FE models, plastic deformation was found at room temperature for off-service coating after thermal cycling with steady state temperature of 1100°C by Hemker et al.[48]. Stress-strain curves for coating is illustrated in Fig. 2.7. For thermal cycled sample, reduction in tensile strength and elastic modulus can also be found.

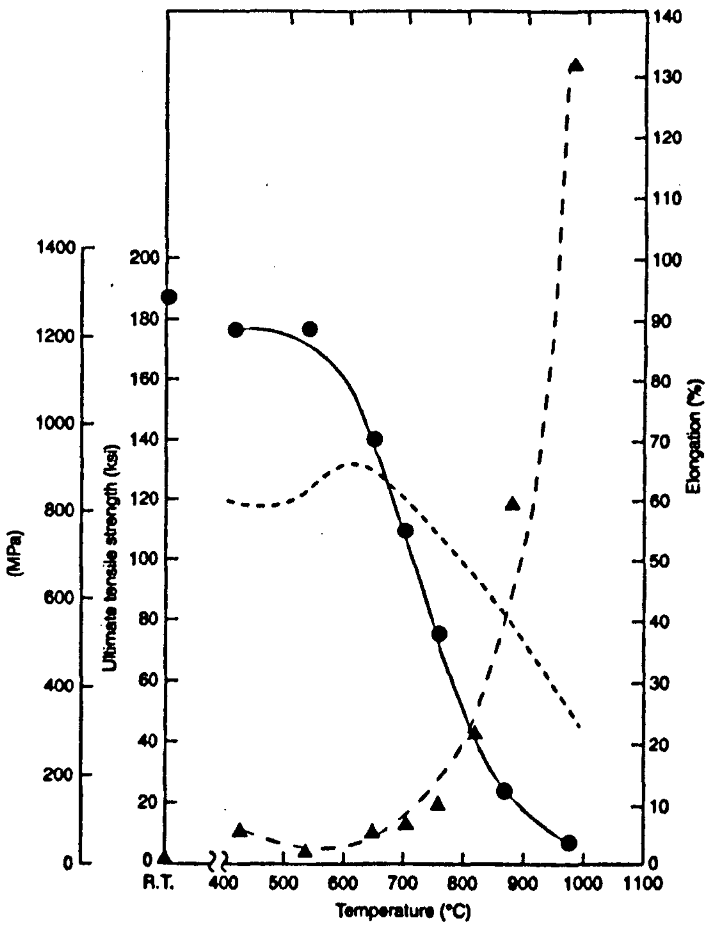

Fig. 2.6: Ductility and yield strength of Co29Cr6AlY (wt%) [49]

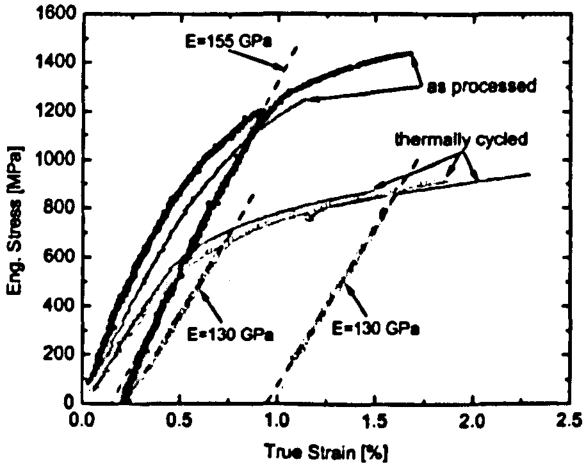

Fig. 2.7: Stress-strain response of Ni18.8Co16.4Cr23.3Al0.3Y0.1Hf0.7Si (wt%) [48]

## 2.7 Creep of coatings

For industrial TBC systems, the coating is exposed to temperature of up to 1300°C for durations of up to 30,000 hours. Therefore, deformation at high temperature by creep of the coatings has to be considered. Creep of the coatings has effects on stresses within the TBC systems and it is a preferred mechanism to relax stresses built up during heat-up, which could otherwise lead to coating spallation. Nevertheless, failure of the coating is possible once the deformation creep strain exceeds the critical strain of coatings; for example failure strain of MCrAlY illustrated in Fig. 2.6. For every coating except the TBC, creep strain rate at steady state can be expressed in Norton's law as shown in Eq (2.29). For the TBC, it has been reported that the creep strain rate of the coating is also dependent on time [50]. After this has been taken into account, creep strain rate of TBC can be expressed as Eq (2.30). Activation energy (Q), prefactor ($A_0$) and power law constant (n), from Eq (2.29) & (2.30), are material data, which need to be determined experimentally.

$$\dot{\varepsilon}_{ij}^{in,BC} = \frac{3}{2} A_o \exp\left( {}^{-Q}\!/\!_{RT} \right) (\bar{\sigma})^{n-1} s_{ij} \tag{2.29}$$

$$\dot{\varepsilon}_{ij}^{in,TBC} = \frac{3}{2} A_o \exp\left( {}^{-Q}\!/\!_{RT} \right) (\bar{\sigma})^{n-1} s_{ij} t^{p} \tag{2.30}$$

Where $s_{ij}$ is deviatoric components of stress

The application of the above Norton's type creep laws within mechanical FE models of TBCs can be found in [16, 24]. These studies have demonstrated the significance of creep parameters for simulating stresses within TBCs and hence various efforts have made to measure creep properties of coatings. In spite of this, very thin geometries of coatings (100-500μm) make the measurements difficult. Methods for investigating creep behaviour of the coatings are reviewed as follows.

### 2.7.1 Conventional uni-axial creep test

The minimum thickness for a tensile test specimen is usually much larger than the thickness of the coating under operation. As a result, a test specimen is usually produced by either hot pressing the bulk powder [51, 52] or multi-pass spraying to achieve the desired thickness [47]. Since the spraying techniques are not usually optimised for thick coatings, the test specimens are porous contrasting with the relatively dense microstructure of the coatings. Therefore, the applicability of the obtained properties within the subsequent modelling work is questionable.

### 2.7.2 Small punch creep test (SPCT)

In contrast to the uniaxial test specimen, the thickness of SPCT specimen is within a similar order of magnitude to the coatings in actual applications. The set-up of the SPCT is illustrated in Fig. 2.8. For the test, the constant load P is applied to the specimen, whose thickness is ideally around 500μm. The displacement at the load tip ($\Delta$) can be measured using a linear variable differential transformer. A typical displacement curve from the SPCT is illustrated in Fig. 2.9. The stages of deformation of a displacement curve are very similar to those of a creep strain curve from uniaxial tensile test.

From Fig. 2.9, initial displacement $\Delta_i$ represents the elastic and plastic deformation before creep deformation. Constant deformation of e at the region b is very similar to the creep strain within the steady state region of the uniaxial tests. Norton's creep constants ($A_0$ and n) are usually extracted from the deformation rate at region b for different applied load P. However, it is still puzzling that large strain (~20%) can be observed from the SPCT test within the steady state region, b, although smaller strain (~5%) is observed from uniaxial tests carried out for the identical material. Therefore, it is arguable that the creep deformation forming the secondary stage of creep is included within the region a. Thus, it is possible that region b actually shows the deformation caused by tertiary creep and the localised necking at the contact area, AB (Fig. 2.8). A more thorough interpretation of SPCT results can be found in [53].

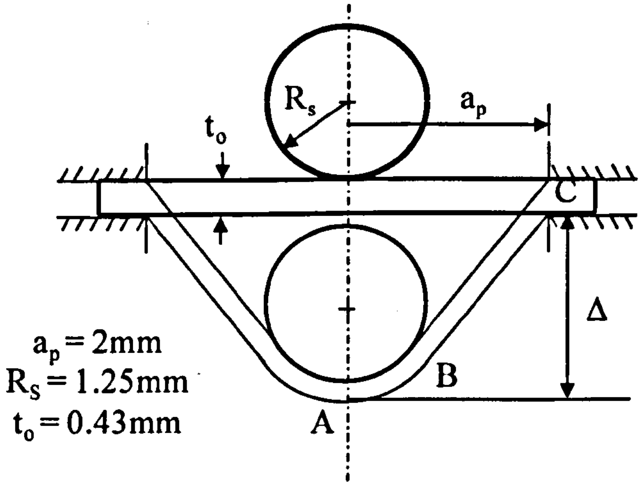

Fig. 2.8: SPCT set-up [53]

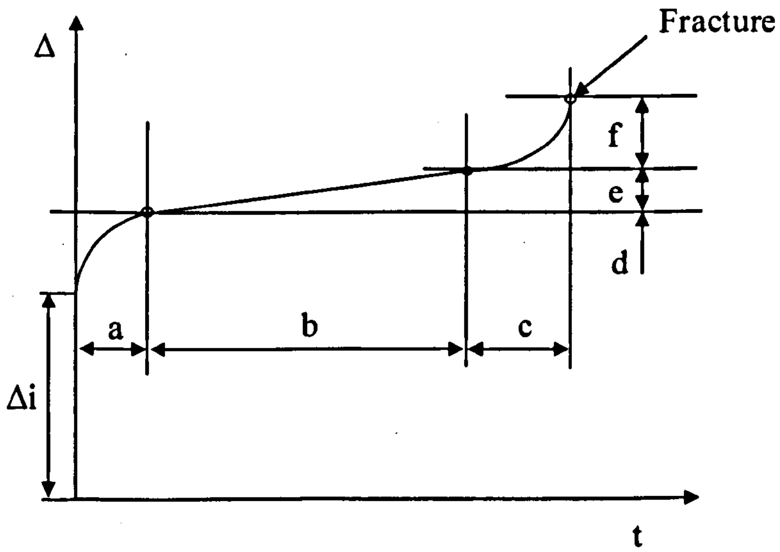

Fig. 2.9: Displacement vs time curve from SPCT

### 2.7.3 Coated tensile specimen method

This novel technique was proposed by Taylor et al. [54]. The creep properties of the coatings were extracted from the uniaxial creep test carried out on the specimen coated with MCrAlY. The cross-section of the specimen can be illustrated as in Fig. 2.10. The main advantage of this method over uniaxial test of bulk coatings is that the testing is conducted on the coatings which have similar microstructures and porosity to those under working conditions.

For the substrate of the test specimen, materials whose creep properties have been well characterised can be used. The sum of forces acting on the coating and the substrate is assumed to be identical to the average forces given by the applied gross tensile stresses. Thereafter, stresses within the coating ($\sigma_{coating}$) can be expressed in terms of stresses of the substrate ($\sigma_{sub}$) and the gross stress ($\sigma_g$) as shown in Eq (2.31). For an identical BC composition, creep strain rate of the coating predicted by the proposed method was found to be higher than the values obtained from uni-axial tests of the monolithic coating.

$$\sigma_{coating} = \frac{\sigma_g(h+2z)-\sigma_{sub}h}{2z} \tag{2.31}$$

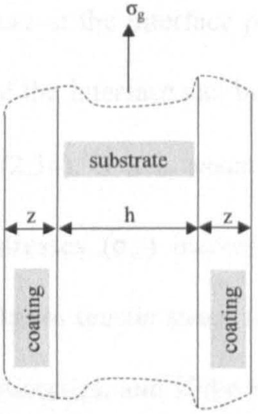

Width of the specimen = w

**Fig. 2.10: Cross-section of the coated specimen on which uni-axial test was carried out [54]**

# 2.8 Effects of coating interface geometry on stresses within the TBC systems

### 2.8.1 Analytical studies

Due to CTE mismatch between coatings, mismatch stresses occurs at the start or end of thermal cycles of engines. These stresses are largely dependent on the shape of the coating interface and the effect can be explained by a simple thermal mismatch phenomenon. If the coating interface is flat at the microscopic scale (e.g. EB-PVD system), the mismatch in-plane stresses within a thin oxide layer between the TBC and the BC can be expressed as shown in (2.32). However, for APS TBC, there is significant microscopic coating roughness. Hence, the in-plane coating stresses also cause stresses in the out-of-plane direction of the global coordinate system as illustrated in Fig. 2.11.

$$\sigma_{in-plane} = \frac{E\,\Delta\alpha\,\Delta T}{1-\nu} \qquad (2.32)$$

At the peak and valley of the coating interface from Fig. 2.11, the out-of-plane stresses can be estimated as stresses at the coating interface of the coated cylinder as explained by Gong and Clarke [55]. Their work showed that the out-of-plane stresses increase as the radius of curvature at the interface peak and valley becomes smaller. The stresses at the hill regions of the interface can be represented in terms of local in-plane stress by Eq (2.33) and (2.34). If it is assumed that shear stresses ($\tau_{xy}$) are negligible, through thickness stresses ($\sigma_{y'}$) increase when the aspect ratio of the coating increases. Through thickness tensile stress ($\sigma_{y'}$) is the main driving force for the openings of the TBC discontinuities, and if the stress magnitude is increased, the subsequent coating spallation is favoured. Therefore, it can be assumed that an increase in the aspect ratio of the coating roughness causes a reduction in coating spallation life.

$$\sigma_{x'} = \frac{\sigma_x + \sigma_y}{2} + \frac{\sigma_x - \sigma_y}{2}\cos 2\theta + \tau_{xy}\sin 2\theta \tag{2.33}$$

$$\sigma_{y'} = \sigma_x + \sigma_y - \sigma_{x'} \tag{2.34}$$

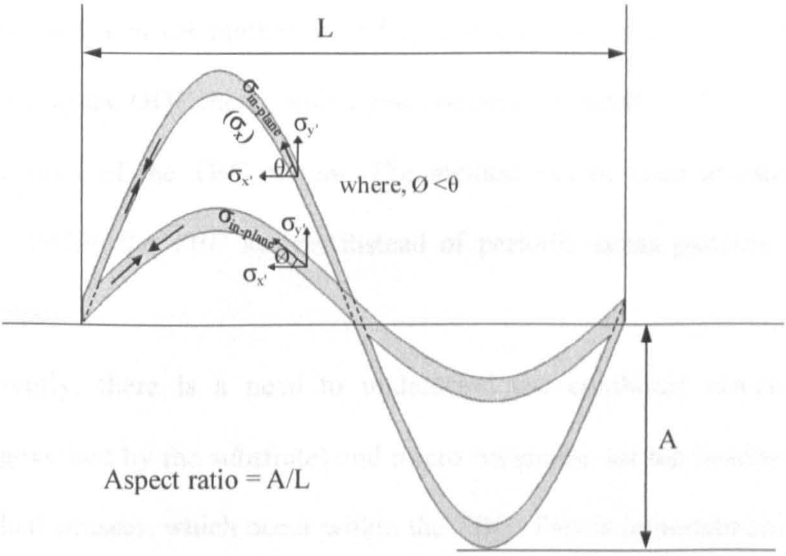

**Fig. 2.11: Local in-plane thermal mismatch stresses of the undulated TGO in terms of stresses in the global coordinate system**

### 2.8.2 Numerical studies

It is difficult to carry out stress analyses analytically for multi-layered coating systems and numerical methods such as FEA have been applied instead. A similar sinusoidal geometry from Fig. 2.11 has been assumed for the TGO interface for FE models since the 1980s such as the one from [56]. Varieties of parametric FE studies utilising different aspect ratios, have been carried out in recent decades by various researchers [13, 16, 57, 58]. These studies have led to a common conclusion that a higher aspect ratio of the interface gives higher out of plane stresses.

In an effort to model the interface shape more realistically, limited studies based on 3D coating interfaces have also been carried out [59, 60]. The study by Glynn et al. [59] demonstrated that a 2D interface model underestimates the out of plane stresses when compared to 3D models with an identical aspect ratio. Despite these efforts in modelling the coating interface realistically, the interface geometries were usually idealised as different simplified shapes (sinusoidal, cone, spherical etc.) without using the actual geometries. In contrary to this traditional approach, Hsueh et al. [57] proposed a novel method based on the OOF approach. The analysis was carried out using the OOF mesh, which was constructed based on 2D micrographs of the cross-sections of the TBC system. The method can be used to estimate actual stress states within the TBC system instead of periodic stress patterns given from idealised shapes.

Currently, there is a need to understand the combined effects of macro curvature (governed by the substrate) and micro roughness (at the coating interfaces) on the residual stresses, which occur within the TBC. This is important since the TBC systems are applied to a wide range of different components used in power generating engines or aero-engines, with various geometries.

## 2.9 Comparison of predicted stresses by FE model to those by experimental measurements

Once stresses are predicted numerically, they need to be compared against data from independent experimental measurements to obtain confidence in the accuracy of the results. Raman spectroscopy (RS) and photo-stimulated luminescence piezo-spectroscopy (PLPS) are the most common experimental techniques for measurement of residual stresses within TBC systems. The frequency shifts obtained from PLPS and RS ($\Delta v$) can be related to the residual stress tensors ($\sigma_{ij}$) using conversion factors ($\pi_{ij}$) as shown in Eq (2.35). Since, the stress tensors are measured in the laboratory reference frame, detailed knowledge about grain structures is required to convert measured residual stresses into individual stress tensor in the principal axes according to the structure of the grains. For the case of a single sapphire crystal, Zhu and Pezzotti [61] had demonstrated that stresses in the direction of the grain can be extracted from the measured frequency shifts by using different Raman bands for a single stress measurement. However, most studies for TBCs [62-64] have measured residual stress by using a laser probe to a volume which is much larger than the grain size due to the ray dispersion through the TBC [65]. Hence, these studies deal with poly-crystals in random orientations and measured stresses can only be related to the trace of the stress tensor.

$$\Delta v = \pi_{ij} . \sigma_{ij} , \tag{2.35}$$

Since the PLPS and RS methods do not give individual stress components, it is difficult to compare the experimental results directly to the stresses predicted from FE analysis. For the case where the stress state is biaxial (e.g. residual stresses at the surface of the TBC [63] or stresses within the TGO of a system without TBC [66]), measured stresses were compared to in-plane stresses predicted from FEA. However, it is widely acknowledged that the out-of-plane stress in the vicinity of the TGO interface is an important influence upon the spallation life of the APS TBC. The comparisons of these out-of-plane stresses to experimental measurements will be impossible unless individual components of stresses can be evaluated from experiments. Nevertheless, in-plane stresses can be compared between FEA and experiments to ensure the accuracy of the FE model. Thereafter, predicted out-of-plane stresses from FEA could be used to estimate the crack initiation and propagation, and the subsequent failure of the TBC.

## 2.10 Modelling of crack growth and failure of TBC

As mentioned in Section 2.6, the ductility of the TBC system is very low at room temperature whereas the BC and the TGO have high ductility at temperatures higher than their BDTTs. Therefore, brittle failure is expected at low temperatures while ductile failure is more probable for failure at the service temperature. Here, only brittle failure of the coatings at room temperature will be considered. The failure is caused by crack growth and subsequent spallation/delamination in the vicinity of the TGO interface, which is driven by out-of-plane tensile stresses. Different methods used for modelling such failures are presented as follows.

### 2.10.1 Modelling crack propagation along the defined trajectories

Cohesive zone modelling [67] (CZM) is widely used to model crack propagation along the trajectories that are defined during the pre-processing stage of numerical analyses. The application of CZM for modelling crack propagation at the TGO interface can be found in [68, 69] whereas Bhatnagar et al. [70] applied CZM for crack propagation within the TBC. Initial and subsequent separations of the CZM interfaces are controlled by a traction-separation model [67]. A parameter (f) can be used to define initiation of damage in terms of either a maximum stress or a maximum strain criterion as shown in Eq (2.36). A quadratic law as shown in Eq (2.37) can be used for damage parameter (f) of mixed-mode failure models. For both cases, the damage initiates when f is unity. Since CZM requires expected crack paths, this method is only suitable for modelling the propagation of a crack and subsequent spallation along the assumed path; in the case of TBC it is the coating interface.

$$f = \frac{\sigma_i}{\sigma_{\max}} \text{ or } \frac{\varepsilon_i}{\varepsilon_{\max}}, \text{ damage initiates when } f \geq 1 \tag{2.36}$$

$$\sum_{n=1}^{i}\left(\frac{\sigma_n}{\sigma_n^{\max}}\right)^2 = 1 \text{ or } \sum_{n=1}^{i}\left(\frac{\varepsilon_n}{\varepsilon_n^{\max}}\right)^2 = 1 \Rightarrow \text{damage initiates} \tag{2.37}$$

### 2.10.2 Modelling arbitrary crack propagation

One of the limitations of CZM is that the direction of crack propagation is independent of damage drivers (stress or strain) within the model. Therefore, changing the crack propagation direction during the processing stage is impossible. Bhatnagar et al. [70] proposed that the change in crack direction (α) can be calculated from the assumption that the strain energy release rate (G(α)) in the propagation direction is equal to the critical strain energy release rate of the coating. G(α) can be related to the traction stresses at the cracking interface (T(α)) and separation of the interface (δ(α)) as shown in Eq (2.38). The effective traction for mixed mode failure T(ζ) can be expressed as shown in Eq (2.39). By substituting Eq (2.39) into (2.38) and applying the boundary conditions for maximum G(α), the crack propagation direction (α) can be evaluated as expressed in Eq (2.40). The change in crack path was modelled by creating the new mesh embedded with the updated crack trajectories modelled by cohesive elements.

$$G(\alpha) = \int_0^{\delta} T(\alpha)\ d\delta \tag{2.38}$$

$$T(\alpha)=\sqrt{T_n^2+\beta^{-2}T_t^2}=\sqrt{\begin{aligned}&\left(\sigma_{xx}\sin^2\alpha-\sigma_{xy}\sin 2\alpha+\sigma_{yy}\cos^2\alpha\right)^2+\\&\beta^{-2}\left(-\frac{1}{2}\sigma_{xx}\sin 2\alpha+\sigma_{xy}\cos 2\alpha+\frac{1}{2}\sigma_{yy}\sin 2\alpha\right)^2\end{aligned}} \qquad (2.39)$$

where $T_n$ and $T_t$ are normal and tangential traction, $\beta$ is an empirical factor

$$\alpha=\sin^{-1}\left(\frac{\sigma_{yy}-\sigma_{xx}\pm\sqrt{\left(\sigma_{xx}-\sigma_{yy}\right)^2+4\sigma_{xy}^2}}{\sqrt{\left(\sigma_{yy}-\sigma_{xx}\pm\sqrt{\left(\sigma_{xx}-\sigma_{yy}\right)^2+4\sigma_{xy}^2}\right)^2+4\sigma_{xy}^2}}\right) \qquad (2.40)$$

Bäker [71] proposed an alternative method for modelling arbitrary crack growths using trial cracks and the application of this method for the crack growth analysis within TBCs can be found in [72]. Different meshes were used to accommodate trial cracks which are placed at different angles from the existing crack. Nodes along the trial cracks are forced to debond using quasi-static crack growth modelling [67] within ABAQUS. Thereafter, the strain energy release rates arising from crack propagation within ±5° from the initial crack were calculated. If the maximum energy is found, the corresponding direction is taken as the crack propagation direction for the next time step. Both this method and Bhatnagar's method [70] require complex remeshing of the geometries whenever there is a change in the direction of crack propagation. Moreover, interpolating the results from the previous mesh to updated mesh is also required. Therefore, a more sophisticated method such as the extended finite element method [67] (XFEM) should be used to implement the arbitrary crack growth within the TBC to save computation time.

## 2.11 Lifetime assessment of TBC systems

Lifetime assessment approaches can be divided into two categories depending on the nature of engine usage. For a continuous operating duration of more than

30,000 hours, failure of the TBC due to oxidation, corrosion and erosion are common. Tensile failure by inelastic strain and creep strain, during operation, are also important. Brittle failure of coatings due to crack development at the end of cooling, driven by tensile mismatch stresses is also expected. For lifetime assessment for engines with high cycle application, degradation of interfacial strength of the coating interface and crack development by fatigue loading, in addition to factors for continuous operation, have to be considered.

### 2.11.1 Life prediction based on oxidation

Chan, et al. [73] related the amount of Al within the β phase of the BC to the failure of the TBC system. The depletion in the aluminium phases within the BC is caused by formation of $Al_2O_3$ and inter-diffusion at the BC-superalloy substrate. It is assumed that the coating reaches its service life when the volume fraction of beta phase ($V_\beta$) at cycle number N, ($V_\beta(N)$), is zero. Otherwise, the remaining life was calculated as the ratio of total cycle life as shown in Eq (2.41). The assumption made here is appropriate since the depletion of Al concentration leads to high tensile out-of-plane stresses due to formation of fast growing oxides of Ni, Cr and Co. Because of these tensile stresses, the TBC could delaminate at the TGO interface.

$$V_\beta(N) = \frac{X_{Al}(N) - X'_{Al}}{X_{Al}(0) - X'_{Al}} \tag{2.41}$$

$X_{Al}(N)$ = Aluminium content in BC at cycle N

$X_{AL}(0)$= Initial aluminium content in BC

$X^{\beta}_{Al}$= Aluminium content in β phase (NiAl)

$X'_{Al}$= Aluminium content in $\gamma / \gamma'$ phase

### 2.11.2 Fracture mechanics based life assessment

Failure of the TBC can also be simulated by means of a fracture mechanics approach. Different methods for simulating crack development were reviewed in Section 2.10. Within those analyses, the durations of heating, creep parameters and material properties can be varied to observe their effects on spallation of TBC or delamination at the oxide interface. For example, Caliez [68] has successfully modelled the delamination process at the BC/TGO interface based on stresses produced from cooling. Another method using trial cracks by Seiler et al [72] has also demonstrated spallation of the TBC. For both methods, crack initiation and propagation are controlled by tensile strength and critical strain energy release rate respectively. Cracks propagate when the energy rate is higher than critical strain energy at the interface or the coating. For two dimensional analyses with only Mode I crack growth, critical strain energies ($G_c$) can simply be evaluated from corresponding fracture toughness values ($K_I^2$) by using Eq (2.42).

$$G_c = \frac{K_I^2}{E} \tag{2.42}$$

where E is Young's modulus

### 2.11.3 Lifetime assessment for cyclic operation

Either thermal or thermo-mechanical load can be considered for evaluating the combined fatigue life of the engine. In the simplest way, lifetime can be predicted using the Manson-Coffin power law relationship between cyclic lifetime ($N_f$) and inelastic strain range ($\Delta\varepsilon_i$) in the TC as shown in Eq (2.43). The inelastic strain range (plastic strain and creep strain) can be found from experiments [74] or direct cyclic analysis using ABAQUS [67]. $\Delta\varepsilon_f$ is the strain range experienced by the TBC system and is expressed via Eq (2.44).

$$N_f = \left(\frac{\Delta\varepsilon_i}{\Delta\varepsilon_f}\right)^b \tag{2.43}$$

$$\Delta\varepsilon_f = \Delta\varepsilon_{f_0}\left(1-\frac{\delta}{\delta c}\right)+\Delta\varepsilon_i\left(\frac{\delta}{\delta c}\right) \tag{2.44}$$

$\Delta\varepsilon_{f_0}$ is the strain range causing failure in one cycle in the absence of oxidation. It can usually be found from shock experiments where a critical temperature drop causes the coating to spall after thermal shock. $\delta$ and $\delta_c$ are the instantaneous TGO thickness and the critical value of TGO thickness before spallation occurs respectively.

Busso et al. [75] proposed a damage based fatigue life analysis by assuming that the failure is caused by many discontinuities in the TBC. The out of plane stress ($\sigma_{22\max}$) can arise from thermal mismatches, the TGO growth and the sintering of the YSZ causes opening of discontinuities. A damage parameter (D) is defined to be 0 at the start of thermal cycling and 1 at the point of failure caused by coalescence of cracks in the TBC as a result of the fatigue loading. The rate of change of D with respect to the number of thermal cycles (N) is given in Eq (2.45).

$$\frac{dD}{dN} = D^{m(\sigma_{22\max})}\left(\frac{\sigma_{22\max}}{F(\sigma_{22\max})}\right)^p \tag{2.45}$$

m, F is a driving force ($\sigma_{22\max}$), which is a function of out-of-plane stresses and p is a material constant.

An empirical damage-based life prediction was proposed by Brodin, et al. [76]. A damage accumulation parameter (D) for the TGO, the TBC and the TGO/TBC interface in terms of total crack lengths at those regions as shown in Eq (2.46), which were measured after thermal or thermo-mechanical load cycles. The ratio of damage growth with respect to number of cycles $\left(\frac{dD}{dN}\right)$ is given as in Eq (2.47).

$$D = \frac{\sum_a l_a^{TGO} + \sum_b l_b^{TC} + \sum_c l_c^{TGO/TC}}{L} \tag{2.46}$$

$l_a^{TGO}$, $l_b^{TC}$ and $l_c^{TGO/TC}$ are summations of crack lengths of those 'a', 'b' and 'c' cracks propagating in the TGO, the TC and the TGO/TC interface respectively.

$$\frac{dD}{dN} = C(\lambda \Delta G)^n \tag{2.47}$$

$\Delta G$ = energy release rate. C and n are power law constants and $\lambda$ is the decrease in crack growth rate when mixed mode I and II are considered as opposed to Mode I alone.

Although there have been advances in simulating crack growths and spallation by using cyclic loads using commercial FE codes [67], implementations of fracture mechanics based fatigue crack growth have yet to be found in the literature.

## 2.12 Conclusions of literature review

This chapter has reviewed a variety of approaches for simulating residual stresses and the subsequent failure of TBC systems. By examining the trends found in the literature, areas where improvements are required are listed as below:

i. Non-isotropic strain associated with the growth of oxide;
ii. Implementation of a constitutive model for TBC sintering, which accounts for increase in both elastic modulus and thermal conductivity of the TBC due to sintering, within the stress analysis model;

iii. Comparisons of creep properties measurements on standalone coatings with relevant numerically calculated values;

iv. Superimposing local micro roughness onto the substrate curvature within the FE unit cell model without compromising computation time drastically;

v. Investigation and implementation of the 3D coating roughness within FE model of the TBC;

vi. Comparison of predicted coating stresses, particularly TBC stresses, to those measured by Raman or PLPS techniques;

vii. Modelling of the growths of cracks within the TBC systems in order to investigate the effects of residual stresses and fracture toughness of coatings on spallation of the TBC;

viii. Modelling fatigue crack growths within the TBC systems.

All tasks, except task (i), (iii) and (viii), have been investigated as part of the current project and are presented in the following chapters. Due to the lack of experimental data available to characterise directional oxide growth, oxide growth was considered to be isotropic. Moreover, carrying out mechanical tests on a standalone coating is outside of the project scope and hence task (iii) cannot be accomplished for the current model. As our main aim is to predict the lifetime of an APS TBC system for industrial gas engines with a minimal start-stop cycle, fatigue failure (task (viii)) is not investigated here. The scope of the thesis is presented as follows.

## 2.13 Scope of the thesis

The effect of the sintering of the TBC on its mechanical and thermal properties (elastic modulus and thermal conductivity) of the TBC was implemented, as a constitutive model, using an Arrhenius-based approach (Chapter 3). The resultant model was then used throughout the thesis to account for changes in material properties due to sintering.

To understand the effect of substrate curvature on the failure of the TBC, a unit cell model of a curved substrate incorporating a representation of microscopic coating roughness was modelled. In order to save computation time, longitudinal and cylindrical periodic boundary conditions were applied (Chapter 4).

To obtain confidence in the complex boundary conditions and material properties applied to FE model, predicted residual stresses and trends in spallation of the TBC were compared against experimental stress measurements from project partners (Chapter 5).

To mimic the actual microscopic roughness of the coating, coating roughness was captured and analysed in 3D to extract specific features of coating interface. These features were then idealised and used to build unit cells for FE model to carry out stress analysis (Chapter 6).

Finally, the onset spallation/delamination of the TBC, due to crack growth driven by stresses developed from thermal mismatch, was also investigated using the extended finite element method (XFEM) (Chapter 7). The method can demonstrate the actual failure of the TBC instead of predicting failure from the stress plots of damage-free system. Moreover, the effects of TBC initial defects on subsequent crack growth and changes in stress fields due to stress relaxation caused by crack openings can also be studied.

Chapter 8 and Chapter 9 provide the conclusions and possible areas of future work respectively.

# Chapter 3

# Effects of TBC sintering on stress distribution within the TBC system

---

## 3.1 Introduction

The APS manufacturing method is commonly used for spraying TBCs onto components of land based engines. The process requires multiple passes of spraying to achieve the required coating thickness. Thus, there are gaps between successive layers of the APS TBC. Moreover, numerous micro-cracks are found within each layer of an APS TBC [38]. The former defects are called inter-splat defects and the latter are intra-splat defects. The overall porosity reduction occurs when there are linkages between inter-splat defect and healing of intra-splat defect due to sintering of the TBC at high temperatures. Because of this porosity reduction, the modulus and the thermal conductivity of the TBC, and the temperature gradients across the TBC are changing simultaneously. The significance of these changes in material properties on the stresses within TBC systems is investigated in this chapter.

The modulus of the TBC affects the stress state due to the mismatch in the thermal expansion between the TBC and its underlying layers. Thus, it is necessary to consider the increase in modulus of the TBC when predicting stresses via FE models. Nevertheless, this effect has often been ignored by researchers; for example, the model in [77] assumed the modulus of the TBC to be a constant value of 20GPa. Ranjbar-Far et al. [16] and Rösler et al. [24], on the other hand, included the temperature dependency of the TBC modulus but ignored the effect of TBC aging. As a result, the predicted stress state can be significantly underestimated by the FE model. An Arrhenius relationship between the modulus of a TBC, and the sintering time and temperature, is formulated in Section 3.2 using empirical measurements of TBC elastic moduli by Zhu and Miller [40].

Most TBC-coated components have internally circulated cooling air (convection cooling) and holes within the substrate to pump cooling air out of the substrate (film cooling). Due to the internal cooling systems, heat flux is created across the TBC. If the heat flux is assumed to be constant over the course of operation, the temperature gradient across the TBC is largely dependent on the thermal conductivities of the TBC. Without considering this interrelation, a temperature gradient, which is unchanged throughout a thermal cycle, has been coupled to FE models of the TBC systems for stress analysis [63] in the past. An analytical 1D relationship between thermal conductivity and temperature variation based on empirical based Larson-Miller parameters (LMP), as presented in [78], is implemented to create a temperature gradient across TBC.

## 3.2 Arrhenius fit for rate of change in modulus of YSZ TBC due to sintering

Sintering is a temperature driven process. When the coating experiences high temperature, grain growth and aggregate densification occur. The longer the temperature is applied, the more activation energy will be available for densification of ceramic particles. Here, an empirically based Arrhenius rate formula, based on experimental measurements of elastic moduli at various sintering temperatures and durations, is derived to represent the change in TBC modulus due to sintering.

An Arrhenius rate equation is used to determine the dependence of the rate of reaction on the temperature at which the reaction takes place [79]; it has the form shown in Eq (3.1), while Eq (3.2) is an alternative expression in a logarithmic form.

$$k = Z * \exp\left(-\frac{Q}{R*T}\right) \tag{3.1}$$

$$\ln(k) = \ln(Z) + \left(\frac{-Q}{R}\right)\left(\frac{1}{T}\right) \tag{3.2}$$

where Q and R are the activation energy of the reaction and the universal gas constant respectively. Z is a constant prefactor in the Arrhenius equation. k is the rate constant, or rate of reaction, at different temperatures.

Q and Z from Eq (3.1) can be obtained by fitting a straight line to a plot of ln(k) versus $\left(\frac{1}{T}\right)$. Various kinetic assumptions can be made to describe the rate of reaction; e.g. it can be constant throughout the reaction period as is the case of a zeroth order reaction. Alternatively, the rate of reaction can be assumed to depend upon the concentrations of one or two reactants. The former situation is known as a first order reaction and the latter is a second order reaction. k can be found from various straight line fits as indicated in Table 3.1.

**Table 3.1: Reaction orders and rate equations [79]**

| Reaction order | Rate law | Straight line fit |
|---|---|---|
| Zeroth | Rate = k | (1-s) Vs time |
| First | Rate = k * $(1-s_0)$ | ln(1-s) Vs time |
| Second | Rate = k * $(1-s_0)^2$ | 1/(1-s) Vs time |

The set of data collected by Zhu and Miller [40], within which the modulus of a 1.5mm thick TBC was measured using the nano indentation technique, at the end of 1h, 11h and 120h of sintering, was used as the starting point for extracting an equation for the sintering rate. Variations in the modulus of the TBC across its thickness, due to the applied thermal gradient, were also taken into consideration. The temperature of the surface of the TBC during the sintering was maintained at 1080°C, while the temperature of substrate was kept at around 100°C. Assuming the spatial variation of temperature, across the TBC, is linear, the variation of the elastic moduli, at different stages of sintering, can be determined as shown in Fig. 3.1.

The temperature range of practical interest in industrial engines is between 800°C and 1000°C. Within this temperature range, two types of sintering can be identified, from the data from Zhu and Miller [40], as demonstrated in Fig. 3.1. The modulus of the YSZ coating increases rapidly from 0h to 1h and from 1h to 11h of sintering but the rate slows down between 11h and 120 h of sintering. It was proposed that a rapid increase in modulus (Type I sintering) is caused by improved bonding between splats of TBC while Type II sintering with slower increase in modulus is caused by the healing of micro cracks within the TBC [38]. The two processes may occur in parallel and the rate of sintering then depends on the porosities of the TBC created by both inter-splat and intra-splat defects. Thompson et al. [38] have illustrated that Type II sintering is not significant at temperatures lower than 1200°C, and it could be the reason for slower increase in modulus between 11h to 120h of sintering (Fig. 3.1). Therefore, it is assumed that only Type II sintering occurs during this period. Only sintering rates between 0h to 11h are fitted by an Arrhenius equation here and the modulus is assumed to be unchanged after 11h of sintering.

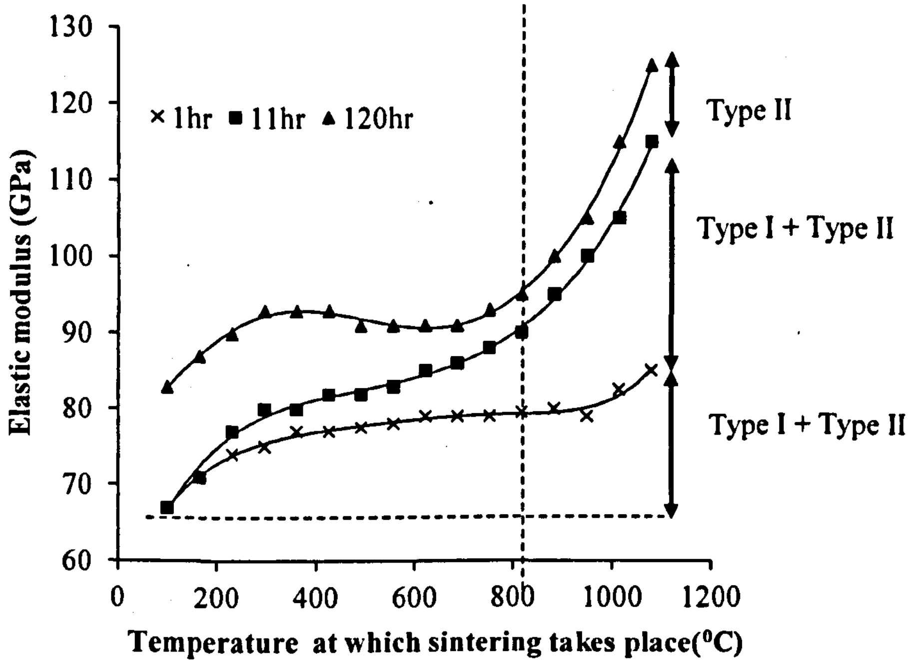

**Fig. 3.1: Variations of elastic modulus with sintering temperature at times of 1h, 11h and 120h for YSZ surface, at 1080°C and substrate, at 100°C [40]**

If it is assumed that the TBC is totally unsintered at the beginning and that it is fully sintered after 120h of heating at 1080°C, the fraction *s* of TBC which has been sintered at any other combination of time and temperature can be calculated by use of Eq (3.3). The modulus of the YSZ coating after 1h of sintering at 100°C and the modulus after sintering at 1080°C for 120 h are taken as the initial ($E_0$) and the final ($E_f$) elastic modulus of the YSZ, respectively.

$$s = \frac{E - E_0}{E_f - E_0} \tag{3.3}$$

The rate of change of the unsintered proportion of the TBC (1−s) denoted as A, at different temperatures $\left(\frac{d(1-s)}{dt}(T) \text{or} \frac{dA}{dt}(T)\right)$ is fitted by an Arrhenius equation. A second order reaction assumption, see Table 3.1, gives the best fit for the rate constants, as shown in Fig. 3.2. The rate constants (k) at different temperatures are found as the slopes of the straight lines plotted from various plots of 1/A versus t, at different temperatures, as shown in Fig. 3.2.

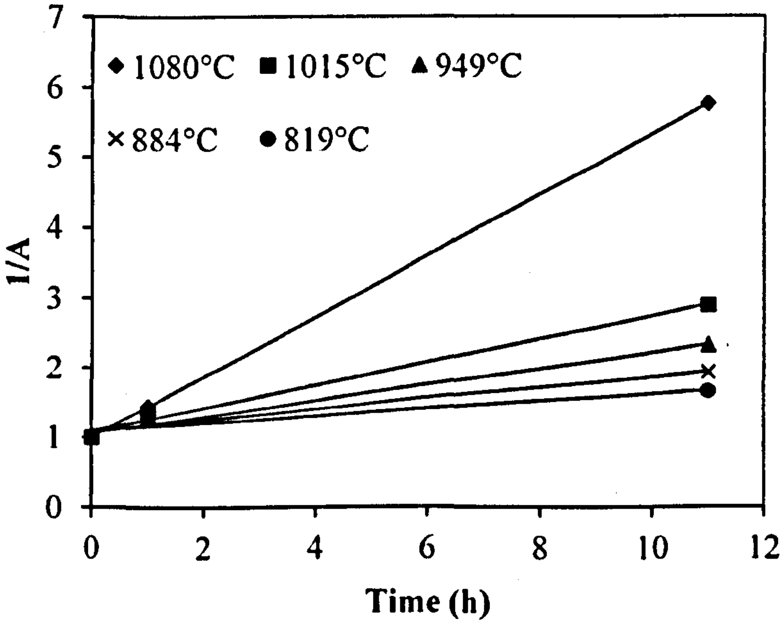

**Fig. 3.2: Second order straight line fit for reaction rate**

Values of k at different temperatures were fitted to an Arrhenius plot, as shown in Fig. 3.3, and the activation energy (Q) and prefactor (Z) were found to be 93.58 kJ/molK and 1327.03, respectively. To check the validity of the Arrhenius parameters, the elastic moduli of the TBC, after sintering for 1h and 11h at temperatures between 819°C and 1080°C, were calculated using the Arrhenius relationship. They were then plotted, together with the experimental results [40], in Fig. 3.4. The elastic moduli fitted by the Arrhenius parameters are within ±10 GPa of empirical values. These results confirm the validity of the Arrhenius fitting process for TBC modulus. With the Arrhenius parameters calculated in this section, the elastic modulus of a TBC can be evaluated at any combination of sintering time and temperature. It should, however, be noted that it is necessary to consider in-situ changes in modulus of the YSZ coating since Zhu and Miller [40] measured the TBC modulus at room temperature after sintering had taken place at various temperatures. The modulus of the TBC could be reduced at higher temperatures and it is possible to scale the elastic moduli of a TBC, using the graph of in-situ temperature dependent TBC moduli given by Qi et al. [80], though the process has not been validated.

Finally, the modulus of the YSZ coating can be expressed as a function of temperature, sintering time and sintered temperature by Eq (3.4).

$$E\left(T,T_{op},t\right)=\frac{E_0\left(T\right)}{E_0}\left[\left\{\left(1-\frac{1}{1+\left[\int_0^t\left(Z\exp\left(-\frac{Q}{RT_{op}}\right)\right)dt\right]}\right)\left(E_f-E_0\right)\right\}+E_0\right] \quad (3.4)$$

where $E_0(T)$ = The modulus of a fresh TBC at temperature T (GPa), T = The temperature of YSZ TBC (°C), t = The sintering time (h), $T_{op}$ = The operation temperature of a gas turbine and R = Universal gas constant ($JK^{-1}mol^{-1}$)

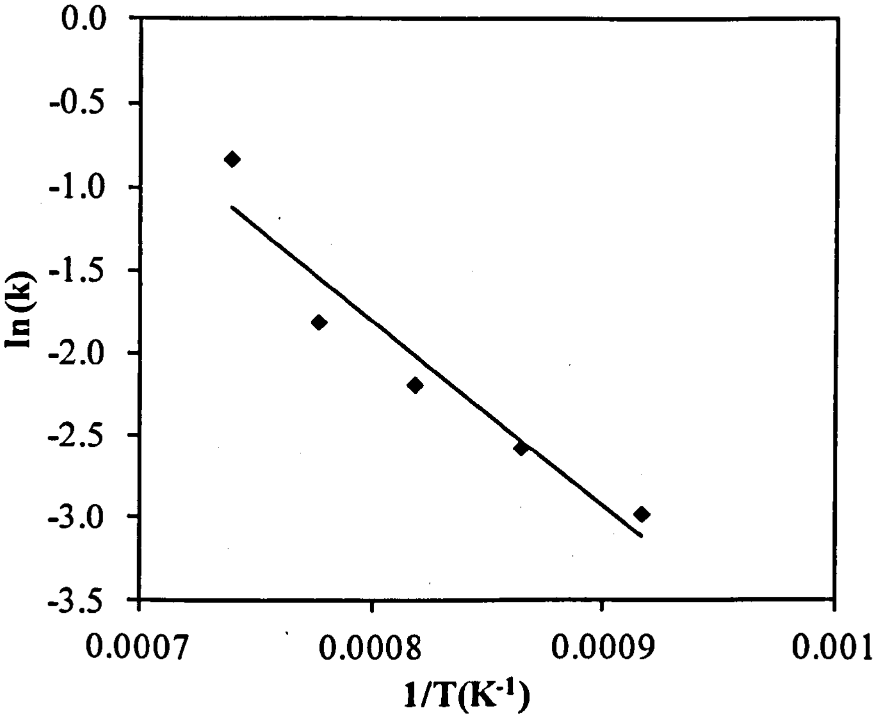

**Fig. 3.3: Arrhenius fit for reaction rates of sintering**

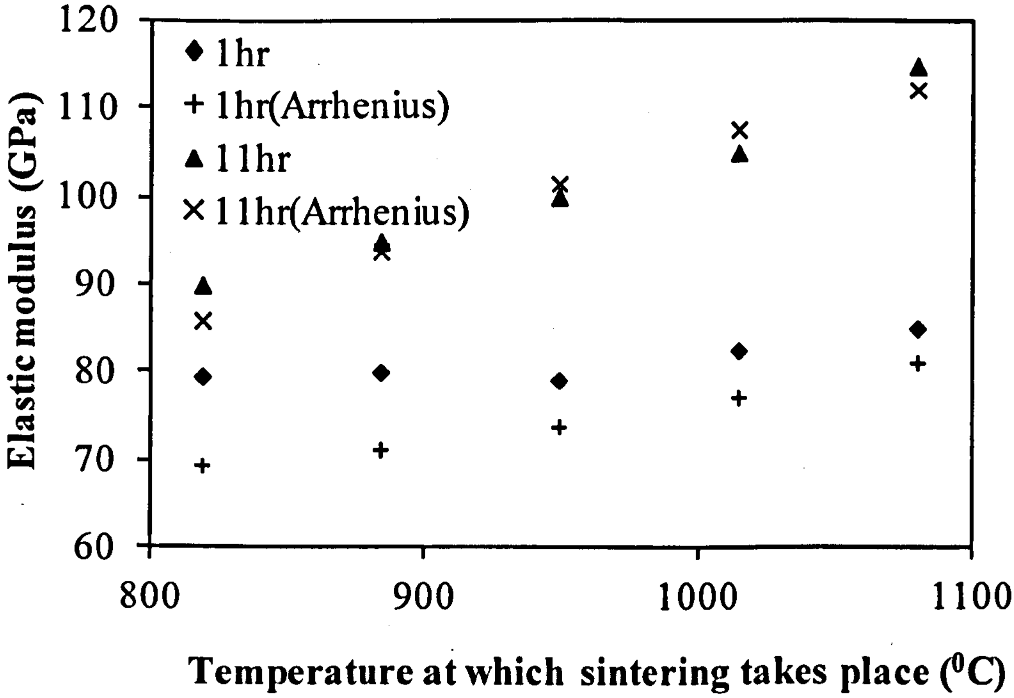

**Fig. 3.4: Experimental elastic moduli [33] compared with Arrhenius fitted values**

## 3.3 1-D thermal conductivity model of sintering

Although it is reasonable to assume isothermal heat treatment for furnace heating of a TBC coated specimen in the laboratory environment, the TBC system is subjected to heat flux during the actual operation, due to internally circulated cooling air. As the TBC is densified through sintering, the volume of trapped air within the pores of the TBC is reduced and the overall thermal conductivity (κ) is increased. As the rate of densification varies throughout the TBC due to the temperature gradient, the rate of increase in κ will be different too. At the same time, the temperature gradient is also dependent on κ.

The heat transfer process within the TBC coated system is rather complicated. There are factors other than thermal conductivity that change the temperature gradient of the system; e.g. pressure of cooling air and its turbulence etc. To take account of these factors, it is necessary to carry out a separate heat transfer analysis to couple the resultant temperature profile with the mechanical FE model of the TBC. To simplify the problem without using coupled thermo-mechanical FE systems, an empirical based model, which relates temperature and thermal conductivity of the TBC, as described in [78], is used to update the temperature field across the TBC. This is a 1D thermal conductivity model and it is based on the concept that the temperature distribution across the TBC can be represented by thermal conductivities at n equally-spaced nodal points along a line through the TBC thickness as shown in Eq (3.5).

$$\hat{T} = \frac{\left[ \dfrac{i - n\hat{x}}{\kappa_i} + \sum_{m=i+1}^{n} \left( \dfrac{1}{\kappa_m} \right) \right]}{\sum_{m=1}^{n} \left( \dfrac{1}{\kappa_m} \right)}; \left( \frac{i-1}{n} \langle \hat{x} \langle \frac{i}{n},\ i = 1,2,3...,n \right) \qquad (3.5)$$

where $\hat{T}$ and $\hat{x}$ are dimensionless parameters of temperature (T) at arbitrary location within the TBC and of distance from TBC surface (x) as shown in Eq (3.6).

$$\hat{T} = {(T - T_n)}/{(T_0 - T_n)}, \hat{x} = {x}/{H} \tag{3.6}$$

where $T_0$ and $T_n$ are temperatures at the TBC surface and at the TGO/TBC interface respectively, and H is the thickness of the TBC.

By substituting a linear relationship between $\kappa$ and $\hat{x}$ as shown in Eq (3.7) into Eq (3.5) and integrating it to represent continuous changes of $\kappa$ along the TBC thickness, $\hat{T}$ and the average thermal conductivity ( $\bar{\kappa}$ ) can be found.

$$\kappa = \mathrm{A} + \mathrm{B}\,\hat{x} \tag{3.7}$$

The parameters A and B from Eq (3.8) are sintering-dependent as $\kappa$ changes according to sintering. A linear relationship between LMP, as shown in Eq (3.8), and natural log of $\hat{\kappa}$ ( $\kappa / \kappa_{as-sprayed}$) is used to describe the evolutions of $\kappa$ due to sintering. Using the LMP, the evolutions of $\kappa$ due to both sintering time and temperature can be represented.

$$LMP = T_{sint}(\ln t + 20) \tag{3.8}$$

The Larson-Miller (L-M) method and the method described in Section 3.2 for the elastic modulus of the TBC (E) are both based on Arrhenius equation. The latter was developed independently to relate E of the TBC with sintering time and temperature. Recently, the L-M method was used by Tan et.al [78] to fit sintering time and temperature dependent κ. Using the LMP, temperature dependency of the parameters can be implemented within a single parameter as shown in Eq (3.9).

$$LMP = C_o T_{sint} + T_{sint}(\ln t + 20) \tag{3.9}$$

where $C_o$ is a linear fitting parameter, which represents the significance of temperature on κ. This parameter is evaluated from linear regressions of in-situ measurements of κ during sintering at different isothermal temperatures.

In-situ measurements of elastic modulus, similar to the one for thermal conductivity to evaluate LMP parameter during sintering at elevated temperature, are not available in the open literature. Hence, the LMP given in Eq (3.9) cannot be applied to evaluate elastic modulus of sintered TBC; the approach described in Section 3.2 is still used.

## 3.4 Finite element model

A finite element model of the TBC is based on the geometry of a cylinder with inner radius of 3.2mm and outer radius 6.2mm. The thickness of the BC is 100μm. The thickness of the TBC is 440μm and 200 μm for the model with and without considering changes in thermal conductivity of the TBC. The latter thickness of the TBC is chosen from the specimen on which measurements of $\lambda$ were carried out in [78] in order to assume an identical heat flux within the TBC of the current FE model. It is assumed that there is 1μm of initial TGO due to oxidation of the BC during the spraying process. The interface of the TGO is assumed to be a sinusoidal shape with an amplitude (A) of 6 μm and a wavelength (L) of 48 μm giving an aspect ratio (A/L) of 0.125. This roughness ratio is one of the sets that has been used for the stress analysis of a range of TBC systems in [21].

The TBC system is modelled as an axisymmetric strip of the cylinder as shown in Fig. 3.5 using axisymmetric elements with reduced integration scheme (CAX4R). It is assumed that the sinusoidal TGO interface is periodic along the axial direction. The nodes, along the bottom surface of the model, are restricted to move in the axial direction to model a symmetric sinusoidal interface. The boundary condition for the periodic plane can be obtained as mentioned in [81]. The symmetry constraint imposes the displacements of nodes at the periodic planes, at $z = b$ and $z = -b$, to be opposite as shown in Eq (3.10). Additional constraint for displacements of nodes at those periodic planes, as shown in Eq (3.11), is needed for periodic boundary conditions of the sinusoidal interface. Using Eq (3.10) and (3.11), finally nodes at the plane where z = b are constrained using Eq (3.12).

$$U_z\big|_{z=b} = -U_z\big|_{z=-b} \tag{3.10}$$

$$U_z\big|_{z=b} - U_z\big|_{z=-b} = 2b\varepsilon_z \tag{3.11}$$

$$U_z\big|_{z=b} = b\varepsilon_z \tag{3.12}$$

A thermal cycle consists of heating the system over a period of 1800s, followed by 900h of holding time at 1000°C before cooling down to 20°C over a period of 1800s. For the temperature gradient models, the surface temperature and heat flux of the TBC are kept constant throughout the steady state. Temperatures along the TBC are updated based on the instantaneous thermal conductivity.

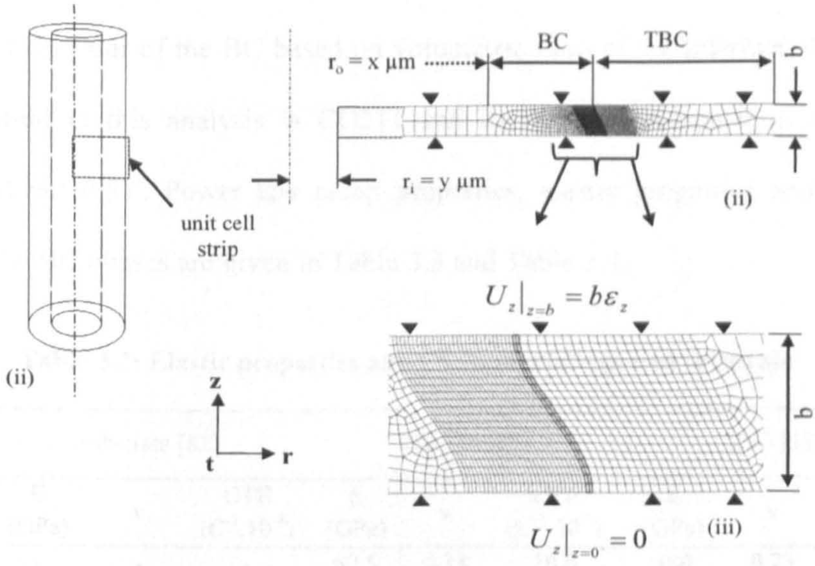

**Fig. 3.5: (i) A coated hollow cylinder; (ii) the geometries and model meshes (iii) detailed meshes near the TGO and boundary conditions of the FE model**

### 3.4.1 Material properties

The material properties of the coatings and the substrate are all assumed to be isotropic and the deformation is calculated according to their elastic and creep behaviours. Consideration was given to whether plasticity of the BC should be included in the FE model; it was omitted for the following reasons. At elevated temperature, creep relaxation within the BC prevents the build-up of stresses large enough to cause plasticity. During cooling, brittle failure due to tensile stresses without significant plastic deformation is a dominant failure mechanism. This is because the ductility of the BC is low at temperatures lower than its ductile-brittle transition temperature (DBTT) [49]. Plasticity of the BC, hence, is not considered for the current analysis. Elastic properties, coefficient of thermal expansion (CTE) and power law creep constants of the substrate and as sprayed coatings except the BC are tabulated in Table 3.2 and Table 3.3. For the material properties of the BC, Eshelby's based model, which considers changes in constituents of its phases during the steady state, by Hermosilla [21] is adopted here. The model predicts elastic properties, CTE and creep behaviour of the BC based on volumetric ratio of the intermetallic phases. The BC used in this analysis is CO211 and its nominal composition in %wt is Co32Ni21Cr8Al0.5Y. Power law creep properties, elastic properties and CTEs of intermetallic BC phases are given in Table 3.3 and Table 3.4.

**Table 3.2: Elastic properties and CTEs of coatings and substrate**

| Temp (°C) | Substrate [82] | | | TBC[40, 83] | | | TGO [17, 83] | | |
|---|---|---|---|---|---|---|---|---|---|
| | E (GPa) | v | CTE $(C^{-1}.10^{-6})$ | E (GPa) | v | CTE $(C^{-1}.10^{-6})$ | E (GPa) | v | CTE $(C^{-1}.10^{-6})$ |
| 20 | - | - | - | 62.5 | 0.18 | 10.0 | 400 | 0.23 | 6.62 |
| 24 | 206 | 0.28 | 11.23 | - | - | - | - | - | - |
| 93 | 195.1 | 0.27 | 11.97 | - | - | - | - | - | - |
| 100 | - | - | - | 59.6 | 0.18 | - | - | - | - |
| 200 | - | - | - | 55.7 | 0.18 | - | 390 | 0.23 | - |
| 204 | 190.3 | 0.27 | 13.23 | - | - | - | - | - | - |
| 316 | 184.8 | 0.28 | 14.4 | - | - | - | - | - | - |
| 400 | - | - | - | 44.9 | 0.18 | - | 380 | 0.24 | - |
| 538 | 175.1 | 0.3 | 16.2 | - | - | - | - | - | - |
| 600 | - | - | - | 29.8 | 0.18 | - | 370 | 0.24 | - |
| 760 | 157 | 0.3 | - | - | - | - | - | - | - |
| 800 | - | - | 18.38 | 22.2 | 0.18 | - | 355 | 0.25 | - |
| 871 | 151 | 0.29 | - | - | - | - | - | - | - |
| 982 | 140 | 0.3 | 19.42 | - | - | - | - | - | - |
| 1000 | - | - | - | 19.8 | 0.18 | - | 325 | 0.25 | - |
| 1200 | - | - | - | - | - | - | - | - | 8.7 |

**Table 3.3: Power law constants of coatings, superalloy substrate and intermetallics**

| | $A_0$ (MPa$^{-n}$s$^{-1}$) | Q(J/mol) | n | Temperature (°C) |
|---|---|---|---|---|
| IN-738LC [82] [a] | $6.68*10^{48}$ | $1.72*10^{6}$ | 9.96<br>6.6 | 850<br>1050 |
| $AL_2O_3$ [17] [a] | 415.12 | $3.23*10^{5}$ | 1.08 | 1200 |
| YSZ [50] [b] | $2.60*10^{-2} \times t^{-0.67}$ | $1.05*10^{5}$ | 0.56 | 1323 |
| γ (Ni) [84] [a] | $2.79*10^{5}$ | $3.81*10^{5}$ | 5.42<br>4.90 | 850<br>1050 |
| γ' ($Ni_3Al$) [85] [a] | $8.19*10^{-14}$ | $2.68*10^{4}$ | 3.14<br>4.3 | 850<br>1050 |
| β (NiAl) [86] [a] | $2.18*10^{-1}$ | $3.15*10^{5}$ | 5.42 | 850-1050 |
| γ (Ni) [84] [a] | $2.79*10^{5}$ | $3.81*10^{5}$ | 5.42<br>4.90 | 850<br>1050 |
| γ' ($Ni_3Al$) [85] [a] | $8.19*10^{-14}$ | $2.68*10^{4}$ | 3.14<br>4.3 | 850<br>1050 |

[a] Power law creep strain rate = $A_0 \exp(-Q/RT) * \sigma^n$, [b] Power law time-dependent creep strain rate for YSZ = $2.60\times10^{-2} \exp(-1.05\times10^5/RT)\times\sigma^{0.56}t^{-0.67}$

**Table 3.4: Elastic properties and CTEs of intermetallics**

| Temp (°C) | γ (Ni) [84] | | | γ' ($Ni_3Al$) [87] | | | β (NiAl) [86] | | | σ (Cr) [84] | | |
|---|---|---|---|---|---|---|---|---|---|---|---|---|
| | E (GPa) | v | CTE | E (GPa) | v | CTE | E (GPa) | v | CTE | E (GPa) | v | CTE |
| 10 | - | - | - | 184.5 | 0.32 | - | - | - | - | - | - | - |
| 27 | 206.7 | 0.31 | 13.4 | - | - | 12.3 | 188 | 0.31 | 11.9 | 304.9 | 0.21 | 4.9 |
| 850 | - | - | - | 142.3 | 0.34 | - | - | - | - | - | - | - |
| 1000 | 132.1 | 0.31 | - | - | - | - | 150 | 0.31 | - | 236.3 | 0.21 | - |
| 1027 | - | - | 18.9 | - | - | 15.6 | - | - | 16 | - | - | 14 |

Unit for CTE is ($K^{-1}10^{-6}$)

## 3.5 Implementation of sintering dependent and constituents dependent material properties of the TBC and of the BC

Two user material (UMAT) subroutines [67] were coded in FORTRAN for the TBC and the BC. Stress increments are updated within the UMAT based on Hooke's law, which can be expressed in tensor form as shown in Eq (3.13).

$$\underline{\dot{\sigma}_{ij}} = \lambda \underline{\dot{\varepsilon}}_{kk}\delta_{ij} + 2\mu\left(\underline{\dot{\varepsilon}}_{ij} - \underline{\dot{\varepsilon}}_{ij}^{in}\right) - 3K\alpha\dot{T}\delta_{ij} \tag{3.13}$$

where the last term of Eq (3.13) is related to thermal strain resulting from CTE of the material (α) and the rate of change in temperature ($\dot{T}$). The thermal stress is calculated by using the bulk modulus (K) as the temperature change results in changes of volumetric strain. $\lambda$ and $\mu$ are Lamé parameters.

If BC and TBC are assumed as isotropic materials, the general stiffness matrix ($C_{ijkl}$), which relates mechanical stress and strain, can be expressed in terms of Lame' parameters as shown in Eq (3.14).

$$C_{ijkl} = \begin{bmatrix} 2\mu+\lambda & \lambda & \lambda & 0 & 0 & 0 \\ \lambda & 2\mu+\lambda & \lambda & 0 & 0 & 0 \\ \lambda & \lambda & 2\mu+\lambda & 0 & 0 & 0 \\ 0 & 0 & 0 & 2\mu & 0 & 0 \\ 0 & 0 & 0 & 0 & 2\mu & 0 \\ 0 & 0 & 0 & 0 & 0 & 2\mu \end{bmatrix} \tag{3.14}$$

As E is updated by Eq (3.4) due to TBC sintering, the relevant Lamé constants are updated too. Lamé constants based on the constituents of the BC were updated using the derivation based on Eshelby's method as shown in [21].

The $\dot{\varepsilon}_{ij}^{in}$ term of Eq (3.13) represents the inelastic strain rate which can be expressed via Eq (3.15) and Eq (3.16) for the TBC and the BC, respectively.

$$\dot{\varepsilon}_{ij}^{in,TBC} = \frac{3}{2} A(\bar{\sigma})^{n-1} s_{ij} t^{p} \tag{3.15}$$

$$\dot{\varepsilon}_{ij}^{in,BC} = \frac{3}{2} A(\bar{\sigma})^{n-1} s_{ij} + \frac{1}{3} \ln(PBR_{Al}) \dot{f}_{ox} \delta_{ij} \tag{3.16}$$

where $\bar{\sigma}$ is the Von Mises equivalent stress, $s_{ij}$ are deviatoric components of stress, $\dot{f}_{ox}$ is oxidation rate, A, n and m are creep power law constants.

Eq (3.15) and first term of Eq (3.16) represent time hardening creep and secondary creep behaviours of the TBC and the BC respectively. As mentioned in [50], changes of elastic modulus of the TBC, due to sintering, does affect the creep strain rate. However, the creep parameters listed in Table 3.3 were measured on the fully sintered TBC and further changes of elastic modulus during the creep test are not expected. Further creep tests on as-sprayed TBC are required to observe the effect of sintering on the creep behaviour of the TBC as outlined in [50].

The second term of Eq (3.16) is the transition strain rate resulting from oxidation of the BC forming aluminium oxide ($Al_2O_3$). The transition strain rate, which is given by the volume increase during formation of $Al_2O_3$, is assumed to be isotropic and it is calculated using the PBR of aluminium as shown in Eq (3.16). It is assumed that the oxidation of the BC occurs when oxygen enters through the permeable APS TBC, and a new oxide layer is formed at the BC/TGO interface. As oxidation continues, part of the BC is consumed to form an oxide. The rate of change of the thickness of the BC due to oxidation, is calculated by using an empirical formula, shown in Eq (3.17) from experiments in [88].

$$\dot{\delta} = n^{ox}\left\{\exp\left[Q^{ox}\left(\frac{1}{T_0}-\frac{1}{T}\right)\right]^{n^{ox}}\right\}t^{n^{ox}-1} \tag{3.17}$$

where $Q^{ox}$ is the oxidation activation energy. $T_0$ and $n^{ox}$ are empirical constants. $\dot{\delta}$ is given as $\mu m^{-1}$.

The temperature gradient across the TBC is updated by a user defined temperature subroutine [67] (UTEMP), according to the 1-D thermal conductivity model for the TBC. Resultant temperatures are then input into UMATs of the TBC and the BC. The relationship between UTEMP and UMAT of the TBC and the BC is illustrated in Fig. 3.6. During the heat-up step, sintering is not considered and temperature dependent κ, within material points of the TBC were assigned as solution dependent variables [67] (DEPVAR). Linear regression between κ and $\hat{x}$ is carried out and the regression constants are passed into UTEMP once the steady state starts. Based on these constants, nodal temperatures are updated and are imported into the UMATs representing the TBC and the BC. The temperature at the BC/TBC interface is taken as the temperature for other layers of the system because of the high value of κ of the BC and the substrate. Based on the updated nodal temperatures, κ values are updated using a linear relationship between LMP and κ. Linear regression between κ and $\hat{x}$ is carried out again and the regression constants are passed into UTEMP. The procedure is repeated throughout the steady state. Existing temperatures are ramped down to 20°C during the cooling stage.

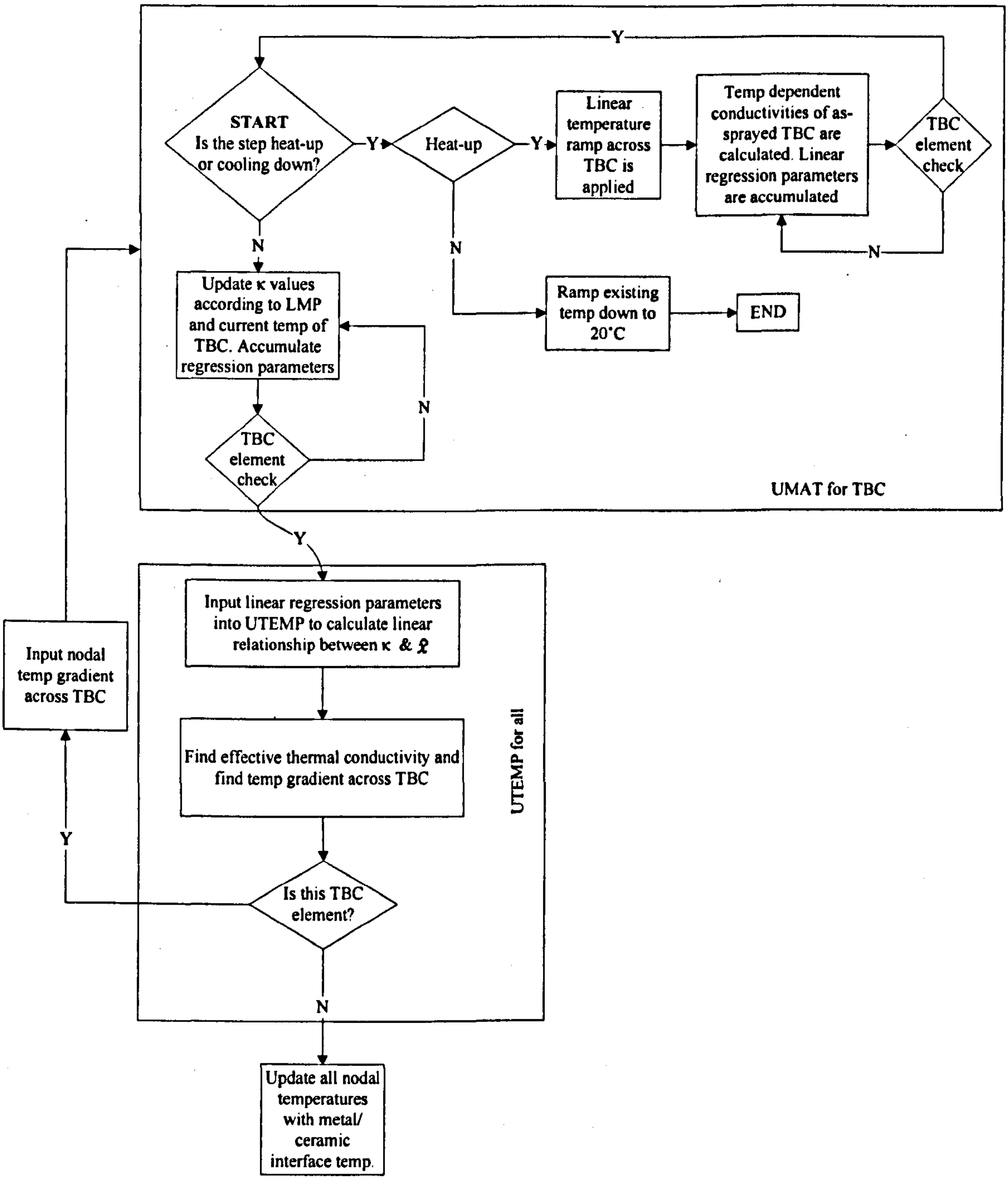

Fig. 3.6: Flowchart for implementing sintering dependent thermal conductivities of TBC and temperature gradient across TBC systems

## 3.6 Results and discussion

### 3.6.1 Effect of increase in elastic modulus of TBC due to sintering on TBC stresses

To investigate the effect of increase in modulus of the sintered TBC on the mismatch stress, the FE model outlined in Section 3.4 was simulated with and without the dependence upon sintering. The thickness of the TBC is 200μm. A constant TBC modulus of 20GPa, as quoted in [77], and temperature dependent modulus from in-situ measurements [80], are used for the TBC models without sintering. The estimated in-plane mismatch stress at the TGO/TBC interface can be related to the modulus of the TBC by Eq (3.18).

$$\sigma_{\text{in-plane}} = \Delta T \times \Delta CTE \times \frac{E_{TBC}}{1 - \nu_{TBC}} \tag{3.18}$$

The in-plane stress becomes higher when the modulus of the TBC increases as a result of sintering. By equilibrium, the increase in in-plane stress will be balanced by interfacial out-of-plane stress at the interface. Therefore, radial stress at the TGO/TBC interface is also expected to increase as the TBC is aged. The mismatch stresses within the TBC at the oxide interface, at the end of the cooling stage, are compared for different systems as shown in Fig. 3.7. If the flexural strength of the TBC, which was quoted as 150MPa by Adams et al. [89] is assumed as the level of stress, which results in cracks within the TBC, cracks are predicted to form not only in the valley of the TBC region but also to span across 65% of the interface for a fully sintered TBC model. This will cause propagation of the cracks which may have been created earlier at the interface and will lead to eventual delamination of the TBC from the TGO interface.

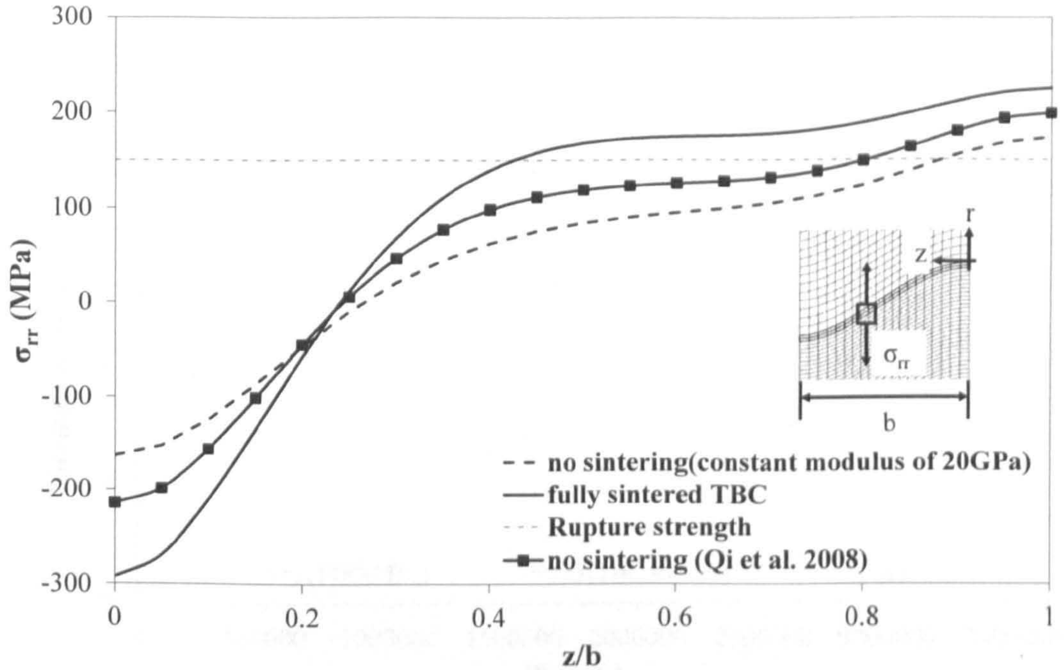

**Fig. 3.7: Effects of increase in elastic modulus of the TBC due to sintering on the out of plane stress within the TBC at the TGO interface (at the end of cooling stage after 900h of operation at 1000°C)**

### 3.6.2 Effects of temperature gradients and increase in thermal conductivity of the TBC due to sintering on TBC stresses

For the temperature gradient model, the surface temperature of the 440μm thick TBC is fixed at 1246°C and the TGO/TBC temperature is 920°C, after heat-up and before sintering takes place. After 900h of sintering, the temperature gradient is updated using the routine shown in Fig. 3.6 and its variation with time is plotted as Fig. 3.8. The decrease in temperature difference is caused by an increase in thermal conductivities and changes in respective conductivities at the TBC surface and at the TGO interface with operation time are also plotted in Fig. 3.8.

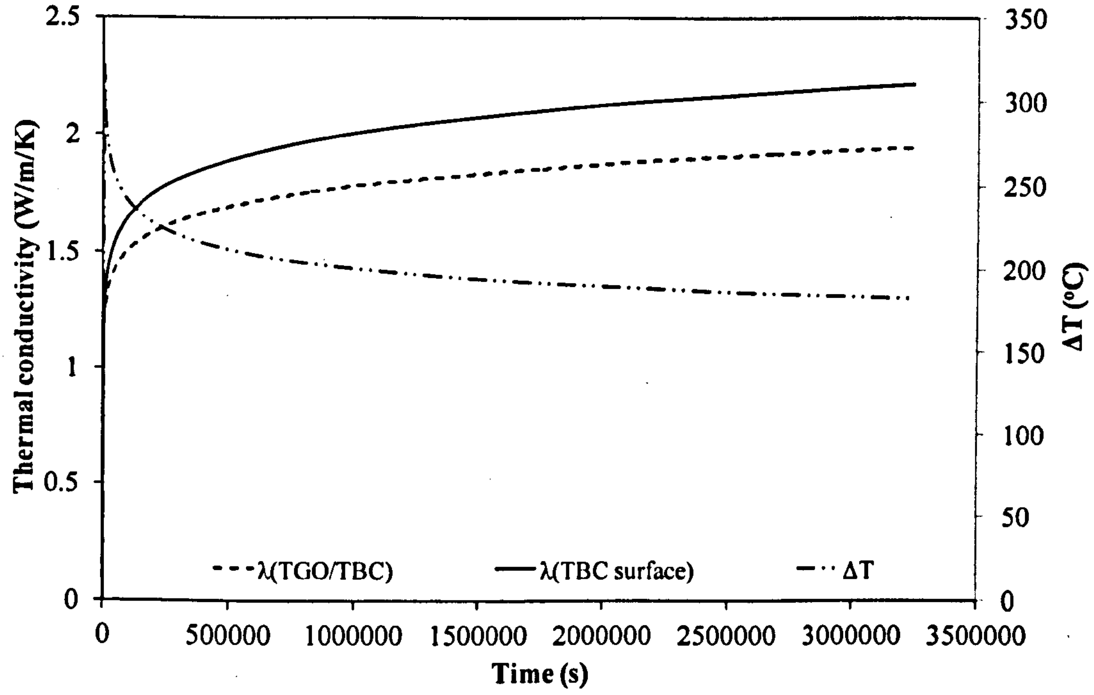

**Fig. 3.8: Temperature difference between the TBC surface and the TGO/TBC interface (surface temperature is kept constant at 1246°C) plotted alongside thermal conductivities at the TBC surface and TGO/TBC interface**

In-plane stresses within the TBC systems are created by either the CTE mismatch strain or due to temperature changes, or due to a combination of both. For the system with the temperature gradient, in-plane stresses vary across the thickness during the heat-up due to different gradients of temperature increases. Moreover, the stress relaxation rate by creep of the TBC at the coating surface is higher than at the inner regions because of the higher temperature. Consequently, the coating surface is almost stress-free at the end of steady state. When cooling is applied at the cooling stage, higher temperature regions of the TBC tend to contract more than lower temperature regions. However, the coating is constrained in the in-plane direction and the in-plane strain has to be the same across the coating system. This will create variation in in-plane stress along the TBC. In-plane stresses across the thickness of

TBC at the end of cooling, for systems with or without temperature gradient, can be plotted as in Fig. 3.9.

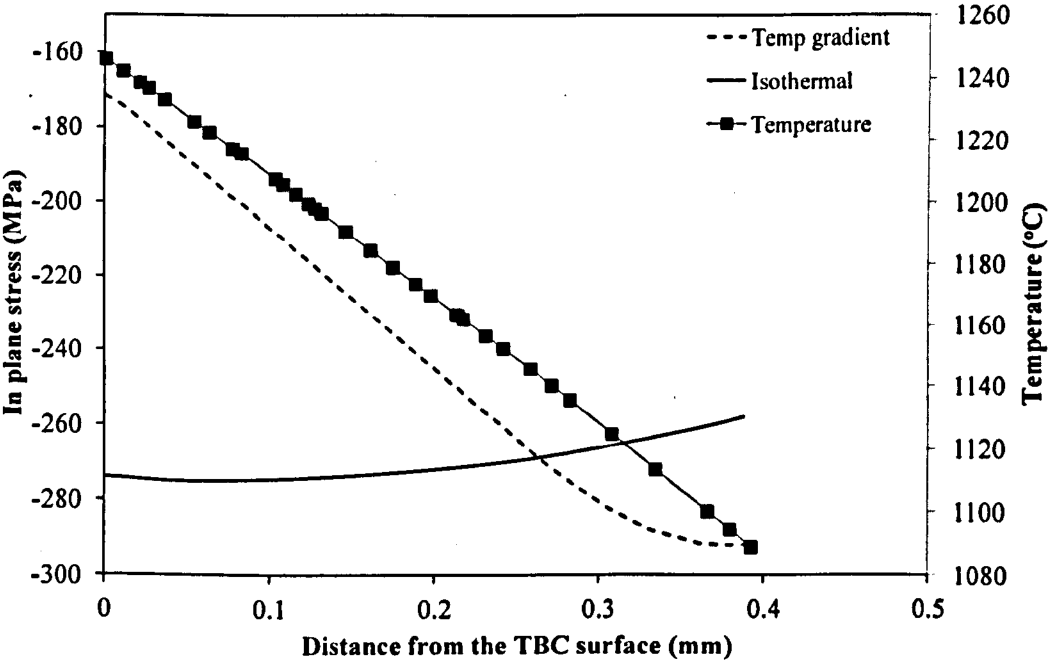

Fig. 3.9: In-plane stresses across the TBC for the isothermal system (steady state temperature – 1000°C) and the system with the temperature gradient plotting alongside the temperature across the TBC during steady state

### 3.6.3 Delamination failure relating to thicker TBC used for thermal insulation

Although a thicker TBC provides better thermal insulation and increases the efficiency of the engine by allowing a higher turbine inlet temperature, detrimental effects of a thicker TBC have to be considered. If it is assumed that the TBC system only has one layer of coating, and both the interface and the substrate are flat, there will be no out of plane stress at the interface. Strain energy stored within the TBC can be calculated from Eq (3.19). This energy is stored at the interface as the TBC is subjected to a thermal cycle. In-plane stress of TBC can be derived by assuming strain compatibility of the coating system [23].

Since the TBC is constrained in the in-plane direction by the substrate, the elastic strains arise from the thermal mismatch strain to achieve equilibrium as shown in Eq (3.20). The elastic strain can be presented as Eq (3.21). Assuming the TBC is much thinner than the substrate, the TBC in-plane stress can be presented as shown in Eq (3.22). By substituting Eq (3.22) into Eq (3.19), strain energy per unit interfacial area at the TGO interface can be expressed as Eq (3.23). This stored energy is released over the period of cooling when delamination cracks are formed at the interface due to high tensile stresses at the interface. Ultimate spallation occurs when $G_i$ is higher than the critical strain energy release rate of the interface ($G_{ic}$). As shown in Eq (3.23), a thicker coating is more prone to spallation since it will release higher strain energy although it reduces coating temperature. The phenomenon has also been found independently from empirical spallation tests of APS TBC [90] that thicker coatings release higher energy during spallation, thus reducing TBC lifetime.

$$G_i = \int_0^V \int_0^\varepsilon \sigma_{TBC}\, d\varepsilon\, dV \tag{3.19}$$

$$\varepsilon_{sub} - \varepsilon_{TBC} = -(\alpha_{sub} - \alpha_{TBC})\Delta T \tag{3.20}$$

$$\varepsilon = \frac{1-v}{E}\sigma \tag{3.21}$$

$$\sigma_{TBC} = \frac{\Delta\alpha \Delta T E_{TBC}}{1\text{-}v_{TBC}} \tag{3.22}$$

$$G_i = \frac{\sigma_{TBC}^2 h}{2E_{TBC}} = \frac{(\Delta\alpha\Delta T)^2 h E_{TBC}}{2(1-v_{TBC})^2} \tag{3.23}$$

where G is strain energy stored within the coating. V is coating volume. σ and ε are in-plane stress and strain. α is CTE and E, v are elastic modulus and Poisson's ratio. ΔT and h are temperature difference and coating thickness. Subscript 'sub' represents substrate.

## 3.7 Conclusions

A new framework has been proposed for modelling the elastic properties of a TBC as they evolve due to sintering. The modulus is represented as a function of thermal history and instantaneous temperature, based on an Arrhenius type temperature dependency of the sintering-related bond formation. For TBC temperature gradient due to heat flux and thermal conductivity changes, a separate thermal analysis was not carried out. Instead, a 1D thermal conductivity model was used to update the nodal temperatures of the TBC as sintering takes place. Both phenomena were implemented together within the stress analysis model of the TBCs to observe the effects of sintering on stresses within the TBC. The following conclusions can be made from the analysis.

- ☐ After cooling, the sintering of a TBC layer has a strong effect with the stresses being increased by a factor of up to two as a result of the increased modulus.
- ☐ The present form of the sintering model for elastic modulus represents a useful and powerful tool; however the assumption of a second order Arrhenius relationship is based upon the evidence of rather limited experimental data. Additional measurements of modulus for sintered TBCs covering the sintering period 1h to 11h would improve confidence in the choice of order of the Arrhenius rate model. There is also scope for incorporating additional terms in the model to represent type II sintering though this would require still more data (covering tests in which type II sintering is predominant) in order that the parameters for these terms could be determined.
- ☐ When a thermal gradient is applied across the TBC, variation of in-plane stresses occurs along the TBC after heat-up.

☐ On-going evolution in the thermal conductivities results in continuous changes in temperatures across the TBC. This in turn results in different creep strain rates and stress relaxation rates across the TBC.

☐ When cooling is applied at the end of a thermal cycle, the difference between the in-plane stresses at the TBC surface and at 0.4mm from the surface is up to 50%. The difference is dependent on the heat flux across the TBC.

☐ When a thicker TBC is used for thermal insulation, it is advisable to check related changes in strain energy stored. This is because delamination is favoured when the strain energy is equal to critical strain energy.

# Chapter 4

# Analysis of TBC stresses as affected by substrate geometry using an FE model with time and temperature dependent material constitutive models

## 4.1 Introduction

It is necessary to predict the failure mechanisms and lifetime of the TBC system accurately in order to avoid loss of TBC and rapid increase in substrate temperature, which reduces the lifetime of the coated components. One of the factors affecting TBC lifetime is the state of stresses generated within the system during cooling down, especially at the TGO interfaces. If both substrate and coating interfaces are flat, there would be no out-of-plane stress at the interface and hence spallation of a TBC will be driven by buckling of the TGO due to compressive stresses built up during the cooling of the system. However, curvature of components for example, vanes and blades of industrial gas turbine engines, and undulations of the

TGO interface within APS TBC systems, create tensile stresses at the TGO interface in the out-of-plane directions. The tensile out-of-plane stresses create opening of existing TBC discontinuities and linkages of cracks within the TBC. Consequently, premature spallation of the TBC could occur when strain energy release from the TBC cracks exceeds the critical strain energy release rate.

Wide applications of TBCs, on components of industrial turbine engines, initiated the need for understanding of the significance of substrate geometry on the development of stresses which can induce spallation of the TBC and reduce the service life of the TBC. The objective of this chapter is to carry out a parametric study of the effect of the substrate curvature on TBC stress distribution. The curvatures used in the parametric studies are those at different positions of TBC coated test specimen that has been developed for spallation tests conducted within the present SuperGen consortium (details are given in Acknowledgements). As a result, it will be possible to compare simulated results to experimental findings.

Although the objective is to study the effects of substrate curvature, the stress analysis will be unrealistic without considering time and temperature dependent material properties. For example, changes in both CTE of the BC due to phase proportion and, changes in the elastic modulus of the TBC have to be considered when mismatch stresses are calculated. Creep deformations of the coatings also redistribute stresses during steady state before cooling is applied. Therefore, a full constitutive material model which takes into account these changes in material properties of the coating and oxidation during steady state is coupled to the stress analysis model of TBC systems.

## 4.2 Model definition

The effects of substrate curvature on the lifetime of the TBC have been estimated using analytical models. Chan and Cheruvu [91] predicted that the cyclic lifetime of the TBC is reduced when the curvature is higher than the critical value. Using an analytical model of a multi-layered cylinder, Mao et.al [92] have predicted that tensile radial stresses at the TBC/TGO interface from CTE mismatch is progressively higher as the curvature of the substrate is increased. The main disadvantage of using analytical models is that it is difficult to calculate overall stresses generated at the coating interface considering both macro curvatures of the substrate and micro roughness of the coating. Additionally, temperature dependencies of material properties are also omitted for simplicity. Consequently, the stress analysis becomes qualitative and predicted values are not comparable to experimental measurements. To overcome the drawbacks associated with analytic study, the FE method will be used to carry out stress analysis of TBC systems.

### 4.2.1 Geometry and boundary conditions of FE model

A FE model for the TBC system is based on the geometry of the curved specimen shown in Fig. 4.1, which was designed within the SuperGen consortium for carrying out isothermal spallation testing of the TBC system. The specimen has an aerofoil shape, which is similar to that of a turbine blade. It will be computationally expensive and will be complicated in terms of boundary conditions to carry out stress analysis using the actual profile of the specimen. For simplicity, curvatures at different positions from the curved specimen are represented within the model as cylinders with comparable radii. In order to represent the pressure and suction sides of the typical blade, the specimen has concave and convex geometries. In terms of modelling, coatings are modelled at either inner or outer sides of the cylinder for negative or positive curvatures of substrate. The outer and inner radii of the cylindrical models are listed in Table 4.1. The coating interface is assumed to consist of periodic sinusoidal waves superimposed along the surface of the cylinder as shown in Fig. 4.2. The peak amplitude and wavelength of the interface are 6μm and 48μm respectively. The thicknesses of the BC and the TBC are 100μm and 200μm, respectively, and the initial TGO thickness is assumed as 1μm.

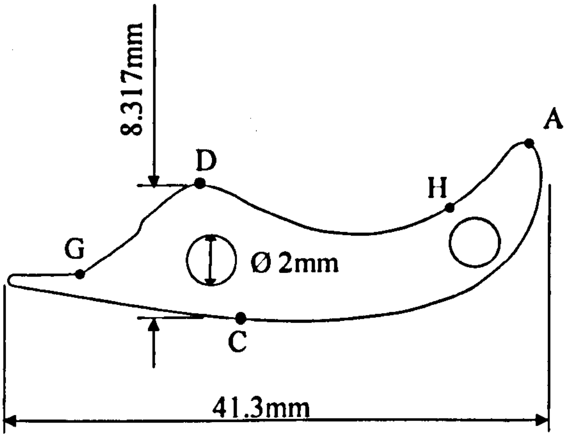

**Fig. 4.1: Geometry of the curved specimen**

**Table 4.1: Radii of curvatures at different positions of the curved specimen**

| Positions | Outer radius (mm) | Inner radius (mm) | Coated surface |
|---|---|---|---|
| D | 6.2 | 3.2 | Convex |
| C | 35 | 27 | Convex |
| A | 1.2 | 0.0 | Convex |
| G | 7.13 | 5.128 | Concave |
| H | 21.6 | 16.1 | Concave |

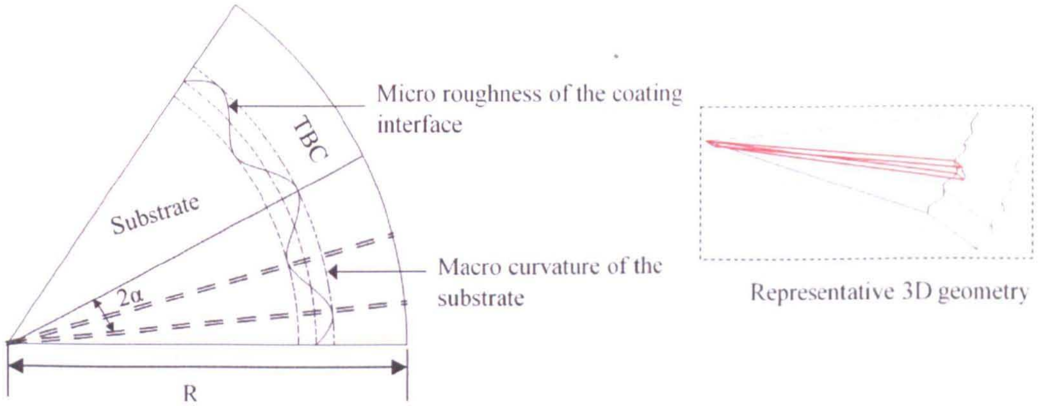

**Fig. 4.2: Sinusoidal TGO interfaces with periodicity in the circumferential direction with wavelength of 2α (A unit cell is highlighted by double dashed line)**

Circumferential movement is constrained to be zero at the planes where t = 0 and t = θ (as shown in Fig. 4.3 (i)) to simulate symmetric and periodic boundary conditions of the coating interface. For the model representing point A, an inner radius of 0.1mm was used to approximate a solid cylinder while avoiding the need to mesh into a sharp wedge angle. The models were chosen to approximate the true outer (and, where appropriate inner) radii of the specimen. However, it has been demonstrated via sensitivity studies that the thickness of the cylinder wall assumed in the model, and indeed whether or not a given cylinder is hollow, has negligible effect (typically around 0.3%) on the stresses. This is because its wall thickness, and hence its stiffness, are much greater than those of the TBC. In accordance with all other FE analyses dealing with creep properties within this thesis, an automatic time increment scheme is applied at time steps. If the analysis converges and the creep strain increment of the BC is less than the creep strain error tolerance (CETOL), the time increment is applied automatically. A reduction factor of 0.25 is applied to the automatic time increment when the condition is not satisfied. CETOL for the analysis is calculated as the ratio of the permissible error in calculated stress ($\sigma_{err}$) to elastic modulus of the material (E). In this case, CETOL is taken as $5e^{-5}$.

### 4.2.2 Finite element mesh

For every FE simulation, it is important to minimise the computation time without sacrificing accuracy of the results by using an appropriate mesh density. Higher mesh densities are required for the regions across which stresses are changing rapidly. CTE mismatch and oxide growth strains cause a steep stress gradient across the TGO interface. For this reason, it is necessary to refine the mesh in the vicinity of the TGO. For the regions away from the interface, a coarser mesh can be used. The geometries, meshes for the FE model and detailed view of the mesh near the TGO interfaces are shown in Fig. 4.3.

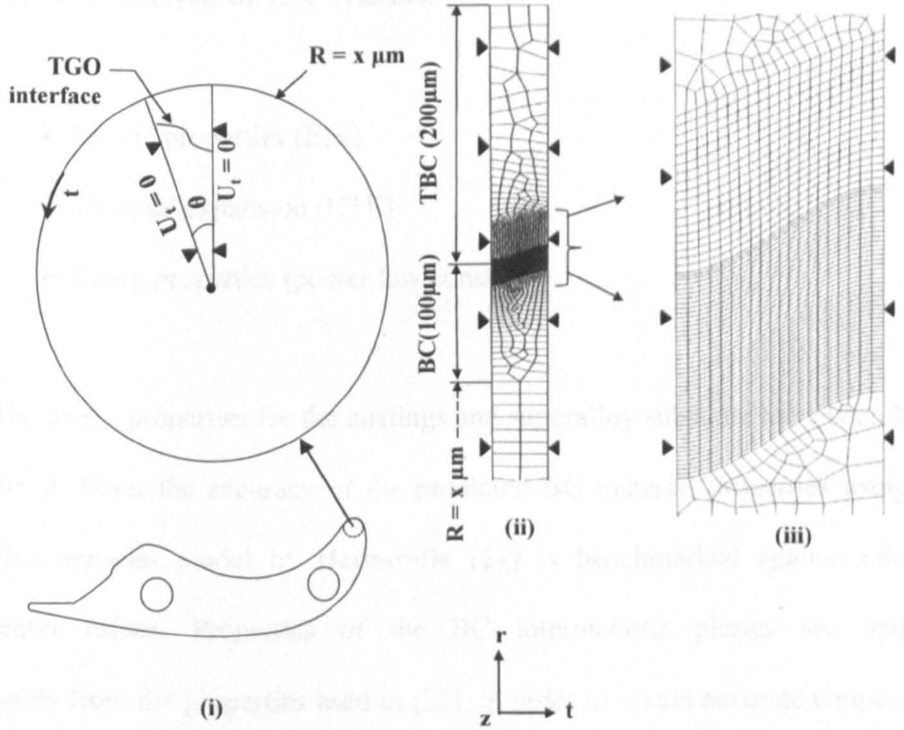

**Fig. 4.3 (i) Geometry and boundary conditions for the generalised, plane strain, FE model (r = radial, z = axial and t = circumferential) (ii) mesh of the FE model and (iii) detailed meshes near the TGO interface**

Generalised plane strain elements with reduced integration scheme (CPEG4R) were used because there is no axial restraint on the specimen as a whole. The centre of the cylinder is taken as the reference point (RP) for CPEG4R elements. All degrees of freedom (D.O.Fs) of the RP other than the displacement in the direction perpendicular the modelling space are constrained. This represents the condition where the model is bounded by two straight rigid parallel planes, which are free to move in the direction perpendicular to the plane while remaining parallel. For the case when the substrate is much thicker than coatings, the strain in the thickness direction is simply the logarithmic strain of the length of cylinder.

## 4.3 Material properties

Three groups of material data are essential in order to carry out thermo-mechanical stress analysis of TBC systems;

- Elastic properties (E, ν)
- Thermal expansion (CTE)
- Creep properties (power law constants)

The above properties for the coatings and superalloy substrate have been listed in Chapter 3. Here, the accuracy of the predicted BC material properties using the constitutive material model by Hermosilla [21] is benchmarked against relevant experimental values. Properties of the BC intermetallic phases are updated appropriately from the properties used in [21], in order to obtain accurate temperature dependent properties of the BC. The constitutive model for the evolution of the elastic modulus of the TBC due to sintering (details are given in Chapter 3) is also coupled to the FE model. A parametric study to understand the significance of TGO creep parameters on TBC stress relaxation during the steady state was also carried out.

### 4.3.1 Constitutive material model for the BC

Due to the heterogeneous nature of the MCrAlY BC, its properties depend not only on the temperature but also on the volumetric compositions of phases within the BC. It is therefore challenging to obtain material properties of the BC experimentally. Firstly, it is difficult to evaluate the properties of a thin BC layer (100-200 μm) using standard tests e.g. uniaxial tensile/creep tests. Usually, raw BC powders are hot pressed into the shape of a standard uniaxial test specimen. Wereszczak et al. [52] and Hebsur and Miner [47] measured creep properties using a similar method. The specimens made up of hot pressed powders have different porosity and grain sizes. Thus, they might exhibit different mechanical properties compared to thin coatings. Secondly, the microstructure of a MCrAlY coating is not fixed but is constantly evolving due to its oxidation at high temperature. Therefore, properties measured on one particular composition of BC cannot be applied to other MCrAlYs with different nominal compositions.

In order to address these difficulties, associated with experimental measurements of the BC properties, Hermosilla et al. [93] formulated a creep constitutive model which can be implemented in ABAQUS and gives creep properties of a BC based on its composition and service temperature. The power law creep model was used for intermetallic phases within the BC to take account of the temperature dependency of the MCrAlY creep. The effect of composition was considered by assuming that creep strain rate of the aggregate MCrAlY is the sum of creep strain rates of constituent phases volumetrically. The approach has also been used by Busso [15] to calculate creep properties of transient oxides within the TBC. Based on Eshelby's approach, Hermosilla et al. [77] also predicted the elastic properties (Young's modulus and Poisson's ratio) and CTE of the BC which are dependent on the evolving composition and the operation temperature. The constitutive material model takes account of the evolution of the material properties of MCrAlY, which will then be used within the FE model, without the need for extensive experimental data gathering. However, the reliability of the model was still a cause for concern.

### 4.3.2 Validation of the constitutive material model for the BC (Modulus of elasticity and CTE)

Temperature dependent properties of the intermetallics are crucial for obtaining accurate material data for MCrAlY. By using elastic properties and CTEs of intermetallics listed in Table 4.2, properties calculated by the constitutive model are validated against the experimental values from the open literature. The elastic moduli of CO211 for temperatures between 500°C and 1000°C were compared against the experimental data from Pointer and Morrell [83]. Numerically calculated elastic moduli using the model from [77] were also compared with those calculated by a simple rule of mixtures (ROM) method. The elastic moduli of the BC resulting from the different methods are plotted in Fig. 4.4.

Nearly identical elastic moduli are obtained from the constitutive model and the ROM at temperatures higher than 850°C. Below 850°C, the constitutive model predicts values of moduli of MCrAlY closer to those from the experimental data compared to the ROM method. Maximum errors for the prediction of the elastic moduli of TBC using the constitutive model and ROM are 6% and 8.4%, respectively, and both methods thus have a satisfactory level of accuracy.

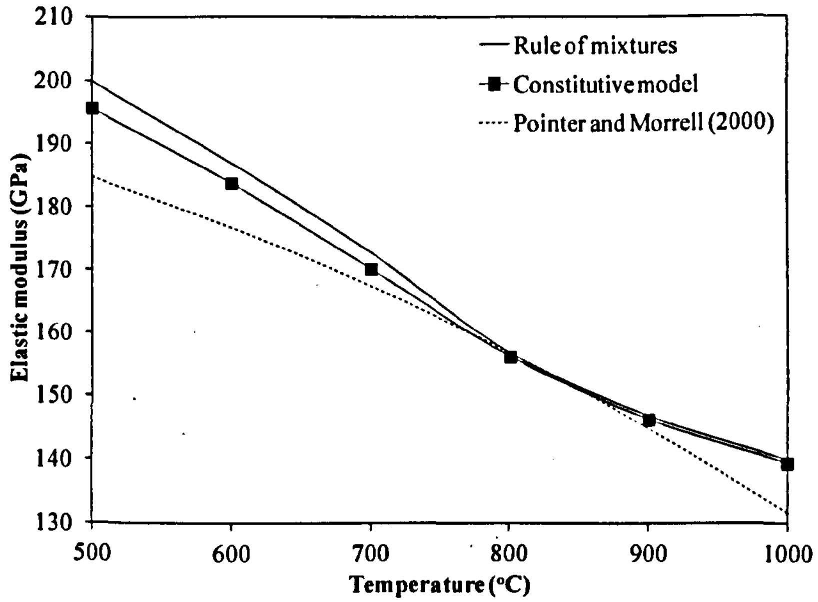

Fig. 4.4: Experimental and calculated BC elastic moduli

Table 4.2: Elastic properties and CTEs of intermetallics

| Temp (°C) | γ (Ni) [84] | | | γ' (Ni3Al) [87] | | | β (NiAl) [86] | | | σ (Cr) [84] | | |
|---|---|---|---|---|---|---|---|---|---|---|---|---|
| | E (GPa) | v | CTE $(K^{-1}10^{-6})$ | E (GPa) | v | CTE $(K^{-1}10^{-6})$ | E (GPa) | v | CTE $(K^{-1}10^{-6})$ | E (GPa) | v | CTE $(K^{-1}10^{-6})$ |
| 10 | - | - | - | 184.5 | 0.32 | - | - | - | - | - | - | - |
| 27 | 206.7 | 0.31 | 13.4 | - | - | 12.3 | 188 | 0.31 | 11.9 | 304.9 | 0.21 | 4.9 |
| 850 | - | - | - | 142.3 | 0.34 | - | - | - | - | - | - | - |
| 1000 | 132.1 | 0.31 | - | - | - | - | 150 | 0.31 | - | 236.3 | 0.21 | - |
| 1027 | - | - | 18.9 | - | - | 15.6 | - | - | 16 | - | - | 14 |

CTEs of the BC with two different sets of nominal compositions were compared to experimental data [83, 94] for a BC with comparable nominal compositions as listed in the Table 4.3. Sets of temperature dependent CTEs for intermetallics from Table 4.2 were used to obtain the aggregate CTE of the BC. The resultant CTEs of the BCs with two different sets of compositions of intermetallics are plotted in Fig. 4.5 and Fig. 4.6, respectively. The figures demonstrate that the calculated CTEs are within ±10% of experimental values.

**Table 4.3: Compositions of MCrAlY used for validation of CTEs**

| Coating | Composition | | | | | |
|---|---|---|---|---|---|---|
| | Co | Ni | Cr | Al | Y | C |
| CoNiCrAlY [94] | 38 | 32.1 | 21.2 | 8.3 | 0.4 | - |
| CO211 [52] | 38.5 | 32 | 21 | 8 | 0.5 | - |
| NiCoCrAlY [94] | 23.2 | 46.9 | 16.9 | 13 | 0.5 | - |
| PWA276 [47] | 20.3 | 48.3 | 17.3 | 14 | 0.5 | 0.01 |

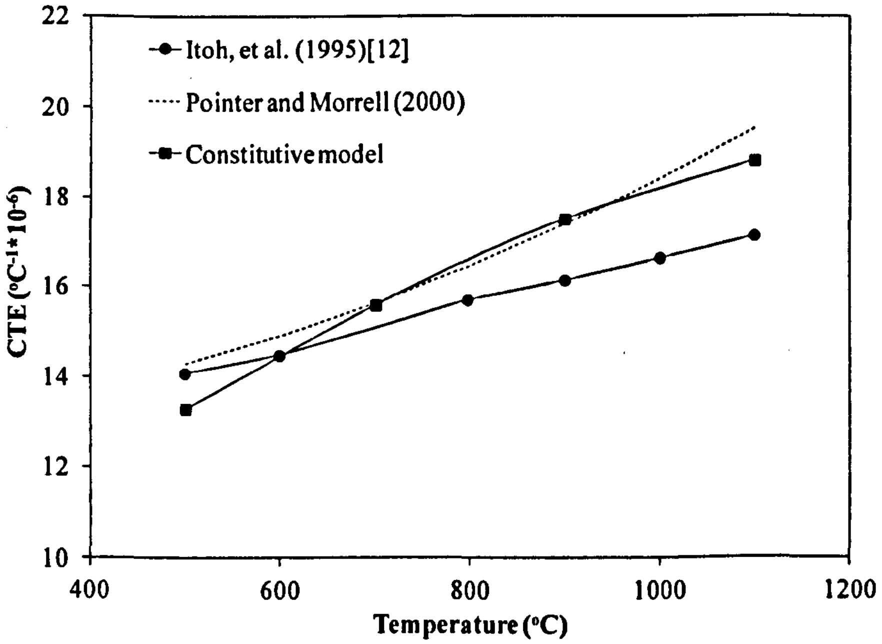

**Fig. 4.5: Comparisons of CTEs calculated using the constitutive models and experimental results for CO211**

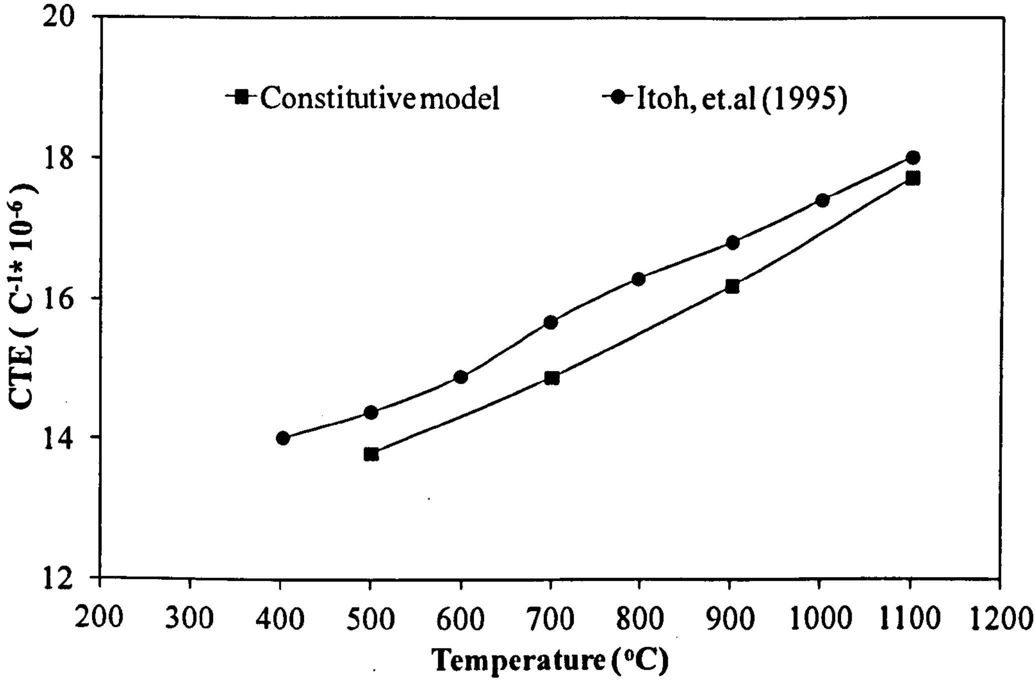

**Fig. 4.6: Comparisons of CTEs calculated using the constitutive models and experimental results for PWA 276**

### 4.3.3 Validation of the constitutive material model for the BC (Creep properties)

Creep strain rates of CO211 BC, at different stress levels at 850°C and 1050°C, are compared against experimental values from [52] as shown in Fig. 4.7. It can be observed that the order of magnitude for creep strain rates from the constitutive model is much higher than the experimental values. Comparison of theoretical creep strain rates to experimental measurements is very difficult due to various reasons. Difficulties in carrying out creep tests on thin coatings have been mentioned in 4.2.3.1. Moreover, the theoretical calculations ignored the influences of grain sizes of inter-metallic phases, although compilations of creep parameters from [86] demonstrate that grain size has a major impact upon creep resistance. Grain growth is especially expected at high temperature because of super-plasticity of MCrAlY [47].

Also, different mechanisms controlling activation energy of creep deformation were also not considered. At temperatures lower than the DBTT of MCrAlY, a dislocation or a viscous flow mechanism controls creep deformation while grain boundary sliding is the dominant deformation mechanism at higher temperatures [47]. These two distinct types of creep deformations are not modelled here since constant activation energies of creep are used for intermetallics within the constitutive model. To illustrate this shortcoming, creep strain rates of CO211 at different stress levels and at different temperatures are evaluated by applying uniaxial stress to the BC specimen in ABAQUS. Nominal compositions of CO211 (%vol) at different temperatures are tabulated in Table 4.4. Resultant creep strain rates of CO211 are plotted in Fig. 4.8. As seen from the figure, significant change in creep strain rate was not observed before and after DBTT of the BC (~ 850°C [49]).

Additional work is required to extract the creep parameters from tests, which are feasible to conduct on thin layer coatings; e.g. the small punch creep test (SPCT) [53]. It will also be preferable to scale of the creep parameters of the constitutive model by using the measured values from relevant tests as a reference point for extrapolation. Nevertheless, the creep properties used in this chapter are calculated from the constitutive model without any scaling.

**Table 4.4: Nominal compositions (%vol) of CO211 at different temperatures**

| Temperature (°C) | $\gamma$ (Ni) | $\gamma'$($Ni_3Al$) | B (NiAl) | $\sigma$ (Cr) |
|---|---|---|---|---|
| 600 | 0.151 | 0.116 | 0.495 | 0.238 |
| 700 | 0.311 | 0.000 | 0.552 | 0.137 |
| 850 | 0.500 | 0.000 | 0.500 | 0.000 |
| 950 | 0.549 | 0.000 | 0.451 | 0.000 |
| 1050 | 0.609 | 0.000 | 0.391 | 0.000 |

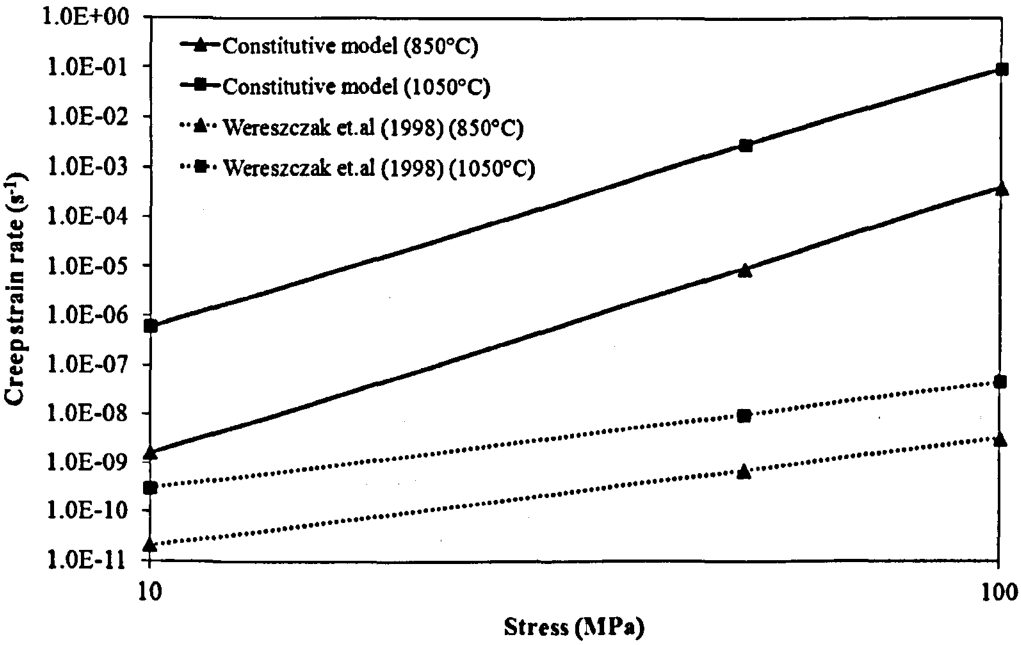

**Fig. 4.7: Creep strain rate of CO211 BC as predicted by the constitutive model [21] and measured by experiments [52]**

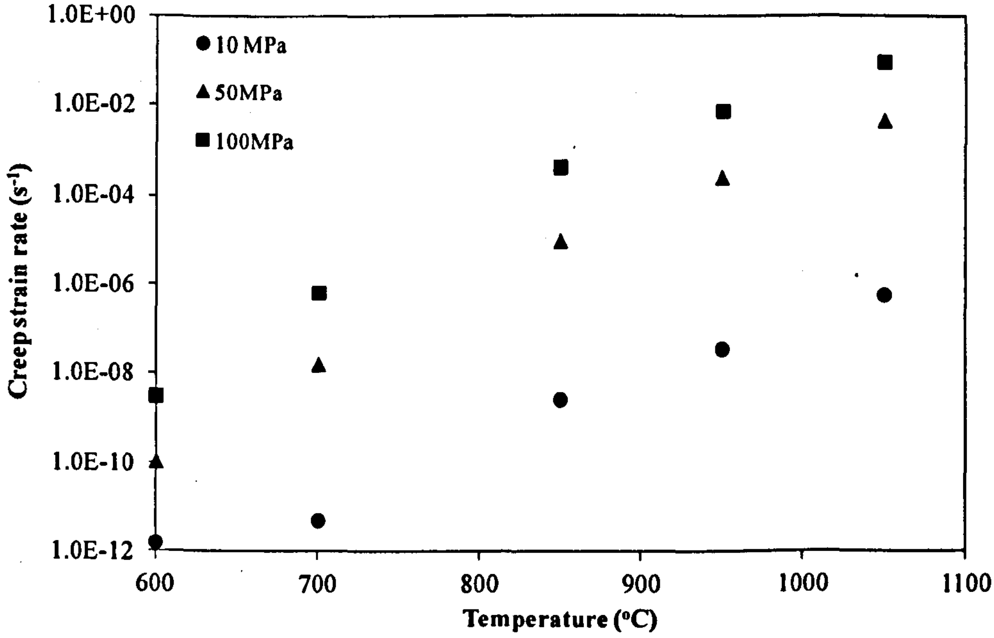

**Fig. 4.8: Creep strain rates CO211 at various constant stresses and at various temperatures**

### 4.3.4 Creep properties of TGO

Creep properties of the TGO are regarded as potentially important since creep causes the relaxation of stresses at the TGO/TBC interface, which are created at the end of heat-up or from the oxide growth. As is the case for MCrAlY coating, it is assumed that steady state creep of alumina is dependent on temperature and stress. A power law relation is used to calculate the creep strain rate. Due to differences in the grain size or impurity (spinels) of the tested specimens, published creep parameters of the TGO from the open literature are different from each other. To demonstrate the significance of TGO creep, three sets of creep parameters from [17, 95, 96], which are tabulated in Table 4.5, were chosen to carry out parametric studies. Steady state creep strain rates for three creep models at constant stress levels at 1000°C are shown in Fig. 4.9.

**Table 4.5: Power law constants of $Al_2O_3$**

| | $A_0$ ($MPa^{-n}s^{-1}$) | Q(J/mol) | n |
|---|---|---|---|
| $AL_2O_3$ (Set 1) [17] (Munro 1997) | 415.12 | $3.23\times10^5$ | 1.08 |
| $AL_2O_3$ (Set 2) [96] (Lin & Becher 1990) | 6800 | $4.24\times10^5$ | 2.3 |
| $AL_2O_3$ (Set 3) [95] (Chevalier et al. 1997) | $1.53\times10^{10}$ | $6.3\times10^5$ | 2.5 |

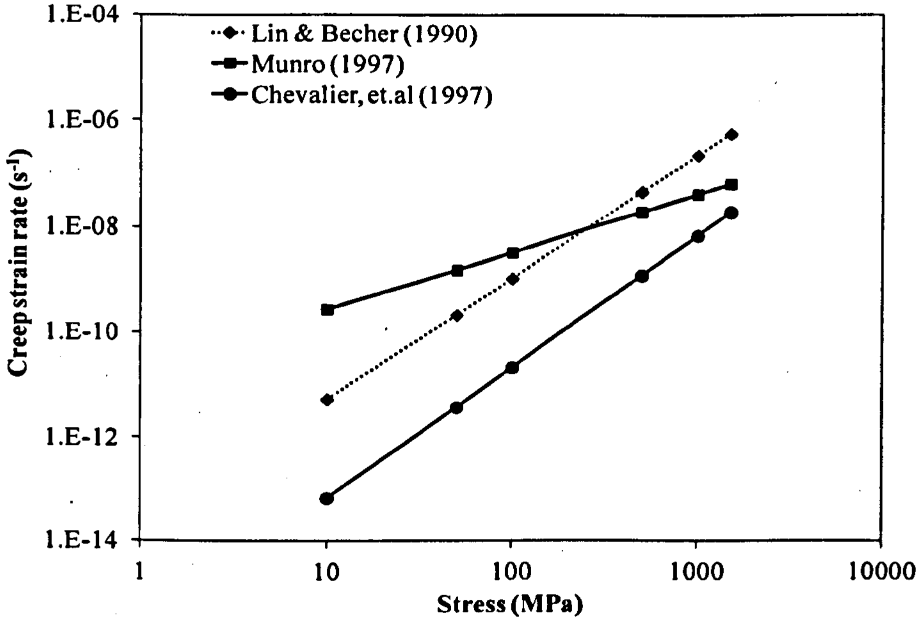

**Fig. 4.9: Steady state creep strain rates of three TGO creep models at 1000°C (Power law constants for creep properties are given in Table 4.5)**

## 4.4 Implementation of the constitutive FE model

The flowchart for the ABAQUS routine, which takes into account material and microstructural evolution of the BC and the sintering of the TBC, is shown in Fig. 4.10. The material properties of the intermetallics, at various operation temperatures, are implemented via a user defined PROPS module. The relevant properties are accessed by a user defined subroutine (UMAT) [67] during the processing stage to calculate the instantaneous aggregate properties of BC and to calculate the elastic moduli of the sintered TBC.

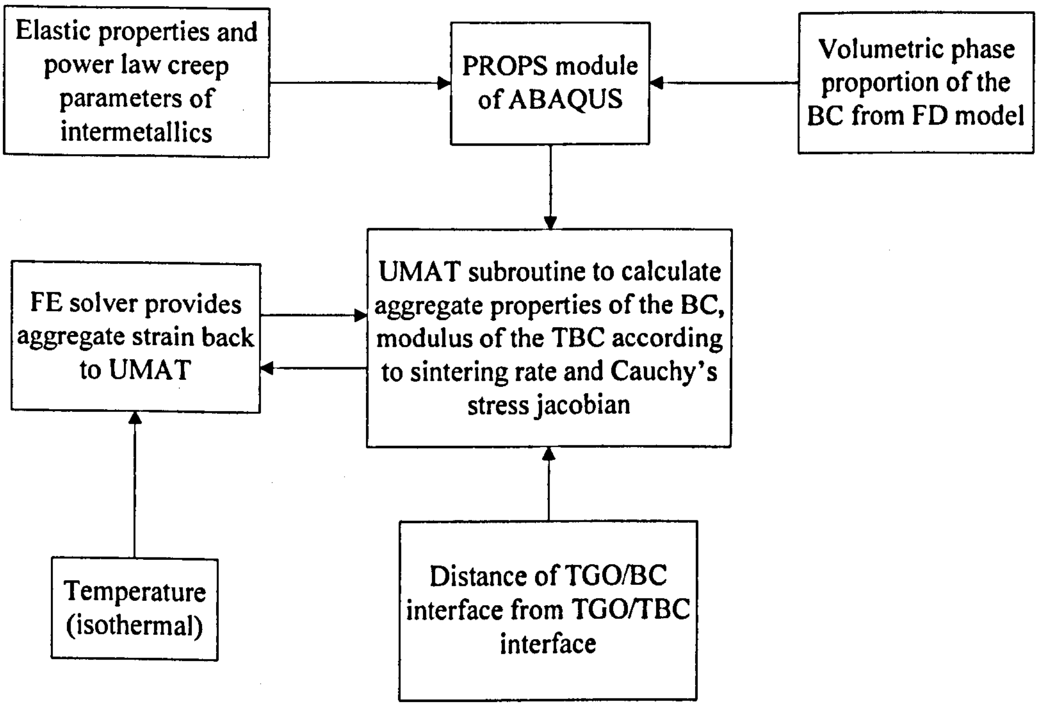

**Fig. 4.10: Flowchart for the FE model which includes the evolution of material properties for the BC and TBC**

A UMAT calculates the aggregate stresses according to the aggregate strain computed by the FE solver using Hooke's law. Volumetric compositions of the BC due to formation of alumina are calculated by Karunaratne et.al using a FD model [22] and were imported into the PROPS modules[67]. A MATLAB code extracts required data for PROPS module from FD files at different thermal exposure times (FD model produces an output file of phase compositions at every 10h interval). The empirical oxidation law proposed by Meier et al. [88] was used to calculate, at every time step, the thickness of BC which has been consumed via oxidiation. The transition strain rate ($\dot{\varepsilon}_{tr}$) arising from the oxidation of the BC can be calculated using the Pilling-Bedworth ratio (PBR) for aluminium-containing phases in the BC (β and γ') and the oxide formation rate $(\dot{f}_{ox})$, as shown in Eq (4.1), assuming that the oxide imposes the growth strain isotropically without introducing shear strain, i.e.

$$\dot{\varepsilon}_{ij}^{tr} = \frac{1}{3}\ln(PBR_{\beta/\gamma'})\dot{f}_{ox}\delta_{ij} \tag{4.1}$$

Eq (4.1) is applied while assuming that the TGO layer is made up of pure alumina. The oxidation processes for β and γ' phases are shown in Eq (4.2) and Eq (4.3), respectively. The PBR of the Al phases, β or γ', is defined as the ratio of the molar volumes of the products of oxidation to the molar volume of the respective phase. Molar volumes for β, γ, γ' and $Al_2O_3$ are 14.52, 6.59, 28.09 and 27.4 $cm^3/mol$ respectively. From these molar volumes, PBRs of both Al phases are given as approximately 1.27. The method is different from the one used during the Stage I of the project for which equivalent PBR of oxidation is calculated using volumetric ratios of the phases ($f_g$) and their respective PBRs [21] as shown in Eq (4.4). Using the method, the PBR will be overestimated if there are non-aluminium phases within the BC. This is because it is assumed that unless there is complete depletion of Al phases, selective oxidation will continue forming $Al_2O_3$, which prevents the formations of other fast growing metal oxides of σ and γ phases.

$$3NiAl(\beta)+1.5O_2 \rightarrow Al_2O_3(\alpha)+Ni_3Al(\gamma') \tag{4.2}$$

$$2Ni_3Al(\gamma')+1.5O_2 \rightarrow Al_2O_3(\alpha)+6Ni(\gamma) \tag{4.3}$$

$$PBReq = \sum_{g=1}^{n} f_g * PBR_g \tag{4.4}$$

For a system with a thermal gradient across the TBC, temperature fields can be updated using a separate heat transfer model or using the constitutive model which takes into account of changes in thermal conductivity of the TBC as shown in Chapter 3. For this chapter, only isothermal heat treatment is considered. Nodal temperatures are defined at the pre-processing stage. The temperature ramps up to the steady state temperature (1000°C) during heat-up. The system is held at that temperature for 900h before cooling it to 20°C. Detailed explanations of the procedure for running the FE model (Fig. 4.10) are outlined in Appendix A.

## 4.5 Results and discussion

### 4.5.1 Effect of substrate curvature on heat-up stresses

At the end of the heat-up process, thermal mismatch causes tensile in-plane stress within the layers with the lower CTE (coatings) and compressive stress within the layer with higher CTE (superalloy substrate). To achieve equilibrium, radial stresses are also created at the interface of the coatings. It can be proved by using Lamé cylinder theory that compressive and tensile radial stresses are created at the convex and concave coating interface respectively, during heat-up. This radial stress becomes larger as the ratio of radius to coating thickness reduces, i.e. as the curvature becomes more prominent. Furthermore, local peaks and valleys of the coating interface also create out-of-plane stresses in much the same way as the substrate; tensile and compressive out-of-plane stresses are created at the peak and valley of the TBC/TGO interface. The stresses created will be more severe due to high radii of curvatures of local asperities. Hence, radial stresses at the coating interfaces are a combination of stresses due to substrate geometry and local asperities. For comparison between models with different curvatures, radial stresses within the TBC in the vicinity of the TGO at the end of heat up are plotted in Fig. 4.11. The figure shows that when the substrate curvature is low, its effects on out-of-plane stresses can be ignored. While those tensile and compressive stresses created by local undulations remain unchanged for the models with more prominent substrate curvature, compressive stresses created by convex curvature cause significant reduction in tensile stresses at the TBC peak and increase in compressive stress at the TBC valley.

This can be appreciated from the plot of out-of-plane stresses for the model with the convex radius of curvature of 1.2mm (Model A) in Fig. 4.11.

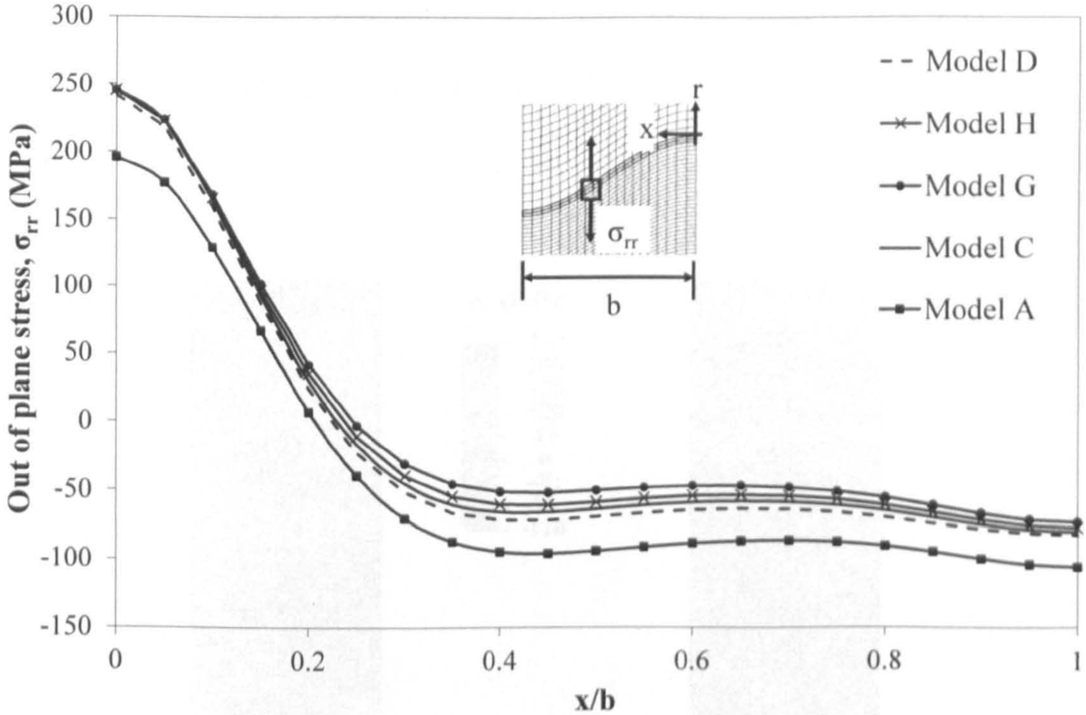

**Fig. 4.11: Out of plane stress within the TBC at the TGO interface, for different positions on the curved specimen at 1000°C after heat-up**

### 4.5.2 Effect of oxide growth on stress distribution during the steady state

Once the system is at the steady state temperature, stress evolution is controlled by two processes; oxidation and creep of coatings. The TGO is assumed to grow by consuming part of the BC. Layers of BC meshes change progressively to TGO as the system is held at 1000°C for 900h. Due to differences in molar volumes of BC and TGO, stress components due to oxides growth is imposed when the BC transforms to TGO. Because of lateral and radial constraints imposed by the BC and the TBC on the growing oxide layer, compressive stresses are formed within the layer. By equilibrium, radial stresses are also formed at the oxide interfaces and surrounding layers. These additional stresses are added to the system whilst stresses from the heat-up stage remain. Meanwhile, because of creep deformations of the coatings at the steady state temperature, stress relaxation occurs. Both oxidation and creep of the TBC cause stress redistribution. Out-of-plane stress reversal at the TBC peak and valley of Model D can be seen after 7 hours of oxidation as depicted in Fig. 4.12.

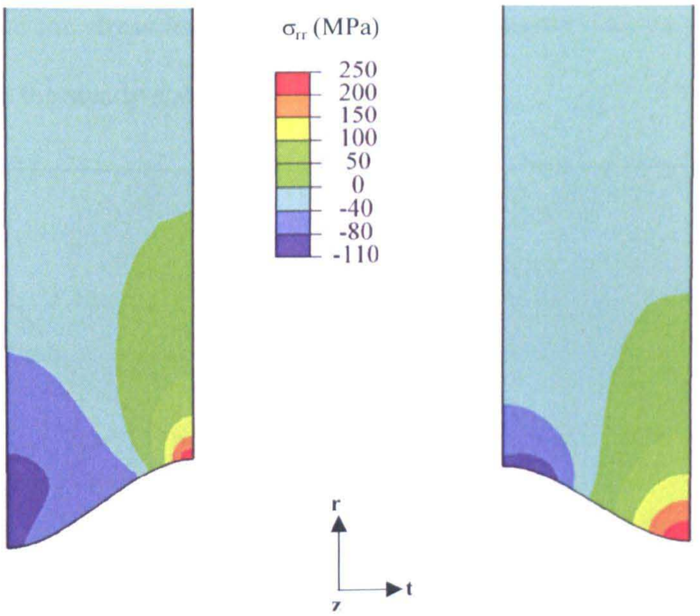

**Fig. 4.12: Out of plane stress, $\sigma_{rr}$, within the TBC for model D i) at 1000°C after heat-up and ii) after 7h of oxidation at 1000°C**

### 4.5.3 Effects of TGO creep on stress distribution during the steady state

During steady state, creep of the TGO causes relaxation of stresses within the TBC and the TGO, which are created from thermal mismatch during heat-up and oxide growth during the steady state. To study the effects of TGO creep on the TBC stress, the out of plane stress evolution at the TBC valley for three creep models is investigated and the results are plotted in Fig. 4.13. The TBC system has the geometry of model D from Table 4.1. The stress levels at the TGO/TBC interface are high for the early hours of steady state as a new TGO layer is forming close to the interface. However, they are reduced as the TGO growth zone is further away from the TGO/TBC interface and the stress is also further relaxed by the creep of the TGO and TBC. There is initially a sharp increase in the stress level at the TBC valley for the Munro model [17]. After 100h into steady state, stress arising from the growth of TGO at the TGO/TBC level is reduced and the Munro model [17] relaxes the stress faster than others. The Chevalier model [95] shows the slowest stress relaxation rate for the TGO and the stress level at the TBC valley is higher than its rupture strength [89] throughout the steady state.

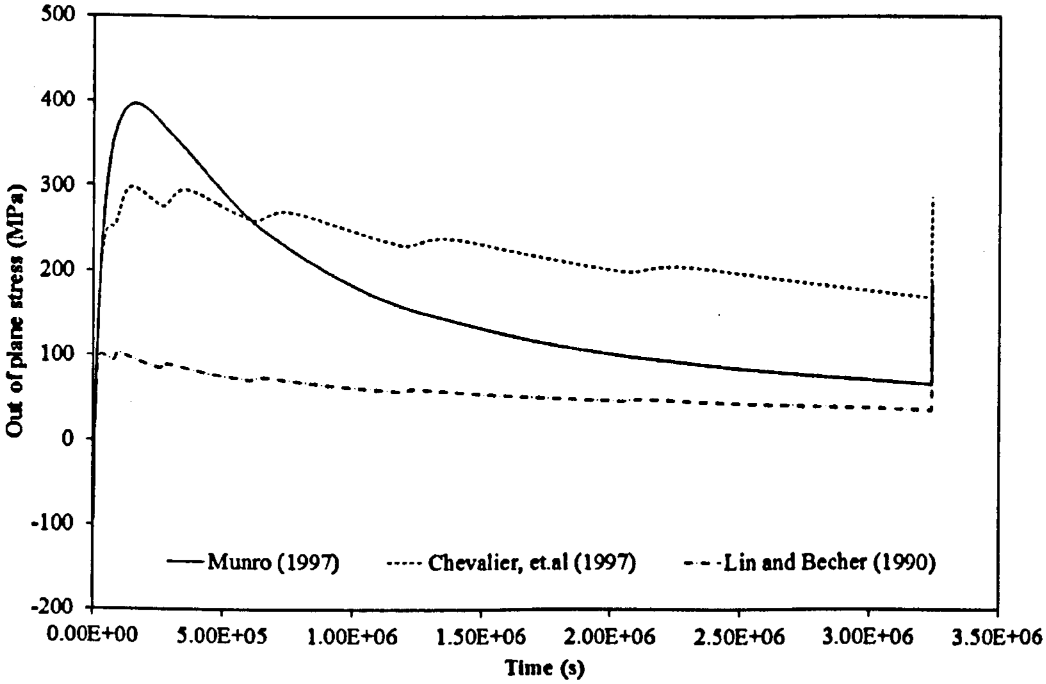

**Fig. 4.13: Evolution of out of plane stress at the TBC valley of model D with different TGO creep properties during steady state at 1000°C**

### 4.5.4 Out-of-plane stresses at the end of steady state

At the end of steady state, due to stress relaxation of the coatings, out-of-plane stresses within the system are low. The highest concentration of out-of-plane compressive stress occurs within the layer of the BC, which is transforming into the

TGO. On the other hand, the highest tensile stresses are formed within the TGO and at the TGO/TBC interface. The radial stresses at the TGO/TBC interfaces at the end of steady state for different substrate curvatures are plotted in Fig. 4.14. It can be observed that the stresses at the end of steady state are only weakly affected by geometry. Moreover, the overall magnitude of the stresses at the end of steady state is lower than the thermal mismatch stresses. From Fig. 4.12-Fig. 4.14, parallel cracks formed within the TBC peak at the end of heat-up will not propagate because of stress reversal during the early stage of the steady state. Cracks formed at the TBC valley and creep of the coatings also release tensile radial stress levels within the TBC during steady state. Hence, brittle failure caused by growth and linkage of TBC cracks is not expected during the steady state.

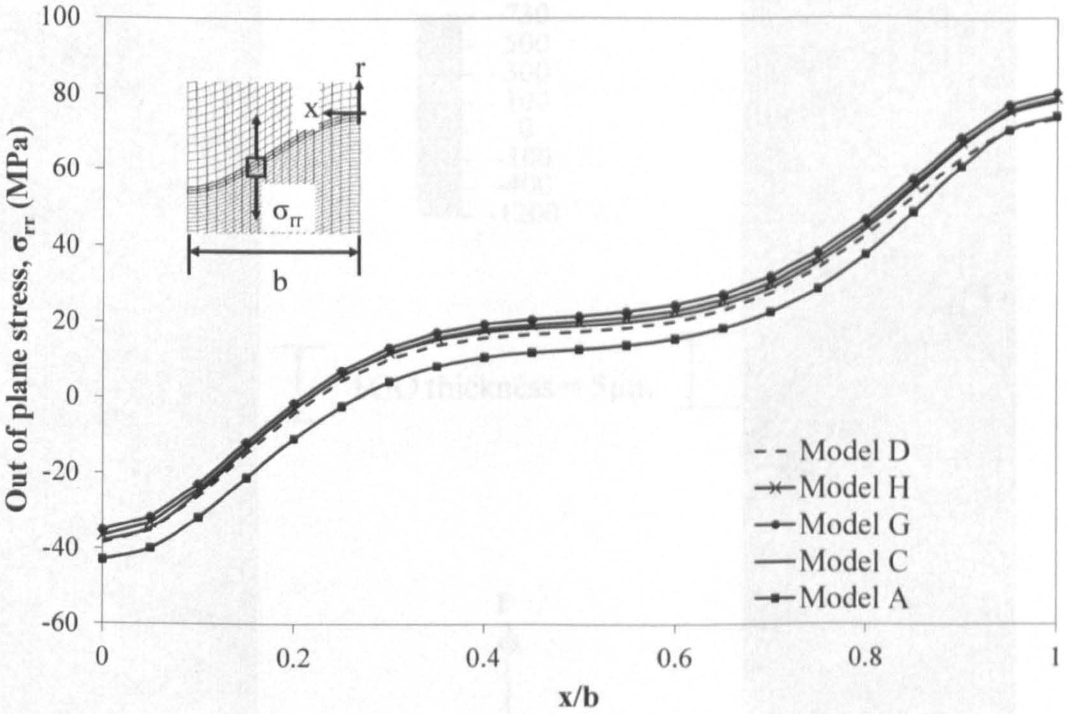

**Fig. 4.14: Out of plane stress within the TBC at the TGO interface, for different positions on the curved specimen at 1000°C after 900h of heating at the same temperature**

### 4.5.5 Out-of-plane stresses at the end of cooling

#### 4.5.5.1 Effect of substrate curvature on cooling TBC stress

The magnitudes of stresses at the end of the cooling cycle are much greater than those at the end of steady state, are expected to be much more significantly affected by geometry. For comparison, contours of through thickness stresses, within the system at the end of steady state and at the end of cooling stage for model D, are illustrated in Fig. 4.15. Concentration of tensile radial stress within the TBC near the TGO interface is of interest since the TBC tends to spall in this region due to propagation of delamination cracks along TGO interfaces, or due to coalescence of cracks within the TBC parallel to the TGO interface [97, 98].

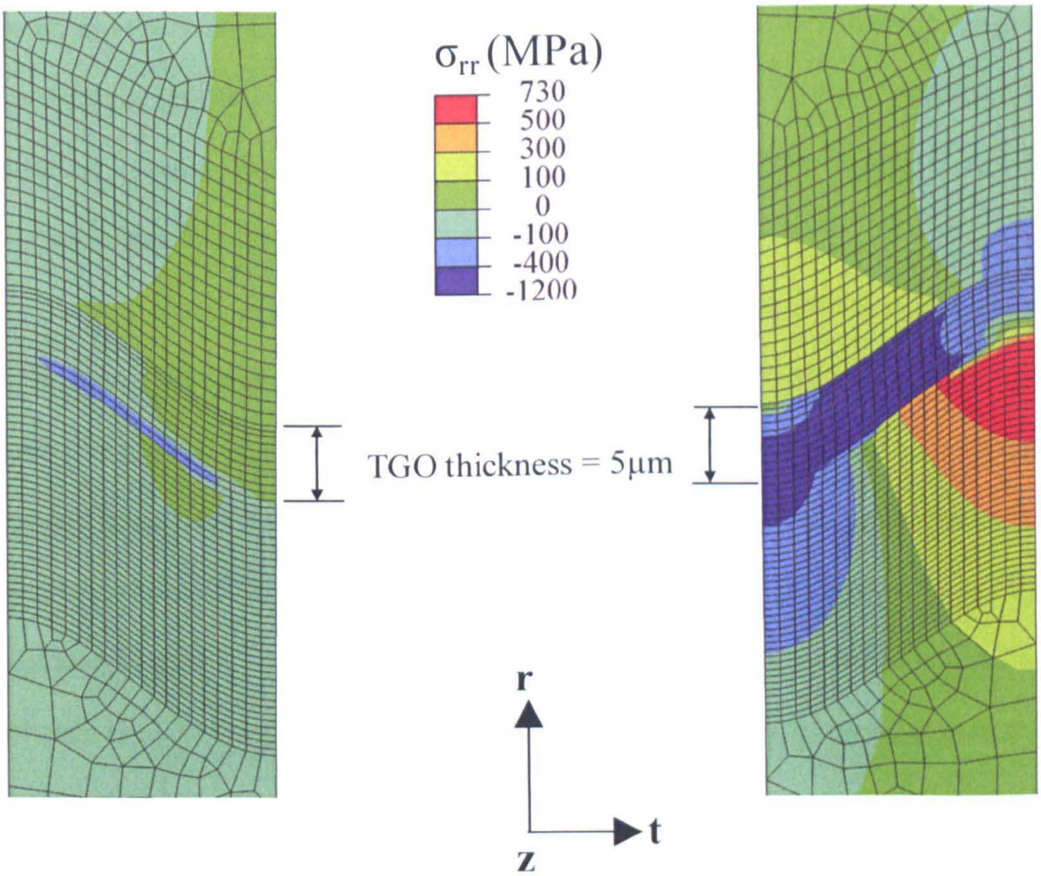

**Fig. 4.15: Out of plane stress, $\sigma_{rr}$, for the hollow cylinder model with a outer radius of 6.2mm and an inner radius of 3mm (i) at the end of the steady state after 900h of heating at 1000°C (ii) at the end of the cooling stage**

The through thickness TBC stress distributions at the TGO/TBC interface for different models at the end of cooling are shown in Fig. 4.16, with tight convex curvature increasing the stress magnitude by around 25% compared to relatively flat sample C. However, the opposite trend has been found for concave curvature as model G with tighter concave curvature reduce stress magnitude which is by 7% lower. Overall, radial stresses at the TGO/TBC interface for concave models are lower than for their convex counterparts. Maximum out of plane stresses within the TBC, for models D, C, A, G and H are 195MPa, 193MPa, 244MPa, 179MPa and 190MPa respectively; these occur at the valley of the TBC at the TGO interface. Those stresses are higher than the flexural strength of the TBC [89]. This means that the propagation of cracks within a TBC near a sharper corner of substrate will be faster, and the spallation life of the TBC is expected to be shorter compared to flatter and concave regions. It is especially noteworthy that the radial stress predicted by model A is now more tensile than for the less sharply curved models C and D, whereas it was less tensile at the end of steady state.

In a similar manner to the heating stresses, the system will then experience differential contraction stresses opposite in sign to those occurring on heat-up. Again these stresses will be most severe for the geometry with the tightest curvature (Model A), and these will not be mitigated by creep relaxation. Therefore, higher radial tensile stresses are created within model A at the TGO/TBC interface because of its substrate curvature. A similar explanation can be given for concave structures too although the radial stress at the TGO/TBC interface caused by substrate curvature is compressive during cooling.

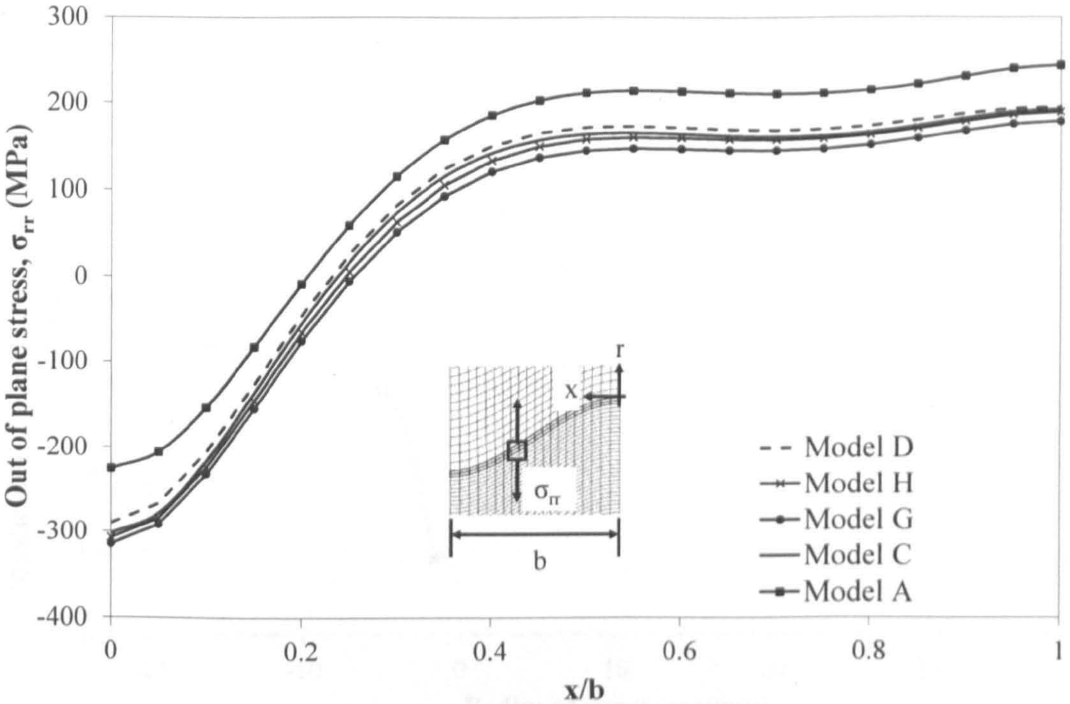

**Fig. 4.16: Out of plane stress within the TBC at the TGO interface, for different positions on the curved specimen at 20°C after 900h of heating at 1000°C**

### 4.5.5.2 Effect of substrate curvature on cooling BC stress

Tensile radial stresses found within the BC are significantly larger than those within the TBC. Stresses at the BC/TGO interface are a crucial factor in creating delamination cracks at the interface. In the simplest prediction, delamination cracks initiate if the tensile stresses at the interface exceed the bond strength. Maximum radial stresses at the BC/TGO interface occur at the peak of the BC. Similar to the stresses at the TGO/TBC interface, maximum radial stresses at the BC/TGO interface are also affected by substrate curvatures. Radial interfacial stresses of the BC peak at the end of cooling for models with varying curvatures are plotted in Fig. 4.17. These values are significantly larger than the interfacial bond strength of the coating as reported in [99]. However, the reliability of the pull out test applied for the bond strength is still questionable since the fracture of the coating is largely dependent on the initial flaws.

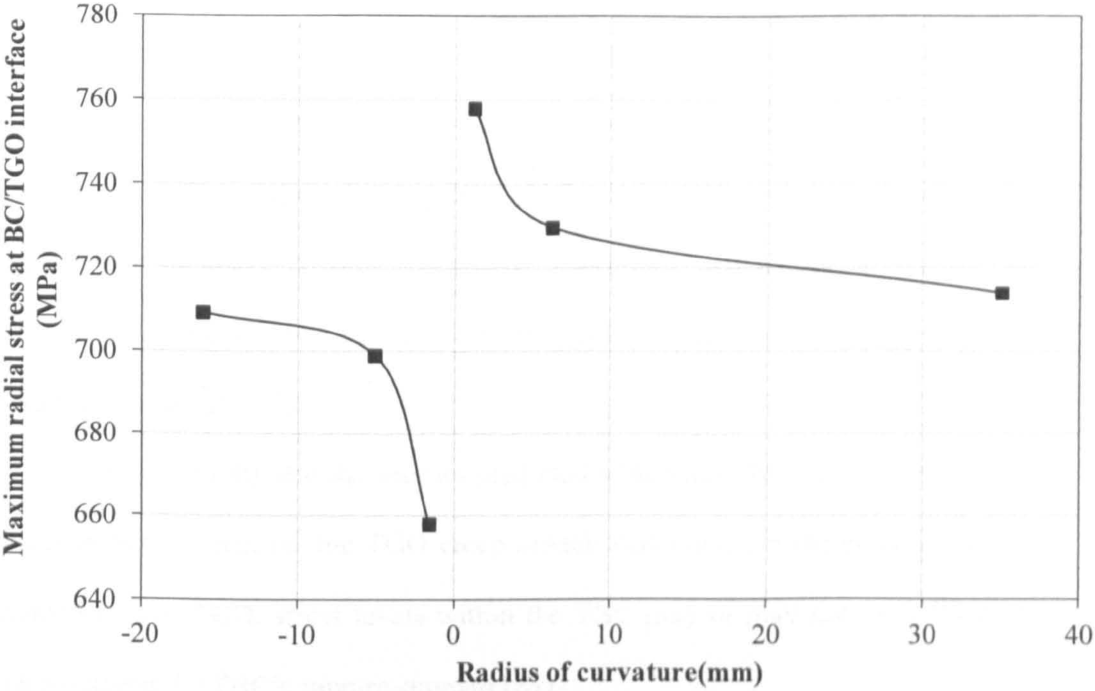

**Fig. 4.17: Maximum radial stress at the BC/TGO interface, for different positions on the curved specimen at 20°C after 900h of heating at 1000°C**

## 4.6 Conclusions

In parallel with the isothermal spallation tests of the aerofoil-shaped specimen by project partners, FE analyses were set up using idealised cylindrical models whose radii represent the curvatures at various locations on the test specimen. While carrying out FE analyses of the TBC systems, the material constitutive model of the BC from [21] is used to take into account of the evolution of the material properties of the coatings and the oxidation process. Calculated material properties of the BC were computed to validate against relevant experimental results. An Arrhenius model, which considers the reduction in strain tolerance of the TBC due to increase in the elastic modulus in the process of sintering from Chapter 3 was also implemented.

In general, the curvature effect on out of plane stresses is apparent whenever there is temperature change within the system. During heat-up, compressive and tensile radial stresses are created at the coating interface because of convex and concave curvatures of the substrate respectively; stresses are created vice versa during cooling down. These stresses are added to radial stresses created by surface roughness of the coating. The magnitude of stress is higher when the radius of curvature gets smaller. For identical coating roughness, maximum differences in tensile and compressive radial stresses between the simulated models with varying substrate curvatures are around 25%.

It is noteworthy that the stresses predicted within the TBC are very sensitive to the parameters chosen for the TGO creep model; depending on the creep properties assumed for the TGO, stress levels within the TBC may or may not be sufficiently high to exceed the TBC's rupture strength [89].

Although the opening of TBC discontinuities near the TBC peak is expected at the end of heat-up, the cracks are arrested because of stress reversal during the steady state, caused by both oxide growth and creep stress relaxation. Crack propagation at the TBC valley during the steady state is expected due to concentration of tensile radial stresses. However, spallation is not possible due to high interfacial compressive stresses at the peak regions. It is possible that the system might fail during the steady state because of creep deformation of the BC being large enough to exceed the failure strain of the MCrAlY BC. Nevertheless, MCrAlY coatings are designed so that their DBTT is around or lower than the operating temperature in order to sustain large strain deformations during operation at high temperatures. Strain to failure of MCrAlY above DBTT is usually very high (~ 130% as mentioned in [100]).

After cooling, interfacial stresses increase significantly again due to CTE mismatch, while sharp convex regions results in the highest tensile radial stresses. The maximum tensile stresses are formed at the BC peak and TBC valley. These will not be mitigated by creep relaxation. Furthermore, the TBC will recover its modulus upon cooling and indeed this will have increased due to sintering, contributing to the high stresses. Once delamination occurs at the BC/TGO interface due to the radial stress being higher the bond strength, strain energy stored at the interface will drive growth of the cracks within the TBC and TGO. By contrast, concave models show lower tensile radial stresses because of compressive stress caused by curvature when the system contracts. Therefore, convex regions with high curvatures have a higher risk of spallation. As increases in radial stresses become obvious only for small radii of curvatures, radial stresses are likely to be affected more by local undulations at the coating interface (waviness and roughness) than by substrate curvature.

By identifying critical levels of curvature for stress developments, this study will help with lifetime optimisation process in design of coating and turbine blades. Primarily, sharp edges should be avoided for blade design. Furthermore, the process of applying MCrAlY coatings should be controlled to reduce local undulations at the surface without compromising much on the mechanical bonding with the TBC, created by those undulations. Validation of predictions for geometry effects on TBC spallation and comparisons of the predicted stresses with experimental results obtained by project partners are elaborated in Chapter 5.

# Chapter 5

# Comparison of FE predictions with experimental measurements of the stresses in and failures for APS TBC specimens

## 5.1 Introduction

Various researchers in recent decades have carried out stress analysis because of the importance of understanding stress distribution within the TBC systems for predicting the lifetime of the coatings. FEA is one of the most popular techniques for stress analysis since the technique is cost effective, and can consider a wide variety of phenomena affecting mechanical response of TBC. However, the reliability of the results is questionable because of the various assumptions made for the geometry of the coating interface, physical and mechanical properties of the coatings etc. due to the complex nature of the TBC systems. While these various assumptions have been implemented within the FE models by researchers to model TBC stress distributions as realistically as possible, comparisons of simulated results against stresses measured using independent methods have remained scarce. The current chapter in turn examines the development of stresses in flat and curved coated specimens both analytically and numerically (FE) using a number of models. Experiments within the consortium [101-103] will then be described briefly. They allow the phenomena explored in the theoretical models to be examined, both in terms of the stresses measured using Raman spectroscopy (RS), and in terms of the failure modes (spallation of the TBC and delamination at the coating interfaces) which result. The comparison between predictions and measurements will give increased confidence in those results for which experiments and predictions are in agreement.

## 5.2 Parameters of test specimens

### 5.2.1 Introduction

Residual stresses after a thermal cycle within two different specimens (a flat specimen and an aerofoil-shaped specimen) were predicted using the FE method and were compared to corresponding experimentally measured values. The flat specimen has no ceramic TBC as opposed to the full TBC system of the aerofoil specimen. In-plane residual stresses within the TGO of the flat specimen and those within the TBC of the curved one were used for the comparison study. Dimensions, manufacturing parameters, coating compositions and details of heat treatments for each specimen are described below.

### 5.2.2 Manufacturing and ageing of specimens

For the flat specimen, the coating is applied to a substrate of approximate thickness 2mm. Two 8mm by 5mm strip specimens were cut for heat treatment and stress measurements. The coated sample was supplied by Saeidi et al. and details of the parameters for the spraying process are presented in [104]. Nominal compositions for the substrate and the MCrAlY BC are listed in Table 5.1. The high velocity oxy-fuel (HVOF) process was used for spray deposition process of the coating, and MCrAlY powder size of 45±20μm supplied by Praxair (CO-210-24) was used as the feedstock. The sample was cooled by a compressed air jet during and after spraying. The thickness of the MCrAlY is ~300μm. The coated specimens were heated isothermally within a furnace at 700°C or 1000°C for 96h then cooled in air.

The modified aerofoil specimen as shown in Fig. 5.1 is made up of a CMSX4 substrate. The BC is made up of Amdry 995 powder which was deposited onto the specimen using the HVOF deposition technique. Afterwards, air plasma sprayed (APS) 7 wt% yttria stabilised zirconia TBC was applied. The compositions for the substrate and Amdry 995 powder are listed in Table 5.2. The thicknesses of the BC and the TBC vary at different positions of the specimen and the values are listed in Table 5.3. The coating process was carried out by Seraffon et al. [102]. For the spallation experiments, the specimens were exposed to different temperatures (900, 925, 950, 975 and 1000°C) until failure occurs.

**Table 5.1: Composition (in wt%) of substrate and BC for the flat specimen**

| Alloy | Ni | Cr | Co | Al | W | Ti | Mo | Ta | Re | Hf | Y |
|---|---|---|---|---|---|---|---|---|---|---|---|
| CMSX-4 | 58.99 | 6.46 | 9.61 | Base | 8.24 | 0.83 | 0.63 | 5.86 | 3.92 | | |
| AMDRY 995 | 32 | 21 | Base | 8 | | | | | | | 0.5 |

**Table 5.2: Composition (in wt%) of modified aerofoil-shaped specimen's substrate and BC**

| Alloy | Ni | Cr | Co | Al | W | Ti | Mo | Ta | Re | Hf | Y |
|---|---|---|---|---|---|---|---|---|---|---|---|
| CMSX-4 | Base | 6.5 | 9.6 | 5.6 | 6.4 | 1 | 0.6 | 6.5 | 3 | 0.1 | |
| AMDRY 995 | 32 | 21 | base | 8 | | | | | | | 0.5 |

**Table 5.3: Coating thicknesses at the different positions of the specimen shown in Fig. 5.1 (Concave curvatures are denoted by a negative sign)**

| Position | P1 | P2 | P3 | P4 | P5 | P6 | P7 |
|---|---|---|---|---|---|---|---|
| **Curvature ($mm^{-1}$)** | 0.006 | 0.33 | 0.866 | 0.178 | 3.023 | -0.062 | -0.195 |
| **TC thickness (μm)** | 220 | 190 | 190 | 210 | 130 | 220 | 250 |
| **BC thickness (μm)** | 110 | 50 | 90 | 100 | 50 | 130 | 135 |

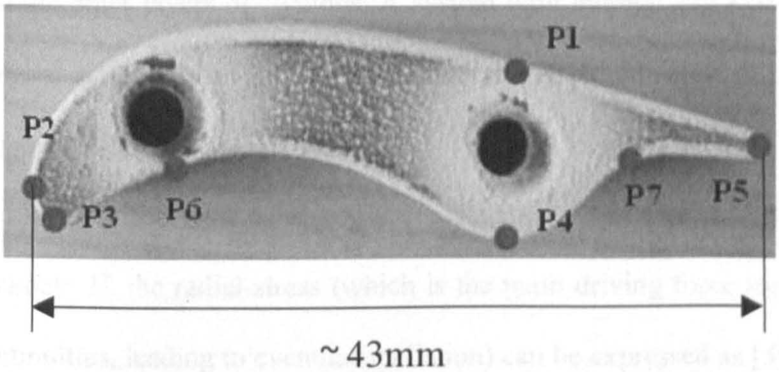

**Fig. 5.1: A modified aerofoil shaped specimen**

## 5.3 Model definitions

The build-up of radial and hoop residual stresses in the coated components is analysed using two very different approaches. A simple analytical model is used to study the influence of global curvature (both concave and convex) upon the stresses in a simple single-layer coating system. A FE model is then used to examine the combined effects of global curvature and local roughness upon the stresses in a more practical system.

## 5.4 Analytical model

This model is based on existing published applications of thick cylinder theory [55]. It considers the influence of thermal expansion mismatch, elastic properties, curvature of the substrate and thickness of the coating. However, it neglects the effects of coating interface roughness, and of the creep and yield of the coatings. It also simplifies the problem by considering only a 'single-layer' coating on a homogeneous substrate, exploiting the facts that the elastic and thermo mechanical properties of the substrate and BC are broadly similar, and that the TGO is much thinner than the other layers of coatings. A system with internal and external coating can be idealised as shown in Fig. 5.2. It is assumed that the thickness of the substrate is much larger than that of the coating.

At the interface of a solid convex component of substrate radius $R_o$ with coating thickness $H$, the radial stress (which is the main driving force for opening of TBC discontinuities, leading to eventual spallation) can be expressed as [55]:

$$\sigma_r^{s,c}(r=R_o) = -\frac{E^c(\alpha^s-\alpha^c)\Delta T\left[\left(\frac{R_o+H}{R_o}\right)^2-1\right]}{1-2\nu^c+\left(\frac{R_o+H}{R_o}\right)^2+\frac{E^c}{E^s}\left(\frac{1-\nu^s}{1+\nu^c}\right)\left[\left(\frac{R_o+H}{R_o}\right)^2-1\right]} \qquad (5.1)$$

where superscripts 's' and 'c' represent substrate and coating, $E$ and $\nu$ are elastic modulus and Poisson's ratio and $\alpha$ is the coefficient of thermal expansion (CTE). Similarly, the radial stress on the concave/inner surface of an infinite component of substrate radius $R_i$ is [55]:

$$\sigma_r^{s,c}(r=R_i)=\frac{E^c(\alpha^s-\alpha^c)\Delta T\left[1-\left(\frac{R_i-H}{R_i}\right)^2\right]}{1-2\nu^c+\left(\frac{R_i-H}{R_i}\right)^2+\frac{E^c}{E^s}\left(\frac{1+\nu^s}{1+\nu^c}\right)\left[1-\left(\frac{R_i-H}{R_i}\right)^2\right]} \tag{5.2}$$

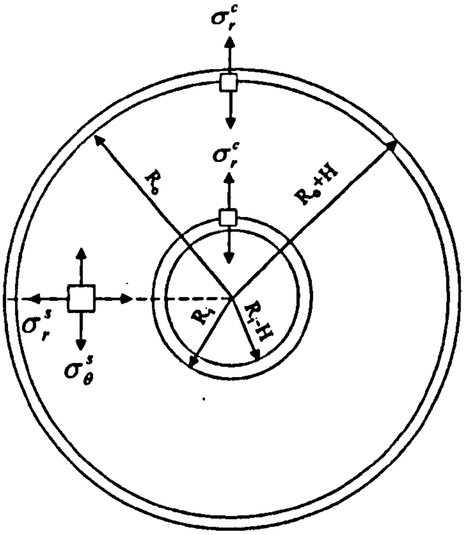

**Fig. 5.2: Schematic diagram of a coating system with internal and external coatings**

Fig. 5.3 shows the radial stresses at the coating interface for various systems with practical materials and a range of convex and concave curvatures; stresses were evaluated using Eq (5.1) & (5.2) for the system that has been cooled down from 925°C to 20°C. The TBC system is assumed to be stress free at 925°C before the cooling takes place. The assumed elastic properties and CTEs of the substrate and the coating are given in Table 5.4. The coating thickness is assumed to be 100μm.

As shown in Fig. 5.3, as the substrate becomes flatter, i.e. as $R_o$ or $R_i$ become large compared with $H$, the radial stresses caused by substrate curvature become insignificant. Significant changes in radial stresses only occur for radii smaller than 20mm. It is noteworthy that the surface profile of the coating surface contains local waviness profiles with radii of curvature which could be up to two orders of magnitude less than that of substrate's overall geometry, and it is stresses from this waviness which are likely to be dominant except at the most sharply-curved features of the substrate. Moreover, since the radial stresses arising from the concave curvatures are compressive, they tend to oppose those causing the TBC spallation, implying that such failure is more likely to occur on convex than concave surfaces. Similarly, hoop stress of the coating can be related to radius of curvature of the substrate. For the thin coating layer, the difference in hoop stresses across the coating thickness can be ignored. Hoop stresses values for different curvatures are plotted in Fig. 5.3. For both concave and convex curvatures, the coating hoop stresses are compressive and the magnitude increases as the substrate becomes flatter.

**Table 5.4: Elastic properties and CTEs of substrate and TBC for analytical stress calculations**

| | Elastic modulus (GPa) | Poisson's ratio | CTE ($10^6$ *$K^{-1}$) |
|---|---|---|---|
| Substrate | 140 | 0.3 | 20.7 |
| TBC | 113 | 0.18 | 10 |

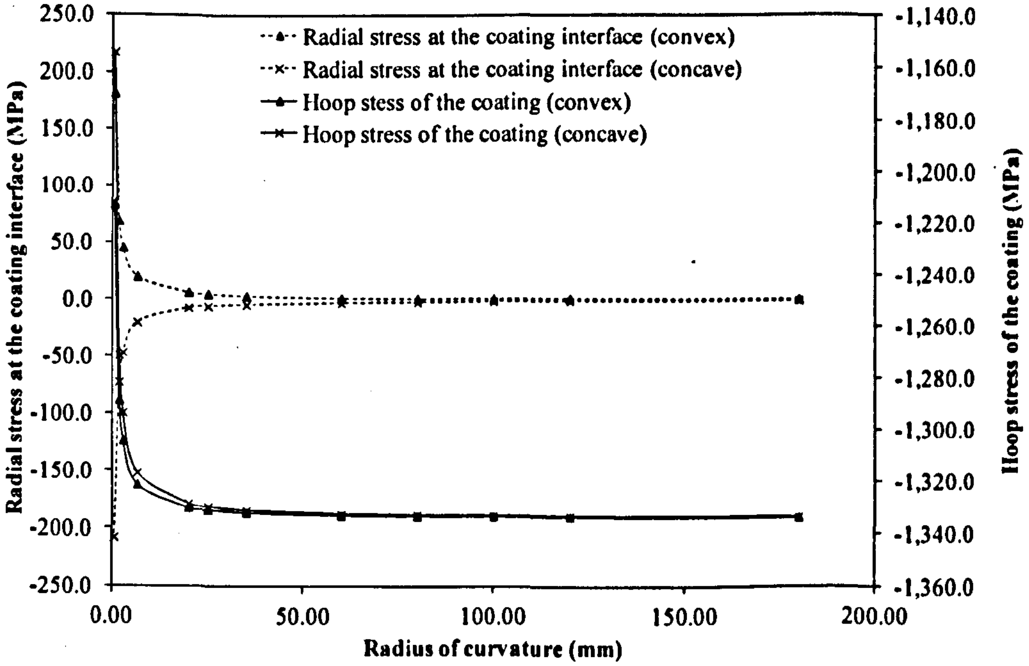

**Fig. 5.3: Effect of radii of curvature on the radial stresses at the concave and convex sides of the coatings at the end of cooling from 925°C (Analytical model)**

From Eq (5.1) and (5.2), it is seen that various factors other than substrate curvature affect radial stresses at the coating interface. To compare the effects of these parameters with the effect given by the substrate curvature, a simple sensitivity study was carried out. Elastic modulus (E), Poisson's ratio (v) and coating thickness were chosen for the study as variations in these parameters, during operation at high temperature, are significant. For example, E for the coating evolves due to densification while changes in the composition due to inter-diffusion at the BC/substrate interface cause changes in the substrate elastic modulus. The calculated radial stresses and parameters for the study are normalised using the values at the reference point (R.P). Material parameters at the R.P are identical to the parameters from Table 5.4 except that the elastic modulus of the TBC is taken as 70GPa. Curvature and thickness of the TBC at the R.P are $0.154mm^{-1}$ and 300μm respectively. In comparison to curvature effects, interfacial radial stresses show significant sensitivity to coating parameters, especially the coating thickness and elastic modulus as shown in Fig. 5.4.

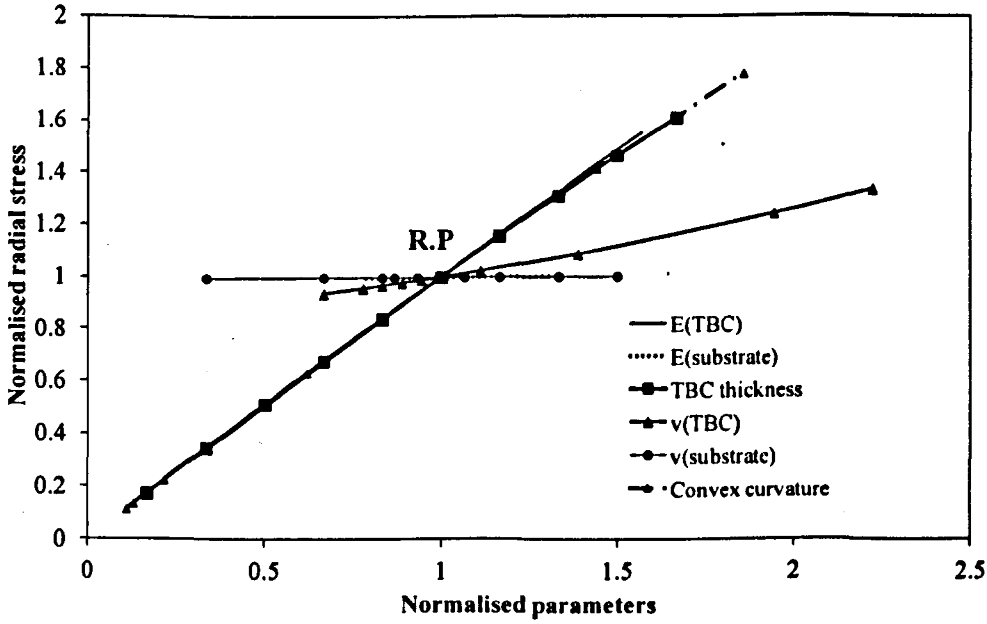

**Fig. 5.4: Parametric study of the effects of input parameters on radial stresses at the coating interface using the analytical model**

## 5.5 Finite element model

It is impractical to extend the analytical model to consider the combination of the macro scale curvature and micro scale roughness, so the FE techniques developed in [21] and [105] are used here; firstly to simulate residual stresses within the flat specimen without a TBC layer and with local coating roughness only, and then to study the interactions between coating roughness and substrate curvature in a TBC coated specimen.

The underlying modelling approach is similar in all cases, using appropriate periodic and symmetry boundary conditions to model a representative unit cell with a repeating pattern of the roughness at the TGO interfaces. Composition changes within the BC and their influence on the creep and elastic properties of the BC [21], sintering of the TBC [105], if applicable, and formation of an alumina layer (internal oxidation) at the BC/TGO interface were also taken into account. As insufficient data could be found to parameterise an anisotropic oxide growth model, isotropic growth strain was applied to a layer of the BC within the FE model, with the value of strain being given by the Pilling-Bedworth ratio (PBR) of the aluminium-containing phases ($\beta/\gamma'$) as described in Chapter 4. A detailed procedure for implementation of those processes within a FE model has been reported elsewhere [105] along with material properties of the TBC system.

The substrate used for the test specimens is CMSX-4 and its properties were extracted from the literature and are listed in Table 5.5. Although anisotropy for both elastic [106] and creep properties of the alloy [107] were observed, for simplicity the alloy is assumed to be isotropic. The assumption is appropriate for temperatures higher than 1000°C since rapid decrease in anisotropy of CMSX-4, for the temperature range of industrial gas turbine (1000-1100°C), has been reported in [107].

It was also assumed that the differences in weight percentage compositions between the substrate of the flat specimen and that of the aerofoil specimens are negligible, and properties from Table 5.5 were applied to both models. For every set of simulations, the TGO interface is assumed to be sinusoidal and its amplitude and wavelength are set to 6μm and 48μm, respectively. Dimensions of the model and mesh diagram for the flat specimen are shown in Fig. 5.5 (i) & (ii). A generalised plane strain element was used because there is no axial restraint on the specimen as a whole, as shown in Fig. 5.5 (iii).

In chapter 4, to represent aerofoil specimens with concave and convex curvatures, FE models of cylinders with coatings at the internal and external surfaces were constructed. However, in reality, an aerofoil shaped specimen has coated areas with both concave and convex curvatures. In order to represent this, an FE model based on a hollow cylinder with internal and external TBC systems as shown in Fig. 5.2 is used. The thicknesses of the BC and the TBC of the model are 100μm and 200μm respectively. Additionally, to understand the effect of TBC thickness, a parametric study was also conducted with different TBC thicknesses. The initial TGO thickness from the spraying process is assumed to be 1μm. It is assumed that the sinusoidal TGO interface is periodic along the axial direction as opposed to being periodic along the circumferential direction. With this assumption, an identical aspect ratio of the TGO interface can be used within the axisymmetric unit cell for both internal and external coating interfaces. A schematic diagram of the axisymmetric unit cell, mesh diagram and boundary conditions for the model are shown in Fig. 5.6.

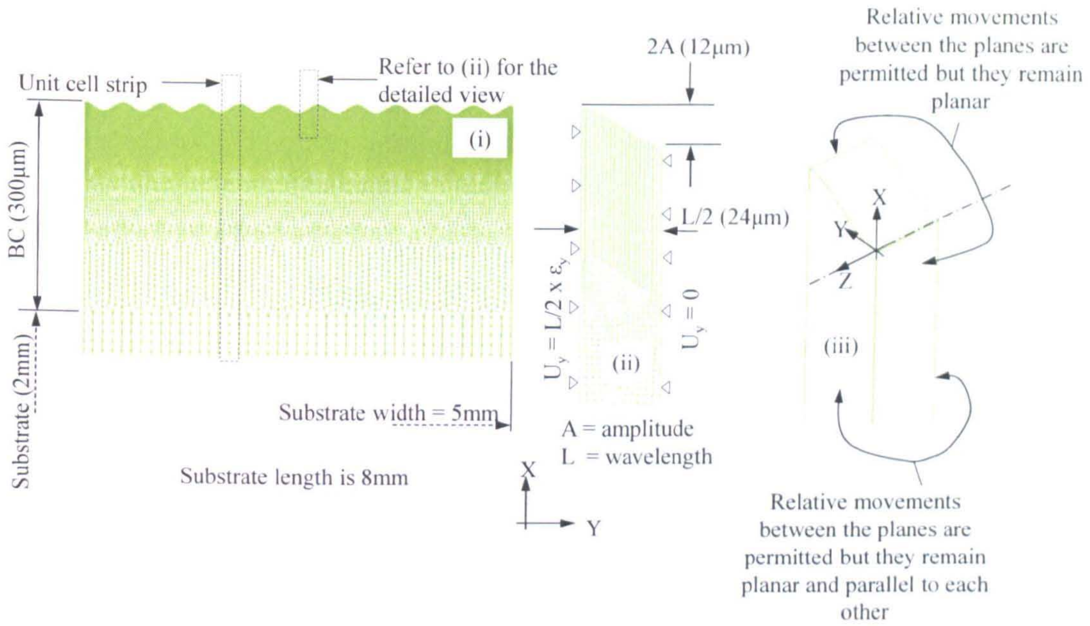

**Fig. 5.5: (i) Dimension of the flat specimen and (ii) boundary conditions and detailed mesh diagram of the unit cell near the TGO (iii) Physical interpretation of generalised plane strain boundary conditions**

**Table 5.5: Material properties of CMSX-4**

| Temperature (°C) | E [106] (GPa) | v [106] | CTE [108] ($C^{-1}.10^{6}$) | $A_0$ [109] ($MPa^{-n}s^{-1}$) | Q [109] (J/mol) | n [109] |
|---|---|---|---|---|---|---|
| 200 | 155.0 | 0.3 | 15.0 | $6.68 \times 10^{48}$ | $1.72 \times 10^{6}$ | 6.6 |
| 630 | 134.0 | - | - | - | - | - |
| 830 | 120.0 | - | - | - | - | - |
| 1200 | 100.0 | - | - | - | - | - |

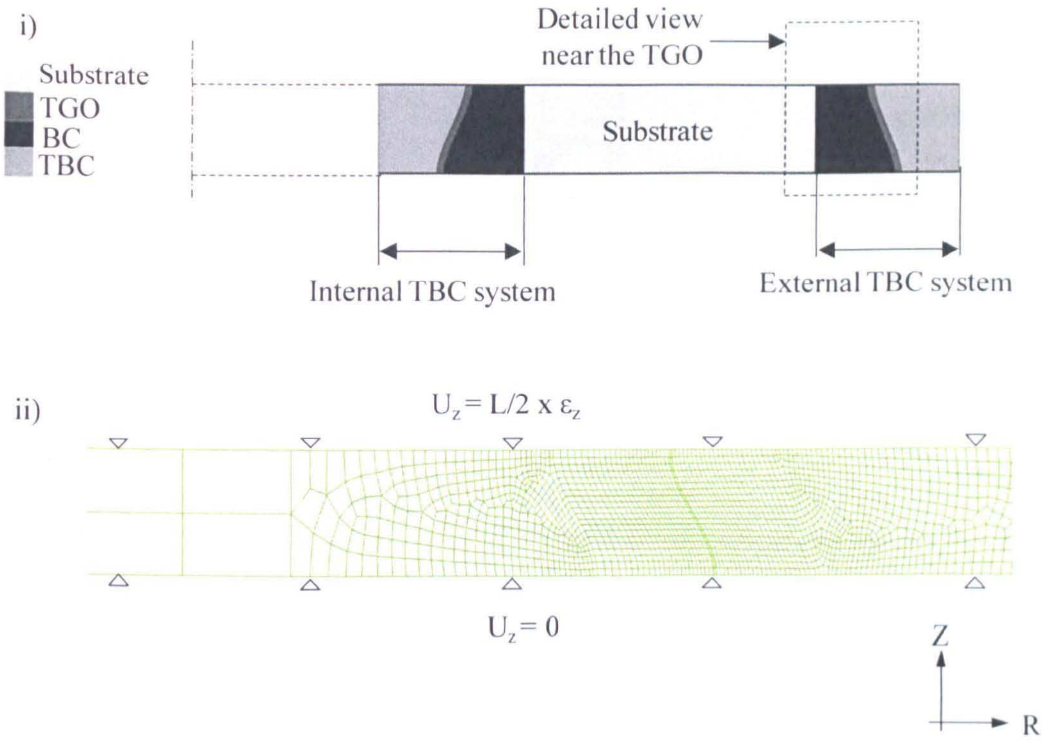

**Fig. 5.6: (i) A schematic diagram of the unit to represent the hollow cylinder model from Fig. 5.2 and (ii) boundary conditions and detailed mesh diagram of the unit cell used near the TGO interface (R-Z axis represents the radial-axial coordinate system)**

### 5.5.1 Residual stresses within the TGO of the strip specimens as predicted by FE model

The model predicts residual stresses within the TGO grown on the BC surface of the flat specimen at the end of the cooling stage after heating at 96h at 700°C or 1000°C. The predicted in-plane compressive residual stresses along the surface of the outermost TGO layers of two specimens are plotted in Fig. 5.7. For the specimen aged at 1000°C for 96h, the compressive stresses are predicted to cover the range between 1 and 3.0 GPa, while the compressive stresses predicted for the 700°C specimen are even higher (around 2.6 to 3.4 GPa).

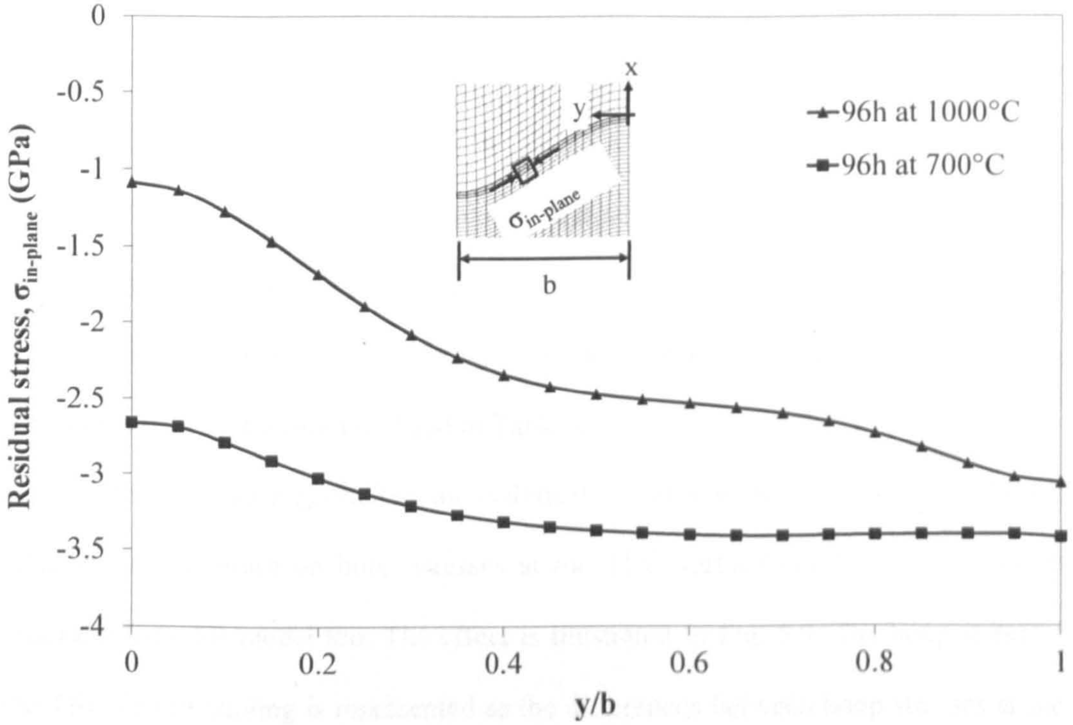

**Fig. 5.7: In-plane compressive stress within a TGO at 20°C after oxidation at 1000°C and 700°C for 96h**

### 5.5.2 Effects of curvature on stresses within the TBC system as predicted by FE model

Studies were carried out using models with different pairs of inner and outer radii of the substrate as shown in Table 5.6 in order to observe effects of curvature on hoop and radial stresses. Due to limitations in the availability of the diffusion model for evolution of the BC phases, and due to the omission of cyclic loading within the FE model, stresses were simulated for a specimen, which had been heated for one 96h cycle at 925°C. At 925°C, creep of the TBC and the TGO does not significantly relax stresses arising from oxide growth at the TGO/TBC interface, which had occurred during the steady state. Therefore, significant stresses remain at the TGO/TBC interface. At the end of steady state, tensile and compressive radial stresses develop at the valley and the peak of the TGO/TBC interface. These stresses will be superimposed onto the compressive thermal mismatch stresses created during cooling. Changes of radial stresses during cooling at the valley of the TGO/TBC interface for different curvatures are illustrated in Fig. 5.8. Similarly, curvature also has a significant effect on the radial mismatch stresses at the BC/TGO interface due to cooling although the interface is almost stress free during steady state due to creep of the BC. Maximum tensile radial stresses at both TGO interfaces at the end of cooling for different curvatures are tabulated in Table 5.6.

Moreover, as suggested by an analytical model from Section 5.4, the influence of substrate curvature on hoop stresses at the TBC surface due to cooling can be observed from FE model too. The effect is illustrated in Fig. 5.9. The hoop stress of the TBC due to cooling is represented as the differences between hoop stresses at the end of steady state and at the end of cooling.

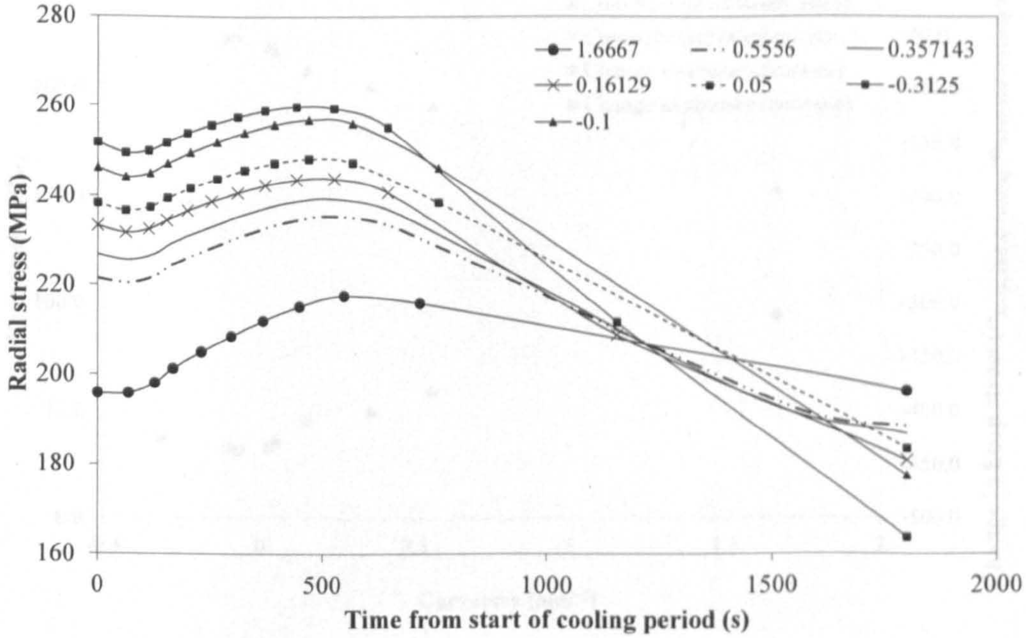

**Fig. 5.8: Differences in evolution of radial stress at the valley of TGO/TBC interface, due to cooling after heating at 925°C for 96h, for different curvatures ($mm^{-1}$)**

**Table 5.6: Maximum radial stress at the TBC/TGO and at the BC/TGO interfaces at the end of cooling after 96h at 925°C**

| Outer radius (mm) | Inner Radius (mm) | $\sigma_{radial}^{max}$ at the TBC/TGO interface; inner coating (MPa) | $\sigma_{radial}^{max}$ at the TBC/TGO interface; outer coating (MPa) | $\sigma_{radial}^{max}$ at the BC/TGO interface; inner coating (MPa) | $\sigma_{radial}^{max}$ at the BC/TGO interface; outer coating (MPa) |
|---|---|---|---|---|---|
| 0.6 | N/A | N/A | 200.4 | N/A | 719.4 |
| 1.8 | N/A | N/A | 193 | N/A | 672.5 |
| 2.8 | N/A | N/A | 190.7 | N/A | 661.1 |
| 6.2 | 3.20 | 154.38 | 180.9 | 603.95 | 648.8 |
| 20 | 10.00 | 177.54 | 183.58 | 620.87 | 641.92 |
| 35 | 15.00 | 180.75 | 183.6 | 625.73 | 639.6 |

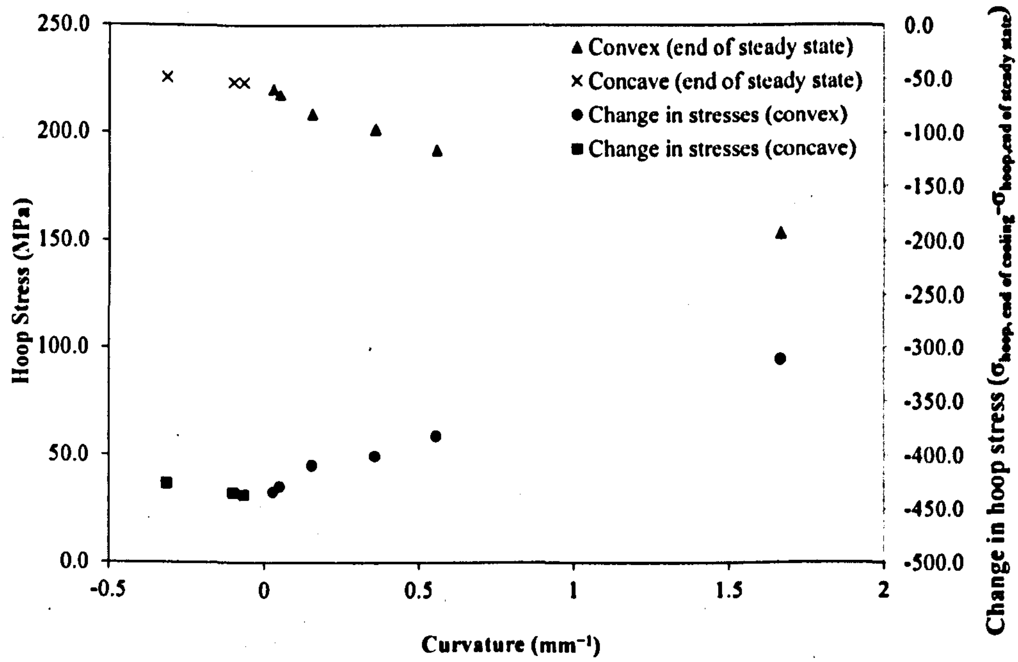

**Fig. 5.9: Hoop stresses at the TBC surface and changes in hoop stresses at TBC surface, for various substrate curvatures, at the end of cooling after 96h of heating at 925°C**

### 5.5.3 Effects of TBC thickness on stresses within the TBC system as predicted by the FE model

It can be observed analytically that the thickness of the TBC affects residual stresses within the coating for a single layer coating system (Fig. 5.4). Therefore, a parametric study was carried out using the FE model to observe the significance of TBC thickness in the multi-layered structure. In contrast to the analytical calculations, the TBC thickness does not significantly affect either the TBC hoop or radial stresses at the TGO/TBC interface. However, an increase in TBC thickness causes a significant increase in radial stress at the BC/substrate interface, which has no local undulations. Therefore, it is believed that stresses at the TBC/TGO interface are dominated by the effect of local undulation instead of the global coating thickness. The effects of TBC thickness on the hoop and radial stresses, within a TBC system, are illustrated by Fig. 5.10.

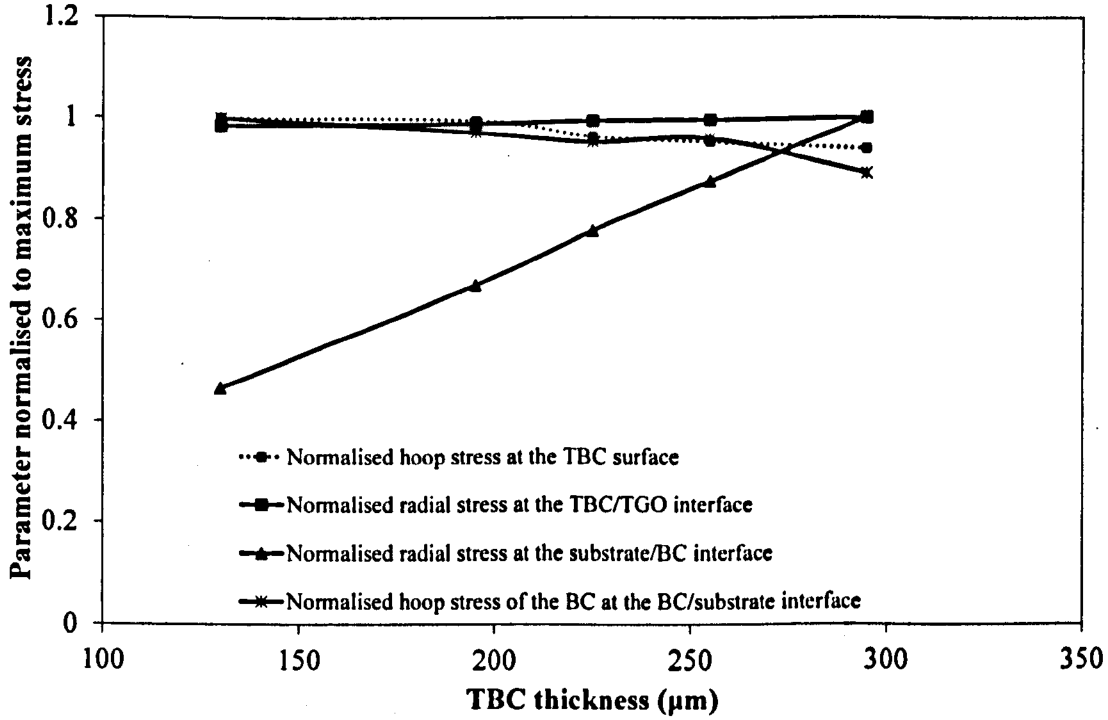

**Fig. 5.10: Effects of TBC thickness on radial and hoop stresses within the TBC system (Stresses are at 20°C after heating for 96h at 925°C)**

# 5.6 Stress measurements using Raman and photo-stimulated luminescence piezo-spectroscopy (PLPS)

## 5.6.1 Theoretical backgrounds

The RS and PLPS methods have been used for measurements of residual stresses within the ceramic top coat and TGO layer of various TBC systems [62, 64, 110, 111]. The apparatus, procedure and calibration for the Raman measurement technique have been described by Liu et al. [112]. The measured frequency shifts on a single crystal of the material ($\Delta v$) can be related to stress tensors ($\sigma_{ij}$) by using piezospectroscopic (PS) tensors ($\pi_{ij}$) [61] as shown in Eq (5.3). It was also shown that $\sigma_{ij}$ is stress tensor in the laboratory reference frame (x-y-z). Conversion into stress tensor in the direction of reference frame of grains (x'-y'-z') can be performed using Euler's transformation matrix ($\phi_{ij}$) as shown in Eq (5.4). Euler's transformation matrix can be expressed as shown in Eq (5.5). $\bar{\phi}_{ij}$ is the inverse matrix of $\phi_{ij}$.

$$\Delta v = \pi_{ij}.\sigma_{ij} \tag{5.3}$$

$$\begin{bmatrix} \sigma_{x'x'} & \sigma_{x'y'} & \sigma_{x'z'} \\ \sigma_{y'x'} & \sigma_{y'y'} & \sigma_{y'z'} \\ \sigma_{z'x'} & \sigma_{z'y'} & \sigma_{z'z'} \end{bmatrix} = \phi_{ij} \begin{bmatrix} \sigma_{xx} & \sigma_{xy} & \sigma_{xz} \\ \sigma_{yx} & \sigma_{yy} & \sigma_{yz} \\ \sigma_{zx} & \sigma_{zy} & \sigma_{zz} \end{bmatrix} \bar{\phi}_{ij} \tag{5.4}$$

$$\begin{bmatrix} \cos\theta\cos\varphi\cos\psi - \sin\varphi\sin\psi & \cos\theta\sin\varphi\cos\psi + \cos\varphi\sin\psi & -\sin\theta\cos\psi \\ -\sin\varphi\sin\psi - \cos\theta\cos\varphi\sin\psi & \cos\varphi\cos\psi - \cos\theta\sin\varphi\sin\psi & \sin\theta\sin\psi \\ \sin\theta\cos\varphi & \sin\theta\sin\varphi & \cos\theta \end{bmatrix} \tag{5.5}$$

$\theta, \varphi$ and $\psi$ are angles between axes of reference laboratory coordinate systems (z, x and y) and corresponding axes of the coordinate systems of a single crystal material (z', x' and y'). However, the present case relates to polycrystalline layers of yttria-stabilised zirconia and alumina for the TBC and TGO studied using RS and

PLPS respectively. In both of these cases the spot size of the incident light is very much larger than the crystal size, so that the piezospectroscopic effect is averaged over many crystals whose orientations may be assumed to be randomly distributed within the space of all possible orientations. The effect of this is to average out any directional sensitivity so that, as shown by Ma and Clarke [113], the observed frequency shift is dependent only upon the trace of the stress tensor and the measured stress can be expressed as hydrostatic. When the PS tensors ($\pi_{11}$, $\pi_{22}$, $\pi_{33}$) are assumed to be identical too, the measured stress will be the mean of the trace of stress tensors $(\bar{\sigma})$. The stress is converted from mean of the frequency shifts $(\Delta v)$ using mean PS tensor $(\Pi)$ as shown in Eq (5.6).

$$\bar{\sigma} = \Delta v / \Pi \tag{5.6}$$

The same assumptions can be applied to measurements of stresses by PLPS at the TGO surface of the flat specimen. Unlike the TBC, TGO is opaque to the laser and thus frequency shifts obtained from PLPS represent local strain at the TGO surface, which has no ceramic top coat. As a result, it can be assumed that out of plane stress at the TGO surface is zero and the measured stress, hence, is biaxial. The relationship between average measured frequency shift and average biaxial stress can be expressed as shown in Eq (5.7).

$$\sigma_{biaxial} = \frac{3}{2}\frac{\Delta v}{\Pi} \tag{5.7}$$

The conversion factor for TBC stresses is 5.60 $GPa^{-1}cm^{-1}$ using the peak centre at 640 $cm^{-1}$ as calibrated in [112]. For average biaxial stress at the surface of the TGO, the conversion factor of 3.38 $GPa^{-1}cm^{-1}$ at the peak centre at 14432$cm^{-1}$ from [114] was used.

### 5.6.2 Residual stresses within the TGO of the strip specimens as measured by PLPS

The stress measurements on the coating surface were made by Liu [115] along trajectories, which are parallel to the length and the width of the strip specimens, using a green laser (λ=514 nm) with spot diameter of approximately 1.5 um. 21 measurements were made for each trajectory of the specimen. The residual stresses within the TGO of 700°C and 1000°C specimens are plotted in Fig 5.11. The mean compressive stresses for the former and latter specimens are 1.06GPa and 0.92GPa with standard deviations (SD) of 0.453GPa and 0.669GPa respectively. The SD of the 1000°C specimen is much higher than the value for the 700°C specimen because of spikes in the measurements. These spikes in residual stresses for 1000°C specimen are proposed to be caused by highly convoluted TGO formation. The TGO thickness of 1000°C specimen, as demonstrated in Fig. 5.12 (i), varies from 0.2 to 1.5μm. Local thickening of the TGO can be observed from the magnified image as shown in Fig. 5.12 (ii). Moreover, surface undulations of 1000°C specimen are more prominent than 700°C specimen and TGO growth along these undulations (Fig. 5.12 (iii)) adds complexity to the residual stress measured. Since TGO is assumed to grow uniformly across the surface for FE model, the spikes in measurements are omitted for comparisons with predicted stresses. Stress measurements for 1000°C specimen lying outside ±1SD are shown as circles in Fig. 5.11. After omitting 4 measurements, which are out of the ±1SD, the updated average compressive stress and SD for 1000°C specimen are 0.7474GPa and 0.41578GPa respectively.

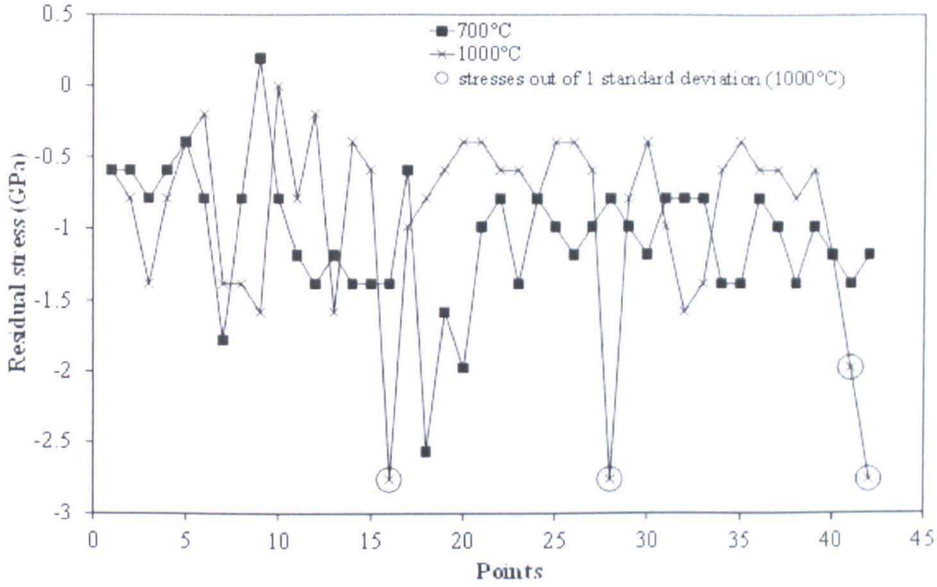

**Fig. 5.11: Experimental residual stresses at the surface of the TGO at 20°C after oxidation at 1000°C and 700°C for 96h [115]**

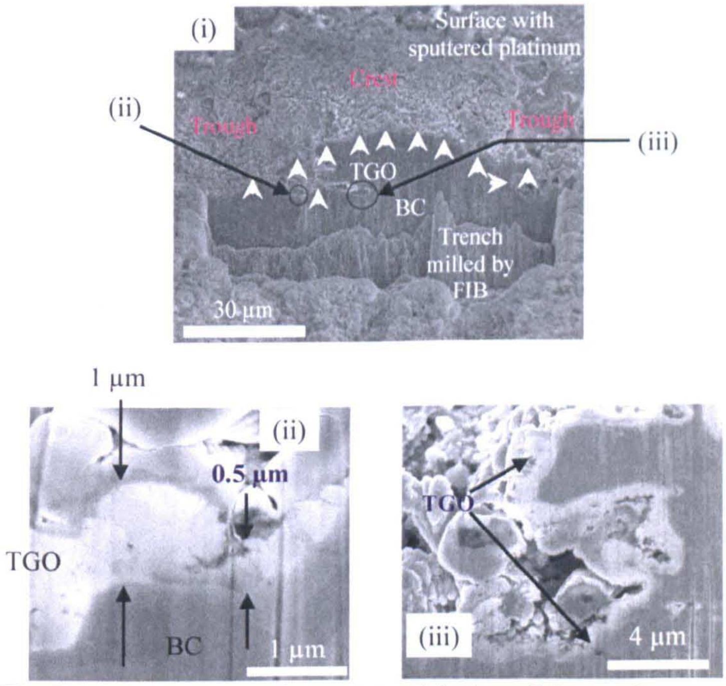

**Fig. 5.12: (i) The TGO layer grows along an undulation of the surface revealed by the FIB trench (the TGO layer is marked by the arrows) (ii) local thickening of the TGO with randomly oriented grains and with various thicknesses from 0.5 µm to 1 µm. (iii) the convoluted growth of the TGO due to surface undulation ;for the specimen that has been heated at 1000°C for 96h [115]**

### 5.6.3 Effects of curvature on stresses within the TBC system of aerofoil specimen as measured by Raman spectroscopy

After 96h of heating at 925°C, the aerofoil specimen was cooled down and residual stress measurements were carried out by Liu et al. [101] using RS. Additionally, residual stresses within the as-sprayed specimen were also measured to observe the effects of manufacturing on initial residual stresses. Stresses within as-sprayed and heat treated specimens are plotted against substrate curvature in Fig. 5.13. Considerable tensile residual stresses result from the rapid cooling of the surface of the TBC after the spraying process and they are in the order of 1GPa. After cooling, the lowest levels of residual stress are found at the regions of the specimen with lowest concave and convex curvatures. Stresses are very high compared to the order of magnitude obtained from FE models. The reason could be that stresses are locally concentrated at small contact areas between splats (splat boundaries) of TBC. When stresses are simulated using FE model, the coating is assumed to be a continuous material without any discrete splat boundaries and hence simulated stresses only represent mismatch stresses between the TBC and BC.

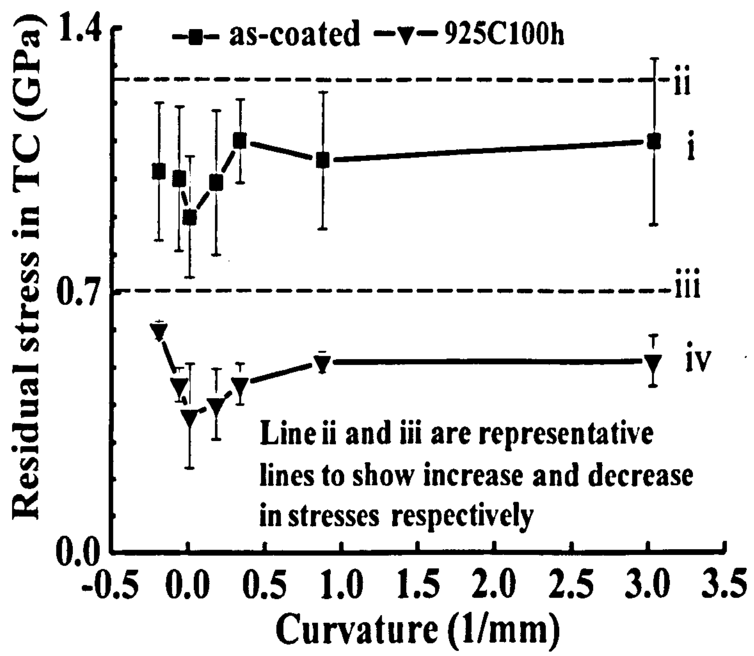

**Fig. 5.13: Residual stress in the TBC changes with substrate curvature in as-coated (i) and 925°C96h specimens (iv) [115], (ii) and (iii) represent perspective stresses at the end of heating to 925°C and at the end of steady state respectively**

## 5.7 Discussion

### 5.7.1 Comparison of residual stresses in the strip specimens

While the measurements from Fig. 5.11 are lower than the in-plane principal compressive stresses from the FE models (Fig. 5.7), the predicted stresses are found to be of similar order of magnitude and in broadly similar ranges to those measured by experiments for both 700°C and 1000°C specimens. The measured stresses for the 700°C specimen show considerably more oscillations than the 1000°C specimen whereas local highly compressive spikes are found for the 1000°C specimen. Specifically, predicted values of compressive stresses within the 700°C specimen (2.0 to 3.5GPa) are a factor of more than 2 larger than the range of experimental results (0.6 to 1.5147GPa) excluding local spikes. Similarly, the predicted range of compressive stress for the 1000°C specimen of around 1.0 to 3.0GPa is also around 2.5 times of one SD range of 0.3 to 1.163GPa.

The discrepancies in stresses might arise from the oxidation law used for the FE model. The oxidation law is fundamental for calculating volume growth because of TGO formation and corresponding growth stresses, and the phase balance within the metallic coating. The law used in the present chapter is based on the empirical formula, which was obtained by extrapolating results from oxidation experiments [88] carried out at temperatures much higher than the range used for the present study. The model may therefore over-predict the oxide growth rate and in turn the levels of stress arising from oxide growth.

Results from two independent studies, demonstrated in this chapter, have shown that higher compressive stresses are predicted within the TGO for the system, which has been oxidised at the lower temperature. Nevertheless, it is expected that a higher temperature drop at the cooling stage could give higher mismatch stresses. This apparent discrepancy can be explained by stresses arising from the oxide growth.

Growth of the TGO is restricted by the underlying BC and this growth produces compressive in-plane stress within the TGO during the steady state [116], while creep of the oxide layer, at the elevated temperature, relaxes built-up stress. As the specimen is left to oxidise further, additional oxide growth occurs between the existing oxide and the BC, both of which oppose the transformation strain associated with the new growth. These stresses within the TGO are much higher than those in the BC because of its lower strain tolerance, and its lower stress relaxation rate by creep.

For the 700°C specimen, due to its slower oxidation rate, oxide forms only in the vicinity of the specimen surface during the steady state and the oxide layer (still represented by a single layer of elements) is in overall compression due to the restraint imposed by the BC layer. By contrast, the continuing oxidation of the 1000°C specimen, after 96h, takes place under a 2μm thick layer of previously-formed oxide which is put into tension by the newly-formed oxide which in turn exhibits compressive stresses.

At the end of the cooling stage, thermo-mechanical stresses arise from CTE mismatch at the BC/TGO interface. Due to the lower CTE value of the TGO, in-plane compressive stress will be created within the TGO. These stresses will be superimposed upon the existing stress states within the TGO; hoop stress is tensile for the 1000°C specimen and is compressive for the 700°C specimen at the end of steady state. Hence, after cooling, overall compressive stress at the surface of the 700°C specimen will be higher than stress at the surface of the 1000°C specimen.

### 5.7.2 Comparison of residual stresses in the aerofoil specimens

The separation of individual stress tensor components from the measurements of RS frequency shift using the method from Section 5.6.1 is challenging because of random orientations of the grain structures within the sample volume, which determines the sensitivity of the shifts to each stress component. As a result, measured stresses by Liu [115] can only be related to the mean of the trace of stress tensors. In reality component of stresses in the out of plane direction of the laboratory reference frame is small near the TBC surface. Hence, the measured stresses can be taken as 2/3 of average in-plane stresses. An additional discrepancy from the side of FEA is that the initial tensile residual stresses from the spraying process were not incorporated into the model, due to the complexity of modelling the development of spraying related residual stresses. Simulation of these residual stresses would require modelling the formation and solidification of layers of YSZ while solving for thermo-mechanical stresses within those layers as mentioned in [117]. For the reasons explained earlier, quantitative comparison of measured values to predicted stresses is still difficult. Therefore, only the trend of the dependency of reduction in in-plane stresses at the TBC surface due to cooling on substrate curvature, as predicted by FE model, was compared against measured data.

To understand the way initial stresses in the TBC from Fig. 5.13 are reduced after a thermal cycle, the following hypothesis is proposed. It can be proved using an analytical model of a single-layered coating system that tensile and compressive mismatch hoop stresses at the TBC surface due to heating or cooling decrease counter-intuitively with increasing substrate curvature. Lower reductions in hoop stresses, due to cooling after spraying, result in higher tensile stresses for higher curvatures as shown in line [i] of Fig. 5.13. However, further reheating to 925°C causes a higher increase in hoop stresses for lower curvatures. For simplicity, it was assumed that the tensile stresses at different regions of aerofoil specimen are the same at the end of reheating to 925°C (line [ii] of Fig. 5.13). These stresses will be relaxed by creep of coatings during steady state to the same level too (line [iii] of Fig. 5.13). When the cooling phase takes place, reductions in stresses are expected because of mismatch strains. As in the case of cooling the system after spraying, reductions in hoop stresses are lower as the curvature is higher resulting in overall higher tensile hoop stress at the end of cooling (line [iv] of Fig. 5.13). A similar inverse relationship between reduction in hoop stress during cooling and global curvature can also be observed from the FE model of multi-layered coating system (Fig. 5.9).

Although there are variations in TBC thickness at different positions of the aerofoil specimen, the sensitivity study using the FE model, for the range of thicknesses between 130 and 300μm, has shown that the changes in thickness do not significantly affect TBC hoop stresses. Therefore, it is reasonable to assume that fixing the TBC thickness for the FE models with different radii of curvatures will not introduces significant errors.

### 5.7.3 Relationship between substrate curvature and spallation or delamination failures

From the analytical model and FE studies on the effects of substrate curvatures, the direct relationship between the TGO interfacial stresses and the convex substrate curvatures can be observed. Meanwhile, an inverse relationship is observed for concave curvatures. Moreover, the radial interfacial stresses predicted for the convex coating are also higher than those for the concave coatings. These out-of-plane stresses play a major role in creating parallel cracks (cracks parallel to the TGO interface) within the TBC in the vicinity of the TGO interface and delamination cracks at the interfaces. Therefore, failure is expected at convex regions of the aerofoil specimens.

Flash thermography studies on failed aerofoil-shaped specimens, which are similar to the one from Fig. 5.1, carried out by Seraffon et al. [102] have also demonstrated that spallation of the coating is favoured at the convex regions of the specimen. Large scale delaminations of TBC were observed at convex regions of the specimen that had been heated for 1050h at 1000°C. Conversely, spallation of coatings was not observed at the concave regions even after 1500h at 1000°C. These results give further confidence to the predictions made from the sensitivity study for the relationships among the TGO interfacial stresses, coating failure and substrate curvatures.

## 5.8 Conclusions

The present chapter demonstrates the comparisons of residual stresses within the TGO and TBC predicted from two different FE models against experimental results obtained within the project consortium. Additionally, sensitivity of radial stresses on substrate curvature and predictions of coating spallation are also compared against experimental thermography studies of coating spallation by project partners. These studies lead to the following conclusions:

☐ For the flat specimen, residual stresses are predicted to be of in a similar order of magnitude to the stresses measured using the RS method. Both techniques demonstrated higher compressive residual stresses within the specimen that had been heated at the lower temperature of 700°C as opposed to 1000°C.

☐ For the aerofoil specimen, because of the slow relaxation of manufacturing-related tensile residual stresses (around 1GPa) within the aerofoil specimen at 925°C, TBC residual stresses after cooling are tensile rather than compressive as predicted by the FE model.

☐ Reduction in hoop stresses due to thermal mismatch, as predicted by the FE model, is inversely proportional to the substrate curvature. The prediction agrees with the trend given by the stresses measured by the RS method.

☐ From the analytical and FE models, it is expected that cracks will be initiated within the TBC and at the TGO interfaces for convex coatings rather than concave, especially at the regions with high curvatures. Failure of the TBC is favoured when there is coalescence of those cracks, and spallation of the TBC is therefore expected at the convex regions. This prediction is confirmed by flash thermography studies [102] of the aerofoil specimens after failure, for which the spallation/delamination of coating is observed at convex regions of the specimens.

There is mutual agreement in experimental results and FE predictions for the trend of dependence of residual stresses and TBC spallation on the global curvature as presented in this chapter. This agreement demonstrates that various assumptions regarding to the geometry of the coating interfaces and the material properties within the FE models, are appropriate for predicting residual stresses and failure of the TBCs. However, quantitative comparison between the predicted residual stresses by the FE model and the experimental measurements is still found to be difficult.

# Chapter 6

# Effects of three-dimensional microscopic features of coating interface on thermo-mechanical stresses and related failure mechanisms

## 6.1 Introduction

The surface roughness of the BC plays a major role in determining the lifetime of an APS TBC coated components. It can be related to the coating durability by analysing stresses generated within the systems with different interface roughness and geometries [16]. However, many FE models from the literature take the form of 2D models, based on the observed cross-section of the coating interface from scanning electron microscope (SEM) images of TBCs. Possible reasons could be inadequate computational power to run FE simulations of a three dimensional (3D) model and difficulty in characterising 3D coating profiles from standalone coatings. Not only do idealised 2D interfaces not represent the actual geometry but are also likely to result in simulated TBC stresses, which are insufficiently accurate for predictions of failure of the TBCs. Therefore, it is desirable to construct a 3D FE unit cell to represent the actual surface geometry and hence to predict stress distributions within the TBC system accurately.

Limited numbers of stress analyses [59, 60] have been carried out using 3D representations of coatings surface asperities, and there are shortcomings for existing 3D TBC models in the literature. Firstly, oxidation of the BC has not been coupled to the model. Due to the non-planar nature of the interface shape, directional oxide growth strain and subsequent stress built up within the system depend on interface geometries. Secondly, the interface shapes are usually proposed without carrying out the capture and measurement of coating asperities in 3D space.

The objective of this chapter is to set up the FE model for 3D microscopic features of coatings, which are extracted from 3D micrographs of coating surfaces. Appropriate boundary conditions presented by Li et al. [81] were applied to reduce the size of the unit cell and hence its computation time. Changes in material properties of the coating due to oxidation and sintering were also incorporated. A simple case study was carried out using simplified 2D and 3D TGO interface idealisations with identical aspect ratios. The study confirms that the additional effort involved in setting up a 3D unit cell (the establishment and validation of boundary conditions, the capture and the extraction of microscopic features and the significantly longer computation time) is worthwhile due to the significant differences in stresses predicted by 2D and 3D models. Subsequently, two FE unit cells based on 3D microscopic features of the BC were built to carry out analysis of stress distribution and relate them to the failure of the TBC.

## 6.2 Geometries of three dimensional coating interface

When 2D unit cells are used to model coating roughness, the isolated peaks and pits of the coating surface [Fig. 6.1] cannot be modelled. Instead, the cell represents a groove-like geometry as shown in Fig. 6.2 (i) and (ii). Furthermore, the aspect ratios obtained from the cross-sectional images of the TBC system might not always represent the actual aspect ratio. The concept can be appreciated from Fig. 6.3. Three different sectioning paths on an idealised surface with identical aspect ratio throughout its surface could form radically different section profiles.

Due to imprecise representations of the coating surface in 2D profiles, the accuracy of predicted thermo-mechanical stresses of FE model is questionable. If only biaxial stresses are simulated, the variation of stresses in the out-of-plane direction of the modelling space cannot be investigated. In reality, however, stress concentrations occur at the peaks and pits of the isolated asperities. Therefore, prediction of spallation and delamination of the coating, based on crack initiation and propagation caused by stresses within 2D TBC models, will be inaccurate too. For these reasons, it is desirable to extract the 3D texture of the coating interface and the process of extracting and analysing the coating interface obtained from image analysis is described as follows.

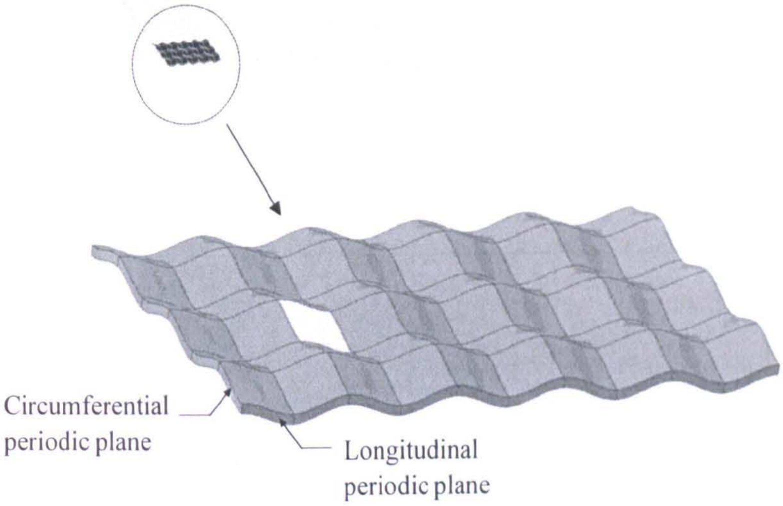

Fig. 6.1: Representative 3D coating surface (A unit cell is highlighted)

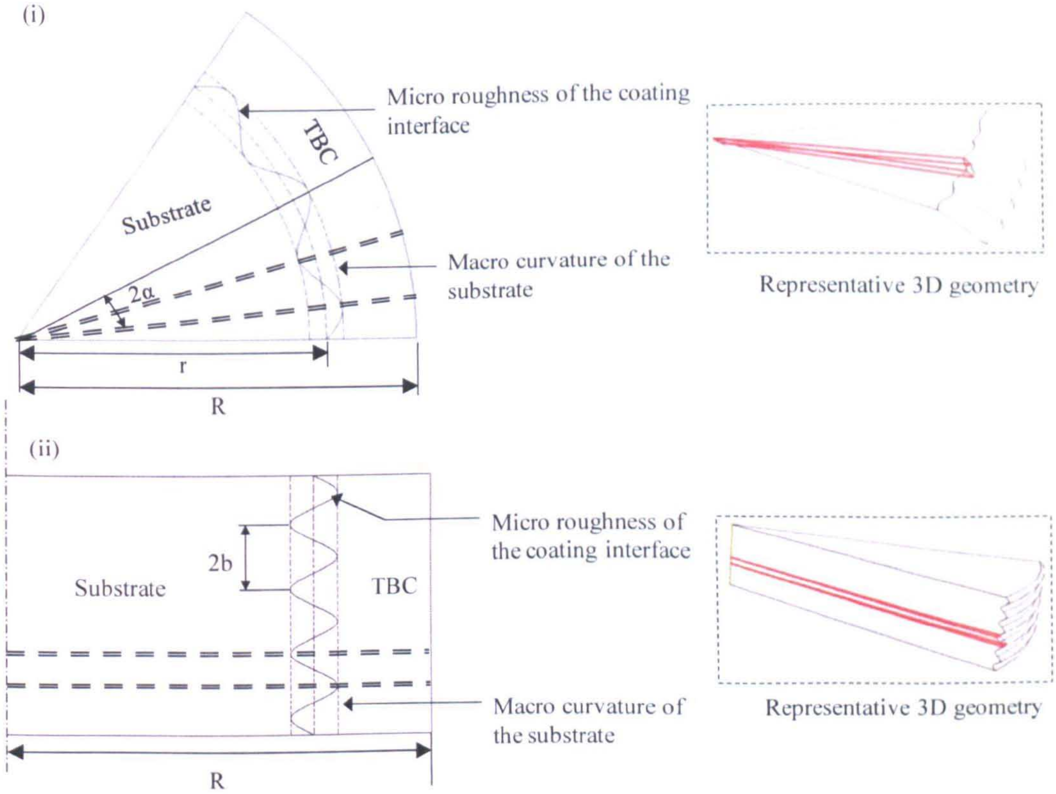

Fig. 6.2: Sinusoidal TGO interfaces i) periodicity in the circumferential direction with wavelength of 2rα and ii) periodicity in the longitudinal direction with wavelength of 2b (Cells bounded by double-dashed line are used for FE unit cells)

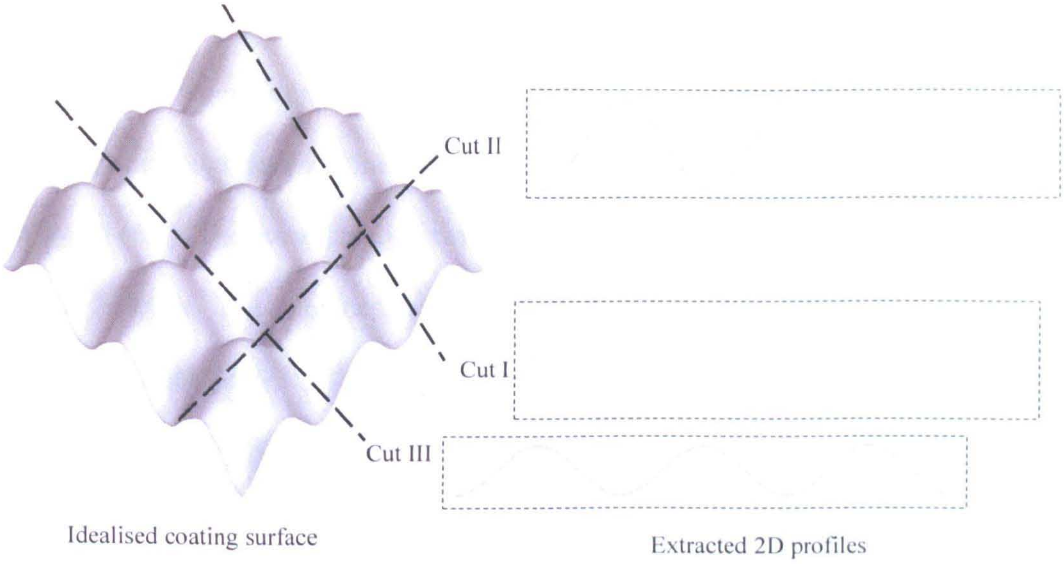

**Fig. 6.3: Possible coating roughness profiles that could be extracted from different cross-sectional micrographs of the coating surface with perfectly periodic asperities**

### 6.2.1 Specimen and post processing of TGO surface texture

A specimen used for the capture of the TGO surface profile is composed of Ni38.5Co21Cr8Al0.5Y (%vol) BC with APS TBC. The specimen was extracted from the system that had been heat treated at 960°C for 500h. The TGO profile was captured by Jepson [118] using the tilted SEM method as used by Sohn et al. [119]. Since the coatings remain bonded to the substrate, the specimen was dissolved in hydrochloric acid (36%) for 36h to dissolve the BC and to reveal the surface texture of the oxide interface. The x-y-z coordinates of the measured surface profile were then saved in ASCII format and were post-processed using 'Fogale nanotech profilometry software' (FNPS) [120]. In order to approximate a constant thickness of TGO layer within the FE model, it is assumed that both TGO interfaces (at the TBC and at BC sides) follow identical geometries.

The measured TGO surface coordinates in ASCII format were imported into FNPS, and the roughness profile (short wavelength undulations) and waviness (longer wavelength and larger sampling length than the roughness profile) of the interface were separated. Standardised Gaussian filtering method (ISO 11562) [121] was applied for the roughness-waviness separation. The weight function of the filter is given by Eq (6.1). The mean line of a raw profile is obtained by convolving it with the weighting function. The roughness and waviness profiles are separated by subtracting the mean line from the raw profile. The transfer function for the roughness profile can be expressed as Eq (6.2).

$$S(x)=\frac{1}{\alpha\lambda_c}\exp\left(-\pi\left(\frac{x}{\alpha\lambda_c}\right)^2\right) \tag{6.1}$$

$$\frac{A_{output}}{A_{input}}=\exp\left(-\pi\left(\frac{\alpha\lambda_c}{\lambda}\right)^2\right) \tag{6.2}$$

where $\alpha=\sqrt{\frac{\ln 2}{\pi}}$, x is the distance from the origin of the weight function, $\lambda_c$ is the cut-off for longer wavelength roughness and $\lambda$ is the actual wavelength of different waves from the raw surface profile.

As observed from Eq (6.1) and (6.2), the filtering process is mainly controlled by the choice of cut-off wavelength ($\lambda_c$). There are several uncertainties in choosing the cut-off wavelength. The wavelength has not only to be short enough to separate waviness profiles but also to be long enough to give a meaningful roughness profile. A longer cut-off wavelength creates smoother roughness profile and vice versa. Since there is no definite standard for the cut-off wavelength, the choice of the wavelength is entirely dependent on the sizes of the asperities, on which analyses to be performed. Currently, a cut-off wavelength of 25μm was used to separate the microscopic roughness features from large protuberances of isolated BC splats. The height contour plots of the roughness and waviness profiles of the TGO/BC interface within the sample area of 200μm x 140 μm are depicted in Fig. 6.4.

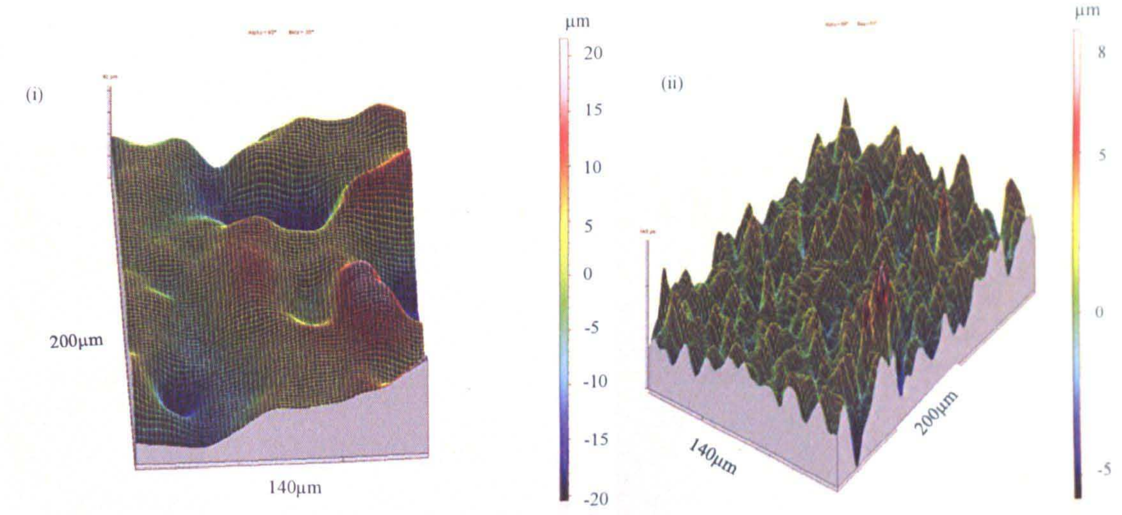

**Fig. 6.4: (i) Waviness and (ii) roughness profiles of the TGO/NiCoCrAlY BC interface with cut off wavelength (λc) = 25μm (profiles were generated using FNPS)**

### 6.2.2 Types of interface geometries

Three types of interface geometries were chosen for the various case studies. They are

i. a set of geometries measured from 2D SEM micrographs across a range of TBC systems

ii. a cell , which was extracted from 3D coating roughness from Fig. 6.4 (i)

iii. a cell , which represents the protuberance of BC splat, whose wavelength is larger than the roughness sampling length (Extracted from Fig. 6.4 (ii))

Firstly, the interface geometry with amplitude (A) of 6μm and wavelength (L) of 48μm (denoted as A6-L48), that has been used in previous studies [21, 105], is used for the axisymmetric and 3D unit cell models as shown in Fig. 6.5 (i) & (ii). Simulated thermo-mechanical stresses at 20°C from those two models, after aging both systems for 900h at 1000°C, will be compared later in the chapter. From this case study, it can be demonstrated that the additional effort involved in using 3D models of microscopic features, is worthwhile in order to predict stresses more accurately.

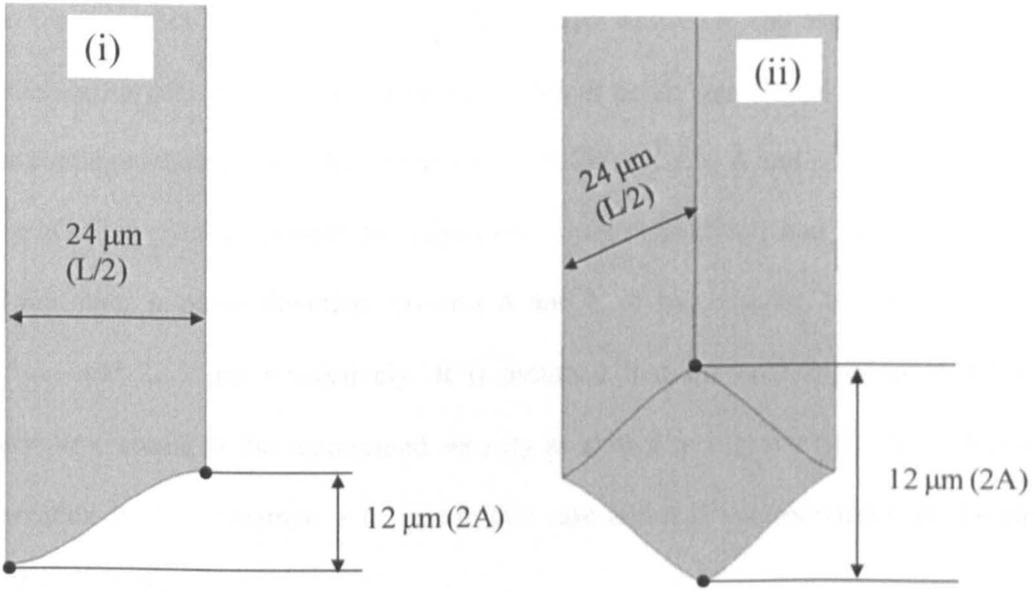

**Fig. 6.5: (i) Axisymmetric unit cell (L= 48μm, A = 6μm) (ii) Comparable 3D unit cell of TBC (Geometry set i)**

To represent the unique features from roughness and waviness profiles from Fig. 6.4, two unit cells were built and their effects on stresses are studied explicitly, by assuming the characteristic of the coating surface is similar to that of the engineering surface finish. This means that the coating surface is assumed to have three levels of undulation at different scales, which are known respectively as form, waviness and roughness. Different models were used to model undulations at different scales since the resultant problem size would be unrealistically large for a FE unit cell which includes all these geometric features. For example, a repeating cell of a waviness profile could contain many small roughness asperities, for which higher mesh density is required. Additionally, it is assumed that the tangential slopes are zero along the symmetry and the periodicity planes of unit cells due to limitations imposed by the boundary conditions for a 3D unit cell (Section 6.2). The assumption allows modelling only a quarter of each microscopic feature.

An asperity extracted from the roughness profile of Fig. 6.4 (ii) is similar to the idealised 3D interface shown in Fig. 6.5 (ii). However, the aspect ratios of the interface for two in-plane directions are different as the actual peaks and troughs of the coatings interface are elliptical as shown in Fig. 6.6 (ii). A and L of the asperity in one of the in-plane directions are 1.5μm and 13μm respectively and 1.8μm and 18μm in the other in-plane direction. Overall A and L of the asperity, therefore, will be 3.3μm and 22.5 μm respectively. It is assumed that the coating is covered with periodic features of the represented asperity as shown in Fig. 6.6 (iii). The substrate curvature for the specimen is 6.2mm in this case and it is incorporated with the unit cell as in [105].

As shown in Fig. 6.7, pits with depths significantly larger than those of the roughness asperities can be observed at the surface of the TGO. This feature hereafter will be referred to as an 'oxide loop'. A similar feature was extracted from the TGO surface of the system with 500h of heat treatment. The length and width of the elliptical oxide loop are 32μm and 24μm respectively, and the depth is 15μm. Because of the extreme aspect ratio of the oxide loop features, the form of the substrate has no significant effects on the local stress field compared to those of the oxide loop. Therefore, the substrate is assumed to be flat for modelling purposes.

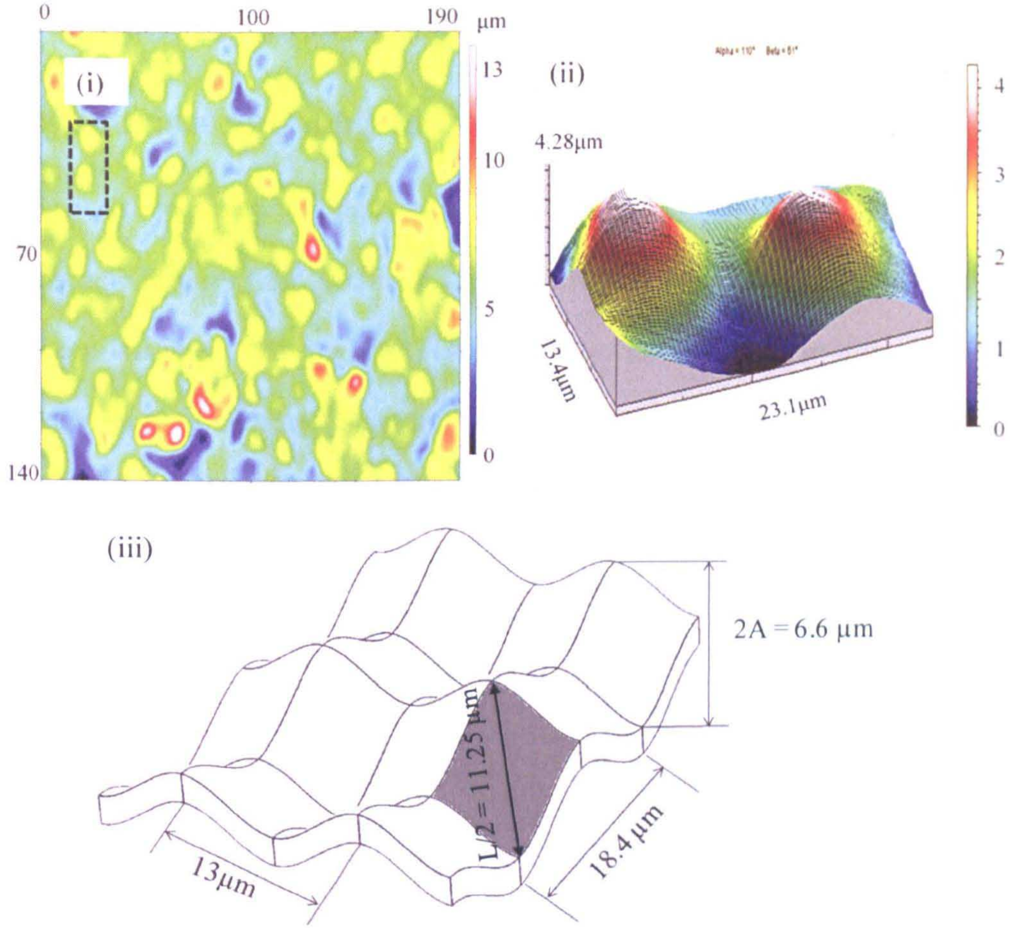

**Fig. 6.6: i) Surface contour plot of roughness profile and ii) 3D view of extracted asperity using FNPS (NiCoCrAlY system after 500h of heat treatment at 940°C) iii) Representative coating roughness by repeating unit cell (Geometry set ii)**

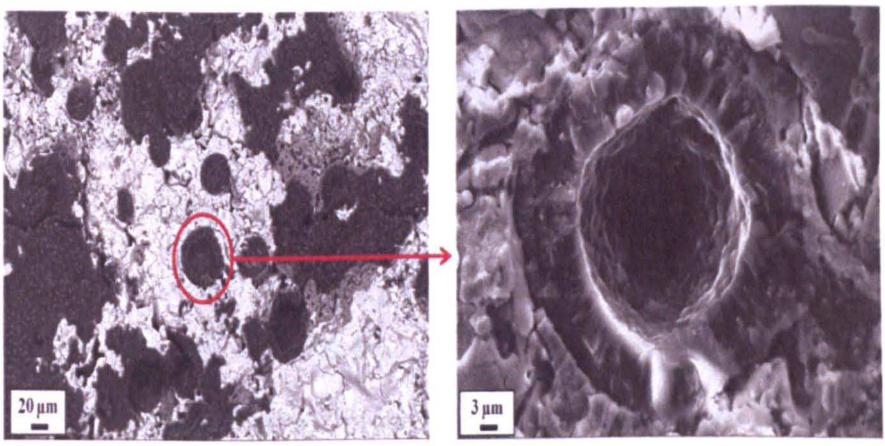

**Fig. 6.7: SEM image of oxide loops features at the surface of the TGO from NiCoCrAlY-APS TBC system, which has been heat treated at 1000C for 10,000h (Geometry set iii) [118]**

## 6.3 Boundary conditions for microscopic features with cylindrical and longitudinal periodicities

It is necessary to apply appropriate boundary conditions to the coating microscopic features from Section 6.2.2 for more efficient computation. In the past, it has been assumed that the BC/TGO interface has a 2D sinusoidal shape and periodicities can be formed either in the circumferential (wavelength = 2rα) or in the longitudinal (wavelength = 2b) direction as shown in Fig. 6.2 (i & ii). For the 3D model, the unit cell can be modelled in the domain shown in Eq (6.3) if the coating surface is composed of the repeating cells as shown in Fig. 6.1.

$$\begin{array}{l} -b \le x \le b \\ 0 \le r \le R \\ -\alpha \le \theta \le \alpha \end{array} \qquad (6.3)$$

where x, r, and θ are longitudinal, radial and circumferential coordinates of the cylindrical coordinate system (CSYS), respectively.

However, if only periodic boundary conditions are applied to planes at which x = ±b and θ = ±α, the tessellations of both surfaces at the periodic planes have to be identical. This restriction imposes difficulties in mesh generation, particularly for 3D models. Therefore, further boundary conditions have to be considered to take into account the reflectional symmetries of the interface. With both conditions for symmetry and periodicity, the translational cell length will be b and circumferential arc length of the unit cell will be R × α.

To implement circumferential periodic boundary conditions within the commercial FE software, modifications to the source code has to be made since commercial FE codes are based on the rectangular CSYS. Thus, boundary conditions based on the global rectangular CSYS are preferred. To achieve this objective, transformation of displacements from a cylindrical CSYS into a rectangular one is required and the respective transformations are shown in Eq (6.4).

$$\begin{aligned} u_x &= u \\ u_r &= v\cos\theta + w\sin\theta \\ u_\theta &= -v\sin\theta + w\cos\theta \end{aligned} \tag{6.4}$$

where $u_x$, $u_r$ and $u_\theta$ are displacements in a cylindrical coordinates system (x-r-θ) and u, v and w are displacement components in a global Cartesian coordinate system (x-y-z) as shown in Fig. 6.8.

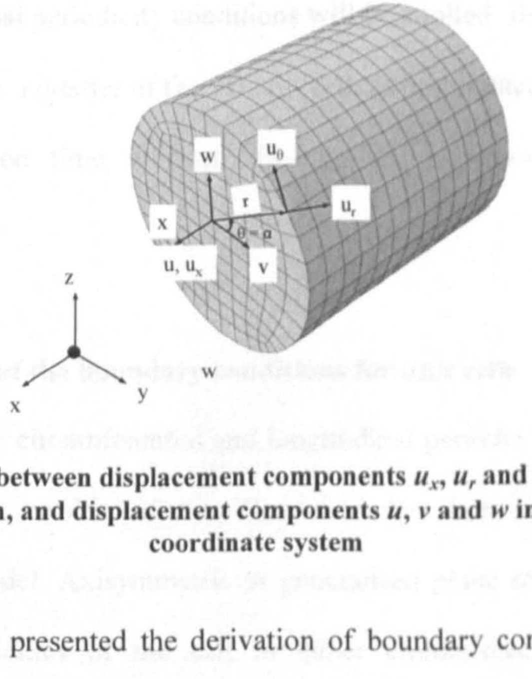

**Fig. 6.8: Relationship between displacement components $u_x$, $u_r$ and $u_\theta$ in cylindrical $x$-$r$-$\theta$ coordinate system, and displacement components $u$, $v$ and $w$ in Cartesian ($x$-$y$-$z$) coordinate system**

Li et al [122] presented the derivation of boundary conditions to represent composite structures with geometrically periodic patterns in terms of a unit cell accurately; micromechanical analysis can be carried out using the unit cell. The derivations were extended for structures with periodicities in cylindrical CSYS in

[81]. These boundary conditions for a 3D unit cell as shown in Fig. 6.1 (iii), for calculation of thermo mechanical stresses, can be represented in Eq (6.5).

$$\begin{gathered}\text{At } x = 0,\ u = 0 \\ \text{At } x = b,\ u = b\varepsilon_x^0 \\ \text{At } \theta = 0,\ w = 0 \\ \text{At } \theta = \alpha,\ -v\sin\theta + w\cos\theta = 0\end{gathered} \tag{6.5}$$

The first two boundary conditions of Eq (6.5) are applied to the unit cell with the length 'b'. The boundary conditions ensure that the unit cell represents the infinitely long cylinder by constraining the plane at x = b to remain parallel while allowing displacement to occur in the longitudinal direction.

Similarly, the last two boundary conditions of Eq (6.5) are applied for symmetry and periodicity conditions in r-θ plane. In the case for which the substrate is flat, only longitudinal periodicity conditions will be applied. By using Eq (6.5), it is possible to model only a quarter of the 3D unit cell, as highlighted in Fig. 6.1, in order to reduce computation time without affecting the accuracy of the numerical calculations.

### 6.3.1 Verifications of the boundary conditions for unit cells

To validate the circumferential and longitudinal periodic boundary conditions from Eq (6.5), each version of the 3D model has been compared against a corresponding 2D model. Axisymmetric or generalised plane strain (GPS) elements represent the periodicities of the cell in either circumferential or longitudinal directions. The meshes of each 2D model are identical to the rotated or extruded generator cross-section of the corresponding 3D mesh. Types of element and element sizes near the TGO interface, at which stress concentration occurs, are presented in

Table 6.1. The elastic and thermomechanical properties used in the benchmarking exercises are presented in Table 6.2.

**Table 6.1: Element types and element size of convergence tests**

| Simulations | Mesh refinement level | Element type | Approx. size of elements at TGO interface in μm (width × length × depth) |
|---|---|---|---|
| Axisymmetric | 1 | CAX4R | 1 × 1 |
| | 2 | CAX4R | 1/2 × 1 |
| | 3 | CAX4R | 1/4 × 1 |
| | 4 | CAX4R | 1/6 × 5/7 |
| | 5 | CAX4R | 1/8 × 3/8 |
| | 6 | CAX4R | 1/10 × 1/5 |
| 3D (Long.periodic) | 1 | C3D8R | 1 × 1 × 3 |
| | 2 | C3D8R | 1/2 × 1 × 3 |
| | 3 | C3D8R | 1/4 × 1 × 1.2 |
| | 4 | C3D8R | 1/6 × 5/7 × 1 |
| | 5 | C3D8R | 1/8 × 3/8 × 0.7 |
| | 6 | C3D8R | 1/10 × 1/5 × 0.7 |
| GPS | 1 | CPEG4R | 1 × 1 |
| | 2 | CPEG4R | 1/2 × 1 |
| | 3 | CPEG4R | 1/4 × 1 |
| | 4 | CPEG4R | 1/6 × 5/7 |
| | 5 | CPEG4R | 1/8 × 3/8 |
| | 6 | CPEG4R | 1/10 × 1/5 |
| 3D (Circumf.periodic) | 1 | C3D8R | 1 × 1 × 3 |
| | 2 | C3D8R | 1/2 × 1 × 3 |
| | 3 | C3D8R | 1/4 × 1 × 3 |
| | 4 | C3D8R | 1/6 × 5/7 × 1 |
| | 5 | C3D8R | 1/8 × 3/8 × 0.63 |
| | 6 | C3D8R | 1/10 × 1/5 × 0.7 |

**Table 6.2: Material properties and key dimensions for models of TBC system**

| Parameter | Values | | | | Units |
|---|---|---|---|---|---|
| Temperatures for substrate properties | 24 | 427 | 760 | 982 | °C |
| Modulus of substrate [82] | 206 | 179.3 | 157 | 140 | GPa |
| Poisson's ratio of substrate [82] | 0.28 | 0.28 | 0.3 | 0.3 | - |
| CTE of substrate [24] | 12 | 13.6 | 15 | 15.8 | $10^{-6}*K^{-1}$ |
| Temperatures for bond coat properties | 20 | 200 | 700 | 1000 | °C |
| Modulus of bond coat[83] | 203 | 200 | 167.7 | 131.6 | GPa |
| Poisson's ratio of bond coat [83] | 0.27 | 0.27 | 0.27 | 0.27 | - |
| CTE of bond coat[83] | 12.7 | 13 | 15.6 | 18.4 | $10^{-6}*K^{-1}$ |
| Temperatures for TGO properties | 20 | - | - | 1500 | °C |
| Modulus of TGO layer[17] | 416 | - | - | 338 | GPa |
| Poisson's ratio of TGO layer[17] | 0.23 | - | - | 0.25 | - |
| CTE of TGO layer[83] | 6.63 | - | - | 9.33 | $10^{-6}*K^{-1}$ |
| Temperatures for TBC properties | 20 | 200 | 700 | 1000 | °C |
| Modulus of aged TBC layer[83] | 198.3 | 204.6 | 252.8 | 346 | GPa |
| Poisson's ratio of aged TBC layer | 0.146 | 0.182 | 0.317 | 0.317 | - |
| CTE of aged TBC layer[83] | 10 | 10 | 10 | 10 | $10^{-6}*K^{-1}$ |
| Inner radius of substrate | 3.0 | | | | mm |
| Outer radius of substrate | 6.2 | | | | mm |
| Mean thickness of bond coat | 100 | | | | µm |
| Thickness of TGO layer | 1 | | | | µm |
| Amplitude of roughness (zero to peak) | 6 | | | | µm |
| Length of unit cell (and half wavelength of roughness for axisymmetric case) | 24 | | | | µm |
| Angle subtended by unit cell (and by half wavelength for prismatic model) | 0.22 | | | | degree |
| Temperature change on cooling | –980 | | | | K |

For the case where TGO periodicity is in the longitudinal direction, out of plane stress within the 3D unit cell is compared to an axisymmetric TBC model and the results are tabulated in Table 6.3. The stress values agree to within around 0.05%. The convergence of the two types of models to the same values is demonstrated within Table 6.3. For the case where the TGO periodicity is in the circumferential direction, out of plane stress in the 3D model is compared to that from a GPS model as this correctly permits out-of-plane (*z*) expansion while preserving planar *x*-*y* cross-sections. It may be noted from Table 6.4 that the 3D and GPS models each converge in a manner very similar to the 3D and axisymmetric models in Table 6.3, except that the 3D and GPS models give out-of-plane stresses which converge to values which are typically around 0.3% different.

## 6.4 FE model

### 6.4.1 Implementation of boundary and loading conditions

Equation constraints are applied at nodes on planes of symmetry and periodic of the unit cell to satisfy boundary conditions from Eq (6.5). A fictitious node is utilised for equation constraints for longitudinally periodic conditions. The constraint imposed is that all nodes at the periodic plane are tied to the fictitious node. While the fictitious node and nodes along the periodic plane are free to move independently, the perpendicular distances between them are always fixed. This constraint will ensure that the constrained surface remains planar. Displacements of nodes along the circumferentially periodic planes are also constrained to satisfy conditions in Eq (6.5). A constant temperature load of 1000°C is applied across the system and the duration of the steady state at 1000°C is 900h before cooling back to room temperature. For the system with preceding heat treatment duration of 500h at 960°C, the thickness of the initial TGO is 4μm; otherwise, the thickness is assumed to be 1μm. However, residual stresses from recent heat treatments were not taken into account and all systems are assumed to be stress-free at the start of the analysis.

**Table 6.3: Stresses at peak and valley regions of TBC and BC of axisymmetric model and 3D model (Axially periodic TGO interface) with different levels of mesh refinements**

| | Position | Mesh refinement level | | | | | |
|---|---|---|---|---|---|---|---|
| | | 1 | 2 | 3 | 4 | 5 | 6 |
| Axisymmetric model | BC peak | 863.192 | 874.433 | 880.724 | 888.047 | 890.955 | 891.14 |
| | BC valley | −714.481 | −753.078 | −774.621 | −797.647 | −806.489 | −808.721 |
| | TBC peak | 378.272 | 393.144 | 399.666 | 400.942 | 401.317 | 401.836 |
| | TBC valley | −565.803 | −576.239 | −581.365 | −585.133 | −586.281 | −586.768 |
| 3D model (Long periodic) | BC peak | 863.09 | 874.3 | 880.547 | 888.352 | 891.073 | 891.433 |
| | BC valley | −714.452 | −752.945 | −774.426 | -797.256 | -806.287 | -808.988 |
| | TBC peak | 378.3 | 393.168 | 399.703 | 400.872 | 401.151 | 401.738 |
| | TBC valley | −565.766 | −576.149 | −581.361 | -585.032 | -586.499 | -586.931 |

**Table 6.4: Stresses at peak and valley regions of TBC and BC of generalised plane strain model and 3D model (Circumferentially periodic TGO interface) with different levels of mesh refinements**

| | Position | Mesh refinement level | | | | | |
|---|---|---|---|---|---|---|---|
| | | 1 | 2 | 3 | 4 | 5 | 6 |
| GPS model | BC peak | 866.304 | 877.846 | 890.051 | 892.399 | 895.865 | 897.034 |
| | BC valley | −694.506 | −730.604 | −758.731 | −765.583 | −766.83 | −767.347 |
| | TBC peak | 376.938 | 390.708 | 395.907 | 397.652 | 397.677 | 397.937 |
| | TBC valley | −553.27 | −564.228 | −572.354 | −574.222 | −577.233 | −578.461 |
| 3D model (Circumf. periodic) | BC peak | 866.345 | 877.859 | 890.225 | 892.61 | 896.015 | 897.204 |
| | BC valley | −694.15 | −731.077 | −759.945 | -766.8 | -769.002 | -769.237 |
| | TBC peak | 375.811 | 390.674 | 395.918 | 397.577 | 397.584 | 397.91 |
| | TBC valley | −554.043 | −564.136 | −572.138 | -574 | -576.112 | -577.905 |

### 6.4.2 Material properties and oxidation kinetics

Material properties of the coatings and substrate can be found elsewhere [105]. It is assumed that the oxidation of the BC produces isotropic strain according to the PBR of aluminium (Al). As in the case for the model in [13], the PBR of Al is taken as 1.28. The oxide formed is made up of pure Al and it is growing towards the BC since oxygen diffusion rate within $Al_2O_3$ is higher than that of Al at the same temperature [123]. The growth strain rate $\left(\dot{\varepsilon}_{ij}^{tr}\right)$ due to oxidation is related to the Pilling-Bedworth ratio (PBR) for aluminium containing phases in the BC (β and γ') and the oxide formation rate $\left(\dot{f}_{ox}\right)$ expressed as Eq (6.6).

$$\dot{\varepsilon}_{ij}^{tr} = \frac{1}{3}\ln(PBR_{\beta/\gamma'})\dot{f}_{ox}\delta_{ij} \tag{6.6}$$

As mentioned by Taylor et al. [27], local aluminium depletion zones and external growth of non-Al oxides (spinels) are expected around the oxide features with high aspect ratio such as the oxide loop. Due to their significantly higher PBR than Al, fast growing oxides of Ni, Co and Cr create rapid increase in out-of-plane tensile stress within the TBC during steady state. The failure caused by this type of metal oxidation, due to aluminium depletion within the BC, is referred to as 'chemical failure'. However, studying chemical failure is outside the scope of this project and no spinel formation due to external oxidation will be considered here.

### 6.4.3 Modelling evolutions of material properties of coatings

For industrial TBC systems, continuous changes in material properties of coatings should be considered since the operation at high temperature changes coatings material properties. The porosity of the TBC changes due to sintering. The constitutive model which considers changes in TBC modulus due to sintering, based on the Arrhenius model, has been coupled to FE model of the TBC system by Kyaw et al. [105]. Proportions of phases within the BC change continuously during the steady state due to oxidation or interdiffusion at the substrate/BC interface. These changes can be calculated by using the FD calculation in combination with themodynamic calculations such as CALPHAD [124] as presented in [125, 126]. The atomic flux of aluminium at the BC/TGO interface is calculated by using empirically derived oxidation law.

Currently, a 1D FD/thermodynamics model developed by Karunaratne, et al [22], is coupled to the FE model of the TBC. Using these proportions of intermetallics phases predicted by the model, Eshelby's theorem and material properties of the pure BC phases, a constitutive material model was developed in [21] for the aggregate properties (elastic & creep properties and CTE) of the BC. The model for the BC will also be adopted here.

To transfer the 1D phase proportion data into the 3D FE models, the BC is modelled as a multilayered structure as shown in Fig. 6.9. The thickness of each layer was predefined at the pre-processing stage and the material points, at which the BC properties are calculated, are assumed to lie along the middle profile of each BC layer as shown in Fig. 6.9. Sporadically, layers of the BC are also transformed into the TGO layer with an appropriate growth strain based on the PBR of Al, to model oxidation. For the regions further away from the TGO interface, distances of material points from the TGO interface are estimated from the interface BC shown in Fig. 6.9. At those regions, errors in estimating distances due to the undulated nature of the interface are tolerable as the change in BC composition is subtle.

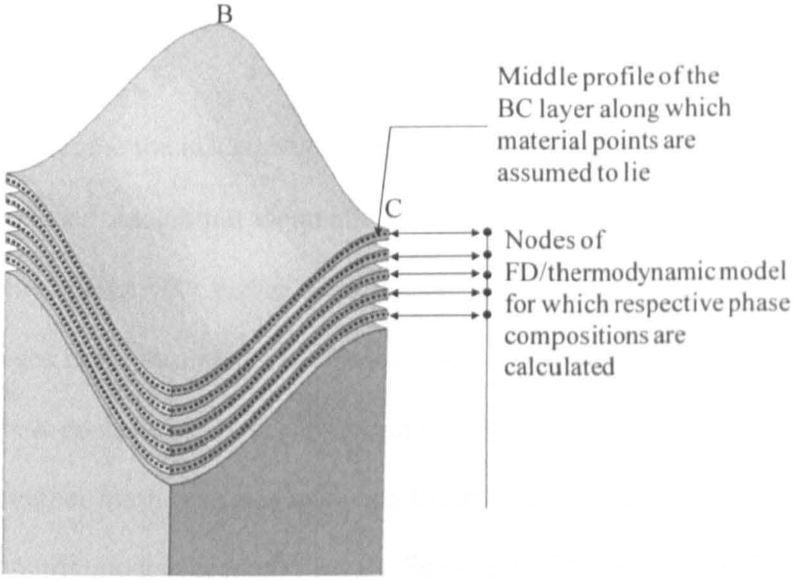

**Fig. 6.9: A multilayered nature of the BC to implement 1D FE model for the composition of the BC**

### 6.4.4 Finite element mesh

Appropriate element type and mesh densities for FE models with interface geometries from Section 6.2.2 are necessary to obtain accurate results with minimum computation time. For the axisymmetric models, 4-node linear axisymmetric elements (CAX4R) were used whereas 8-node linear brick elements (C3D8R) were used for the 3D models. Respective shapes of element, for axisymmetric and 3D models, are quadrilateral and hexahedral.

The stress and strain calculations for the current chapter are evaluated using displacement based FE formulations. The elements with the full integration scheme for displacement based FEA tend to overestimate the element stiffness matrix. Hence, fewer Gauss (integration) points are advised for such simulations. A reduction in the number of Gauss points also reduces computation time especially for 3D problems with a high quantity of elements. For these reasons, a reduced integration scheme was applied to elements.

To overcome the inaccuracies in interpolating stress and strain at nodal points for linear reduced integration elements (only one integration point at the centre of each element), a relatively higher mesh density is necessary around the regions with abrupt changes in displacements and hence in the resultant stress and strain. For TBC systems, stress concentrations occur around the TGO interface due to CTE mismatch and hence, higher mesh densities were applied at those regions. A mesh diagram for the axisymmetric model (geometry set (i), Section 6.2.2) was illustrated in Chapter 3 while mesh diagrams for geometry set (ii) and (iii) are illustrated in Fig. 6.10 and Fig. 6.11, respectively.

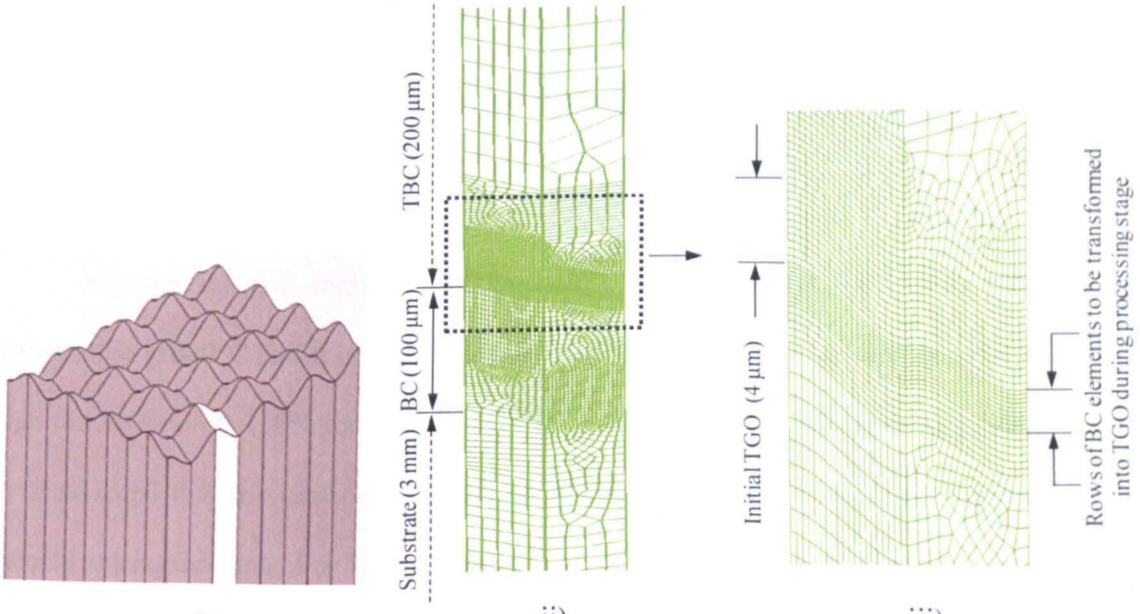

i) ii) iii)

**Fig. 6.10: i) Topography of the repeated sinusoidal oxide interface with highlighted unit cell for ii) FE mesh for the unit cell iii) Detail of mesh in the vicinity of the TGO**

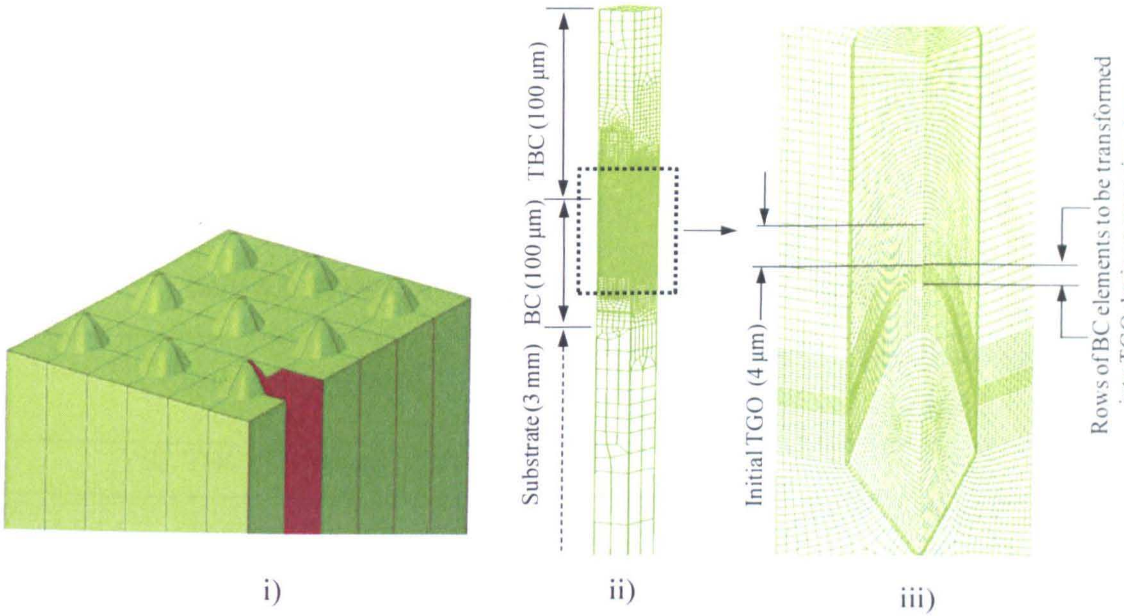

**Fig. 6.11: i) Topography of the repeated oxide loop interface with highlighted unit cell ii) FE mesh for the unit cell iii) Detail of mesh in the vicinity of the TGO**

## 6.5 Predicting crack formations and related failure of the TBC system based on stress distributions within the TBC system

For the current analysis, ductile failure of the BC at the steady state temperature (1000°C and it is above the DBTT of the BC[127]) is ignored because of high failure strain (~130% for Co29Cr6AlY BC) of the BC at high temperature [100]. It is assumed that the coating only fails in a brittle manner due to tensile stresses created during cooling. For the undulated interface, CTE mismatch creates out-of-plane tensile stresses near the TGO interfaces. These out-of-plane tensile stresses in turn cause propagation or coalescence of the existing TBC discontinuities and delamination cracks at the TGO interfaces. It can be estimated, for brittle coatings and interface, that cracks parallel to the TGO interface nucleate either within the coating or at the interface when the out-of-plane tensile stresses exceed respective tensile strengths. The tensile strengths of coatings and their interfaces were extracted from literature and are listed in Table 6.5.

**Table 6.5: Tensile strength of coatings and their interfaces**

| Coatings or interface | Temperature (°C) | Tensile strength (MPa) |
|---|---|---|
| YSZ TBC (8% yttira) [128] | - | 200 |
| Co29Cr6AlY BC [49] | 20 | 1300 |
| | 550 | 1200 |
| | 700 | 800 |
| | 850 | 150 |
| | 980 | 50 |
| TGO [17] | - | 250 |
| Bond strength at the TGO/TBC interface [129] | - | 30-50 |

When there are initial cracks at the BC/TGO interface and the interface is relatively flat, compressive in-plane stress, during cooling, within the oxide layer causes the layer to buckle. Strain energy stored at the buckled TGO/TBC interface (G) per unit area is related to in-plane residual stresses $\left(\sigma_{xx}^{TGO}\right)$ [130] as presented in Eq (6.7); $h^{TGO}$ and $h^{BC}$ respresent thicknesses of TGO and BC respectively. Delamination at the interface occurs when G is greater than critical strain energy release rate of the interface.

$$G=\frac{\sigma_{xx}^{TGO^2}h^{TGO}}{2*E^{TGO}}*\left\{1+\left(\frac{h^{TGO}}{h^{BC}}\right)\left(\frac{E^{TGO}}{E^{BC}}\right)\right\} \tag{6.7}$$

Therefore, in-plane compressive and out-of-plane tensile stresses play important roles for predicting crack initiation and propagation as well as the related failure of the TBC systems. These stresses for different geometries of coating microscopic features are presented in the following sections.

## 6.6 Stresses predicted by the TBC models with axisymmetric and 3D interfaces with identical aspect ratio

For both axisymmetric and 3D models, tensile out of plane stresses are predicted at the peak of the BC and valley of the TBC. Meanwhile compressive stresses are predicted at the valley of the BC and the peak of the TBC after cooling. A comparison of out-of-plane TBC stresses at 20°C after 900h of ageing at 1000°C, for 3D and 2D models, are demonstrated in Fig. 6.12. As seen from the figure, when 3D model was employed, maximum tensile out-of-plane stresses at the TGO/TBC interface increases by a factor of nearly two.

Higher stress concentrations at the TGO/TGO interfaces for the 3D model can be explained by a simple Lamé approach as described by Gong and Clarke [55]. Local interfacial stresses at the peak and valley regions of 2D and 3D model can be idealised as stresses at the coating interface for cylindrical and spherical substrates respectively. If the coating system is simplified as a single-layered system, the interfacial radial stresses of cylindrical and spherical substrate can be expressed as Eq (6.8)and (6.9). Analytically, it can be proved that, for an identical radius, radial stress at the coating interface for a spherical substrate is around 1.5 times higher compared to the cylindrical substrate. Analytical stresses of both systems are compared for different radii for the spherical and cylindrical substrates in Appendix B.

$$\sigma_r^{cylinder}(r = R_o) = -\frac{E^c\left(\alpha^s - \alpha^c\right)\Delta T\left[\left(\frac{R_o + H}{R_o}\right)^2 - 1\right]}{1 - 2\nu^c + \left(\frac{R_o + H}{R_o}\right)^2 + \frac{E^c}{E^s}\left(\frac{1 - \nu^s}{1 + \nu^c}\right)\left[\left(\frac{R_o + H}{R_o}\right)^2 - 1\right]} \tag{6.8}$$

$$\sigma_r^{spherical}(r = R_o) = -\frac{E^c\left(\alpha^s - \alpha^c\right)\Delta T\left[\left(\frac{R_o + H}{R_o}\right)^3 - 1\right]}{1 - 2\nu^c + \frac{1 + \nu^c}{2}\left(\frac{R_o + H}{R_o}\right)^3 + \frac{E^c}{E^s}\left(1 - 2\nu^s\right)\left[\left(\frac{R_o + H}{R_o}\right)^3 - 1\right]} \tag{6.9}$$

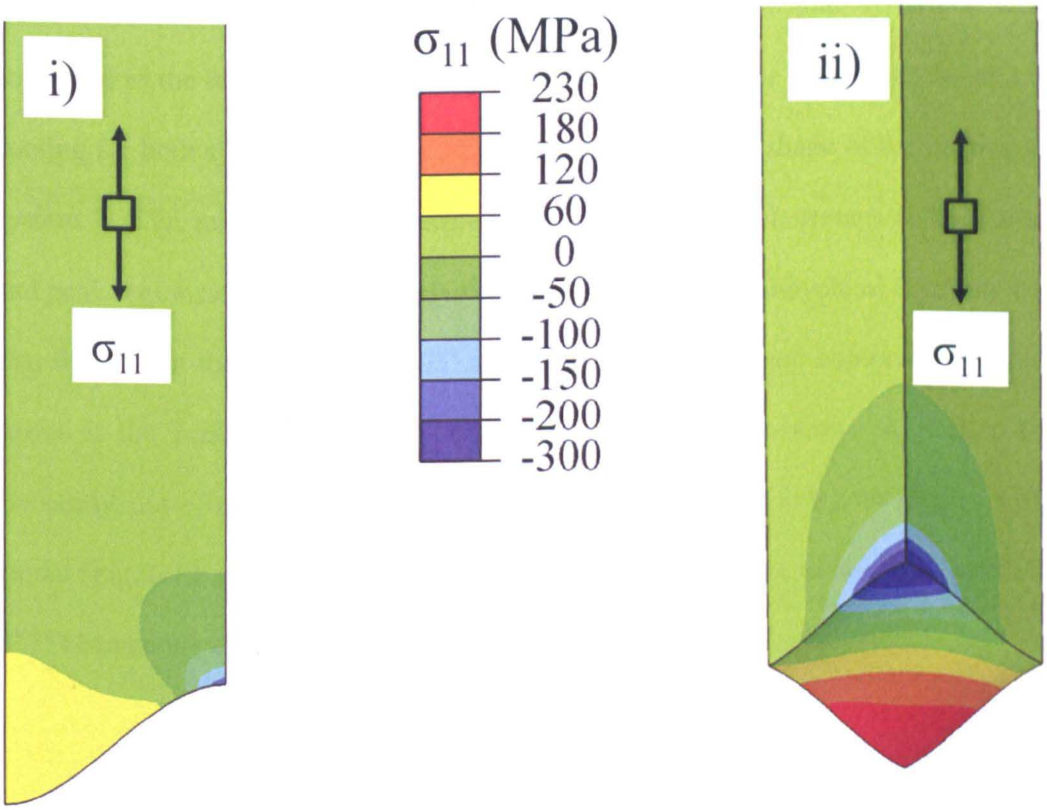

**Fig. 6.12: Out of plane tensile stress within the TBC with i) axisymmetric TGO interface ii) 3D TGO interface at 20°C after heating at 1000°C for 900h**

## 6.7 Stresses predicted by the TBC models with 3D sinusoidal interface geometry extracted from the aged specimen

To investigate the significance of the aspect ratio and the thermal ageing on stresses within the TBC, two different simulations were carried out, both having the same interface geometry as that shown in Fig. 6.6. System 1 is an as-sprayed system with an assumed initial TGO thickness of 1μm. By contrast, for the thermally aged sample, system 2, the initial TGO is 4μm thick and the TBC is assumed to be fully sintered after 500h of heating at 940°C. Firstly, stresses within system 1 were compared to the idealised 3D model. The trend of out-of-plane stresses at the end of cooling for both systems is similar despite the unsymmetrical shape of the coating of system 1. CTE mismatch gives tensile and compressive radial stresses at the valley and peak regions of the TBC respectively at the end of thermal cycle as illustrated in Fig. 6.13 . On the other hand, CTE mismatch gives tensile and compressive radial stress at the peak and valley of the BC/TGO interface as shown in Fig. 6.14. Generally, out-of-plane stresses are higher than those predicted using the idealised 3D model (Fig. 6.13 and Fig. 6.14). This is due to the higher aspect ratio of the interface (0.15) compared to the ratio of the idealised 3D model (0.125).

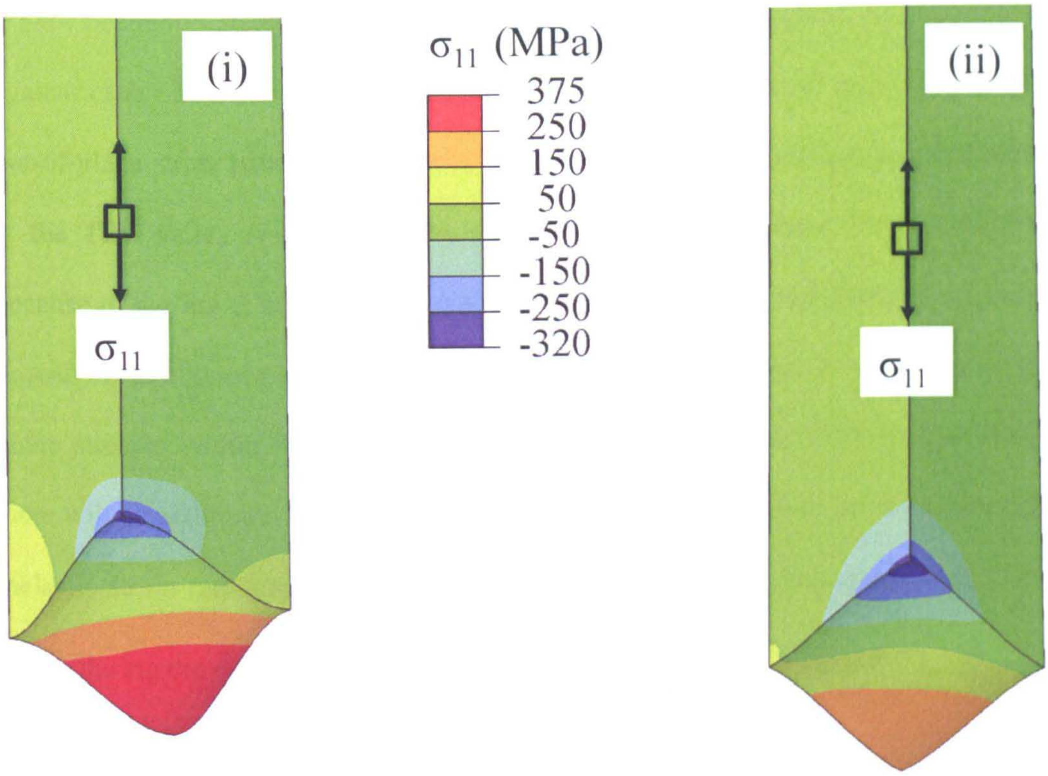

**Fig. 6.13: Through thickness stress ($\sigma_{11}$) in the vicinity of the TBC for (i) system 1 and (ii) idealised 3D interface at 20°C after heating at 1000°C for 900h**

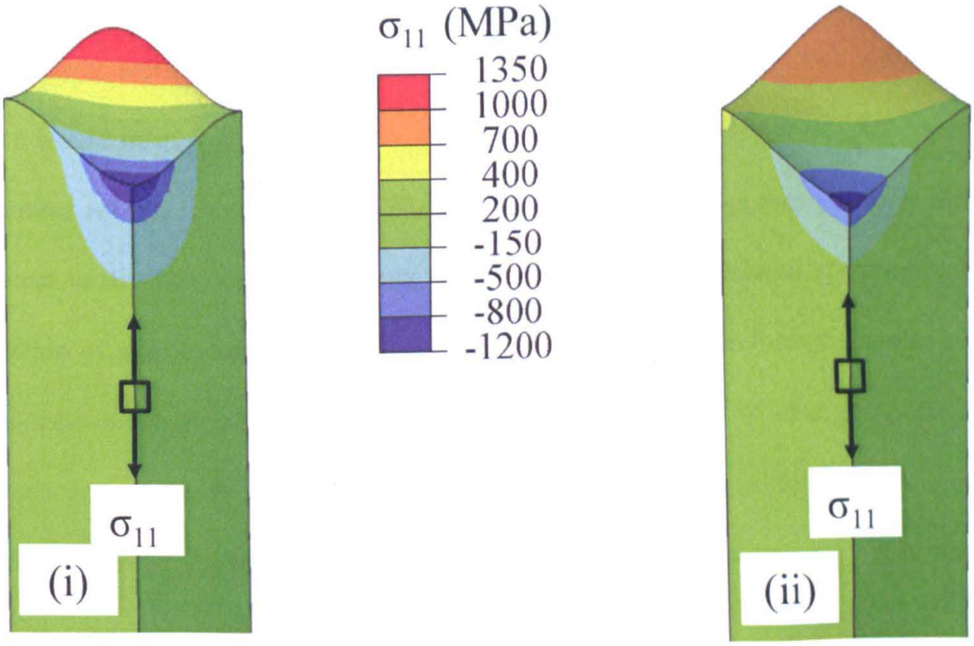

**Fig. 6.14: Through thickness stress ($\sigma_{11}$) in the vicinity of the BC for (i) system 1 and (ii) for idealised 3D interface at 20°C after heating at 1000°C for 900h**

Secondly, stresses occurring within system 1 and system 2 were compared against each other. At the end of the heating period, both systems produce a similar out-of-plane stress pattern, with tensile stress at the TBC peak and compressive stress at the TBC valley (Fig. 6.15). The higher magnitude of stresses for system 2 is because of the lower strain tolerance of the aged TBC. During the steady state, oxide growth occurs. Since oxide growth is constrained laterally, it imposes compressive in-plane stresses within the layer, which is growing to form the TGO. Concurrently, there will be additional creep strain of the TGO to relax the built-up stresses. The total inelastic strain rate tensor$\left(\dot{\varepsilon}_{ij}^{total,ox}\right)$ of the layer which is being transformed into new oxide, during the steady state, can be expressed as Eq (6.10).

$$\dot{\varepsilon}_{ij}^{total,ox} = \dot{\varepsilon}_{ij}^{cr} + \dot{\varepsilon}_{ij}^{ox} \qquad (6.10)$$

where $\dot{\varepsilon}_{ij}^{cr}$ is the creep strain rate and $\dot{\varepsilon}_{ij}^{ox}$ is the oxide growth rate

Compressive in-plane stress within the growing oxide layer will impose tensile and compressive out-of-plane stresses at the valley and peak at the TGO interfaces. These oxidation stresses are opposed to the initial thermal mismatch stresses and hence would be expected to lead eventually to stress reversal. In the case of system 1, the stress reversal occurs rapidly after heat-up as the newly-grown oxide is almost adjacent to the TBC layer. However, in the case of the heat treated specimens, both depletion of aluminium phases and a thicker TGO make oxide formation rate within the system much slower than system 1. Accordingly, the rate of change of the TBC stresses due to oxide growth is much slower, and stress reversal does not occur rapidly as shown in Fig. 6.15 as demonstrated in Fig. 6.15. Moreover, oxide growth stresses produced at the TBC/TGO interface during the steady state for system 1 are significantly higher than those produced by system 2 at the end steady state (Fig.

6.15). As a result, out of plane stresses at the TBC/TGO interface for system 1 after cooling are at least 40% higher than those predicted from system 2.

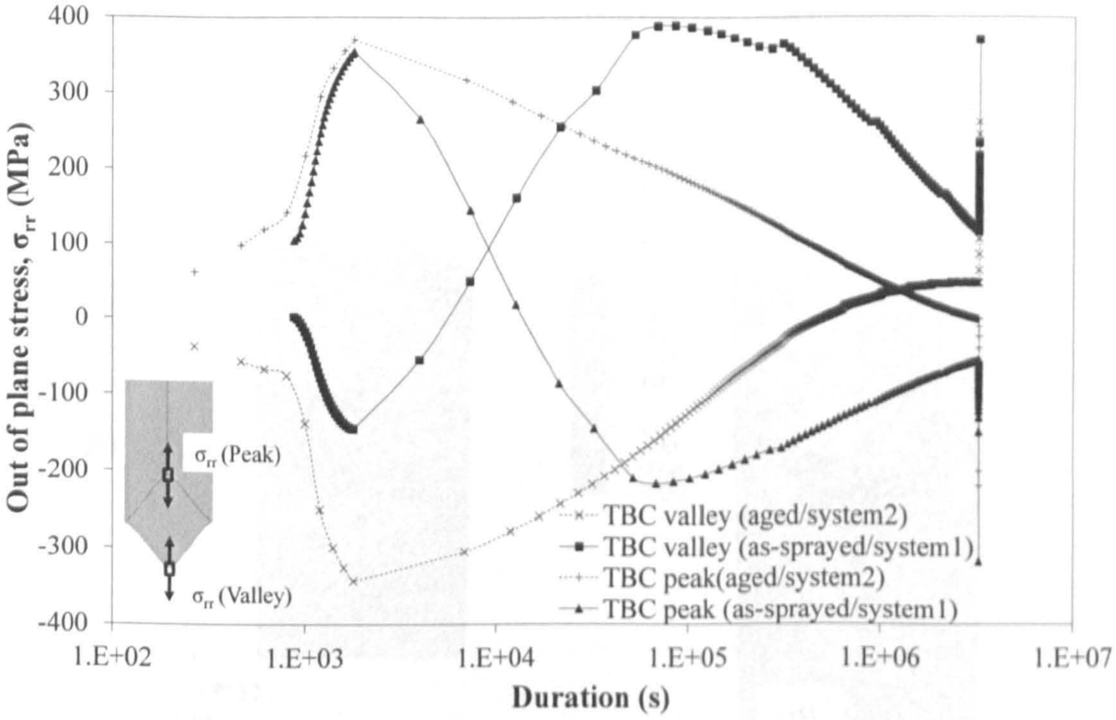

**Fig. 6.15: Out-of-plane stress at the TBC peak and valley for as-sprayed and aged TBC system with the identical coating asperity**

## 6.8 Stresses predicted by the TBC models with oxide loop geometry

Because of the convoluted geometry of the oxide loop, high tensile through thickness stresses are concentrated at the TBC peak at the end of heating to 1000°C, as shown in Fig. 6.16 (i). In reality, these stresses will be relaxed through formation of parallel cracks or by creep of the coatings during the steady state. Only the latter process was considered in this case. Due to stress relaxation by coating creep, tensile out-of-plane stresses at the TGO interfaces at the end of steady state are below the rupture strengths of the interfaces. When the cooling is applied at this stage, thermal mismatch will produce tensile out-of-plane stress at the BC peak and at the middle of the TBC/TGO interface as shown in Fig. 6.16 (ii). In the region where the interfacial geometry is flat, out-of-plane stresses are negligibly small although high compressive in-plane stresses of up to 6.5GPa are created within the TGO due to cooling.

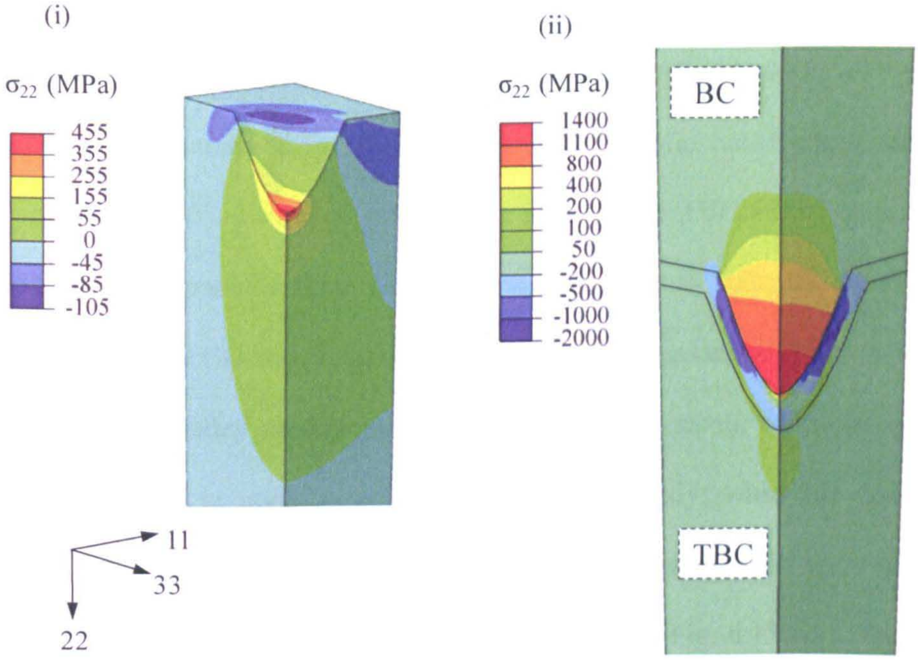

**Fig. 6.16: Through thickness stresses (i) within the TBC at the end of heating at 1000°C and (ii) within the TBC system near the TGO interfaces at the end of cooling after heating at 1000°C for 900h**

## 6.9 Prediction of crack development and failure of the TBC system based on stress distributions within the system

### 6.9.1 Axisymmetric coating interface

For the case of an axisymmetric interface, parallel cracks within the TGO and opening of existing TBC cracks are expected around the TBC peak, at the end of heat-up from room temperature, due to concentration of tensile out-of-plane stress as shown in Fig. 6.17 (i). However, propagation towards the TBC valley is restricted because of high compressive stress at the valley. During steady state, the combination of the growth of the TGO and creep relaxation of the coatings causes stress reversal at the TBC peak and valley as shown in Fig. 6.17 (ii). As a result, additional parallel cracks are expected to nucleate at the TBC valley. Finally, when the cooling is applied, due to CTE mismatch, tensile out-of-plane stresses occur in the vicinity of the peak of BC, valley and hill of the TBC as depicted in Fig. 6.17 (iii). Therefore, parallel cracks are expected to form at the TBC hill and coalescence with existing TGO cracks is also expected. On the other hand, formation of parallel cracks at the BC peak is not possible due to its high tensile strength [49] at low temperature.

Since out-of-plane tensile stresses at the BC/TGO interface at the end of cooling are higher than those at the TGO/TBC interface, delamination cracks are more likely to form at the BC/TGO interface if both interface have the same adhesive strength. Moreover, once the interface is cracked, the strain energy release will be available to drive propagation of existing TBC and TGO cracks. The above predictions of possible parallel crack formations at different stages of a thermal cycle based on radial stresses within the system (Fig. 6.17), can be schematised as Fig. 6.18.

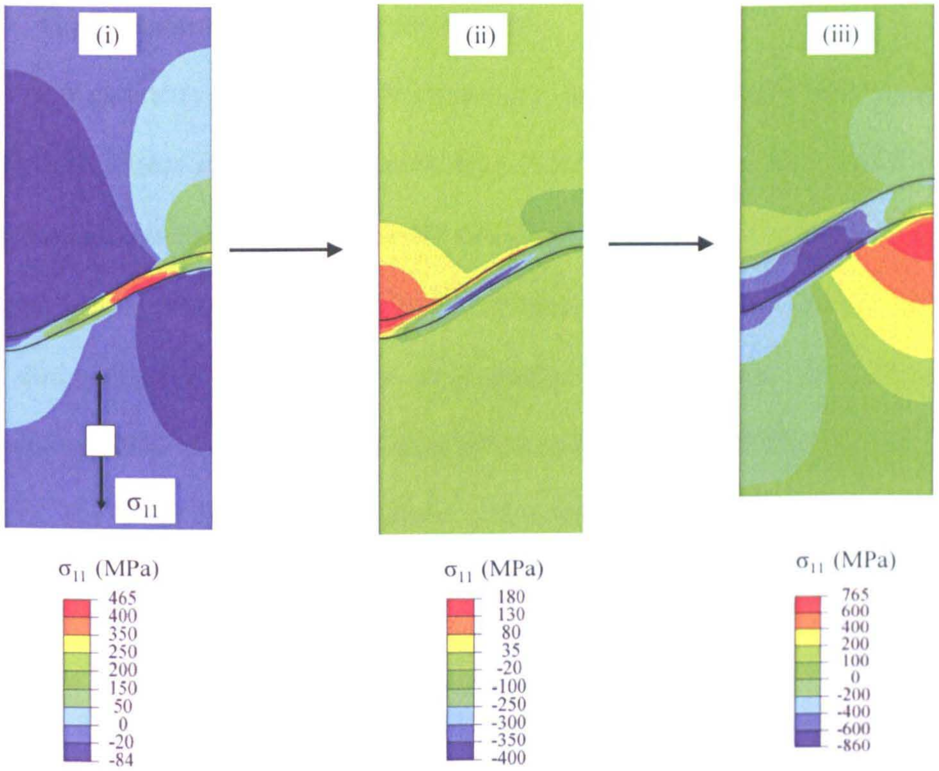

**Fig. 6.17: Through thickness stress state ($\sigma_{11}$) within the TBC system with axisymmetric TGO interface at (i) at the end of heating (ii) after heating at 1000°C for 13h (iii) at 20°C after heating at 1000°C for 90h**

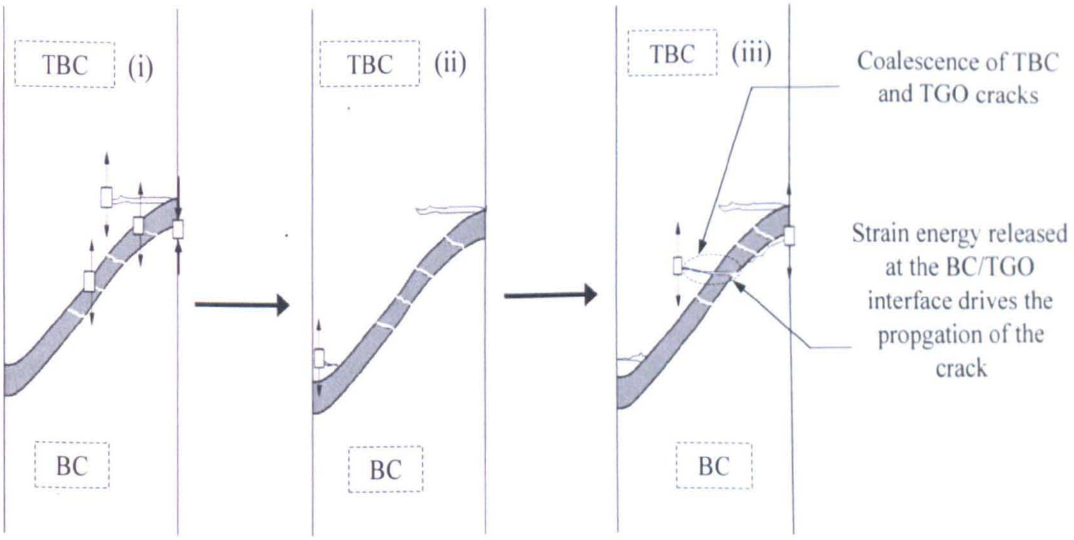

**Fig. 6.18: Stages of predicted crack growths within the TBC system with axisymmetric TGO interface relating to stress states from Fig. 6.17 (Note: Aspect ratio of the TGO interface is exaggerated)**

### 6.9.2 Three-dimensional coating interfaces

For geometry set (ii) from Section 6.2.2, heating up causes concentration of tensile radial stress near the TBC peak leading to the formation of parallel cracks. Moreover, the reversal of stresses at the peak and valley TBC stresses is slower for the aged system as described in Section 6.7. Hence, parallel cracks formed at the TBC peak during heat-up will continue to propagate, during steady state. Therefore, premature spallation of the TBC during steady state is expected for thermally aged systems. The possible premature failure is demonstrated in Fig. 6.19. On the other hand, because of high TGO growth stresses for as-sprayed systems, higher out of plane tensile stresses resulted near TBC valley at the end of steady state and cooling. However, crack propagation towards TBC peak is not possible because of high compressive stresses, and complete spallation is not expected.

For the oxide loop model, parallel cracks at the peak and hill regions (region between peak and flat interface) of the TBC and the TGO and delamination cracks at the TBC/TGO interface are expected during heat-up due to concentration of out-of-plane tensile stresses (Fig. 6.16). On the other hand, BC/TGO interface is in compression after heat-up and separation at the interface is not expected. Cracks nucleated at the TBC peak region will continue to propagate due to slow stress reversal for the oxide loop model with thick TGO layer, resulted from prior heat treatment. After cooling, delamination cracks are expected at the BC/TGO interface, due to the high normal tensile stress concentration as shown in Fig. 6.16. Additionally, the TGO is also expected to buckle at the flat interfacial regions due to high concentration of in-plane compressive stresses within the TGO at the end of the thermal cycle. Buckling is favoured especially if there are significant decohesion zones at the interface [131]. For a flat TGO interface shown in Fig. 6.20, the minimum compressive stress, for initiation of buckling failure, is directly proportional to the thickness of the coatings (t) and inversely proportional to the temperature changes (ΔT) and half of the length of interfacial decohesion (b), according to the analytical derivation by Choi et al. [132]. For the current system, large scale buckling is not expected unless there are very long interfacial decohesion zones (in an order of 500μm). Expected crack growth patterns within the oxide loop after heat-up and cooling down are illustrated in Fig. 6.21.

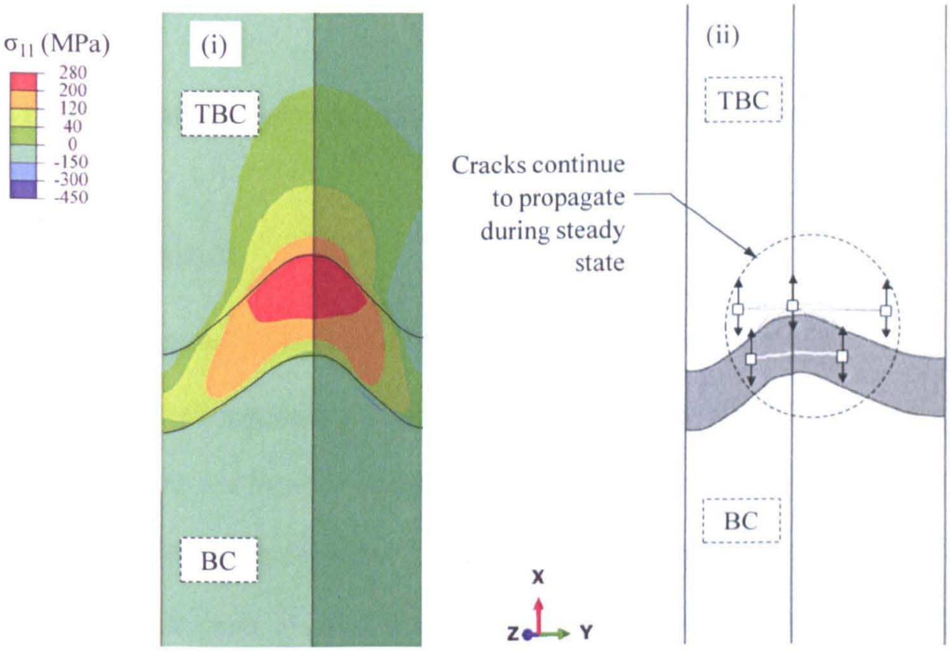

**Fig. 6.19: (i) Out-of-plane stress after 14h of steady state at 1000°C (ii) Parallel TBC cracks and delamination cracks at the TGO/TBC interface that lead to premature TBC spallation**

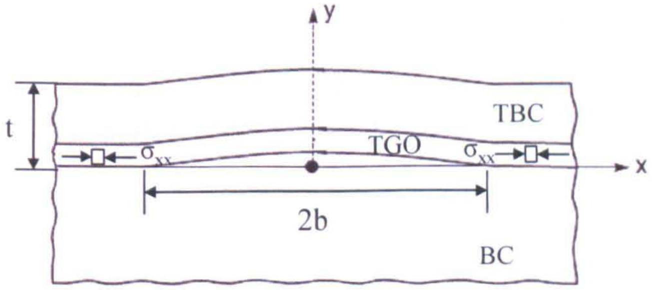

**Fig. 6.20: Schematic diagram of interfacial decohesion at the flat TGO/BC interface**

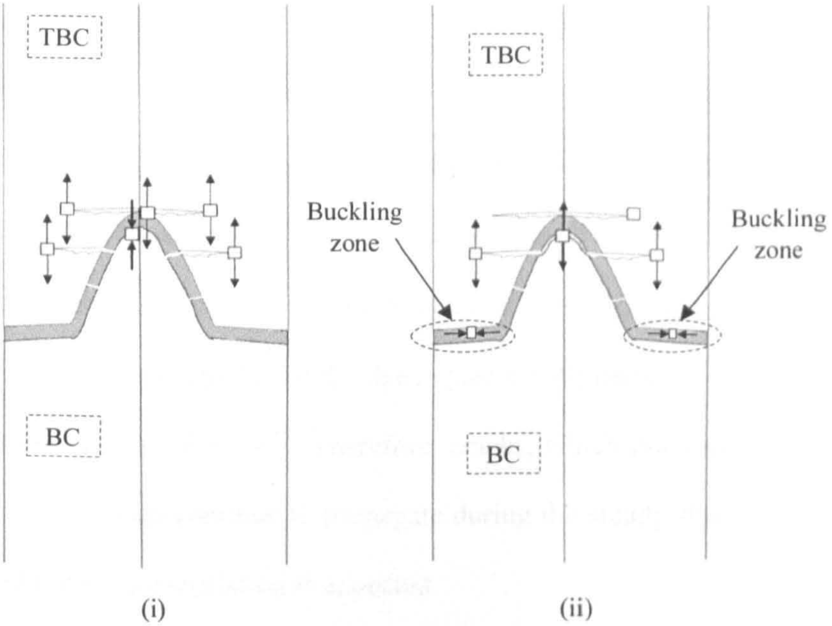

**Fig. 6.21: Predicted crack growth within the oxide loop model i) at the end of heating ii) at the end of cooling**

## 6.10 Conclusions

In this chapter, a framework for 3D stress analysis of the TBC system is presented. A unit cell approach with appropriate boundary conditions was applied to reduce problem size and hence computation time. In order to extract geometries of the TGO interface, 3D coordinates of the TGO surface roughness from tilted SEM images [118] were used. A series of stress analyses was then carried out using extracted 3D profiles of coating asperities. Based on predicted stress development within the systems, possible crack development and failure mechanisms of the system are also predicted. The following conclusions can be made from the analyses carried out.

☐ For identical aspect ratios, maximum compressive and tensile radial stresses at the TBC/TGO interface of the 3D model are around twice the values predicted using the axisymmetric (2D) model. The finding agrees well with analytical results [55], which shows more than 1.5 times increase in tensile radial stress for the spherical interface compared to the cylindrical one.

- ☐ For all geometries of the coating interface chosen in this chapter, tensile stresses are concentrated at the TBC peak and the openings of cracks are expected at the end of heat-up. The stresses near these cracks relax while their propagation towards the valley region is opposed by high compressive stress.
- ☐ After the heat-up stage, stress reversal at the TBC peak and valley regions does not occur rapidly for the aged system with thick initial TGOs compared to the as-sprayed system. Therefore, cracks, which nucleate at the TBC peak during heat-up continue to propagate during the steady state for aged systems and premature spallation is expected.
- ☐ At the end of cooling, tensile delamination cracks are expected to occur at the peak of the TGO/BC interface especially for an oxide loop asperity due to its high aspect ratio. Once the interface has delaminated, strain energy stored during the steady state will be released. If the coalescence of TBC and TGO cracks also occurs in the vicinity of the interfacial crack opening (Fig. 6.18), strain energy release at the interface may drive further crack propagation leading to spallation.
- ☐ Additionally, buckling failure at the TGO interface is also expected at the flat regions of the TGO interface due to the high in-plane compressive stresses, which occur at the end of cooling as observed from the oxide loop model.

The stress analyses, presented in this chapter, based on different unit cells of coating asperities, assume that the coating surface is covered with an infinite tessellation of identical asperities. However, in reality, the coating surface has several irregular microscopic features. Nevertheless, the presented framework, for setting up FE models of TBC systems, with 3D microscopic features, can be applied to future studies utilising different geometries of asperities, to carry out parametric studies.

# Chapter 7

# Modelling crack growth and failure within the TBC systems using cohesive bonds and the extended FE method

## 7.1 Introduction

The growth of parallel cracks within the coating and interfacial delamination cracks can be predicted based on simulated stress distribution within the system. While the prediction is reasonable, it does not take into account stress relaxation as a result of the growth of cracks. In this chapter, the spallation failure of TBC systems for power generation gas turbines will be explored by implementing the mechanisms for modelling the growth of cracks both at the coating interfaces and within the bulk coatings.

Stresses which concentrated around the TGO interface at the end of the thermal cycle have been assumed as the major cause of the spallation of the TBC. Tensile stresses originate from the mismatch strains between layers of the TBC system during the start up or the shutdown of the engines. These stresses, when they exceed the fracture strengths of the TBC layers or the TGO interfaces, create cracks within the bulk layers and weaken the mechanical bonds of the TGO by creating delamination cracks. The fracture toughness of the TGO interfaces and the TBC layers determine the propagation of those cracks and the lifetime of TBC system.

Failures of TBC systems based on cracks created within the TBC and the TGO layers have been investigated experimentally by various researchers [12, 98]. Naumenko et al. [12] observed that failure of the APS TBC system mainly occurs within the TBC layer near the TGO/TBC interface as a significant amount of TBC is still attached to the substrate, after failure, compared to EBPVD systems.

Delamination and spallation failures have been simulated using cohesive bonds with predefined crack paths [68, 70] but the models could not show arbitrary crack propagation within the TBC as the crack paths need to be defined at the pre-processing stage. Although an iterative crack propagation scheme as presented in [72] can be used for modelling arbitrary propagations of cracks, excessive re-meshing around the crack tip is required, and it is therefore computationally expensive especially for 3D models.

In this chapter, the extended FE method (XFEM) is applied to simulate arbitrary crack propagation within the TBC and the TGO while cohesive interfaces are applied at the TGO/TBC interface to investigate the degradation of interface bonding. Furthermore, using XFEM, initial discontinuities within the TBC are also implemented in the model and their influence on TBC spallation is studied.

## 7.2 Geometry and boundary conditions

In the present chapter, initiation and propagation of cracks within the TBC system are modelled when it is cooled down from the steady state temperature (1000°C) to 20°C. The TBC model consists of a nickel based superalloy cylinder with an inner and an outer radius of 3.2mm and 6.2mm respectively. The BC and the TBC with respective thicknesses of 100 μm and 200 μm are coated onto the cylindrical substrate. The dimensions of the TGO interface have been taken as a wavelength of 48μm and an amplitude of 6μm; these values are within the range of the typical TGO interface as measured in [21].

Similar unit cell and boundary conditions to those used in Chapter 4 are applied here. Although generalised plane strain elements (CPEG4R) are more suitable for constructing 2D representation of a 3D coated cylinder with a finite length, the commercially available XFEM enrichment scheme in ABAQUS [67] is not formulated for CPEG4R. Therefore, usage of user defined element (UEL) [67] would be required. For simplicity, only plane strain elements with reduced integration scheme (CPE4R) are used by assuming the cylinder is constrained against axial expansion or contraction.

The TBC system is assumed to be defect-free during the pre-processing (assembly) stage for the first part of analysis. Initial TBC cracks were implemented in the second part of the analysis in order to understand their influences on spallation as depicted in Fig. 7.1. Two types of APS TBC cracks were considered for implementation at the pre-processing stage: cracks which originate from the intersplat boundaries, which are parallel to the TGO interface (parallel cracks), and cracks that are vertical to the interface (segmented cracks). The formation of cracks is driven by out-of-plane and in-plane tensile stresses of the TBC systems under thermal cyclic load. Moreover, since higher strain tolerance of the TBC can be achieved with segmented cracks, they are deliberately introduced to the system using proprietary spraying processes such as solution-precursor plasma sprayed process (SPPS) as explained in [133]. When initial XFEM cracks are inserted at the pre-processing stage, it is not possible to predefine the damage parameter (which will be explained in Section 7.4) of the crack plane. Hence, it is always taken as unity for initial crack plane at the start of the processing stage.

Various researchers [23, 134, 135] have explored the relationship between the failure of the TBC system and the thickness of the TGO layer. To observe the crack growth related to TGO thickness, parametric studies with different TGO thicknesses varied from 1 to 4μm were carried out while keeping the same aspect ratio for the sinusoidal TGO interface for initially crack-free model. The TGO thickness, for the model with initial defects, is set up 4μm to simulate the final spallation of the TBC. The thickness is close to critical thickness of the TGO when the spallation occurs [135]. The TBC system is considered to be stress-free at the end of steady state due to stress relaxation within the BC in accordance to the assumptions made by Rösler [136].

XFEM enrichment was applied to the TGO and the TBC layers based on the principal stress criterion. The adhesion between the TGO and the TBC layer and subsequent degradation of the interface from interfacial crack opening is modelled by using the cohesive surface interaction method [67] (CIM). The CIM is only applied to the TGO/TBC interface since it has been shown experimentally [12] that spallation of the TBC in the vicinity of the TGO is more common for APS TBCs.

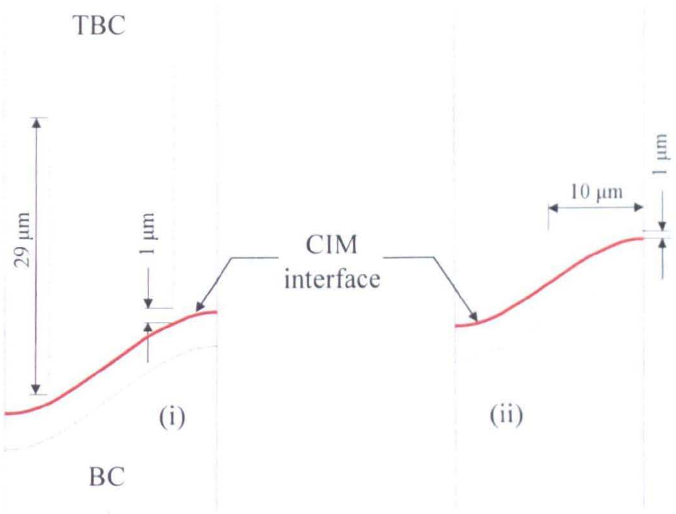

**Fig. 7.1: (i) Segmented and (ii) parallel initial cracks within the TBC (CIM interface are shown in red)**

## 7.3 Fracture mechanics based XFEM enrichment

Until recently, techniques for fracture mechanics available within ABAQUS (Virtual crack closure, cohesive method etc.) only allowed crack growth along the predefined path following the element boundaries. This has limited the modelling of arbitrary crack growths within the model. Moreover, expensive mesh optimisation is required at the tip of the crack during its propagation. By using a displacement interpolation scheme [67] as shown in Eq (7.1), XFEM can model initiation of cracks without specifying priori crack paths. It was introduced by Belytschko and Black [137] by further enhancing the partition of unity method introduced by Melenk and Babuska [138].

$$u^h(x) = \sum_{I \in N} N_I(x) \left[ u_I + [\operatorname{sgn}(x)\, a_I]_{I \in N_H} + \left[ \sum_{\alpha=1}^{N_{tip}} F_\alpha(x)\, b_I^\alpha \right]_{I \in N_{tip}} \right] \tag{7.1}$$

where $N_I(x)$ is a conventional shape function of elements regardless of whether XFEM enrichment is used. $u_I$ represents degree of freedom (d.o.f) of nodes for the FE calculations of ordinary isoparametric elements while $a_I$ and $b_I^{\alpha}$ are enriched d.o.f for implementation of discontinuities within the elements as illustrated in Fig. 7.2. $a_I$ represents additional d.o.f created by the crack face.

The Heaviside function, H(x), accounts for the displacement jump across the crack face. The sign function, sgn(x), can be related to H(x) using Eq (7.2). H(x) is determined by the distance between the integration point (z), and its nearest projection on the crack face is ($z^*$) as illustrated in Fig. 7.2. H(x) can be expressed as shown in Eq (7.3).

$$\operatorname{sgn}(x) = 2H(x) - 1 \tag{7.2}$$

$$\mathrm{H(x)} = \begin{bmatrix} 1 & \text{if } (\mathrm{z}-\mathrm{z}^*).\mathrm{n} \geq 0 \\ -1 & \text{otherwise} \end{bmatrix} \tag{7.3}$$

For stationary cracks, additional d.o.f $b_I^{\alpha}$ are applied to take into account of the crack tip singularity. As demonstrated in [139], the d.o.f related to the crack tip singularity in polar coordinates (p or crack propagation length and θ or crack propagation direction) can be derived from crack tip asymptotic displacement fields shown in Eq (7.4). The d.o.f function $F_\alpha(x)$ related to the crack tip singularity [67] can be expressed in Eq (7.5).

$$\begin{aligned} u_x &= \frac{1}{\mu}\sqrt{\frac{p}{2\pi}}\left[K_I \cos\frac{\theta}{2}(k - \cos\theta) + K_{II} \sin\frac{\theta}{2}(k + \cos\theta + 2)\right] \\ u_y &= \frac{1}{\mu}\sqrt{\frac{p}{2\pi}}\left[K_I \sin\frac{\theta}{2}(k - \cos\theta) - K_{II} \cos\frac{\theta}{2}(k + \cos\theta - 2)\right] \end{aligned} \tag{7.4}$$

where μ is shear modulus, $K_I$ and $K_{II}$ are stress intensity factors and k is a material constant

$$F_\alpha(x) = \left\{\sqrt{p}\sin\theta/2, \sqrt{p}\cos\theta/2, \sqrt{p}\sin\theta\sin\theta/2, \sqrt{p}\sin\theta\cos\theta/2\right\} \tag{7.5}$$

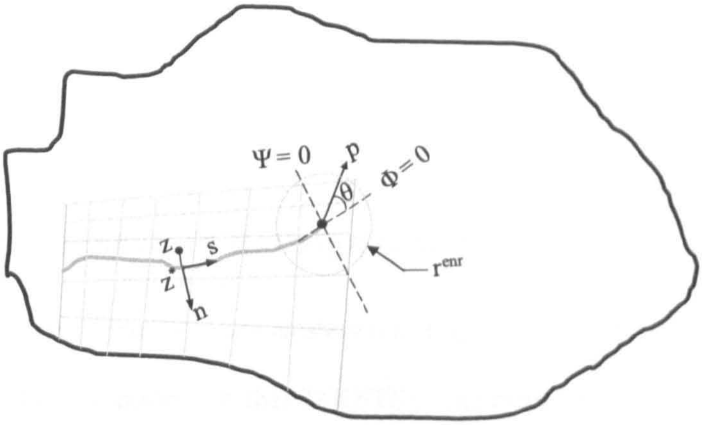

**Fig. 7.2: Enriched d.o.f for crack face and crack tip and level-set functions ($\Phi$, $\Psi$) for crack location**

To save computation time, enrichments in d.o.f for discontinuities are applied to selected nodes within the system. The nodes are selected using Ø and $\Psi$ functions (Fig. 7.2). When both functions are zero, crack tip enrichments are applied for the node set, $N_{tip}$ (Eq (7.1)), within the enrichment radius ($r^{enr}$). For nodes in the node set $N_H$ (Eq (7.1)), which includes nodes of the elements within which the crack is enclosed, is enriched with the sign function, sgn (x) from Eq (7.2).

For propagating cracks, the traction-separation model (which will be explained in Section 7.4) is applied using phantom nodes. Phantom nodes are superimposed onto the nodes of the elements through which the crack has passed. These phantom nodes at opposite sides of the crack will be separated causing opening of the crack face as the loading is applied. The magnitude of the separation is governed by the fracture toughness of the material. For propagating cracks, the crack tip asymptotic singularity [Eq (7.4)] is not considered. Therefore, it is assumed that a crack propagates fully through the element once it is initiated within the element.

In terms of engineering applications, XFEM can be used to predict arbitrary solution-dependent crack initiation and propagation within structures under loading. It can be used in parallel with adhesive failure modelled by cohesive methods. Here, it is used to model crack propagation within the TBC and TGO in conjunction with the CIM model for the propagation of a delaminating crack at the TGO/TBC interface.

## 7.4 Traction-separation damage model

A linear traction-separation law as shown in Fig. 7.3 was applied as a damage model for both cohesive nodes of the TGO/TBC interface and XFEM enriched elements. k from Fig. 7.3 is cohesive stiffness and it is the ratio of traction stress ($\underline{T}$) and separation ($\underline{\delta}$) at which damage initiation occurs. Damage or crack initiation can be determined by either a critical principal stress or a critical separation criterion. Stresses at the interface or within the bulk materials will be reduced while the cohesive interface or the crack plane is separating during degradation. If unloading is applied at point Y (refer to Fig. 7.3), the cohesive stiffness is reduced to (1-D)*k for the next loading step. D is the damage parameter and it can be defined as shown in Eq (7.6).

$$D = \frac{\delta_z(\delta_y - \underline{\delta})}{\delta_y(\delta_z - \underline{\delta})} \qquad (7.6)$$

Final failure occurs when the strain energy release rate from the crack propagation is higher than the critical strain energy release rate ($G_C$). The strain energy release rate can be calculated as the area under the traction-separation graph (Fig. 7.3). The type of failure largely depends on the value of $G_C$; high $G_C$ means ductile failure and low $G_C$ means brittle failure.

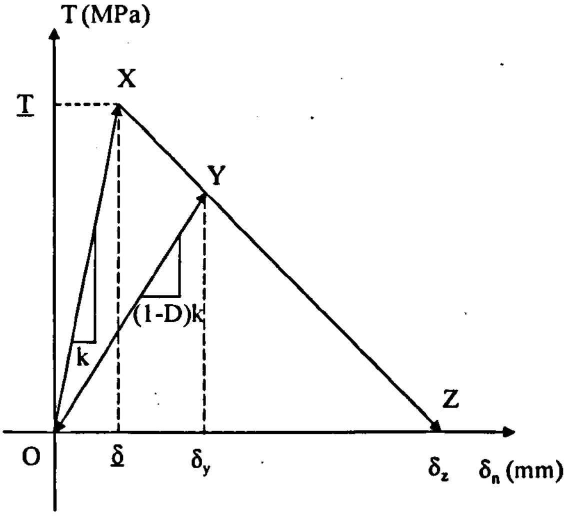

**Fig. 7.3: Linear traction-separation law**

The critical crack opening ($\delta_z$) depends on the fracture stress ($\underline{T}$) and fracture toughness ($K_C$) as shown in Eq (7.7).

$$\delta_z = \frac{2K_C^2}{E\underline{T}} \tag{7.7}$$

If a shear mode of failure is taken into account, the effective critical separation ($\delta_{eff}$) can be expressed using normal crack opening ($\delta_n$) and tangential crack opening ($\delta_{slip}$) as shown in Eq (7.8). For mixed mode failure, a quadratic stress criterion can be used for damage initiation and the crack nucleates when the parameter (f) as shown in Eq (7.9) becomes unity.

$$\delta_{eff} = \sqrt{\delta_n^2 + \delta_{slip}^2} \tag{7.8}$$

$$f = \left(\frac{\langle\sigma\rangle}{\sigma_c}\right)^2 + \left(\frac{\tau}{\tau_c}\right)^2 \tag{7.9}$$

where σ and τ are nodal direct and shear stresses and $\sigma_c$ and $\tau_c$ are critical direct and shear stresses. The Macaulay bracket means only tensile direct stress is considered for crack initiation.

If $\tan\beta = \frac{\tau}{\langle\sigma\rangle}$, then the effective traction stress for the damage initiation can be described as in Eq (7.10). β is phase angle for mixed mode failure.

$$\underline{T} = \sigma_C \left( \cos^2\beta + \frac{\sigma_C^2}{\tau_C^2} \sin^2\beta \right)^{-0.5} \tag{7.10}$$

The equivalent critical strain energy release rate for mixed mode damage evolution can be calculated by different methods [67]; a B-K law for the effective critical strain energy release rate ($G_{eq}$) is, as an example, shown in Eq (7.11).

$$G_{eq} = G_{IC} + (G_{IIC} - G_{IC}) \left( \frac{G_{II} + G_{III}}{G_I + G_{II} + G_{III}} \right)^n \tag{7.11}$$

where $G_{IC}$ and $G_{IIC}$ are critical strain energy release rates of two modes of failure and n is a constant power, which is usually determined empirically.

Currently, it is assumed that the critical stress for the initiation and evolution parameters of damage are independent of failure modes. The experimental data for the shear strengths and mode dependent fracture toughness of coatings are placeholders to allow implementation of mixed-mode failure.

## 7.5 Material properties

### 7.5.1.1 Elastic and thermal properties

Due to limitations of ABAQUS, XFEM cannot simulate crack propagation for the system with time dependent material properties. Therefore, the coating layers are considered to be elastic during cooling down. The assumption is reasonable since the cooling time for the TBC system is usually less than one hour and hence creep deformation during the period can be ignored. Elastic and thermal properties for the substrate, the TGO and the coating layers are tabulated in Table 7.1.

**Table 7.1: Elastic properties and CTEs of coatings and substrate**

| Temperature (°C) | Substrate [82] | | | TBC [40, 83] | | | TGO [17] | | | BC [83] | | |
|---|---|---|---|---|---|---|---|---|---|---|---|---|
| | E (GPa) | v | CTE, K$^{1}$.10$^{6}$ | E (GPa) | v | CTE, K$^{1}$.10$^{6}$ | E (GPa) | v | CTE, K$^{1}$.10$^{6}$ | E (GPa) | v | CTE, K$^{1}$.10$^{6}$ |
| 20 | - | - | - | 120 | 0.18 | 10.0 | 400 | 0.23 | 6.62 | 202.9 | 0.27 | 20. |
| 24 | 206 | 0.28 | 11.23 | - | - | - | - | - | - | | | |
| 50 | - | - | - | - | - | - | - | - | - | 202.7 | 0.27 | 50. |
| 93 | 195.1 | 0.27 | 11.97 | - | - | - | - | - | - | | | |
| 200 | - | - | - | - | - | - | 390 | 0.23 | - | 199.92 | 0.27 | 200. |
| 204 | 190.3 | 0.27 | 13.23 | - | - | - | - | - | - | | | |
| 316 | 184.8 | 0.28 | 14.4 | - | - | - | - | - | - | | | |
| 400 | - | - | - | - | - | - | 380 | 0.24 | - | | | |
| 500 | - | - | - | - | - | - | - | - | - | 184.8 | 0.27 | 500. |
| 538 | 175.1 | 0.3 | 16.2 | - | - | - | - | - | - | | | |
| 600 | - | - | - | - | - | - | 370 | 0.24 | - | | | |
| 700 | - | - | - | - | - | - | - | - | - | 167.72 | 0.27 | 700. |
| 760 | 157 | 0.3 | - | - | - | - | - | - | - | | | |
| 800 | - | - | 18.38 | - | - | - | 355 | 0.25 | - | | | |
| 871 | 151 | 0.29 | - | - | - | - | - | - | - | | | |
| 982 | 140 | 0.3 | 19.42 | - | - | - | - | - | - | | | |
| 1000 | - | - | - | - | - | - | 325 | 0.25 | - | 131.6 | 0.27 | 1000. |
| 1200 | - | - | - | - | - | - | - | - | 8.7 | 100.52 | 0.27 | 1200. |

### 7.5.2 Tensile strengths of coatings

To apply the traction-separation law, maximum stress and cohesive interface stiffness for damage initiation and critical strain energy release rate for damage evolution and failure have to be defined. Tensile strength was taken as the maximum stress for damage initiation by assuming that both TGO and TBC are brittle with no yielding at the point of failure. Tensile strength of the TGO is 260MPa as reported by Munro [17]. The strength does not vary significantly for the temperature range between 20°C and 1000°C although it falls linearly to 10MPa between 1000°C and 1400°C [17]. The fracture stress of the YSZ TBC is largely dependent on yttria content as demonstrated in [128]. It was observed that at high concentration of yttria, the tensile strength is almost equal to the flexural strength. Since the temperature dependent tensile strength values are rarely reported, the temperature dependent flexural strengths of YSZ with 6.5 mol% of yttria in [89] are taken as the fracture strength of the TBC. The strength of the sintered YSZ varies from 150 MPa to 50MPa between 20°C to 1000°C.

### 7.5.3 Interfacial tensile strength

Coating failure is strongly dependent on the adhesion strength of the interface under tensile loading. Various techniques have been proposed to obtain the tensile adhesion strength of the TBC. The most common standardised methods are DIN 50160 and ASTM D7234-05. They are both tensile pull tests and they have been applied in [99, 129]. A diagram for the experiment, according to DIN 50160 standard, is illustrated in Fig. 7.4. For the pull test, the metal is sprayed with the coating for which adhesion strength to be measured. Another metal die is usually bonded to the coating using an epoxy based adhesive. The specimen is then subjected to an increasing load in a testing machine until the coating delaminates. The applied load at the failure and the bonded area are used to calculate the bond strength of the coating.

The pull test is simple to set up and the bond strength is easily obtained. However, it is doubtful that the measured bond strength represents the actual adhesion strength at the coating interface as the measured values [99, 140] are much lower than predicted mismatch stress at the interface. To obtain reliable strength from a pull test, the bonding strength of the epoxy has to be stronger than that of the coating in order to avoid failure at the epoxy interface. Moreover, because of the porous nature of APS TBC, the adhesive can seep into the coating and this might alter the strength of the coating/metal interface. Finally, at the point of coating failure, the ratio of failure load to coated area is taken as the bond strength without considering the area of any initial flaws. Therefore, the predicted bond strengths from pull tests such as the one in [99] are much lower than maximum out-of-plane tensile stresses at the interface simulated using FE models. An alternative method, which is based on experimental spallation tests and the FE method, is proposed as below.

The alternative method of determining the interface strength assumes that the coating delaminates at the end of cooling due to mismatch stress. Experimentally, the critical thermal load for delamination can be obtained by applying different thermal cycles to the TBC system. According to data from spallation tests carried out within the consortium [102], the coating delaminates at the end of the cooling stage after heating at 1000°C for 1050h. When the same thermal cycle was applied to the FE model of the TBC system from [105], the maximum tensile out-of-plane stress at the TGO/TBC interface is found to be 196.5MPa, at the end of cooling. This maximum stress is taken as the delamination strength of the interface.

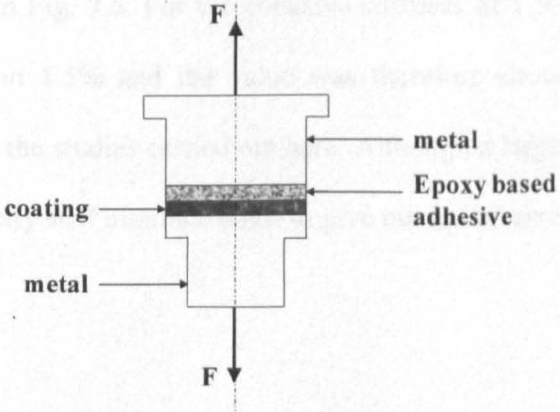

Fig. 7.4: Adhesion tensile pull test (DIN 50160)

### 7.5.4 Interfacial cohesive stiffness

Unlike physical properties (e.g. tensile strength or toughness of materials), the cohesive stiffness is the assumed property without a direct physical interpretation, which is used to model the behaviour of the interface before the damage initiates. Some researchers [141] have suggested to use the stiffness which is equal to the ratio of the modulus of the adhesive to its thickness. However, the physical thickness of the adhesive has no relevance to the case of a cohesive bond as in the model applied here. Therefore, a sensitivity study was carried out to obtain a useful interface cohesive stiffness.

The objective of the study is to obtain a cohesive stiffness which gives the values of radial stress at the cohesive interface, within the linear elastic region, similar to the stresses predicted from the model with completely tied interfaces. The value of traction stress for damage initiation at the TGO/TBC interface is assumed to be 3 GPa to ensure the mismatch stresses will not initiate delamination cracks and affect the stress distribution. Cohesive stiffnesses ranging from $1.5\times10^{8}$ to $1.5\times10^{11}$ MPa/mm were applied at the TGO/TBC interface within the sensitivity study.

Maximum percentages of differences between radial tensile stresses at the interface compared to the model with the tied interface are plotted for different cohesive stiffnesses in Fig. 7.5. For the cohesive stiffness of $1.5\times10^{11}$ MPa/mm, the difference is less than 1.5% and the value was therefore chosen as the cohesive interface stiffness for the studies carried out here. Although a larger cohesive stiffness can be chosen, an overly stiff interface tends to give numerical errors.

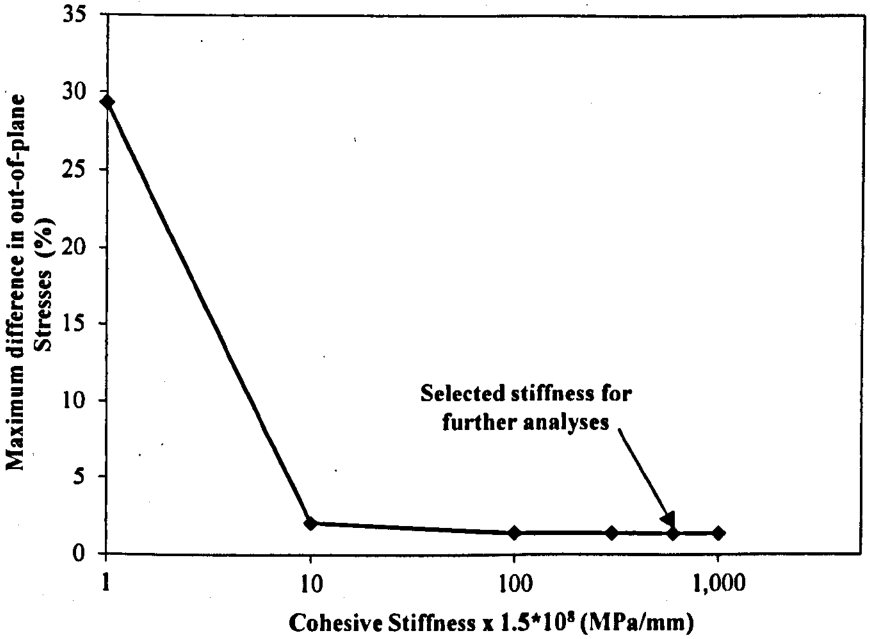

**Fig. 7.5: Maximum percentages of difference in tensile stresses at the interface with different cohesive stiffness compared to the model with the tied interface**

### 7.5.5 Critical strain energies and fracture toughness

The critical strain energy release rate can be related to the bulk/interfacial fracture toughness ($K_I$) and modulus (E) as $G_C = K_I^2/E$ for simple Mode I failure. For the interface, the apparent modulus of the interface acquired from the load-depth indentation curve according to ISO 14577 can be used as shown in [142]. The fracture toughness values for a TGO film (thickness = 0.38μm) and bulk TBC (thickness = 1mm) were measured by Stollberg, et al. [143] using nanoindentation method. The corresponding values are 2.22±0.31 and 1.3±0.29 $MPa\sqrt{m}$. Yamazaki, et.al [142] investigated the TGO/TBC interface toughness and it estimated the value to be around 3.5 $MPa\sqrt{m}$.

## 7.6 Results and discussion

### 7.6.1 Parametric study of influence of TGO thickness on crack growth within the bulk coatings

For initially defect-free systems, principal stresses within the TBC systems for different TGO thicknesses, after cooling down from 1000°C to 20°C, are demonstrated in Fig. 7.6. For thicker TGOs (3 μm and 4 μm), tensile principal stresses are also concentrated at the peak of the TGO and the flanks of the TBC at the end of cooling. These stresses are higher than tensile strengths of coatings and can cause initiation of further cracks. However, in this case, new cracks are not generated due to the limitations in the XFEM enrichment within ABAQUS [67]. Although XFEM allows initiation of multiple cracks, the damage initiation criteria at integration points of multiple elements have to be satisfied at the same time increment step. Otherwise formation of new cracks is not allowed in the vicinity of the existing crack until the complete separation of the existing crack face occurs. As seen from damage parameter contours for XFEM cracks shown in Fig. 7.7, the existing cracks have some regions with damage parameters less than 1. This prevents the initiation of new cracks near the regions of the existing cracks.

Both TBC and TGO cracks are initiated near the peak of the interface for every model. From Fig. 7.6 & Fig. 7.7, it can be seen that the changes in crack propagation direction for the TBC cracks are not as significant as the changes in direction for TGO cracks. The former cracks are growing towards the valley of the TBC while the latter cracks are growing towards the TGO/TBC interface. The strong relationship between coating crack length and the TGO thickness is observed from Fig. 7.7. For a TGO thicker than 2 μm, the TBC crack propagates completely through the periodicity plane AB of the model. Therefore, coalescence of cracks within TBC and the spallation of the TBC are expected when the TGO is getting thicker due to ageing of the system at high temperature.

### 7.6.2 Parametric study of influence of TGO thickness on crack growth at the TGO/TBC interface

The status of a delamination crack at the interface can be checked by referring to the contact opening variable. For mixed-mode failure, the effective opening ($\delta_{eff}$) can be calculated from direct (COPEN, $\delta_n$) and shear crack opening (CSLIP, $\delta_{slip}$) variables as shown in Eq (7.8). The crack opens when $\delta_n$ or $\delta_{slip}$ is higher than $\underline{\delta}$ and the complete failure occurs when $\delta_{eff}$ reaches the critical separation ($\delta_z$) as shown in Fig. 7.3. For this case, ($\underline{\delta}$) and $\delta_z$ are $1.31 \times 10^{-09}$ mm and $1.597 \times 10^{-3}$ mm respectively. $\delta_n$ and effective separations along the TGO/TBC interfaces are plotted for systems with different TGO thicknesses as shown in Fig. 7.8 & Fig. 7.9 respectively.

Generally, tangential separations are around half an order to an order of magnitude higher than normal separations (Fig. 7.8 & Fig. 7.9). This indicates that it is necessary to incorporate the shear failure mode into the definition of interfacial delamination. None of the models shows a completely delaminated interface while contact separations in both directions are higher for thicker TGOs. However, the separations for the model with 4μm TGO are lower compared to the values from the system with 3μm TGO. The reason might be higher stress relaxation at the interface for 4μm TGO model due to the formation of multiple cracks as shown in Fig. 7.7. The trend of higher contact separation due to increase in the TGO thickness indicates that the delamination failure at the TGO/TBC interface is favoured when the TGO becomes thicker.

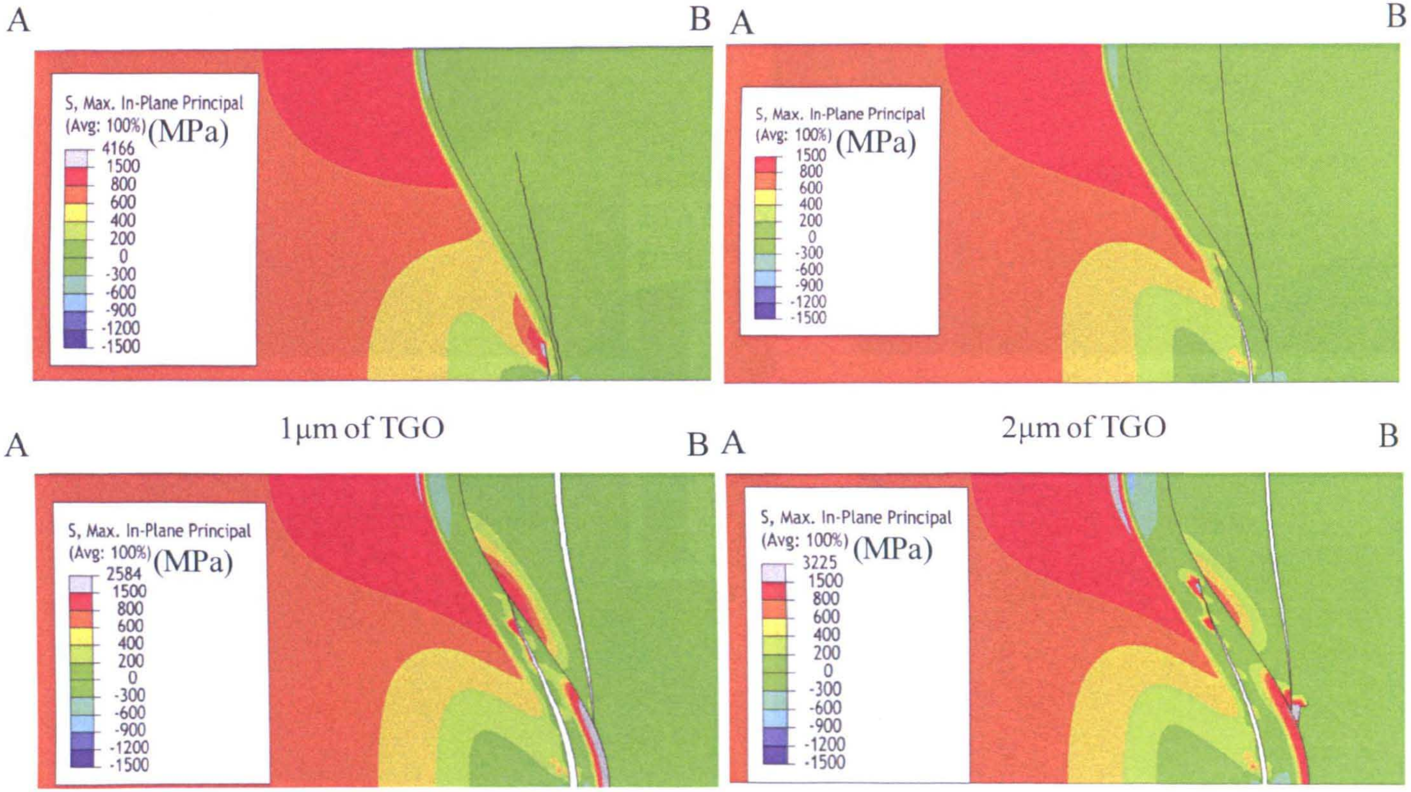

1μm of TGO

2μm of TGO

3μm of TGO

4μm of TGO

**Fig. 7.6: Radial stresses for the models with different TGO thicknesses**

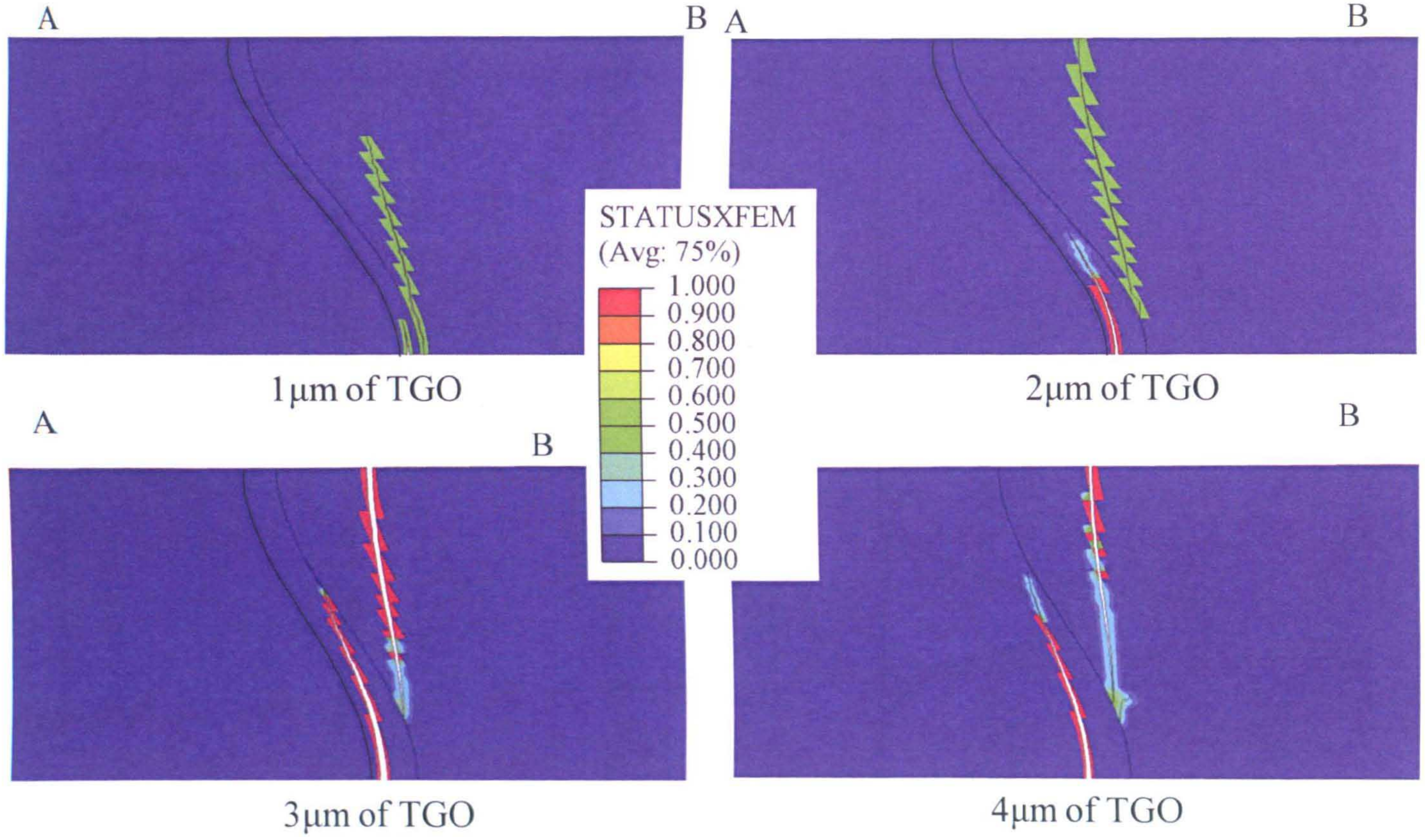

1μm of TGO

2μm of TGO

3μm of TGO

4μm of TGO

**Fig. 7.7: Status of XFEM elements for the models with different TGO thicknesses (The value is between 1 and 0; 1 means the element is completely cracked with no traction stress across the cracked surfaces)**

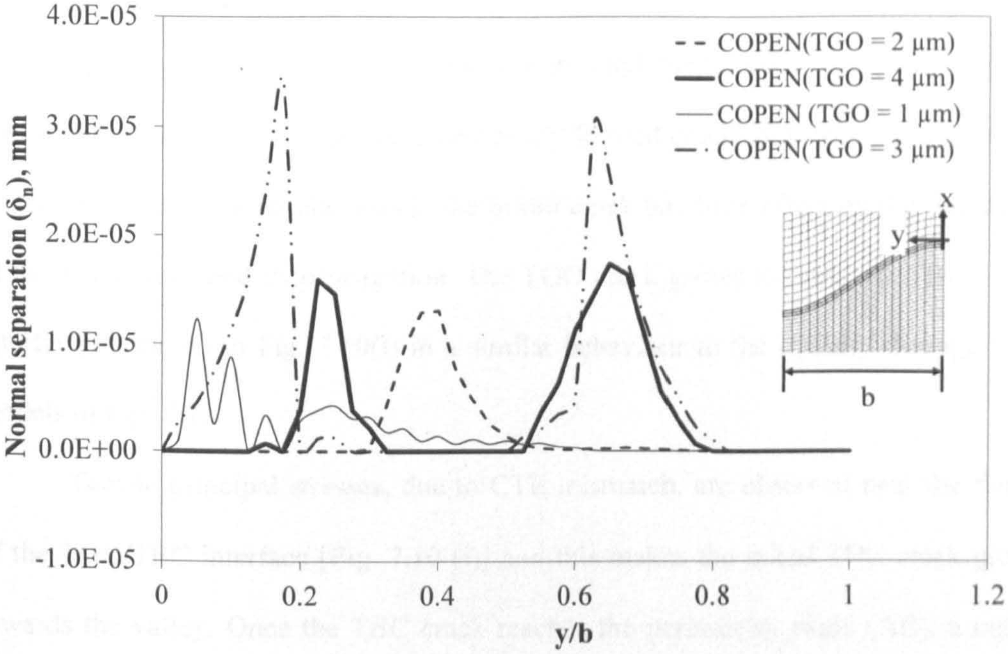

**Fig. 7.8: Normal separations at the TGO/TBC interface for the models with different TGO thicknesses**

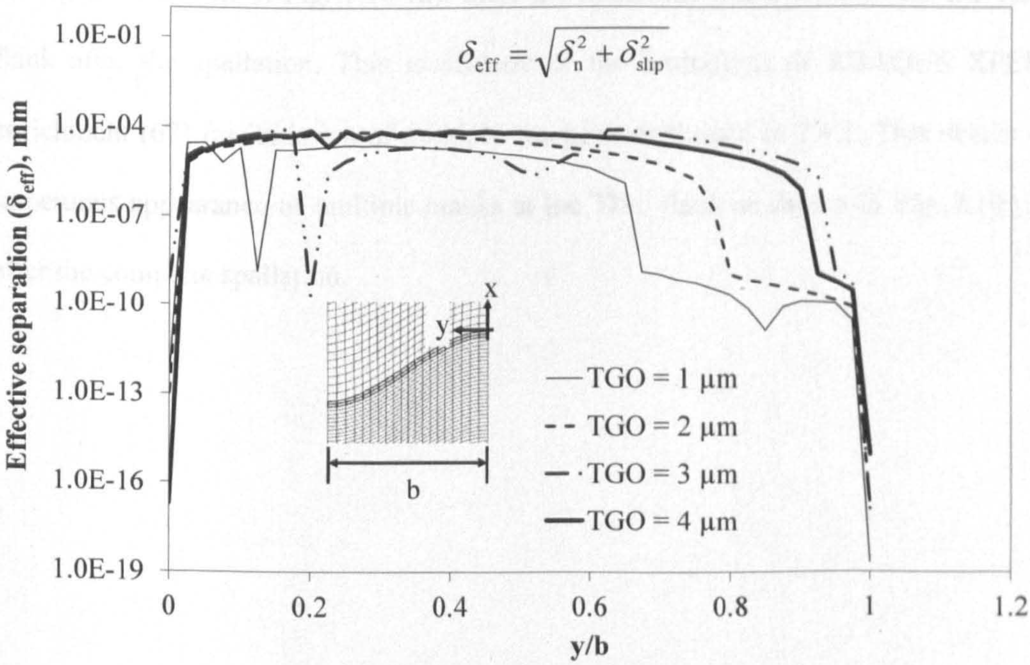

**Fig. 7.9: Effective separations at the TGO/TBC interface for the models with different TGO thicknesses**

### 7.6.3 Influence of initial parallel TBC cracks on crack on crack growth within the TBC system

As shown in Fig. 7.1, initial cracks were implemented with the TBC to study propagations of these existing cracks and newly formed cracks during cooling. For the system with an initial parallel crack, the initial crack has little effect on the initiation of the TGO crack and its propagation. The TGO crack grows towards the TBC/TGO interface as shown in Fig. 7.10(i) in a similar behaviour to the initially damage-free models of Fig. 7.7.

Tensile principal stresses, due to CTE mismatch, are observed near the flank of the TGO/TBC interface [Fig. 7.10 (i)] and this makes the initial TBC crack grow towards the valley. Once the TBC crack reaches the periodicity plane (AB), a rapid separation of the TBC cracked planes occurs according to a linear traction separation law. Principal stress distribution at the complete spallation is demonstrated in Fig. 7.10 (ii). As shown in Fig. 7.10 (ii), there are numerous micro-cracks near the TBC flank after the spallation. This is because of the limitations of ABAQUS XFEM enrichment [67] for initiation of multiple cracks as explained in 7.4.1. This results in impetuous appearance of multiple cracks at the TBC flank as shown in Fig. 7.10 (ii) after the complete spallation.

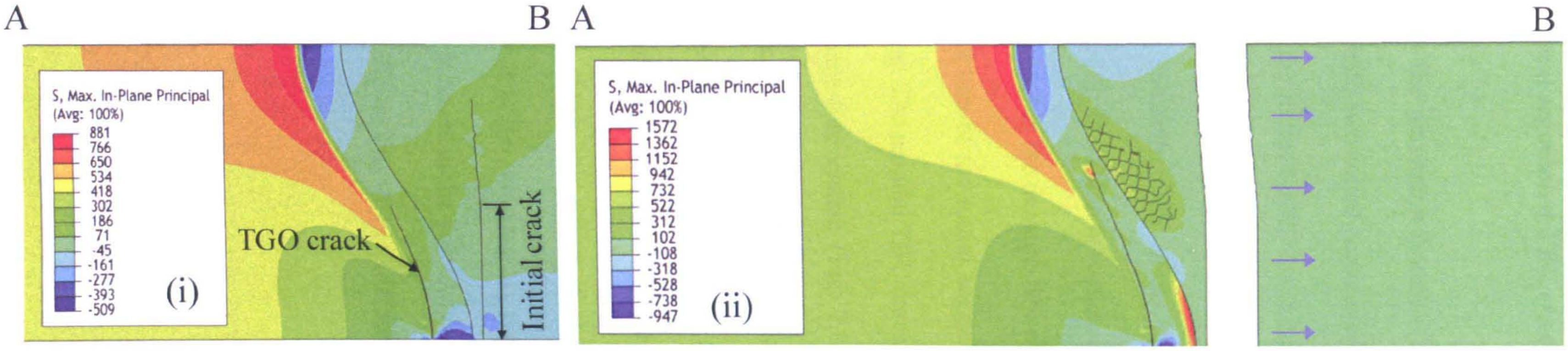

**Fig. 7.10: i) Tensile principal stresses at the tips of growing TBC and TGO cracks ii) complete TBC spallation of the system with an initial parallel TBC crack after cooling to 20°C from 1000°C**

### 7.6.4 Influence of initial segmented TBC cracks on crack growth within the TBC system

Fig. 7.11 shows the maximum principal stresses and cracks within the bulk coating for the system with two initial segmented cracks. When cooling is applied to the system, opening of the initial cracks is not expected to occur. This is because the in-plane mismatch stress within the TBC is compressive due to its lower CTE compared to BC and substrate. The initial cracks also have no effect on the propagation direction of a TGO crack, which is growing towards the TGO/TBC interface in a similar manner to the damage-free models (Fig. 7.6).

In the vicinity of one of the initial segmented cracks, two parallel cracks are developed during cooling. The parallel TBC cracks are significantly shorter than those within an initially damage-free system (Fig. 7.7). One of the parallel cracks away from the TGO interface stops growing as it reaches the crack surface of the initial segmented cracks while another parallel crack penetrates the TBC/TGO interface. This penetration is expected to weaken the interfacial bond by initiating the interface separation. In order to check this effect at the TBC/TGO interface, normal and effective contact openings at the interface are plotted as shown in Fig. 7.12. Contact separation significantly increase at the point where one of the parallel crack penetrates the interface (y/b = 0.72 in Fig. 7.12). At that point, the delamination crack is expected to nucleate.

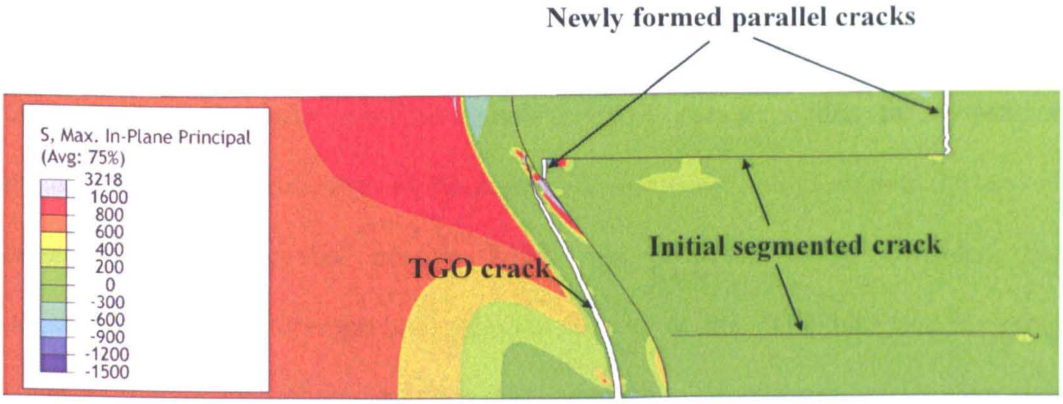

**Fig. 7.11: XFEM cracks within the TBC systems with initial segmented cracks after cooling to 20°C from 1000°C (4μm TGO)**

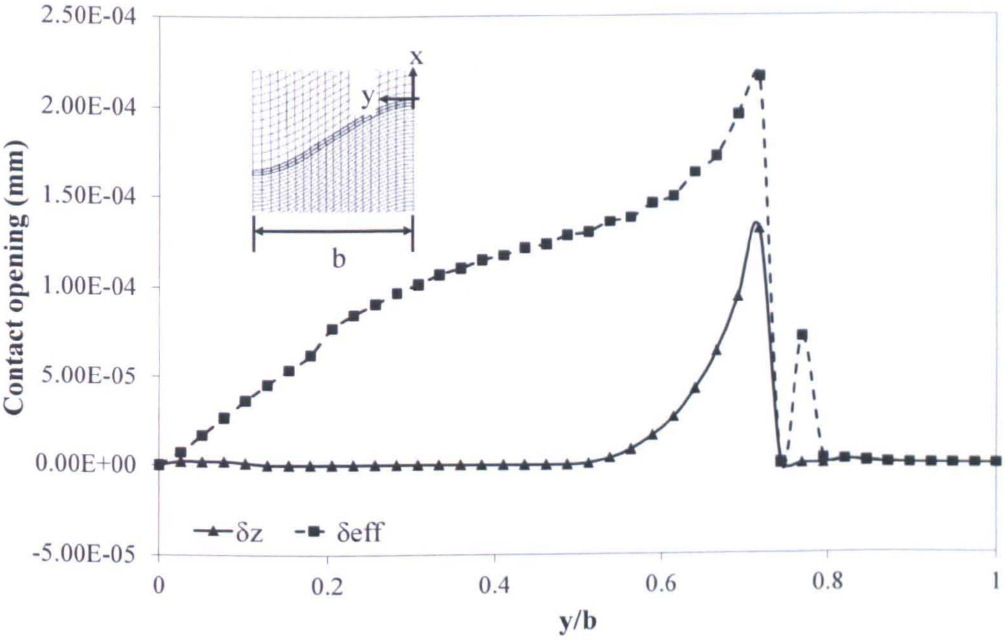

**Fig. 7.12: Normal and effective contact openings at the TGO/TBC interface for the system with initial segmented cracks within the TBC**

## 7.7 Conclusions

The present chapter describes a method of predicting the failure of the TBC system by using a XFEM based fracture mechanics approach. This is radically different from the usual prediction from residual stresses within the system or prediction using the cohesive interface fracture mechanics based models. Instead of assuming completely tied coating layers, the proposed model considers the degradation in bond strength and adhesive failures at the TGO interface by using cohesive surface modelling. Initiation and propagation of arbitrary cracks were also modelled using XFEM. Two sets of parametric study were carried out; the first study concentrates on the effects TGO thicknesses, whereas the second study considers effects of initial TBC cracks on the propagations of cracks at the TGO/TBC interface, and within the TGO and the TBC. The conclusions made from these parametric studies are as follows.

- ☐ The thicker the TGO is, the longer the parallel cracks within the TBC and the TGO are. Coalescence of these cracks within the TBC can lead to partial spallation of the TBC.
- ☐ The delamination crack opening at the TGO/TBC interface, as observed from contact openings at the interface, also become higher when TGO becomes thicker.
- ☐ In general, tangential contact separations at the TGO/TBC interface are an order higher than normal separations. It indicates that it is necessary to implement the shear mode of interfacial failure.
- ☐ Inclusion of initial segmented cracks in the TBC increases strain tolerance of the TBC and reduces the risk of spallation as they prevent the propagations of

parallel cracks. As a result, the lengths of the parallel cracks are significantly shorter for the model with initial parallel cracks (Fig. 7.11). This confirms that spraying TBC with a method which creates segmented cracks after deposition (e.g. SPPS), is likely to be beneficial for coating life.

☐ On the other hand, initial parallel micro-cracks within the TBC lead to complete spallation of the TBC and the depositions process has to be optimised to reduce this type of crack.

The algorithm presented in this chapter can be utilised to predict the failure of TBC systems. However, various sets of data (e.g. fracture toughness and interfacial bond strengths) for mixed-mode fracture behaviour of bulk coatings and interfaces are not currently taken into account due to lack of experimental data. Moreover, improvements in XFEM element formulations, instead of the default enrichment scheme within ABAQUS, are required to accommodate time dependent creep deformation during steady state.

# Chapter 8

# Conclusions

## 8.1 Mechanical properties of coatings

Firstly, mechanical properties of the coatings (elastic, creep properties, etc.) were surveyed to set up FE model for TBC systems. This is the continuing effort from Stage I of the Supergen project. The aggregate properties of the BC evaluated using homogenisation techniques [21] from Stage I of the project were benchmarked against surveyed experimental values. Results show differences of less than 10% for both elastic modulus and CTEs. In contrast, differences of several orders of magnitude were observed for creep strain rates of the BC.

Changes in material properties of the TBC due to sintering were implemented using Arrhenius based approaches. It was found that the modulus of TBC is increased by 40% due to sintering at 1000°C for 900h. This means strain tolerance of the TBC is reduced leading to an increase in through-thickness stresses upon cooling, at the TGO/TBC interface, by a factor of two. Increase in tensile through thickness stresses can cause crack nucleation and ultimately spallation of coatings.

The increase in thermal conductivity of the TBC due to sintering was also implemented within the model coupling with a temperature gradient across the TBC.

At the end of sintering for 900h, the difference between the temperature at the TBC surface and that of the TGO interface decreased by a factor of two while TBC surface temperature is fixed throughout the simulation. This demonstrates the importance of using a sintering model to predict continuous changes in temperature at the TGO interfaces since the temperature could reach the capability limit of the substrate.

## 8.2 Effects of undulations at the coating interface on residual stresses and coating failure

For APS TBC systems, undulations at the coating interface were observed at different scale levels. At the largest scale level, the undulation is given by the curvature of the substrate. The influence of this curvature on the stresses developed within the system was studied using different magnitudes and directions of curvatures. The effect is important since the TBC is widely applied to the engine components which have different curvatures. High curvatures especially convex curvatures compared to concave curvatures were shown to cause higher out-of-plane tensile stresses at the TGO interface. This could create spallation or delamination of the coating. The study agrees with flash thermography studies on heat treated aerofoil shaped specimens, which showed the coating delamination is favoured at the convex regions of the specimen. The study will aid in the design process of engine components for which critical curvature values can be determined from the model.

Microscopic undulations at the coating interfaces were observed from 3D tilted-SEM images of the interface. Various geometries of asperities at different microscopic scales were extracted and they were used to create unit cells for FE models. This approach contrasts with the traditional approach, which involves extracting 2D undulations data from SEM images of cross-sections of the TBC systems. The main advantage of the current approach is that it reveals entire geometric features at the coating interface. By way of comparison, the radial stresses predicted from the 3D model, for an identical aspect ratio, are twice of those predicted from the axisymmetric model. The current approach can be applied to analyse the effect of coating interface roughness of industrial coating systems on residual stresses and corresponding local crack growths at the interface. As a result, surface roughness of the BC can be optimised for maximum lifetime by applying appropriate surface treatments such as laser treatment, before APS TBC is applied.

## 8.3 Comparisons of predicted stresses within the TBC system against experimental results

In the past, stress analyses were carried out on the FE model without comparing the results to other independent methods. Therefore, those FE analyses have been qualitative ones involving study of the sensitivities of stresses to specific factors such as coating roughness, creep of coatings etc. Due to the availability of experimental measurements of stresses within the Supergen project consortium, a comparative study was carried out for predicted stresses from current FE analyses. Stresses were measured using Raman spectroscopy (RS) and photo-stimulated luminescence piezo-spectroscopy (PLPS) methods.

For the flat specimen without TBC, predicted in-plane stresses within the TGO after heating at 700°C and 1000°C for 96h are a factor of 2-2.5 times higher than experimental results. Meanwhile, discrepancies in the magnitude of results were observed for stresses within the TBC of the aerofoil shaped specimen. Nevertheless, higher reduction of in-plane TBC residual stresses for higher substrate curvatures upon cooling, after heating at 925°C for 96h, can be observed from both FE models and experiments.

## 8.4 Simulation of spallation/delamination of coating

Until recently, crack propagation within the TBCs driven by stress and strain within the system was modelled by defining initial crack trajectories. Hence, various trial steps are required along with remeshing according to crack tip direction. In contrast to the method, an attempt to model arbitrary crack growth within the TBC using XFEM is presented in this thesis. The method was applied in addition to traditional cohesive crack growth at the TGO interface. Therefore, the proposed model can simulate propagation of delamination cracks at the interface and crack growth within the coatings simultaneously. Moreover, it can also be used for simulating growth of initial cracks within the system when subsequent thermal cycles are applied. An example of complete spallation of the TBC system with initial parallel cracks has been demonstrated in Chapter 7.

In conclusion, the model can not only predict but also illustrate the failure scenario of the TBC system based on interactions between initial cracks and stresses developed within the coatings, which in turn are dependent on various mechanical properties and geometries of coatings interfaces.

# Chapter 9

# Recommended future work

## 9.1 Creep properties of the MCrAlY BC

Experimental results, to compare with the creep properties of the BC predicted from the homogenisation technique (predicting aggregate creep properties based on creep properties of the intermetallics within the BC) are sparse. This is because current experimental methods (such as uni-axial tests carried out on the pressed MCrAlY powder) are not applicable to thin layers such as MCrAlY coatings. Therefore, more appropriate techniques such as small punch creep tests (SPCT) are required to determine the experimental data for coatings materials. Moreover, relevant scaling factors can also be applied to evaluated creep properties of the BC by the homogenisation technique based on experimental values.

It has been reported that various mechanisms control activation energy for the creep deformation of BCs below and above its DBTT. The reason for this change in BC creep behaviour at high temperature could be understood by conducting additional research on creep deformation mechanisms of intermetallics for a wider temperature range, preferably between 600°C and 1200°C.

The effects of intermetallic grains size on aggregate creep strain rate should also be investigated and implemented within the homogenisation model for BC creep. This is because published models (e.g. Garofalo's model [144]) have shown interrelations between creep strain rates and grain sizes.

## 9.2 Sintering of the TBC

When sintering effects were considered for this project, Arrhenius fitting was applied to empirical data of elastic modulus and thermal conductivity. To obtain these material data extensive experimental work is required. Alternatively, innovative techniques such as object oriented finite element analysis (OOF) can be applied. Using OOF, only micrographs of the TBC are required to evaluate material properties elastic and thermal conductivity. This eliminates the additional experiments to measure material properties such as cantilever bend test to obtain elastic modulus and laser flash technique for thermal conductivity measurements. It has been demonstrated that with an appropriate sample size, the results from OOF are within the 5% error range of experimental values [43]. Therefore, using OOF reduces the cost of experiments dramatically although the method remains a purely predictive method without direct experimental validation.

There is also limited data for modulus evolutions due to sintering, which is driven by fusion of microcracks. Hence, more studies are required to better understand the changes in TBC modulus, which occurs during this stage of sintering.

## 9.3 Benchmarking predicted stresses to experimental measurements

When predicted stresses from FE model were compared to experimental results from Raman spectroscopy (RS) or photo-stimulated luminescence piezo-spectroscopy (PLPS) method, discrepancies occur because of the shortcomings from both FE method and experiments. Current FE models of the project ignore the initial stress states within the as-sprayed coating systems. These stresses, in reality, are created during cooling down after spraying process at high temperature. Significant residual stresses were observed within the aerofoil shaped specimen according to the experiments carried out within the consortium [101]. On the other hand, it is required to separate stresses measured by RS or PLPS into individual stress tensor components. This is necessary because currently stresses measured from RS and PLPS are expressed in the form of hydrostatic stresses, and quantitative comparison to predicted stress tensors in specific direction has not been accomplished.

## 9.4 Implementations of other relevant phenomena within the FE model

In Stage I of the project, the stresses developed within the TBC system, during the steady state at high temperature, was considered. In Stage II, a single thermal cycle was applied and stresses at the end of cooling were studied to predict the failure of coating systems. This paves the way to extend the project further by incorporating start-stop cycles or carrying out low-cycle fatigue analysis for industrial TBC systems. Other phenomena to be improved for existing FE model are listed below.

- Currently, only Al phases are assumed to be oxidised to form alumina although other fast growing metal oxides such as $NiCr_2O_4$ are expected after a long period of oxidation according to Wagner's theory [10]. Although this type of oxidation has been implemented elsewhere [13], the oxidation was modelled explicitly by applying an empirical oxide growth law, without considering the relationship between oxide growth rate and various BC compositions.
- Additionally, further experiments are required to investigate the anisotropic growth of the oxide layer. Utilising anisotropic growth will have a significant effect on the related strain from oxide growth and, hence stresses at the oxide interfaces. Currently, it is assumed that the oxide growth and corresponding growth strain are isotropic.
- The effect of curvature on stresses which causes TBC spallation has been demonstrated in this thesis by incorporating curvature within the FE unit cell with local coating roughness. However, when the coating interface was experimentally investigated, undulations were also found for which the wavelength is much larger than that of roughness. They are termed waviness. Further analysis is necessary to superimpose undulations of coating roughness onto waviness of the interface while retaining the curvature of the substrate.

## References

[1] D. Pauschert. Study of Equipment Prices in the Power Sector. ESMAP Technical Paper 122/09. (2009).

[2] R.C. Reed. The Superalloys: Fundamentals and Applications. Cambridge University Press: Cambridge. (2006).

[3] C.R. Morse. Comparison of National Bureau of Standards ceramic coatings L-7C and A-417 on turbine blades in a turbojet engine. NACA Research Memo E8120. (1948).

[4] F.J. Brooks. GE gas turbine performance analysis. Presented at the General Electric State-of-the-Art Technology Seminar, March 96, Riyadh, Saudi Arabia. (1996).

[5] H.E. Evans. High Temperature Coatings: Protection and Breakdown. Richardson, J.A. et al. (eds.) Shreir's Corrosion, volume 1, pp. 691-724. ((2010)).

[6] F.G. Garrett, C.A. Gyorgak. Adhesive and Protective Characteristics of Ceramic Coating A-417 and Its Effects on Engine Life of Forged Refractory-26 (AMS 5760) and Cast Satellite (AMS 5385) Turbine Blades NACA RM-E52130. (1953).

[7] S. Stecura. Two-Layer Thermal Barrier Coating for Turbine Airfoils- Furnace and Burner Rig Test Results. NASA TM X-3425, National Aeronautics and Space Administration. (1976).

[8] C.H. Liebert, F.S. Stepka. Potential Use of Ceramic Coating as a Thermal Insulation on Cooled Turbine Hardware. NASA TM X-3352. (1976).

[9] G.W. Goward. Seventeen years of thermal barrier coatings. Paper presented at the 1987 Proceedings of the Workshop on Coatings for Advanced Heat Engines, Castine, Maine, July 27-30. Washington D.C.: U.S. Department of Energy. (1987).

[10] C.Wagner. J.Electrochem. Soc., 99. (1952) pg 369.

[11] L. SwadŸba;, G. Moskal;, B. Mendala;, T. Gancarczyk. Characterisation of APS TBC system during isothermal oxidation at 1100°C. Materials Science and Engineering. Volume 28 (2007) Pages 757-64.

[12] D. Naumenko, V. Shemet, L. Singheiser, W. Quadakkers. Failure mechanisms of thermal barrier coatings on MCrAlY-type bondcoats associated with the formation of the thermally grown oxide. Journal of Materials Science. 44 (2009) 1687-703.

[13] E.P. Busso, H.E. Evans, Z.Q. Qian, M.P. Taylor. Effects of breakaway oxidation on local stresses in thermal barrier coatings. Acta Materialia. 58 (2010) 1242-51.

[14] C. Johnson, J.A. Ruud, A.C. Kaya, H.G. Lorenzi. In Proceedings of the Eight National Thermal Spray Conference. (1995) 415-20.

[15] E.P. Busso, J. Lin, S. Sakurai, M. Nakayama. A mechanistic study of oxidation-induced degradation in a plasma-sprayed thermal barrier coating system.: Part I: model formulation. Acta Mater. 49 (2001) 1515-28.

[16] M. Ranjbar-Far, J. Absi, G. Mariaux, F. Dubois. Simulation of the effect of material properties and interface roughness on the stress distribution in thermal barrier coatings using finite element method. Materials & Design. 31 (2010) 772-81.

[17] R.G. Munro. Evaluated Material Properties for a Sintered alpha-Alumina. J. Am. Ceram. Soc. 80 (1997) 1919-28.

[18] A. Cipitria, I.O. Golosnoy, T.W. Clyne. Sintering Kinetics of Plasma-Sprayed Zirconia TBCs. Sintering Kinetics of Plasma-Sprayed Zirconia TBCs. In, 2007 International Thermal Spray Conference, Beijing, China, 14 - 16 May 2007. ASM International, 434-439.

[19] S. Heiroth, R. Ghisleni, T. Lippert, J. Michler, A. Wokaun. Optical and mechanical properties of amorphous and crystalline yttria-stabilized zirconia thin films prepared by pulsed laser deposition. Acta Materialia. 59 (2011) 2330-40.

[20] J.D. Eshelby. The determination of the elastic field of an ellipsoidal inclusion, and related problems. Proceedings of the Royal Society A, 241:376{
396, 1957.

[21] U. Hermosilla. MECHANICAL MODELLING OF THERMAL BARRIER COATINGS AT HIGH TEMPERATURES, Thesis (PhD). University of Nottingham. (2008).

[22] M.S.A. Karunaratne, S.L. Ogden, S.D. Kenny, R.C. Thomson. A multicomponent diffusion model for prediction of microstructural evolution in coated Ni based superalloy systems. Materials Science and Technology. Volume 25 (2009) 287-99.

[23] M. Martena, D. Botto, P. Fino, S. Sabbadini, M.M. Gola, C. Badini. Modelling of TBC system failure: Stress distribution as a function of TGO thickness and thermal expansion mismatch. Engineering Failure Analysis. 13 (2006) 409-26.

[24] J. Rösler, M. Bäker, K. Aufzug. A parametric study of the stress state of thermal barrier coatings: Part I: creep relaxation. Acta Mater.. 52 (2004) 4809-17.

[25] A.M. Karlsson, A.G. Evans. A numerical model for the cyclic instability of thermally grown oxides in thermal barrier systems. Acta Materialia. 49 (2001) 1793-804.

[26] M. Jinnestrand, S. Sjöström. Investigation by 3D FE simulations of delamination crack initiation in TBC caused by alumina growth. Surface and Coatings Technology. 135 (2001) 188-95.

[27] M.P. Taylor, W.M. Pragnell, H.E. Evans. The influence of bond coat surface roughness on chemical failure and delamination in TBC systems. Materials and Corrosion. 59 (2008) 508-13.

[28] C. Che, G.Q. Wu, H.Y. Qi, Z. Huang, X.G. Yang. Uneven growth of thermally grown oxide and stress distribution in plasma-sprayed thermal barrier coatings. Surface and Coatings Technology. 203 (2009) 3088-91.

[29] E.P. Busso. Oxidation-induced stresses in ceramic-metal interfaces. J. Phys. IV France. 09 (1999) Pr9-287-Pr9-96.

[30] B. Budiansky, T.T. Wu. Theoretical prediction of plastic strains in polycrystals. In Proceedings of the fourth U.S. National Congress of Applied Mechanics. volume 2 (1962) pages 1175-85.

[31] B. Budiansky. On the elastic moduli of some heterogeneous materials. Journal of the Mechanics and Physics of Solids, 13. (1965) 223-7.

[32] W. Wakashima, M. Otsuka, S. Umekawa. Thermal expansions of heterogeneous solids containing aligned ellipsoidal inclusions. Journal of Composite Materials 8 (October 1974) 391-404.

[33] G.J. Weng. A self-consistent relation for the time-dependent creep of polycrystals. International Journal of Plasticity. 9 (1993) 181-98.

[34] T. Mura. Micromechanics of Defects in Solids (Mechanics of Elastic and Inelastic Solids) Springer; 2nd ed. (1987).

[35] V. Lughi, V.K. Tolpygo, D.R. Clarke. Microstructural aspects of the sintering of thermal barrier coatings. Materials Science and Engineering: A. 368 (2004) 212-21.

[36] E.P. Busso, Z.Q. Qian. A mechanistic study of microcracking in transversely isotropic ceramic–metal systems. Acta Materialia. 54 (2006) 325-38.

[37] T.J. Lu, C.G. Levi, H.N.G. Wadley, A.G. Evans. Distributed Porosity as a Control Parameter for Oxide Thermal Barriers Made by Physical Vapor Deposition. Journal of the American Ceramic Society. 84 (2001) 2937-46.

[38] Thompson.J.A, Ji.W, Klocker.T, Clyne T.W. SINTERING OF THE TOP COAT IN THERMAL SPRAY TBC SYSTEMS UNDER SERVICE CONDITIONS. Ninth International Symposium on Superalloys. (2000) 685-92.

[39] S.A. Tsipas, I.O. Golosnoy, R. Damani, T.W. Clyne. The effect of a high thermal gradient on sintering and stiffening in the top coat of a thermal barrier coating (TBC) system. Journal of Thermal Spray Technology, 13, (3), 370-376. (2004).

[40] D. Zhu, R. Miller. Thermal conductivity and elastic modulus evolution of thermal barrier coatings under high heat flux conditions. Journal of Thermal Spray Technology. 9 (2000) 175-80.

[41] W.J.Parker, R.J.Jenkins, C.P.Butler, G.L.Abbott. A Flash Method of Determing Thermal Diffusivity, Heat Capacity, and Thermal Conductivity. J. Appl. Phys. 32, 1679. (1961).

[42] F. Cernuschi, L. Lorenzoni, S. Ahmaniemi, P. Vuoristo, T. Mäntylä. Studies of the sintering kinetics of thick thermal barrier coatings by thermal diffusivity measurements. Journal of the European Ceramic Society. 25 (2005) 393-400.

[43] E. Fuller-Jr., J. Ruud, N.S.Hari, J. Grande, A. Mogro-Campero. Thermal Property Prediction via Finite-Element Simulations. The International Conference on Advanced Ceramics & Composites in Cocoa Beach, Florida. (2002).

[44] PPM2OOFsoftware. http://www.ctcms.nist.gov/oof. (Dec 2012).

[45] V.R. Coffman, A.C.E. Reid, S.A. Langer, G. Dogan. OOF3D: An image-based finite element solver for materials science. Mathematics and Computers in Simulation. 82 (2012) 2951-61.

[46] Demasi-Marcin, J. T., K.D. Sheffler, S. Bose. Mechanisms of degradation and failure in a plasma deposited thermal barrier coating. ASME, Gas Turbine and Aeroengine Congress and Exposition, Toronto, Canada, June 4-8, 1989.

[47] M.G. Hebsur, R.V. Miner. High temperature tensile and creep behaviour of low pressure plasma-sprayed Ni-Co-Cr-Al-Y coating alloy. Materials Science and Engineering. 83 (1986) 239-45.

[48] K.J. Hemker, B.G. Mendis, C. Eberl. Characterizing the microstructure and mechanical behavior of a two-phase NiCoCrAlY bond coat for thermal barrier systems. Materials Science and Engineering: A. 483-484 (2008) 727-30.

[49] R.W.Smith. Mechanical properties of a low-pressure-plasma- applied Co-Cr-Al-Y coating. Thin Solid Films. 84 (1981) 59-72.

[50] D. Zhu, R.A. Miller. Determination of Creep Behavior of Thermal Barrier Coatings Under Laser Imposed Temperature and Stress Gradients. Technical memo. ((1997) ).

[51] R.C. Folweiler. Creep Behavior of Pore-Free Polycrystalline Aluminum Oxide. Journal of Applied Physics, Vol. 32, p.773-778. (1961).

[52] A.A. Wereszczak, J.G. Hemrick, T.P. Kirkland, J.A. Haynes, T.J. Fitzgerald, J.E. Junkin. Stress relaxation of MCrAlY bond coat alloys as a function of temperature and strain. In International Gas Turbine & Aeroengine Congress & Exhibition Proceedings
(1998) page 1-7.

[53] T.H.Hyde, M. Stoyanov, W. Sun, C.J. Hyde. On the interpretation of results from small punch creep tests. The Journal of Strain Analysis for Engineering Design. Volume 45 (2010) 141-64.

[54] M.P. Taylor, H.E. Evans, C.B. Ponton, J.R. Nicholls. A method for evaluating the creep properties of overlay coatings. Surface and Coatings Technology. 124 (2000) 13-8.

[55] X.Y.Gong, D.R.Clarke. On the Measurement of Strain in Coatings Formed on a Wrinkled Elastic Substrate. Oxid. Met.. 50 (1998) 355-76.

[56] R.V. Hillery, B.H. Pilsner, R.L. Mcknight, T.S. Cook, M.S. Hartle. Thermal Barrier Coating Life Prediction Model Development. NASA-CR-180807, NAS 1.26:180807, R87-AEB586. (1988).

[57] C.-H. Hsueh, J.A. Haynes, M.J. Lance, P.F. Becher, M.K. Ferber, E.R. Fuller, et al. Effects of Interface Roughness on Residual Stresses in Thermal Barrier Coatings. Journal of the American Ceramic Society. 82 (1999) 1073-5.

[58] M. Ahrens, R. Vaßen, D. Stöver. Stress distributions in plasma-sprayed thermal barrier coatings as a function of interface roughness and oxide scale thickness. Surface and Coatings Technology. 161 (2002) 26-35.

[59] M.L.Glynn, K.T.Ramesh, P.K.Wright, K.J.Hemker. Modelling effects of material properties and three-dimensional surface roughness on thermal barrier coatings. Mat. Res. Soc. Symp. Proc. Vol. 645E. (2001).

[60] Z. Han, H. Wang. Relation between 3 dimension interface topography and residual stress in thermal barrier coatings. Adv. Mater. Res. Vols. 217-218 (2011) (2011) pp 964-8.

[61] W. Zhu, G. Pezzotti. Raman analysis of three-dimensionally graded stress tensor components in sapphire. Journal of Applied Physics. 109 (2011) 073502--13.

[62] R.J. Christensen, D.M. Lipkin, D.R. Clarke, K. Murphy. Nondestructive evaluation of the oxidation stresses through thermal barrier coatings using $Cr^{3+}$ piezospectroscopy. Applied Physics Letters. 69 (1996) 3754-6.

[63] A.M. Limarga, R. Vaßen, D.R. Clarke. Stress Distributions in Plasma-Sprayed Thermal Barrier Coatings Under Thermal Cycling in a Temperature Gradient. Journal of Applied Mechanics. 78 (2011) 011003.

[64] V. Teixeira, M. Andritschky, W. Fischer, H.P. Buchkremer, D. Stöver. Analysis of residual stresses in thermal barrier coatings. Journal of Materials Processing Technology. 92–93 (1999) 209-16.

[65] D. Liu, O. Lord, O. Stevens, P.E.J. Flewitt. The role of beam dispersion in Raman and photo-stimulated luminescence piezo-spectroscopy of yttria-stabilized zirconia in multi-layered coatings. Acta Materialia. (2012).

[66] G. Hilson, P. Flewitt. Stresses Developed within Thermally Grown Oxides on a Coated Superalloy Substrate. Key Engineering Materials. 417-418 (2010) 5-8.

[67] ABAQUS. 6.9 User's Manual.

[68] M. Caliez, J.L. Chaboche, F. Feyel, S. Kruch. Numerical simulation of EBPVD thermal barrier coatings spallation. Acta Materialia. 51 (2003) 1133-41.

[69] H. Yuan, J. Chen. Computational analysis of thin coating layer failure using a cohesive model and gradient plasticity. Engineering Fracture Mechanics. 70 (2003) 1929-42.

[70] H. Bhatnagar, S. Ghosh, M.E. Walter. A parametric study of damage initiation and propagation in EB-PVD thermal barrier coatings. Mechanics of Materials. 42 (2010) 96-107.

[71] M. Bäker. Finite element crack propagation calculation using trial cracks. Computational Materials Science. 43 (2008) 179-83.

[72] P. Seiler, M. Bäker, J. Rösier. FEM simulation of oxidation induced stresses with a coupled crack propagation in a TBC model system. IOP Conference Series: Materials Science and Engineering. 10 (2010) 012056.

[73] K.S. Chan, N.S. Cheruvu, G.R. Leverant. Coating Life Prediction for Combustion Turbine Blades. Journal of Engineering for Gas Turbines and Power. 121 (1999) 484-8.

[74] J. Gayda, T.P. Gabb, R.V. Miner, Jr. The low cycle fatigue behavior of a plasma-sprayed coating material. TMS-AIME Annual Meeting; 2-6 Mar. 1986; New Orleans, LA; United States. (1986 ).

[75] E.P. Busso, J. Lin, S. Sakurai. A mechanistic study of oxidation-induced degradation in a plasma-sprayed thermal barrier coating system. - Part II: Life prediction model. Acta Materialia. 49 (2001) 1529-36.

[76] Brodin.H, Jinnestrand.M, Johansson.S, Sjostrom.S. THERMAL BARRIER COATING FATIGUE LIFE ASSESSMENT. Siemens AG. ( 2006).

[77] U. Hermosilla, M.S.A. Karunaratne, I.A. Jones, T.H. Hyde, R.C. Thomson. Modelling the high temperature behaviour of TBCs using sequentially coupled microstructural-mechanical FE analyses. Mater. Sci. Eng. A. 513-514 (2009) 302-10.

[78] Y. Tan, J.P. Longtin, S. Sampath, D. Zhu. Temperature-Gradient Effects in Thermal Barrier Coatings: An Investigation Through Modeling, High Heat Flux Test, and Embedded Sensor. Journal of the American Ceramic Society. 93 (2010) 3418-26.

[79] J.C. Kotz, P. Treichel, J.R. Townsend, ,. Chemistry and chemical reactivity , Volume 2, Stamford. (2009).

[80] H.Y. Qi, L.Z. Zhou, H.Q. Ma, X.G. Yang, L. Xu. In-situ measurement of elastic modulus for ceramic top-coat at high temperature. Journal of Central South University of Technology. 15 (2008) 372-6.

[81] S. Li, S. Kyaw, A. Jones. BOUNDARY CONDITIONS RESULTING FROM CYLINDRICAL AND LONGITUDINAL PERIODICITIES (In preparation for resubmission). Computers and Structures. (2013).

[82] The International Nickel Company Inc. Alloy IN-738 technical data.

[83] C.F.H. Pointer, P. Morrell. Private Communication.

[84] H.J. Frost, M.F. Ashby. Deformation-mechanism maps, The plasticity and creep of metals and ceramics. Pergamon Press. (1982).

[85] J. Wolfenstine, H.K. Kim, J.C. Earthman. Elevated-temperature deformation mechanisms in Ni3Al. Materials Science and Engineering A. 192-193 (1995) 811-6.

[86] N.S. Stoloff , V.K. Sikka. Physical metallurgy and processing of intermetallic compounds, Chapman & Hall. (1996).

[87] R.W. Dickson, J.B. Wachtman Jr, S.M. Copley. Elastic constants of single-crystal Ni3Al from 10°to 850°c. Journal of Applied Physics. 40 (1969) 2276-9.

[88] S.M. Meier, D.M. Nissley, K.D. Sheffler. 'Thermal barriercoating life prediction model development' Phase II Final Report,Technical Report NASA Contractor Report 18911/NAS3-23944,National Aeronautics and Space Administration, NASA LewisResearch Cente. (1991).

[89] J.W. Adams, R. Ruh, K.S. Mazdiyasni. Young's Modulus, Flexural Strength, and Fracture of Yttria-Stabilized Zirconia versus Temperature. Journal of the American Ceramic Society. 80 (1997) 903-8.

[90] S. Maya, T.W. Clyne. A methodology, based on sintering-induced stiffening, for prediction of the spallation lifetime of Plasma sprayed TBCs. Presented at Energy Materials Conference. (2012).

[91] K. Chan, S. Cheruvu, R. Viswanathan, , . Development of a thermal barrier coating life model. Proceedings of ASME Turbo Expo, Atlanta paper number GT2003-38171. (2003).

[92] W. Mao, J.P. Jiang, Y.C. Zhou. Effects of Substrate Curvature Radius, Deposition Temperature and Coating Thickness *on the Residual Stress Field of* Cylindrical thermal Barrier Coatings. Surface and Coatings Technology. Volume 205, Issues 8-9 (2011) Pages 3093.

[93] U. Hermosilla, M. Karunaratne, I.A. Jones, T. Hyde, R.C. Thomson. MCrAlY creep behaviour modelling by means of finite-element unit cells and self-consistent constitutive equations. IMechE. Vol. 223 (2009) 41-51.

[94] Y. Itoh, M. Saitoh, M. Miyazaki. "Microstructure and Residual Stress of Low-Pressure Plasma-Sprayed MCrAlY Coatings". Nippon Kikai Gakkai Ronbunshu A Hen/Transactions of the Japan Society of Mechanical Engineers. Part A, Vol. 61 ((1995)) 87-92.

[95] J. Chevalier, C. Olagnon, G. Fantozzi, H. Gros. Creep behaviour of alumina, zirconia and zirconia-toughened alumina. Journal of the European Ceramic Society. 17 (1997) 859-64.

[96] H.T. Lin, P.F. Becher. Creep Behavior of a SiC-Whisker-Reinforced Alumina. Journal of the American Ceramic Society. 73 (1990) 1378-81.

[97] N.S. Cheruvu, K.S. Chan, D.W. Gandy. Effect of Time and Temperature on Thermal Barrier Coating Failure Mode Under Oxidizing Environment. Journal of Engineering for Gas Turbines and Power. 131 (2009) 022101-7.

[98] K.W. Schlichting, N.P. Padture, E.H. Jordan, M. Gell. Failure modes in plasma-sprayed thermal barrier coatings. Materials Science and Engineering A. 342 (2003) 120-30.

[99] M. Gell, J. Eric, V. Krishnakumar, K. McCarron, B. Barber, Y.-H. Sohn, et al. Bond strength, bond stress and spallation mechanisms of thermal barrier coatings. Surface and Coatings Technology. 120–121 (1999) 53-60.

[100] S. Bose. High temperature coatings. Elsevier Butterworth-Heinemann, 2007.

[101] Dong Liu, Peter EJ Flewitt, K.R. Hallam. The Measurement of Residual Stresses in Thermal Barrier Coated Model Aerofoils. Key Engineering Materials. 9-12 (2012).

[102] M. Seraffon, N.J. Simms, J.R. Nicholls, J. Sumner, J. Nunn. Performance of thermal barrier coatings in industrial gas turbine conditions. Mater. High Temp. 28 (2011 ) 309-14.

[103] Dong Liu, Peter EJ Flewitt, O. Lord. FACTORS THAT INFLUENCE THE MEASUREMENT OF RESIDUAL STRESSES IN THERMAL BARRIER COATED TURBINE BLADES. Engineering Structural Integrity Assessment: From plant and structure design, maintenance to disposal. (2011).

[104] S. Saeidi, K.T. Voisey, D.G. McCartney. The Effect of Heat Treatment on the Oxidation Behavior of HVOF and VPS CoNiCrAlY Coatings. JOURNAL OF THERMAL SPRAY TECHNOLOGY. Volume 18 (2009) 209-16.

[105] S.T. Kyaw, I.A. Jones, T.H. Hyde. Predicting failure within TBC system: Finite element simulation of stress within TBC system as affected by sintering of APS TBC, geometry of substrate and creep of TGO. Eng. Fail. Anal. 27 (2013) 150-64.

[106] H. Takagi, M. Fujiwara, K. Kakehi. Measuring Young's modulus of Ni-based superalloy single crystals at elevated temperatures through microindentation. Materials Science and Engineering A (2004) 348-51.

[107] V. SASS, U. GLATZEL, M. FELLER-KNIEPMEIER. ANISOTROPIC CREEP PROPERTIES OF THE NICKEL-BASE SUPERALLOY CMSX-4. Acra mater. Vol. 44, No. 5, pp. 1967-1977, 1996.

[108] K. Mills. Recommended Values of Thermophysical Properties for Selected Commercial Alloys. Woodhead Publishing. (2002 ).

[109] D. Woodford. Accelerated High Temperature Performance Evaluation for Alloy Optimization, Embrittlement, and Life Assessment. CORROSION (2005).

[110] A. Selcuk, A. Atkinson. Analysis of the Cr3+ luminescence spectra from thermally grown oxide in thermal barrier coatings. Materials Science and Engineering: A. 335 (2002) 147-56.

[111] Y. Sohn, K. Schlichting, K. Vaidyanathan, M. Gell, E. Jordan. Nondestructive evaluation of residual stress for thermal barrier coated turbine blades by $Cr^{3+}$ photoluminescence piezospectroscopy. Metallurgical and Materials Transactions A. 31 (2000) 2388-91.

[112] Dong Liu, Oliver Lord, P.E.J. Flewitt. Calibration of Raman spectroscopy in the stress measurement of air-plasma-sprayed yttria-stabilized zirconia. Appl Spectrosc. 66 (2012 Oct ) Pg 1204-9.

[113] Q. Ma, D.R. Clarke. Stress Measurement inSingle Crystal and Polycrystalline CeramicsUsing Their Optical Fluorescence. J. Am.Ceram. Soc., 76. ((1993)) 1433-40.

[114] J. He, D.R. Clarke. Determination of the Piezospectroscopic Coefficients for Chromium-Doped Sapphire. Journal of the American Ceramic Society. 78 (1995) 1347-53.

[115] D. Liu. (Personal Communication).

[116] S. Maharjan, X. C. Zhang, F. Z. Xuan, Z. D. Wang, S.T. Tu. Residual stresses within oxide layers due to lateral growth strain and creep strain: Analytical modeling. J. Appl. Phys. 110, 063511 (2011). (2011).

[117] D.Y. Ju, M. Nishida, T. Hanabusa. Simulation of the thermo-mechanical behavior and residual stresses in the spray coating process. Journal of Materials Processing Technology. 92–93 (1999) 243-50.

[118] M. Jepson. (Personal Communication).

[119] Y.H. Sohn, J.H. Kim, E.H. Jordan, M. Gell. Thermal cycling of EB-PVD/MCrAlY thermal barrier coatings: I. Microstructural development and spallation mechanisms. Surface and Coatings Technology. 146–147 (2001) 70-8.

[120] FOGALE-NANOTECH. http://www.fogale.fr/optical_profilers/pages/software.php. (2008).

[121] ISO 11562. Geometrical product specification (GPS)—surface texture: profile method—metrological characteristics of phase correct filters. Geneva: International Organization for Standardization. (1996).

[122] S. Li, A. Wongsto. Unit cells for micromechanical analyses of particle-reinforced composites. Mech. Mater.. 36 (2004) 543-72.

[123] P. Kofstad. High-temperature oxidation of metals. Wiley. (1966).

[124] R.H. Davies, A.T. Dinsdale, J.A. Gisby, J.A.J. Robinson, S.M. Martin:. CALPHAD, 2002, 26, (2), 229-271.

[125] H.E. Evans, M.P. Taylor. Diffusion Cells and Chemical Failure of MCrAlY Bond Coats in Thermal-Barrier Coating Systems. Oxidation of Metals. 55 (2001) 17-34.

[126] C.Che, G.Q.Wu, H.Y.Qi, Z.H. and, X.G.Yang. Depletion Model of Aluminum in Bond Coat for Plasma-Sprayed Thermal Barrier Coatings. Advanced Materials Research (Volume 75) (June, 2009) 31-5.

[127] R.W. Smith. Mechanical properties of a low pressure plasma applied CoCrAlY coating. Thin Solid Films. 84 (1981) 59-72.

[128] J. Kondoh, H. Shiota, K. Kawachi, T. Nakatani. Yttria concentration dependence of tensile strength in yttria-stabilized zirconia. Journal of Alloys and Compounds. 365 (2004) 253-8.

[129] M. Okazaki, Y. Yamazaki, K. Namba, K. Ogawa, M. Ohki, K. Fujiyama, et al. Collaborative Research on Adhesion Strength of Thermal Barrier Coatings in JSMS. Journal of Solid Mechanics and Materials Engineering, Volume 4, Issue 2, pp. 252-263 (2010).

[130] T.W. Clyne, S.C. Gill. Residual Stresses in Thermal Spray Coatings and Their Effect on Interfacial Adhesion: A Review of Recent Work. JTTEE5 5:401-418. (1996 Dec).

[131] S. Timoshenko. 'Theory of Elastic Stability'. McGraw-Hill, New York. (1936) p 367.

[132] S.R. Choi, J.W. Hutchinson, A.G. Evans. Delamination of multilayer thermal barrier coatings. Mechanics of Materials. 31 (1999) 431-47.

[133] L. Xie, D. Chen, E.H. Jordan, A. Ozturk, F. Wu, X. Ma, et al. Formation of vertical cracks in solution-precursor plasma-sprayed thermal barrier coatings. Surface & Coatings Technology 201 ((2006)) 1058-64.

[134] A. Rabiei, A.G. Evans. Failure mechanisms associated with the thermally grown oxide in plasma-sprayed thermal barrier coatings. Acta Materialia. 48 (2000) 3963-76.

[135] P.K. Wright, A.G. Evans. Mechanisms governing the performance of thermal barrier coatings. Current Opinion in Solid State and Materials Science. 4 (1999) 255-65.

[136] M. Bäker, J. Rösler, G. Heinze. A parametric study of the stress state of thermal barrier coatings Part II: cooling stresses. Acta Materialia. 53 (2005) 469-76.

[137] T. Belytschko, T. Black. Elastic crack growth in finite elements with minimal remeshing. International Journal for Numerical Methods in Engineering. 45 ((1999)) 601-20.

[138] J.M. Melenk, I. Babuska. Approximation with harmonic and generalized harmonic polynomials in the partition of unity method. Comput. Assist. Mech. Eng. Sci. 4 (1997) 607-32.

[139] S. Mohammadi. Extended Finite Element Method: for Fracture Analysis of Structures. Wiley-Blackwell; 1 edition. (2008).

[140] C. Berndt. Instrumented tensile adhesion tests on plasma sprayed thermal barrier coatings. Journal of Materials Engineering. 11 (1989) 275-82.

[141] F. Krasucki, S. Lenci. Analysis of interfaces of variable stiffness. International Journal of Solids and Structures. 37 (2000) 3619-32.

[142] Y.YAMAZAKI, S.KUGA, T.YOSHIDA. Evaluation of interfacial strength by an instrumented indentation method and its application to an actual TBC vane. Acta Metallurgica Sinica(English letters). Vol.24 (2011) 109-17.

[143] D.W. Stollberg, J.M. Hampikian, L. Riester, W.B. Carter. Nanoindentation measurements of combustion CVD Al2O3 and YSZ films. Materials Science and Engineering A. 359 (2003) 112-8.

[144] F.Garofalo, W.F.Domis, F.v. Gemmingen. Tans.TMS-AIME 240, 1460. (1964).

[145] S. M. Meier, D.M. Nissley, K.D. Sheffler:. 'Thermal barrier coating life prediction model development', Phase II Final Report. Technical Report NASA Contractor Report 18911/NAS3-23944, National Aeronautics and Space Administration, NASA Lewis Research Center, 1991.

# Appendix A

# Procedure for running the FE model coupling BC phase evolution, TGO transformation and TBC sintering

---

The procedure for running FE models with various material constitutive models will be explained at each stage of the simulation; pre-processing and processing stages.

## *Pre-processing stage*

- Phase proportion in mass of the BC phases (γ, γ', β and σ) and distances of FD nodes from the TGO/BC interface, at which phase calculations were made, were supplied by Karunaratne et al. [22].
- The data were supplied as text files and they are named as 'PxxxxW'; 'xxxx' represents oxidation time at which phases proportions are calculated. For e.g.

P0001W contains BC phase data after 10h of oxidation and P0002W contains data after 20h of oxidation and etc.

- Within the FD files, the parameters are grouped into different columns and they were extracted using MATLAB software. Phase proportions (% mass) of the BC phases were also changed into volumetric compositions using relevant densities of phases.
- Additional to the data from FD files, material properties such as elastic, CTE, creep properties of the intermetallics phases, TBC and TGO were also allocated into the user material modules (PROPS) of user material subroutine [67] (UMAT).

## *Processing stage*

During the processing stage, mechanical constitutive behaviours of the TBC and the BC were evaluated within UMAT of ABAQUS using different material data inputs. A single UMAT file was coded for both TBC and BC and it serves as a directory linking to respective user subroutines for the BC and the TBC namely UMAT_TBC and UMAT_BC respectively. The names are consistent with the material names defined within the CAE module of ABAQUS. For both UMATs, two main tasks are necessary; firstly calculating material properties and secondly calculating stress increments. The only external load applied to the system is the temperature which includes long steady state allowing creep deformation to occur. It is assumed that all stress and strain tensors are symmetric i.e. $\sigma_{12} = \sigma_{21}$, $\varepsilon_{13} = \varepsilon_{31}$, etc.

**UMAT_TBC**

- Elastic modulus (E) and thermal conductivity (k) of TBC are calculated using Arrhenius based models for TBC from Chapter 3 utilising experimental data [40, 78] within the UMAT_TC.
- An analytical model for updating temperature distribution, based on evolutions of thermal conductivity of the TBC, is implemented within user defined temperature routine (UTEMP).
- UTEMP is linked to UMAT_TBC and UMAT_BC to update temperature gradient across coatings. Flowchart for the implementing user defined temperature distribution from Chapter 3 is re-drawn here as Fig A1 for convenience.
- Creep strain rate of the TBC is implemented using a time dependent power law relation as shown in Eq (A1).

$$\dot{\varepsilon}_{ij}^{tbc,cr} = \frac{3}{2} A(\sigma)^{n-1} s_{ij} t^{-s} \tag{A1}$$

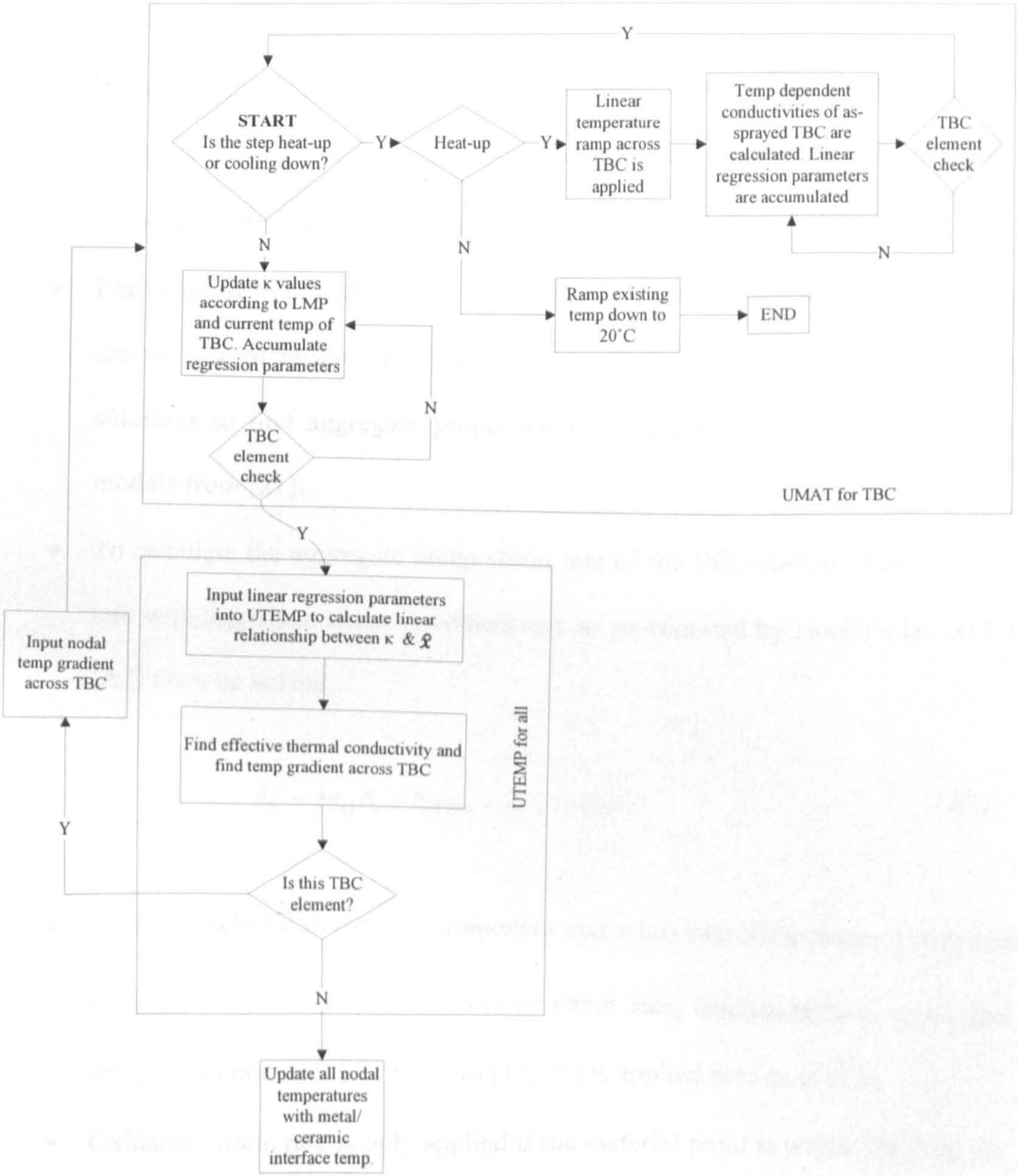

**Fig A1: Flowchart for implementing sintering dependent thermal conductivities of TBC and temperature gradient across TBC systems**

## UMAT_BC

- Intermetallic phase properties, which were implemented within PROPS modules during the pre-processing stage, were extracted according the distance of the material points from the BC/TGO interface.
- Elastic properties and CTE of aggregate BC are initially calculated using a simple rule of mixture approach. The results are then used as the starting solutions to find aggregate properties according to the material constitutive models from [21].
- To calculate the aggregate creep strain rate of the BC, relation of creep strain rate with aggregate stress increment rate as represented by Hooke's law as Eq (A2) must be solved.

$$\dot{\sigma}_{ij} = \lambda \dot{\varepsilon}_{kk}\delta_{ij} + 2\mu\left(\dot{\varepsilon}_{ij} - \dot{\varepsilon}_{ij}^{in}\right) - 3K\alpha\dot{T}\delta_{ij} \tag{A2}$$

- $\dot{\varepsilon}_{ij}^{in}$ is an inelastic strain rate component and it has two components; creep and oxidation strain rate. For the former strain rate, microstructural dependent creep strain rate derived by Busso [15, 29] is applied here as in [21].
- Oxidation strain rate is only applied if the material point is within the zone for which TGO is forming. The rate of change in thickness of the TGO was calculated using empirical formula [145] shown in Eq (A3). Selective oxidation is assumed and oxide formed is assumed as pure alumina. The strain rate due to oxide formation, assuming isotropic strain rate, can be expressed as Eq (A4).

$$\dot{\delta} = n\left\{\exp\left[Q\left(\frac{1}{T_0} - \frac{1}{T}\right)\right]\right\}^n t^{n-1} \tag{A3}$$

$$\dot{\varepsilon}_{ij}^{ox} = \frac{1}{3}\dot{f}^{ox}\ln\left(PBR_{Al}\right)\delta_{ij} \tag{A4}$$

# Appendix B

# Cooling stresses for a single-layered coating system with cylindrical and spherical substrates

---

The geometries around the peak and valley of 2D and 3D sinusoidal coating interfaces, from Chapter 6, can be idealised as cylinder and sphere. For simplicity, the BC is assumed to have similar mechanical and thermal properties as the substrate and there is no TGO layer. The system then can be idealised as a single-layered coating system. According to Lamé [55], analytical radial and circumferential stresses at the substrate/coating interface for cylinder and sphere substrate can be expressed as shown in Eq (B1-B4).

$$\sigma_r^{cylinder,A} = \frac{c_1}{r^2} + c_2 \tag{B1}$$

$$\sigma_\theta^{cylinder,A} = -\frac{c_1}{r^2} + c_2 \tag{B2}$$

$$\sigma_r^{sphere,A} = \frac{c_5}{r^3} + c_6 \tag{B3}$$

$$\sigma_\theta^{sphere,A} = -\frac{c_5}{r^3} + c_6 \tag{B4}$$

$c_1$&$c_2$ and $c_5$&$c_6$ are constants and similar formulae can be written for coating using constants $c_4$&$c_5$ and $c_7$&$c_8$. Therefore, there will be four constants for each system and they can be found using boundary conditions given in Eq (B5-B9).

$$\text{At r} = 0,\ \sigma_r^A = \sigma_\theta^A \neq 0 \tag{B5}$$

$$\text{At r} = \text{R},\ \sigma_r^A = \sigma_r^o \tag{B6}$$

$$\text{At r} = \text{R},\ \varepsilon_\theta^A = \varepsilon_\theta^o \tag{B7}$$

$$\text{At r} = \text{R+t},\ \sigma_r = 0 \tag{B8}$$

$$\varepsilon_z^{cylinder,A} = \varepsilon_z^{cylinder,o} \tag{B9}$$

Superscripts A and o represent the substrate and the coating while subscripts r, θ and z represent radial, hoop and axial stresses respectively. σ, ε, R and tare stress, strain, radius of curvature and thickness of coating respectively.

By using Eq (B5), $c_1$ and $c_5$ become zero. Other constants can be found from using Eq (B6 - B9) and they are listed in Eq (B10 - B15).

$$c_2 = \frac{(2tE_o(1+\nu_o)E_A\Delta T(\alpha_A-\alpha_o)(R+0.5t))}{((-1-\nu_o)E_A+(-1+\nu_A+2\nu_A^2)E_o)t^2-(2((1+\nu_o)E_A+(1-\nu_A-2\nu_A^2)E_o))Rt+(2\nu_o^2-2)E_AR^2} \tag{B10}$$

$$c_3 = \frac{\Delta T E_A E_o R^2(\alpha_A-\alpha_o+\nu_o\alpha_A-\nu_o\alpha_o)(R^2+2Rt+t^2)}{(2\nu_o{}^2R^2E_A-2E_AR^2-2E_oRt-E_ot^2+2E_o\nu_ARt+E_o\nu_At^2+4E_o\nu_A^2Rt+2E_o\nu_A^2t^2-2E_ARt-E_At^2-2E_A\nu_oRt-E_A\nu_ot^2)} \tag{B11}$$

$$c_4 = \frac{-\Delta TE_AEoR^2(\alpha_A-\alpha_o+\nu_o\alpha_A-\nu_o\alpha_o)}{(2\nu_o^2R^2E_A-2E_AR^2-2E_oRt-E_ot^2+2E_o\nu_ARt+E_o\nu_At^2+4E_o\nu_A^2Rt+2E_o\nu_A^2t^2-2E_ARt-E_At^2-2E_A\nu_oRt-E_A\nu_ot^2)} \tag{B12}$$

$$c_6 = \frac{-2t(3R^2+3Rt+t^2)\Delta TE_AE_o(\alpha_A-\alpha_o)}{(3E_AR^3+6E_oR^2t+6E_oRt^2+2E_ot^3-12E_ov_AR^2t-12E_ov_ARt^2-4E_ov_At^3+3E_AR^2t+3E_ARt^2+E_At^3+12E_A\nu_oR^2t+12E_A\nu_oRt^2+4E_A\nu_ot^3)} \tag{B13}$$

$$c_7 = \frac{-2\Delta TE_AE_oR^3(\alpha_A-\alpha_o)(R^3+3R^2t+3Rt^2+t^3)}{(3E_AR^3+6E_oR_2t+6E_oRt^2+2E_ot^3-12E_o\nu_AR^2t-12E_o\nu_ARt^2-4E_o\nu_At^3+3E_AR^2t+3E_ARt^2+E_At^3+12E_A\nu_oR^2t+12E_A\nu_oRt^2+4E_A\nu_ot^3)} \tag{B14}$$

$$c_8 = \frac{2\Delta TE_AE_oR^3(\alpha_A-\alpha_o)}{(3E_AR^3+6E_oR^2t+6E_oRt^2+2E_ot^3-12E_o\nu_AR^2t-12E_o\nu_ARt^2-4E_o\nu_At^3+3E_AR^2t+3E_ARt^2+E_At^3+12E_A\nu_oR^2t+12E_A\nu_oRt^2+4E_A\nu_ot^3)} \tag{B15}$$

Subscripts A and o represent the substrate and the coating. E, t, $\nu$, $\alpha$, $\Delta T$ and R are elastic modulus, thickness of coating, Poisson's ratio, CTE, temperature difference and radius of curvature respectively. Using the above constants and material properties for the coating and the substrate listed in Table B1, radial stresses at the substrate/coating interface can be found. Radial interfacial stresses for cylindrical and spherical substrates are plotted in Fig B1.

**Table B1: Elastic properties and CTEs of substrate and TBC for analytical stress calculations**

| | Elastic modulus (GPa) | Poisson's ratio | CTE*$10^6$ |
|---|---|---|---|
| Substrate | 140 | 0.3 | 20.7 |
| TBC | 113 | 0.18 | 10 |

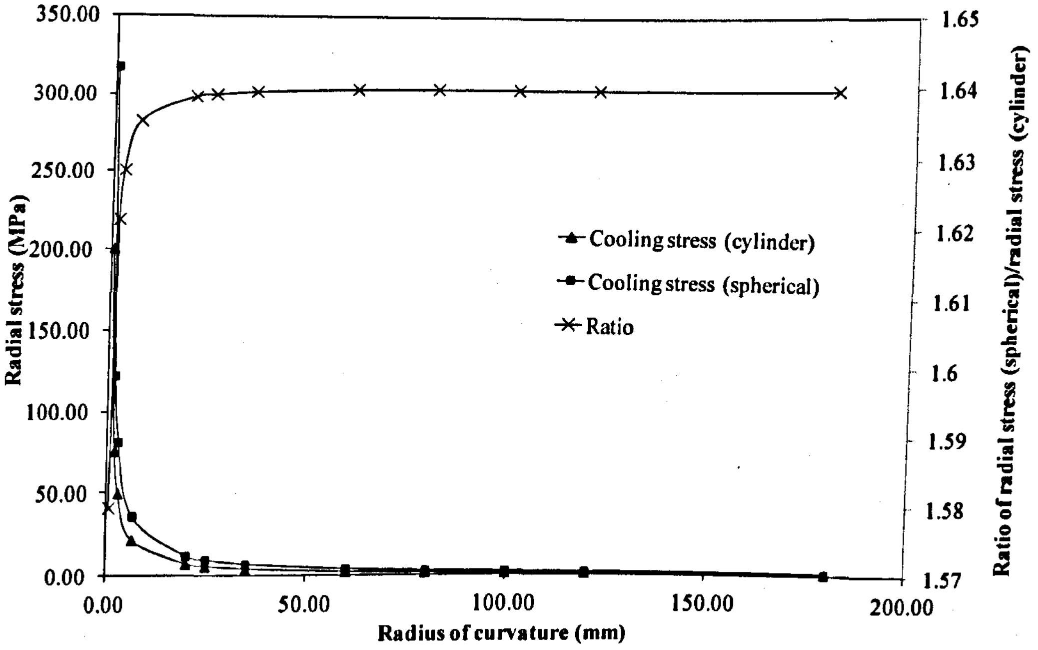

**Fig B1: i) External cooling stresses and ii) ratio of cooling stresses at the external and internal coating interface for cylindrical and spherical substrate**